EFFICIENT ANALYSIS OF MICROWAVE POLARIZER WITH FINITE METALLIZATION THICKNESS AND NOVEL DESIGN OF POLARIZATION ROTATOR

ANG TENG WAH

(B.Eng.(Hons.), M.Eng., NTU)

A THESIS SUBMITTED

FOR THE DEGREE OF DOCTOR OF PHILOSOPHY

DEPARTMENT OF ELECTRICAL AND COMPUTER

ENGINEERING

NATIONAL UNIVERSITY OF SINGAPORE

2011

Declaration

I hereby declare that this thesis is my original work and it has been written by me in its entirety. I have duly acknowledged all the sources of information which have been used in the thesis.

This thesis has also not been submitted for any degree in any university previously.

Ang Teng Wah

29 November 2011

Acknowledgment

I would like to express my sincere gratitude to my supervisor, Professor Yeo Tat Soon, for his guidance and continuous support of my Ph.D study and research. His advice, patience and understanding is greatly appreciated and will not be forgotten.

My heartfelt appreciation to friends and colleagues: Huang Yingying, Ho Kwee Yian, Loh Kar Wing Isaac and Neo Hong Kim Anders, who generously provided their friendship, help and advice over the years. The journey would have been much tougher without them.

My deepest gratitude goes to Chan Kwok Kee – an inspiring mentor and long-time friend who never fails to amaze me with his knowledge, advice and sense of humor.

Eternal gratitude goes to my parents (Boh Ha and Siam Kiaw) and sisters (May Pheng and Mei Ling) for their loving support and encouragement. Many thanks for supporting me in all my pursuits and the comforting words whenever I feel down.

My grateful and loving thanks to my wife, Hui Ming, for her patience and constant support while I juggle both work and study. It would have been impossible for me to complete my Ph.D study and research without her love, encouragement and understanding.

For God – from whom all wisdom and knowledge flow

Contents

Summary

Microwave polarizers are used extensively in commercial and military applications as they provide an effective means to convert electromagnetic waves from one polarization state/angle to another desired polarization state/angle. With the advent of modern communications and scanning array systems in recent years, the polarization rotator (180° microwave polarizer) has found many applications in commercial and military systems. However, most of the reported polarization rotators are cumbersome and complex to implement as they are constructed from multiple layers of linear grids spaced approximately quarter wavelength apart. In addition, little information on the performance against oblique incidence and rotation angles are available. In this dissertation, a novel polarizer rotator design which minimizes the number of rotating mechanism while maintaining good cross polarization isolation is proposed. The design, which is based on back-to-back stacking of two 90° polarizer incorporated with a linear grid layer, is simple to implement as it requires no more than two rotating mechanism. Depending on application, various implementation configurations are possible. A Ku band polarizer rotator based on the proposed concept was fabricated and characterized for various configurations against different wave incidence and polarization rotation angles. The viability of the proposed concept is validated by the good agreement between measured results and prediction.

In addition to a good design concept, it is equally critical that the method

used for analyzing the microwave polarizer is accurate and efficient. Currently, the numerical techniques used for the design and analysis of microwave polarizers either do not take into account the finite metallization thickness of the meanderline grid or requires excessive computation time. For microwave polarizer operating at high frequencies or constructed from heavy metal cladding, the omission of grid thickness will result in relative error between the actual and predicted performance. In this dissertation, a new method for analyzing microwave polarizer that takes into account the finite metallization thickness is presented. The method utilizes transverse resonance coupled with generalized scattering matrix and singular value decomposition to achieve a highly efficient algorithm suitable for design optimization routine. Numerical accuracy and efficiency of the proposed approach are validated by comparison with measurement results and finite element method.

List of Figures

List of Tables

Acronyms

BW	Bottom Wall
CW	Center Wall
EM	Electromagnetic
FEM	Finite Element Method
GRS	Golden Ratio Search
GSM	Generalized Scattering Matrix
LW	Left Wall
MLG	Meanderline Waveguide
PEC	Pecfert Electric Conductor
PMC	Perfect Magnetic Conductor
RW	Right Wall
SATCOM	Satellite Communications
SVD	Singular Value Decomposition
TE	Transverse Electric
TEM	Transverse Electromagnetic
TM	Transverse Magnetic
TW	Top Wall
VSAT	Very Small Aperture Terminal

Chapter 1

Introduction

1.1 Overview

Polarizers are used in practice to convert Electromagnetic (EM) waves from one polarization state/angle to another desired polarization state/angle. The applications of polarizer are many and varied, ranging over much of the electromagnetic spectrum from microwave to the optical region. In the microwave region, polarizers are often used in conjunction with antennas to achieve various radiation characteristics which would otherwise be impossible or too costly to realize. Examples of commercial and military applications where microwave polarizers are employed include: reduction of aperture blockage and feed mismatch in Cassegrain antennas [1; 2], conversion of linear to circular polarization for Satellite Communications (SATCOM) [3], low-inertia and fast mechanical polarization steering system for seeker antennas [4–6], automatic target recognition system for achieving polarization diversity [7], and reduction of radar cross-section [8].

In general, microwave polarizers can be broadly classified into three classes: (1) 180° polarizer, also known as polarization rotator, which rotates a linearly polarized EM field by an arbitrary angle while maintaining the field's linearly polarized state; (2) 90° polarizer which converts a linearly polarized EM field into a circularly polarized EM field and vice versa, and (3) linear grid polarizer that is used to reject EM field that is non-orthogonal to the grid axis.

To illustrate the usefulness of the microwave polarizer, consider an array of vertically polarized horn antennas shown in Figure 1.1 below. The horn array has limited scan range as the width of the waveguide feed section, a, is typically 0.6 – 0.7 wavelength in length. To overcome this limitation, the horn antennas can be arranged in a horizontally polarized configuration and a polarization rotator (180° microwave polarizer) employed to achieve a 90° polarization angle rotation for the wave emanating from the horn antennas as shown in Figure 1.2. While the vertically polarized scanning array could also be realized using a two dimensional array, the use of microwave polarizer, together with horn array, minimizes the RF losses and implementation complexity.

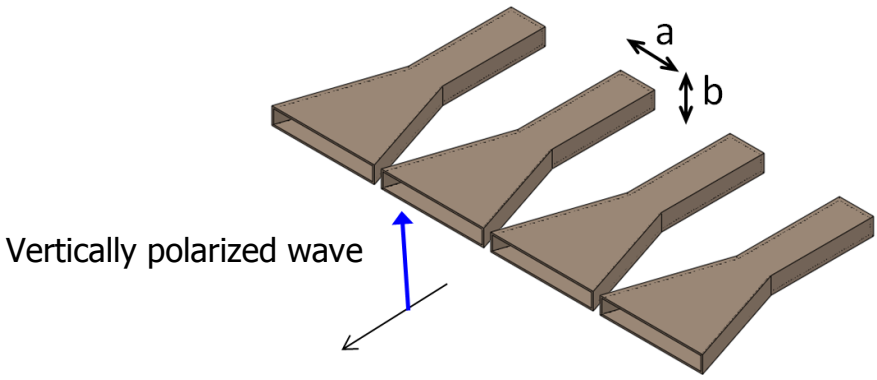

Figure 1.1: Vertically polarized horn array

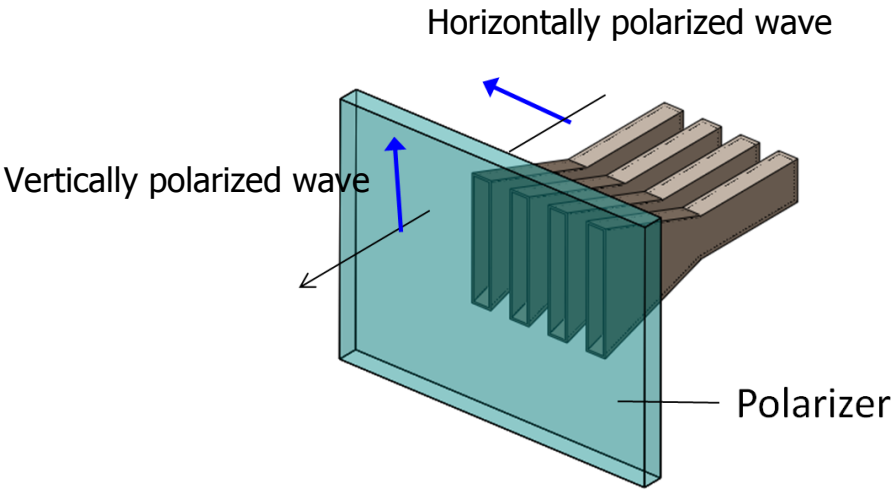

Figure 1.2: Horn array with microwave polarizer

In recent years, there is also increasing interest to replace conventional reflector antennas with phased array antenna for mobile satellite communications. In satellite communications, the satellite operators frequently employ polarization diversity as one of the means to increase capacity. As such, cross polarization isolation better than 20 – 25 dB are typically imposed on users transmitting at maximum allowable power. While 25 dB cross polarization isolation is achievable in reflector antenna, it is a significant challenge for phased array antenna because the plane of wave incidence does not usually coincide with the antenna principal planes. While electronic polarization tracking can be implemented, the prohibitive costs required to realize and implement such a design is likely to deter its widespread adoption. A more pragmatic approach is to make use of a polarization rotator (180° microwave polarizer) to achieve polarization tracking while the phased array antenna handles the beam scanning function. In this way, costs and complexity can be reduced significantly as the phased array antenna can be single polarized instead of dual polarized.

Currently, most of the 180° polarizers reported in literatures are constructed from multiple layers of independently rotating linear grids which require complex rotating mechanism to realize. In addition, discussion on design and elec-

trical performance are mainly confined to normal incidence. Given that scanning array antennas with polarization tracking capabilities are gaining prevalence in many commercial and military SATCOM systems, there is a strong desire for polarization rotator design that is relatively simple to implement and can function well under both on- and off-axis conditions.

Besides a pragmatic design concept, it is also critical that appropriate numerical methods are developed to model and analyze microwave polarizer. Since microwave polarizer design is a parametric optimization process that involves multiple iterations, efficiency is an extremely important criterion besides numerical accuracy. While various authors have dealt with efficient analysis of microwave polarizers in the past [1; 9–13], the key assumption has always been that metallization thickness of the grid is assumed to be infinitely thin. For operating frequency above X-band or when heavy metal cladding is used, this approximation will result in noticeable discrepancy between the measured and predicted performance.

1.2 Contributions

This dissertation strives to solve some of the challenges associated with the design, analysis and implementation of practical microwave polarizer. The original contributions arising from the dissertation are,

1. A new method for analyzing microwave polarizer with finite metallization thickness through the use of transverse resonance, generalized scattering matrix and singular value decomposition. This method overcomes the limitations of current techniques, such as network model method, periodic Green's function, and grid current approach, by allowing the thickness of the meanderline grid to be modelled which is otherwise assumed to be zero. The accuracy and efficiency of the proposed method makes it well suited for use as a microwave polarizer design tool.
2. A novel design concept for 180° meanderline polarizer with good cross polarization isolation that enables up to 45° off-axis illumination. The concept is based on back-to-back stacking of two 90° polarizers incorporated with a linear grid layer. This design is able to achieve good cross polarization isolation using no more than two rotating layers. Compared to conventional multiple rotating grids design, the proposed design is an effective solution for tracking systems which require polarization tuning capabilities with minimal implementation complexity.
3. Investigation into electrical properties and performance of polarization rotators. Performance characteristics such as insertion loss and cross polarization isolation for different wave incidence angles and vector rotation are measured and analyzed. Such data, which has not been reported in open literatures, provides important guideline and performance limits for use in design of polarizer rotators.

1.3 Publications

The publications arising from the work in this dissertation are as follows,

1. K. K. Chan, T. W. Ang, T. H. Chio and T. S. Yeo. Accurate Analysis of Meanderline Polarizers with Finite Thickness Using Mode Matching. *IEEE Trans. Antennas and Propagat.*, AP-56(11): 3580 – 3585, November 2008.
2. T. W. Ang, Y. Y. Huang and K. K. Chan. Investigation of a Low Profile Phased Array for Mobile Ku-Band Satcom Terminals. *Int. Symp. on Antennas and Propagat.*, Macao, China, November 2010.
3. T. W. Ang, K. K. Chan, T. S. Yeo and J. T. Goh. Analysis and Design of Polarization Rotator. To appear in *Asia Pacific Microwave Conference*, Melbourne, Australia, December 2011.
4. T. W. Ang, K. K. Chan and T. S. Yeo. An Efficient Method for Analyzing Microwave Polarizer with Finite Grid Thickness. To appear in *Progress in Electromagnetics Research Symposium*, Kuala Lumpur, Malaysia, March 2012.
5. T. W. Ang, T. S. Yeo and K. K. Chan. An Efficient Approach to Root Finding for Transverse Resonance and Modal Analysis Problems. *IEE Electronics Letter*, (manuscript in preparation).
6. T. W. Ang, T. S. Yeo and K. K. Chan. Design, Analysis and Measurement of Polarization Rotator with Good Cross-Polarization Isolation. *IEEE Trans. Microwave Theory and Techniques*, (manuscript in preparation)

1.4 Thesis Organization

This thesis is organized into six chapters. Chapter 1 provides a review of the work conducted by various researchers on the analysis of microwave polarizer and design of polarization rotators. Chapter 2 describes a novel polarization rotator design concept that minimizes the number of rotating mechanisms while maintaining good cross polarization isolation for wave incidence up to 45°. Chapter 3 presents the measurement results of a polarization rotator designed and fabricated using the concept described in Chapter 2. An efficient and accurate method to analyze meanderline polarizer with finite metallization thickness is presented in Chapter 4. In Chapter 5, validation of the new method against measurement data and other numerical tools are presented. Finally, concluding discussion and recommendations for follow-on research are discussed in Chapter 6.

1.5 Literature Review

The first practical microwave polarizer based on printed technology was demonstrated by Lerner [14]. A 90° polarizer was designed and fabricated by Lerner using three sheets of copper clad fiberglass laminate spaced by fiberglass honeycomb core and photo-etched with strips and rectangular patches. The fabricated polarizer has approximately 20 percent bandwidth with insertion loss and axial ratio within 0.5 dB and 1.7 dB respectively. However, one problem of Lerner's design was the need to fabricate very thin copper traces in the order of 4–6 thousandth of a wavelength; and such fine tolerances were difficult to achieve in those days.

In 1966, Stanford Research Institute conceived the meanderline polarizer and reported the computer program used in the design in 1969 [15]. The concept behind the meanderline polarizer is that it appears to be predominantly

inductive to one polarization and predominantly capacitive to the orthogonal polarization. Compared to Lerner's design at the same bandwidth and center frequency, meanderline structure is larger in dimension and hence much easier to fabricate. In addition, meanderline elements are effective over a wider bandwidth and scan angle. Expanding on the work of Stanford Research Institute, Young et al. [16] demonstrated a four layer meanderline polarizer with foamed plastic spacer that exhibited an axial ratio of better than 1.5 dB at normal incidence over the 8–12 GHz band. Since the pioneering work by Stanford Research Institute, meanderline element has been widely regarded as the *de facto* configuration to use when constructing 90° and 180° microwave polarizers.

Numerical techniques commonly used to analyze and design microwave polarizers can be broadly divided into two categories: network model based technique [1; 9; 10; 16] and numerical techniques based on periodic formulations such as Floquet Mode Expansion [11–13; 17] or periodic Green's function [18–22]. In network model based technique, the polarizer is modelled using equivalent circuit with lumped inductive and capacitive elements where the values of the inductors and capacitors are found empirically or numerically. This technique is conceptually easy to understand and requires relatively little computing resources. Thus, it was used extensively by early researchers designing meanderline polarizers [14–16; 23–25].

Chu and Lee [10] derived empirical formulas for the admittances of meanderline polarizer with respect to the incident frequency and polarization. The formulas were then used to construct the T-matrix of the equivalent network model of a multilayer meanderline polarizer. In the paper, only the results for normal incident plane waves were presented and these showed fair agreement with the theory developed.

Although network model provides an intuitive way to design meanderline polarizers, results showed that accuracy of the empirical network model de-

grades with increasing angle of incidence. According to Chan et al. [12], this is because network model did not take into account the effect of mode coupling at each grid interface. The pursuit for better correlation between numerical models and experiments led some researchers to apply Floquet Mode Expansion Moment Method to the modelling of meanderline polarizer. In Floquet Mode Expansion method, the incident plane wave is represented using Floquet mode expansion and the scattering characteristics of the polarizer are obtained by solving for the currents on the polarizer elements using techniques such as integral equations, modal analysis, etc. Using full wave analysis, it is possible to achieve accurate solution for most polarizer configuration.

Compared to the network model method, the Floquet Mode Expansion method requires significantly more computational resources as the formulation and solution processes are more rigorous. As practical polarizers deployed in operational systems are usually constructed from complex multilayered configuration in order to meet the bandwidth and scan angle requirements, this was one of the main reason why practical polarizers designed using Floquet Mode Expansion method were reported only from the 1990s onward when computers are sufficiently powerful and affordable to enable design optimization to be conducted efficiently.

The theoretical foundation for Flouqet Mode Expansion analysis of meanderline polarizer can be attributed to the work of Chen [26] and Montgomery [27]. The problem of scattering by an infinite array of thin plates arranged in a doubly periodic grid in free space was treated by Chen using Floquet's theorem and integral equations formulation. Montgomery expanded on the work to treat the unsymmetrical problem of scattering by an infinite periodic array of thin conductors on a dielectric sheet. Although Chen and Montgomery did not apply their techniques to the analysis of meanderline polarizer, the concepts presented in their publications were later employed by researchers working on

meanderline polarizer.

One of the first published work on the analysis of meanderline polarizer using Floquet Mode Expansion technique was by Terret et al. [9]. In the paper, Floquet mode expansion of the incident plane wave and point matching were used to compute the susceptance of meanderline arrays. Comparison between the computed and measured susceptance showed good agreement. Subsequently, various authors have published works in support of the accuracy of this approach [17; 19; 28].

Chan and Gauthier [11]; Chan et al. [12] were one of the first to report a fabricated broadband widescan meanderline polarizer using modal technique similar in concept to that described by Montgomery [27]. By representing the current distribution on the conducting surface as a collection of strip currents flowing along the meanderline structure, the authors mentioned they are able to treat a wider variety of configurations. A seven layer meanderline polarizer was fabricated and the axial ratio and insertion loss were measured to be less than 2.2 dB and 0.2 dB respectively over the band 4–8 GHz for incident angles up to 40° [12].

In both the network model and Floquet Mode Expansion Moment Method that have been published to date, the metallization thickness is assumed to be infinitely thin, this assumption is especially essential for methods based on the later technique. However, for microwave polarizers with electrically thick metallization, this assumption will lead to discrepancies between the measured and predicted polarizer performance.

In the early days, most of the published works on microwave polarizers were on 90° meanderline grids which are used for the conversion between linear and circular polarization state [2; 3; 10; 12; 14–16; 23]. With the advent of modern communications and scanning array systems, the 180° polarizer has found many important commercial and military applications although the design of

such polarization rotators are rarely discussed in detail. Examples include Very Small Aperture Terminal (VSAT) systems which requires rapid and precise polarization tracking to maintain communication link between satellites and mobile ground platforms [29–32], defense systems which make use of polarization sensing to defeat incoming threats [33; 34], and Cassegrain antennas [35].

To date, the 180° polarizers published are mostly based on multiple layers of linear or straight grids spaced approximately quarter wavelength apart [36–38]. In such a linear grid polarizer rotator system, the layers are arranged in various inclination angles to rotate the polarization of a linearly polarized wave. Depending on the angle of rotation, wave incidence angle and frequency bandwidth, a complex rotator system is required as three or more independent rotating polarizer layers are typically needed. Examples include a four grid design reported by Gimeno et al. [36] and a five layer design by Lech et al. [38] recently.

Published papers on polarization rotators have little information on the electrical properties and performance such as cross-polarization discrimination, frequency bandwidth and mismatch for oblique incidence against rotation angles. Only one paper, published by Wu [39], investigated the use of 180° meanderline polarizer for rotation of linearly polarized EM wave. Even then, there are results only for normal incidence and one angle of rotation.

Chapter 2

Novel Design of Microwave Polarizer Rotator

The basic working principle of a meanderline polarizer is illustrated in Figure 2.1. An incoming EM wave impinging on a meanderline polarizer can be decomposed into two orthogonal components, i.e. Transverse Electric (TE) and Transverse Magnetic (TM) components. Through judicious design of the meanderline grid, the TE and TM components can be made to undergo a 90° or 180° relative phase difference after passing through the screen. A 90° relative phase shift will generate a circularly polarized wave while a 180° phase shift will result in a rotation of the polarization angle.

While 90° meanderline polarizers are well discussed in literatures [2; 3; 10; 12; 14–16; 23], it is the polarization rotator (180° polarizer) that has attracted many important commercial and military applications in recent years [29–35].

In this chapter, a novel polarizer rotator design for arbitrary rotation of linearly polarized wave with good cross-polarization discrimination will be proposed. The design minimizes the number of rotating mechanisms required; leading to less complex rotator and controller network compared to conventional rotators [36–38]. A series of rotator configurations based on this novel

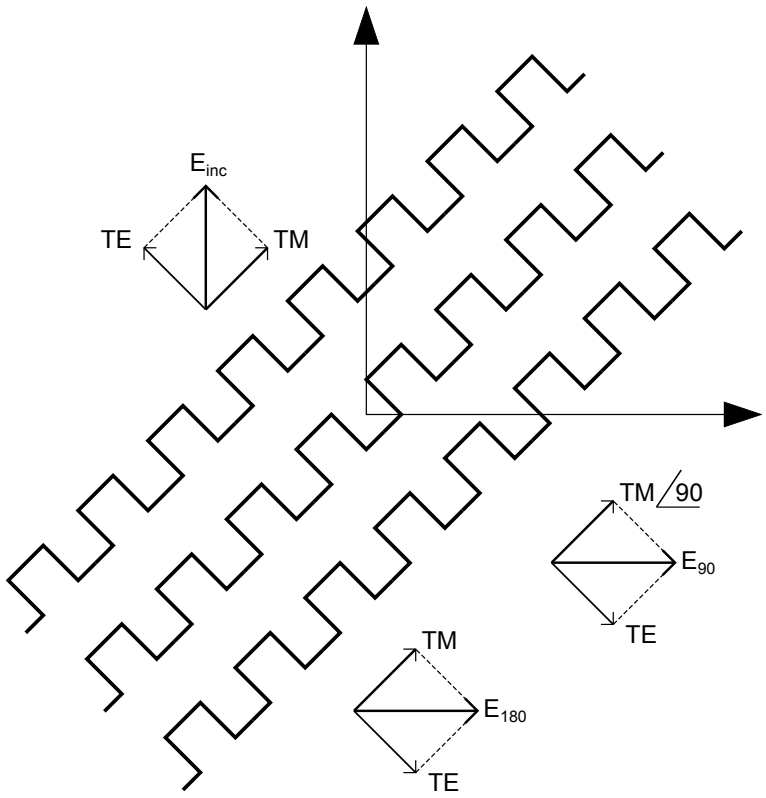

Figure 2.1: Basic principle of meanderline polarizer

design will be analyzed to quantify their electrical performances.

2.1 Analysis Approach

There exist a number of approaches to analyze periodic structures such as polarizer screen [10; 12; 13; 16; 24; 28; 40]. This section describes a method, based on grid current and mode matching techniques, that was used to analyze and design the polarization rotator.

Microwave meanderline polarizers can be viewed as a form of periodic structure in which each periodic cell consists of two vertical and three horizontal metallic strips as shown in Figure 2.2. By assuming the meanderline line polarizer to be infinite in extent, an accurate mathematical modelling based on Floquet's theorem [41] is applicable to the problem.

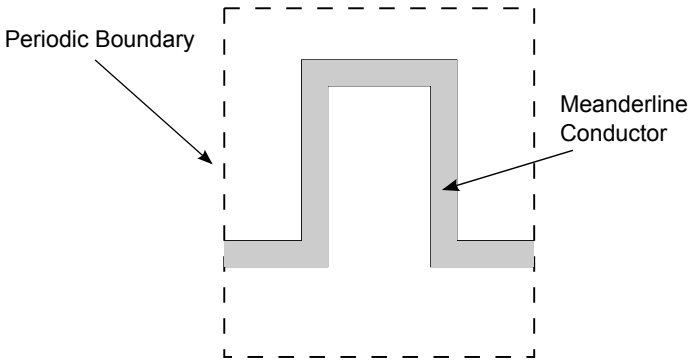

Figure 2.2: Periodic meanderline cell

Using Floquet theorem, the fields above each meanderline periodic cell can be expressed in terms of a complete orthogonal set of modes termed Floquet modes. These Floquet modes and the induced current on the meanderline metallic strips will enable the formulation of the meanderline polarizer boundary value problem in terms of a series of integral equations.

Consider the case of a single layer meanderline polarizer screen illustrated in Figure 2.3. An EM wave incidenting at an angle (θ, ϕ) will generate induced current on the metallic conductors which manifests itself as reflected and transmitted waves. Different scattering characteristics can be generated by changing the geometrical dimensions of the meanderline.

The meanderline polarizer screen can be viewed as constructed from an array of identical meanderline cells as shown in Figure 2.4. The fields induced in each cell by an incident EM wave will be identical except for a phase shift between adjacent cells. Using Floquet theorem, the problem reduces to the solution of scattering from a unit cell of meanderline element with periodic boundary conditions as imposed by the vector Floquet modes. The vector Floquet modes can then be used to derive the vector TE and TM Floquet modes, where TE and TM modes have no electric field and magnetic field component in the direction of propagation (z direction), respectively.

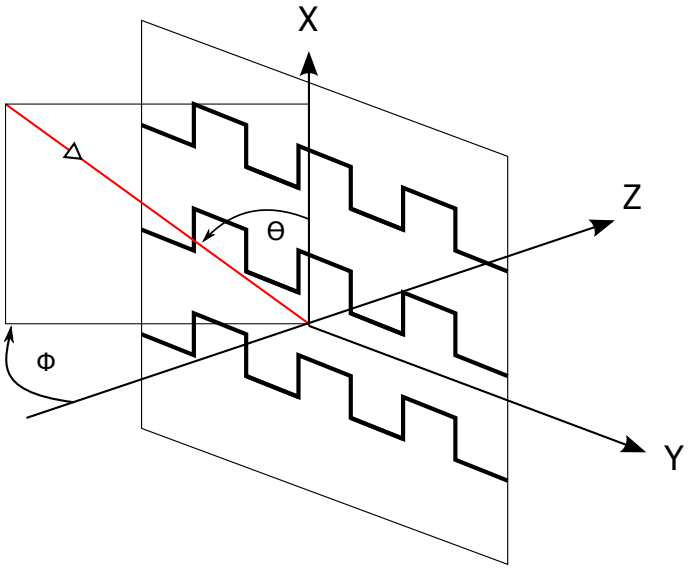

Figure 2.3: Meanderline polarizer with incident wave

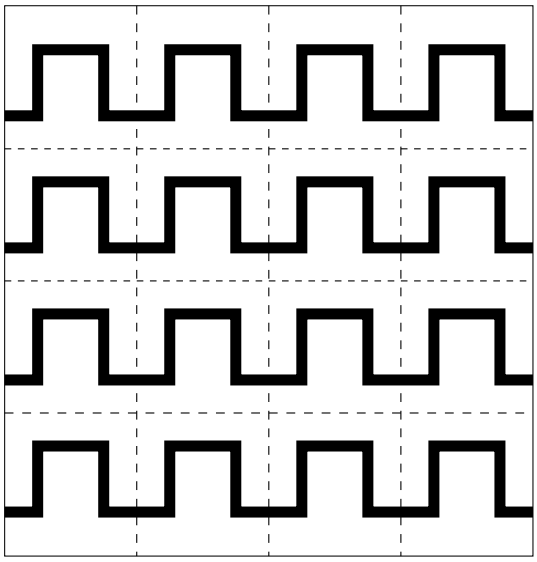

Figure 2.4: Rectangular lattice of meanderline array

2.1.1 TE modes

Let $\xi_{mn}(x,y) = H_{z_{mn}}(x,y)$ and $E_z = 0$. The corresponding transverse fields are then derived from $H_{z_{mn}}$ by [42],

$$\begin{aligned} \bar{E}_{t_{mn}} &= \frac{j\omega u}{k_{r_{mn}}^2}\hat{u}_z \times \nabla_t H_{z_{mn}} \\ \text{and} \quad \bar{H}_{t_{mn}} &= \frac{j\Gamma_{mn}}{k_{r_{mn}}^2}\nabla_t H_{z_{mn}} \end{aligned}$$

where $k_{r_{mn}}$ and Γ_{mn} are the wavenumbers associated with the propagation vector $\bar{k}$,

$$\begin{aligned} k_{r_{mn}}^2 &= k_{x_m}^2 + k_{y_n}^2 = k^2 - \Gamma_{mn}^2 \\ \text{and} \quad \nabla_t &= \hat{u}_x\frac{\partial}{\partial x} + \hat{u}_y\frac{\partial}{\partial y} = j(\hat{u}_x k_{x_m} + \hat{u}_y k_{y_n}) \end{aligned}$$

To obtain the orthonormalized vector Floquet mode, define :

$$\bar{E}_{t_{mn}} = \frac{\omega\mu}{k_{r_{mn}}}\Psi_{1mn}(x,y)$$

From above,

$$\bar{E}_{t_{mn}} = \frac{j\omega\mu}{k_{r_{mn}}^2}\left(-\hat{u}_x\frac{\partial\xi}{\partial y} + \hat{u}_y\frac{\partial\xi}{\partial x}\right)$$

From the scalar Floquet modes,

$$\bar{E}_{t_{mn}} = \frac{\omega\mu}{k_{r_{mn}}}\sqrt{\frac{1}{bd}}\left(\frac{k_{y_n}\hat{u}_x - k_{x_m}\hat{u}_y}{k_{r_{mn}}}\right)e^{j(k_{x_m}x + k_{y_n}y)}$$

Therefore, the orthonormalized vector TE Floquet mode is given by,

$$\bar{\Psi}_{1mn} = \sqrt{\frac{1}{bd}}\left(\frac{k_{y_n}\hat{u}_x - k_{x_m}\hat{u}_y}{k_{r_{mn}}}\right)e^{j(k_{x_m}x + k_{y_n}y)}$$

Similarly,

$$\iint_{A_p} \Psi_{1mn}\Psi^*_{1m'n'}\,\mathrm{d}x\,\mathrm{d}y = \delta_{mm'}\,\delta_{nn'}$$

The TE modal admittance is given by,

$$Y_{1mn} = \frac{\Gamma_{mn}}{\omega\mu}$$

2.1.2 TM modes

Let $\xi_{mn}(x,y) = E_{z_{mn}}(x,y)$ and $H_z = 0$. The corresponding transverse fields are then derived from $E_{z_{mn}}$ by,

$$\begin{aligned}
\bar{H}_{t_{mn}} &= \frac{j\omega\epsilon}{k^2_{r_{mn}}}\hat{u}_z \times \nabla_t E_{z_{mn}} \\
\text{and}\quad \bar{E}_{t_{mn}} &= -\frac{j\Gamma_{mn}}{k^2_{r_{mn}}}\nabla_t E_{z_{mn}} \\
\text{where}\quad k^2_{r_{mn}} &= k^2_{x_m} + k^2_{y_n} = k^2 - \Gamma^2_{mn} \\
\nabla_t &= \hat{u}_x\frac{\partial}{\partial x} + \hat{u}_y\frac{\partial}{\partial y} = j(\hat{u}_x k_{x_m} + \hat{u}_y k_{y_n})
\end{aligned}$$

To obtain the orthonormalized vector Floque mode, define :

$$\bar{E}_{t_{mn}} = \frac{\Gamma_{mn}}{k_{r_{mn}}}\Psi_{2mn}(x,y)$$

From above,

$$\bar{E}_{t_{mn}} = -\frac{j\Gamma_{mn}}{k^2_{r_{mn}}}\left(\hat{u}_x\frac{\partial\xi}{\partial x} + \hat{u}_y\frac{\partial\xi}{\partial y}\right)$$

From the scalar Floquet modes,

$$\bar{E}_{t_{mn}} = \frac{\Gamma_{mn}}{k_{r_{mn}}}\sqrt{\frac{1}{bd}}\left(\frac{k_{x_m}\hat{u}_x + k_{y_n}\hat{u}_y}{k_{r_{mn}}}\right)e^{j(k_{x_m}x + k_{y_n}y)}$$

Therefore, the orthonormalized vector TM Floquet mode is given by,

$$\bar{\Psi}_{2mn} = \sqrt{\frac{1}{bd}} \left(\frac{k_{x_m}\hat{u}_x + k_{y_n}\hat{u}_y}{k_{r_{mn}}} \right) e^{j(k_{x_m}x + k_{y_n}y)}$$

Similarly,

$$\iint_{A_p} \Psi_{pmn}\Psi^*_{pm'n'}\,\mathrm{d}x\,\mathrm{d}y = \delta_{pp'}\delta_{mm'}\,\delta_{nn'}$$

where $\delta_{pp'}$ indicated that the TE and TM modes are mutually orthogonal. The TM modal admittance is given by,

$$Y_{2mn} = \frac{\omega\epsilon}{\Gamma_{mn}}$$

2.1.3 Integral Equation Formulation

Based on the coordinate axes shown in Figure 2.3, the transverse incident electric and magnetic field vectors in the negative z-region are given by,

$$\begin{aligned} \bar{E}_t^{inc(-)}(r) &= \bar{E}_t^{TE} + \bar{E}_t^{TM} \\ &= \sum_p \sum_m \sum_n \frac{e^{-jk_{z_{mn}}z}}{\sqrt{bd}} e^{-j(\bar{k}_{t_{mn}}\cdot\hat{r}_t)} \hat{k}_{pmn}\sqrt{\eta_{pmn}}a^-_{pmn} \end{aligned}$$

$$\begin{aligned} \bar{H}_t^{inc(-)}(r) &= \bar{H}_t^{TE} + \bar{H}_t^{TM} \\ &= \sum_p \sum_m \sum_n \frac{e^{-jk_{z_{mn}}z}}{\sqrt{bd}} e^{-j(\bar{k}_{t_{mn}}\cdot\hat{r}_t)} \frac{a^-_{pmn}}{\sqrt{\eta_{pmn}}} \hat{z} \times \hat{k}_{pmn} \end{aligned}$$

$$\eta_{1mn} = \frac{\omega\mu}{k_{z_{mn}}} \quad , \quad \eta_{2mn} = \frac{k_{z_{mn}}}{\omega\epsilon}$$

where $p = 1$ or 2 denotes TE or TM incident wave, respectively.

Similarly, the transverse reflected fields in the negative z-region are given

by,

$$\bar{E}_t^{ref(-)}(r) = \sum_p \sum_m \sum_n \frac{e^{+jk_{z_{mn}}z}}{\sqrt{bd}} e^{-j(\bar{k}_{t_{mn}}\cdot\hat{r}_t)} \hat{k}_{pmn}\sqrt{\eta_{pmn}} b^-_{pmn}$$

$$\bar{H}_t^{ref(-)}(r) = \sum_p \sum_m \sum_n \frac{e^{+jk_{z_{mn}}z}}{bd} e^{-j(\bar{k}_{t_{mn}}\cdot\hat{r}_t)} \frac{b^-_{pmn}}{\sqrt{\eta_{pmn}}} \hat{z} \times \hat{k}_{pmn}$$

In the positive z-region, the transverse incident electric and magnetic field vectors are given by,

$$\bar{E}_t^{inc(+)}(r) = \sum_p \sum_m \sum_n \frac{e^{+jk_{z_{mn}}z}}{\sqrt{bd}} e^{-j(\bar{k}_{t_{mn}}\cdot\hat{r}_t)} \hat{k}_{pmn}\sqrt{\eta_{pmn}} a^+_{pmn}$$

$$\bar{H}_t^{inc(+)}(r) = \sum_p \sum_m \sum_n \frac{e^{+jk_{z_{mn}}z}}{\sqrt{bd}} e^{-j(\bar{k}_{t_{mn}}\cdot\hat{r}_t)} \frac{a^+_{pmn}}{\sqrt{\eta_{pmn}}} \hat{z} \times \hat{k}_{pmn}$$

Similarly, the transverse reflected fields in the positive z-region are given by,

$$\bar{E}_t^{ref(+)}(r) = \sum_p \sum_m \sum_n \frac{e^{+jk_{z_{mn}}z}}{\sqrt{bd}} e^{-j(\bar{k}_{t_{mn}}\cdot\hat{r}_t)} \hat{k}_{pmn}\sqrt{\eta_{pmn}} b^+_{pmn}$$

$$\bar{H}_t^{ref(+)}(r) = \sum_p \sum_m \sum_n \frac{e^{+jk_{z_{mn}}z}}{\sqrt{bd}} e^{-j(\bar{k}_{t_{mn}}\cdot\hat{r}_t)} \frac{b^+_{pmn}}{\sqrt{\eta_{pmn}}} \hat{z} \times \hat{k}_{pmn}$$

Enforcing the continuity of electric field across the meanderline screen,

$$\bar{E}_t^{inc(-)} + \bar{E}_t^{ref(-)} = \bar{E}_t^{inc(+)} + \bar{E}_t^{ref(+)}$$

$$\sum_p \sum_m \sum_n \frac{e^{-jk_{z_{mn}}z}}{\sqrt{bd}} e^{-j(\bar{k}_{t_{mn}}\cdot\hat{r}_t)} \hat{k}_{pmn}\sqrt{\eta_{pmn}} (a^-_{pmn} + b^-_{pmn})$$
$$= \sum_{p'} \sum_{m'} \sum_{n'} \frac{e^{+jk_{z_{m'n'}}z}}{\sqrt{bd}} e^{-j(\bar{k}_{t_{m'n'}}\cdot\hat{r}_t)} \hat{k}_{p'm'n'}\sqrt{\eta_{p'm'n'}} (a^+_{p'm'n'} + b^+_{p'm'n'})$$

$$\sum_{p}\sum_{m}\sum_{n}\Psi_{pmn}(x,y,0)(a^{-}_{pmn}+b^{-}_{pmn}) = \sum_{p'}\sum_{m'}\sum_{n'}\Psi_{p'm'n'}(x,y,0)(a^{+}_{p'm'n'}+b^{+}_{p'm'n'})$$

Using the orthogonality of Floquet modes,

$$a^{-}_{pmn}+b^{-}_{pmn}=a^{+}_{pmn}+b^{+}_{pmn} \tag{2.1}$$

The boundary magnetic field must be continuous except at locations of the current on the meanderline conductors where it will be discontinuous,

$$\hat{z}\times\left(-\bar{H}_t^{inc(+)}+\bar{H}_t^{ref(+)}\right)-\hat{z}\times\left(\bar{H}_t^{inc(-)}+\bar{H}_t^{ref(-)}\right)=\bar{J}_s \tag{2.2}$$

where $\bar{J}_s$ denotes the induced current on the meanderline conductors.

$$\hat{z}\times\left\{-\sum_{p'}\sum_{m'}\sum_{n'}\frac{e^{-j(\bar{k}_{t_{m'n'}}\cdot\hat{r}_t)}}{\sqrt{bd}}\frac{\hat{z}\times\hat{k}_{p'm'n'}}{\sqrt{\eta_{p'm'n'}}}(a^{+}_{p'm'n'}-b^{+}_{p'm'n'}) -\sum_{p}\sum_{m}\sum_{n}\frac{e^{-j(\bar{k}_{t_{mn}}\cdot\hat{r}_t)}}{\sqrt{bd}}\frac{\hat{z}\times\hat{k}_{pmn}}{\sqrt{\eta_{pmn}}}(a^{-}_{pmn}-b^{-}_{pmn})\right\}=\bar{J}_s$$

$$\sum_{p'}\sum_{m'}\sum_{n'}\frac{e^{-j(\bar{k}_{t_{m'n'}}\cdot\hat{r}_t)}}{\sqrt{bd}}\frac{\hat{z}\times\hat{k}_{p'm'n'}}{\sqrt{\eta_{p'm'n'}}}(b^{+}_{p'm'n'}-a^{+}_{p'm'n'}) -\sum_{p}\sum_{m}\sum_{n}\frac{e^{-j(\bar{k}_{t_{mn}}\cdot\hat{r}_t)}}{\sqrt{bd}}\frac{\hat{z}\times\hat{k}_{pmn}}{\sqrt{\eta_{pmn}}}(a^{-}_{pmn}-b^{-}_{pmn})=\bar{J}_s\times\hat{z} \tag{2.3}$$

Taking the vector cross product of Equation (2.3) with Ψ^{*}_{quv} and integrating over the area of a periodic meanderline cell at the plane $z=0$, the first term

on the LHS of Equation (2.3) will be,

$$\iint_{A_p} \sum_{p'} \sum_{m'} \sum_{n'} \frac{1}{\sqrt{bd}} \quad \frac{e^{-j(\bar{k}_{t_{m'n'}} \cdot \hat{r}_t)}}{\sqrt{bd}} \frac{\hat{z} \times \hat{k}_{p'm'n'}}{\sqrt{\eta_{p'm'n'}}} (b^+_{p'm'n'} - a^+_{p'm'n'}) \times \Psi^*_{quv} \, \mathrm{d}\bar{s} = \frac{\left(a^+_{p'm'n'} - b^+_{p'm'n'}\right)}{\sqrt{\eta_{p'm'n'}}} \delta_{p'q} \, \delta_{m'u} \, \delta_{n'v}$$

Similarly,

$$\iint_{A_p} \sum_{p} \sum_{m} \sum_{n} \frac{1}{\sqrt{bd}} \quad \frac{e^{-j(\bar{k}_{t_{mn}} \cdot \hat{r}_t)}}{\sqrt{bd}} \frac{\hat{z} \times \hat{k}_{pmn}}{\sqrt{\eta_{pmn}}} (b^-_{pmn} - a^-_{pmn}) \times \Psi^*_{quv} \, \mathrm{d}\bar{s} = \frac{\left(a^-_{pmn} - b^-_{pmn}\right)}{\sqrt{\eta_{pmn}}} \delta_{pq} \, \delta_{mu} \, \delta_{nv}$$

Therefore,

$$\begin{aligned} \frac{\left(a^+_{p'm'n'} - b^+_{p'm'n'}\right)}{\sqrt{\eta_{p'm'n'}}} + \frac{\left(a^-_{p'm'n'} - b^-_{p'm'n'}\right)}{\sqrt{\eta_{p'm'n'}}} &= \iint_{A_p} \left[\left(\bar{J}_s \times \hat{z}\right) \times \bar{\Psi}^*_{p'm'n'}\right] \cdot \hat{z} \, \mathrm{d}s \\ &= \iint_{A_p} \bar{J}_s \cdot \bar{\Psi}^*_{p'm'n'} \, \mathrm{d}s \end{aligned} \tag{2.4}$$

Since there exist only scattered fields from the induced current,

$$\begin{aligned} a^- &= a^+ = 0 \\ b^-_{pmn} &= b^+_{pmn} \end{aligned}$$

Substituting Equation (2.5) into (2.4),

$$\begin{aligned} -2\frac{b^-_{pmn}}{\sqrt{\eta_{pmn}}} &= \iint_{A_p} \bar{J}_s \cdot \bar{\Psi}^*_{pmn}(x, y, 0) \, \mathrm{d}s \\ \therefore \quad b^+_{pmn} = b^-_{pmn} &= -\frac{\sqrt{\eta_{pmn}}}{2} \iint_{A_p} \bar{J}_s \cdot \bar{\Psi}^*_{pmn}(x, y, 0) \, \mathrm{d}s \end{aligned}$$

Alternatively, if there is no incident wave on the positive z-region of the mean-

derline screen, i.e. $a^{+}_{pmn} = 0$, the continuity of electric field implies that,

$$a^{-}_{pmn} + b^{-}_{pmn} = b^{+}_{pmn}$$

From the discontinuity of the magnetic field,

$$\begin{aligned} -\frac{b^{+}_{pmn}}{\sqrt{\eta_{pmn}}} + \frac{a^{-}_{pmn} - b^{-}_{pmn}}{\sqrt{\eta_{pmn}}} &= \iint_{A_p} \bar{J}_s \cdot \bar{\Psi}^{*}_{p'm'n'} \, \mathrm{d}s \\ -2\frac{b^{-}_{pmn}}{\sqrt{\eta_{pmn}}} &= \iint_{A_p} \bar{J}_s \cdot \bar{\Psi}^{*}_{p'm'n'} \, \mathrm{d}s \\ b^{-}_{pmn} &= -\frac{\sqrt{\eta_{pmn}}}{2} \iint_{A_p} \bar{J}_s \cdot \bar{\Psi}^{*}_{pmn} \, \mathrm{d}s \end{aligned}$$

The scattered electric field in the negative z-region is then given by,

$$\bar{E}^{ref(-)}_{t}(r) = -\sum_{p}\sum_{m}\sum_{n} \frac{e^{+jk_{z_{mn}}z}}{bd} e^{-j(\bar{k}_{t_{mn}}\cdot\hat{r}_t)} \hat{k}_{pmn} \frac{\eta_{pmn}}{2} \iint_{A_p} \bar{J}_s \cdot \hat{k}_{pmn} e^{+j(\bar{k}_{t_{mn}}\cdot\hat{r}_t)} \, \mathrm{d}s$$

On the surface of the meanderline conductors at $z = 0$, the total electric field will cease to exist, thereby giving the following integral equation,

$$\bar{E}^{inc(-)}_{t}(r) + \bar{E}^{ref(-)}_{t}(r) = 0 \qquad r \in A'$$

where A' is the meanderline conductor area.

$$\begin{aligned} &\sum_{p}\sum_{m}\sum_{n} \frac{e^{-j(\bar{k}_{t_{mn}}\cdot\hat{r}_t)}}{\sqrt{bd}} \hat{k}_{pmn} a^{-}_{pmn} \sqrt{\eta_{pmn}} \\ &\quad = \sum_{q}\sum_{u}\sum_{v} \frac{e^{-j(\bar{k}_{t_{uv}}\cdot\hat{r}_t)}}{bd} \hat{k}_{quv} \frac{\eta_{quv}}{2} \iint_{A'} \bar{J}_s \cdot \hat{k}_{quv} e^{+j(\bar{k}_{quv}\cdot\hat{r}_t)} \, \mathrm{d}s \end{aligned} \qquad (2.5)$$

The Integral Equation (2.5) above relates the unknown induced current, $\bar{J}_s$, to the incident modes, a^{-}_{pmn}, which are known. This unknown current can be represented as a collection of mesh or linear elements and solved using numerical techniques such as Boundary Element Method.

2.2 Proposed Polarization Rotator Concept

The use of multiple layers of linear or straight grids spaced approximately quarter wavelength apart to realize the 180° polarizer has been proposed by many authors [36–38]. In such a design, each of the linear grids is rotated slightly with respect to the preceding grid. The polarization of the incident and transmitted waves are orthogonal to linear grid #1 and #N, respectively. As the wave passes through each of the linear, grid, the polarization angle of the wave is rotated by a slight angle as shown in Figure 2.5. The major drawback for such a design is the need for three or more independent rotating polarizer layers. This poses significant challenge and complexity to the design of the rotator control system.

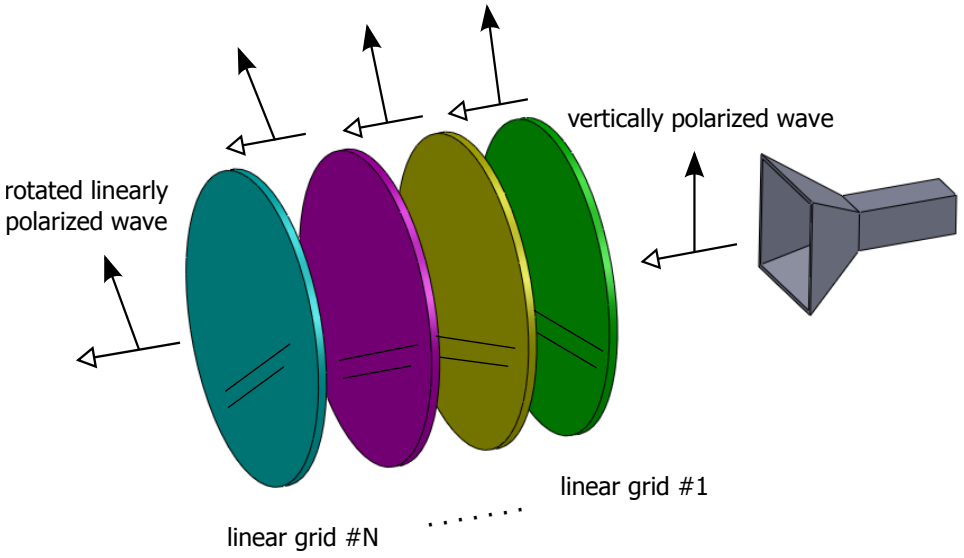

Figure 2.5: Conventional polarization rotator

To overcome the complexity of current design, this thesis proposes a polarizer rotator design that can: (1) achieve full polarization rotation of ±90°; (2) meets the 20 dB cross polarization isolation stipulated for typical satellite communications; and (3) requires no more than two rotating motors to implement.

To minimize the number of rotating layers, the polarizer rotator is constructed using two multi-layered 90° meanderline polarizers cascaded in a back-to-back configuration. The first 90° polarizer will convert the linearly polarized wave into circularly polarized wave. The wave is converted back to linearly polarized wave by the second 90° polarizer, Figure 2.6. To achieve cross polarization isolation better than 20 dB, a linear grid is incorporated on top of the back-to-back 90° meanderline polarizers.

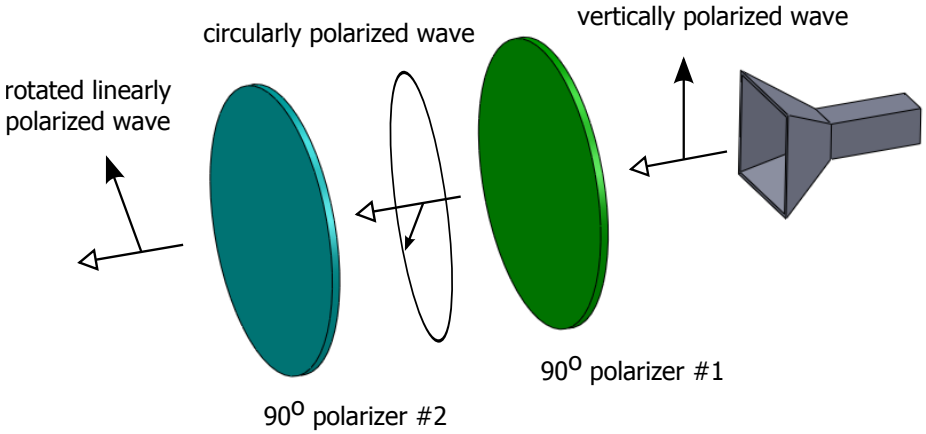

Figure 2.6: Concept of proposed polarization rotator

A number of configurations were derived from this rotator design. Configuration A is based on rotating both 90° polarizer in tandem with respect to the incidence wave. The polarization rotation angle will be twice the angle between the incident wave and polarizer axis. When the polarizer grid axis is parallel to the polarization of the incidence wave, there is no net rotation effect.

In Configuration B, the 90° polarizer grid #1 is fixed at 45° with respect to the underlying antenna array. By rotating the 90° polarizer grid #2, the circularly polarized wave generated by grid #1 will be converted back to linearly polarized wave whose angle is dependent on the angular offset between grid #1 and #2. When grid #2 is set to be orthogonal with respect to grid #1, there will be no polarization rotation effect.

2.3 Design of Polarizer

The 90° meanderline polarizer is the fundamental building block in the construction of the novel 180° polarizer. To minimize its thickness, a three layer design is chosen to realize the 90° meanderline polarizer. The polarizer design is optimized for operating frequency between 10.7 – 12.75 GHz and scan angle from 0° to 45°. The optimization criteria for the polarizer are: reflection coefficient less than -15 dB and axial ratio better than 2:1.

Design of the microwave polarizer is achieved using parametric optimization on the grid size, meanderline width, height, and spacing. The process begins with an initial grid size chosen such that there will be no onset of grating lobes at the highest frequency of operation and the widest scan angle. The thinnest meanderline width permitted by fabrication is set as the lower bound constraint. The final design is obtained using parametric optimization to achieve the best match for the required relative transmission phase across the frequency band of operation. The layout of the 3-layer 90° polarizer is shown in Figure 2.7 and the optimized dimensions of the individual grids are illustrated in Figure 2.8 and 2.9.

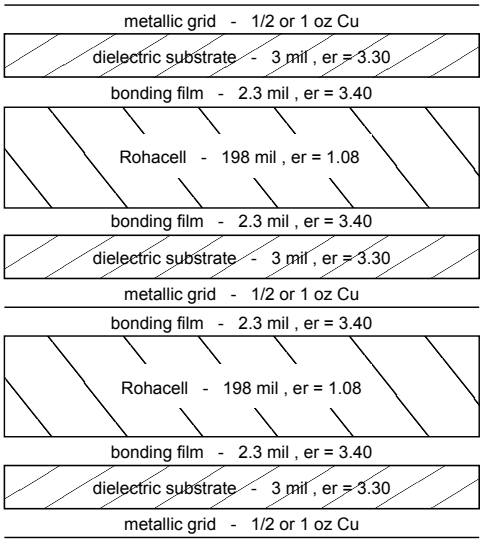

Figure 2.7: Geometry of 3-grid 90° meanderline polarizer

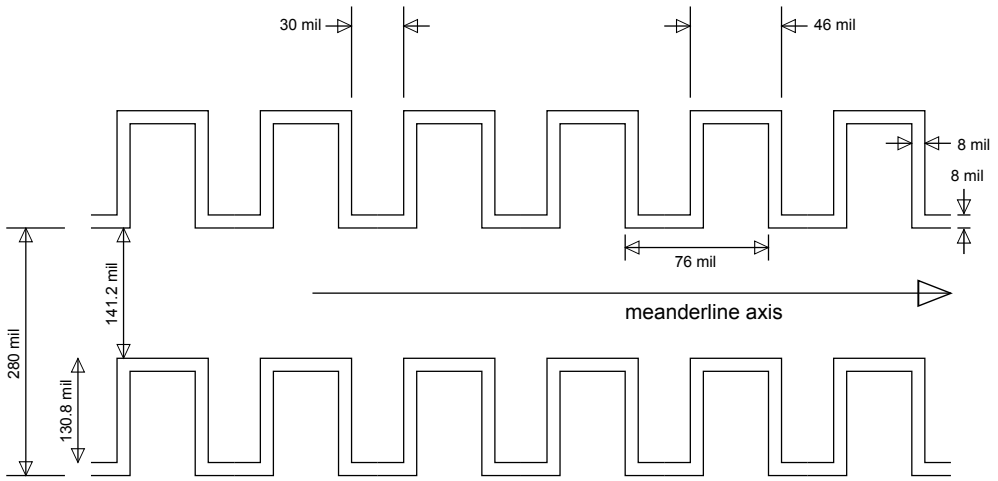

Figure 2.8: Dimension of metallic grid #1 and #3 for 90° meanderline polarizer

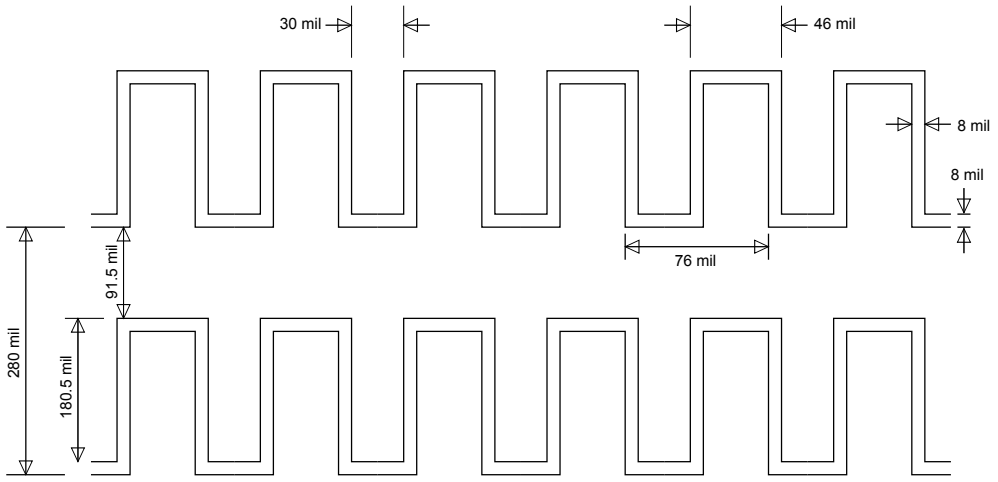

Figure 2.9: Dimension of metallic grid #2 for 90° meanderline polarizer

The reflection coefficient and axial ratio of the 90° polarizer are plotted in Figure 2.10 and 2.11, respectively. The results showed that the reflection coefficient and worst case axial ratio of 1.6:1 are better than the design targets. A good reflection coefficient and axial ratio are necessary to minimize the mismatch and cross-polarization isolation when two of these polarizers are cascaded together to form the 180° polarizer.

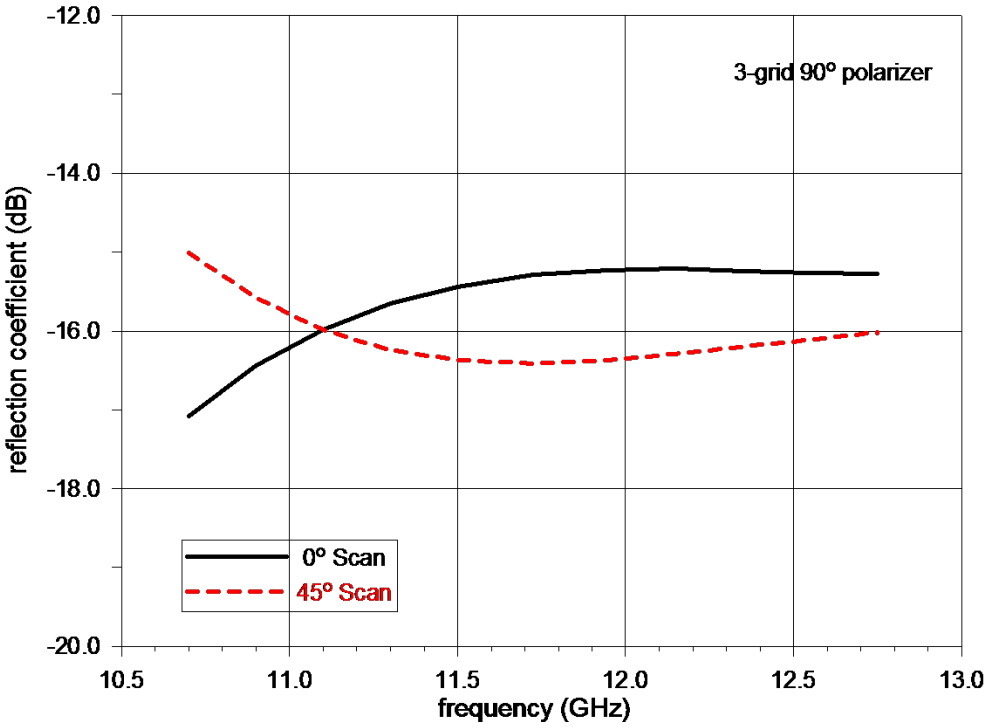

Figure 2.10: Reflection coefficient of 3-grid 90° meanderline polarizer

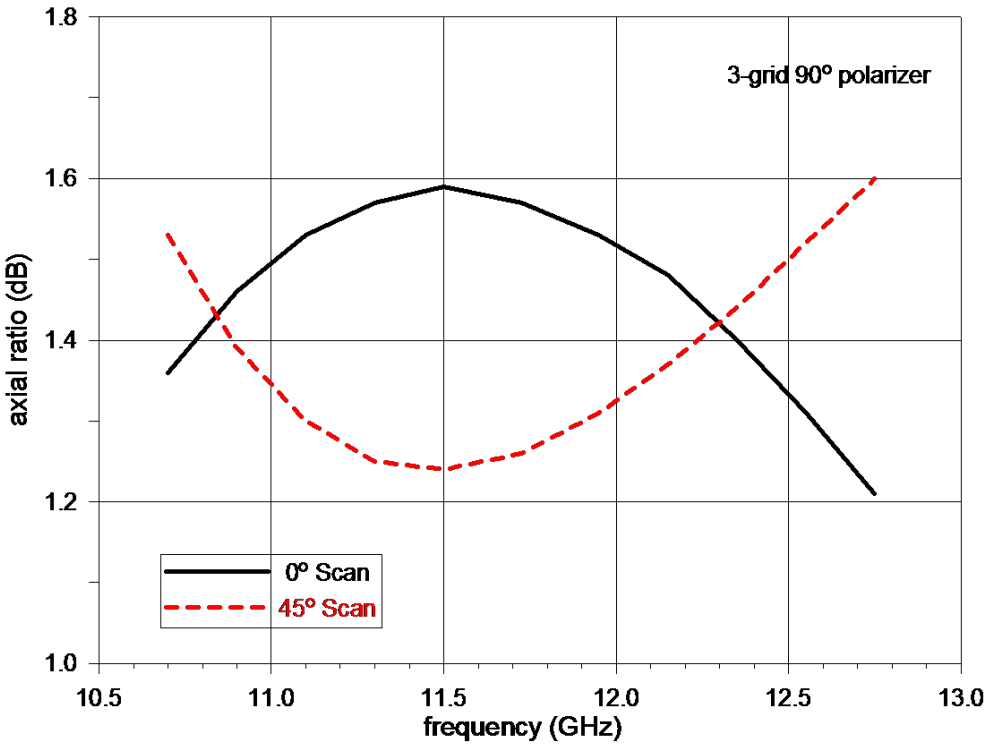

Figure 2.11: Axial ratio of 3-grid 90° meanderline polarizer

2.4 Configuration A

There are two approaches to implement the 180° polarizer and these will be termed Configuration A and B. In Configuration A, both the 90° polarizers are rotated in tandem. A separate linear grid polarizer, which rotates independently, can be added to improve the cross polarization isolation. The basic operation of Configuration A is illustrated in Figure 2.12 below. The 180° polarizer lies in the X-Y plane while plane of wave incidence is the Y-Z plane. The polarization of the incident electric field is parallel to the X-axis and the meanderline axis is at an angle Ψ_g with respect to the X-axis. The incident wave is decomposed into TE and TM components with respect to the meanderline axis. After passing through the 180° polarizer, the TE component is phase shifted 180° with respect to the TM component. The resultant wave polarization vector is inclined at an angle Ψ_p from the X-axis – where $\Psi_p = 2\Psi_g$.

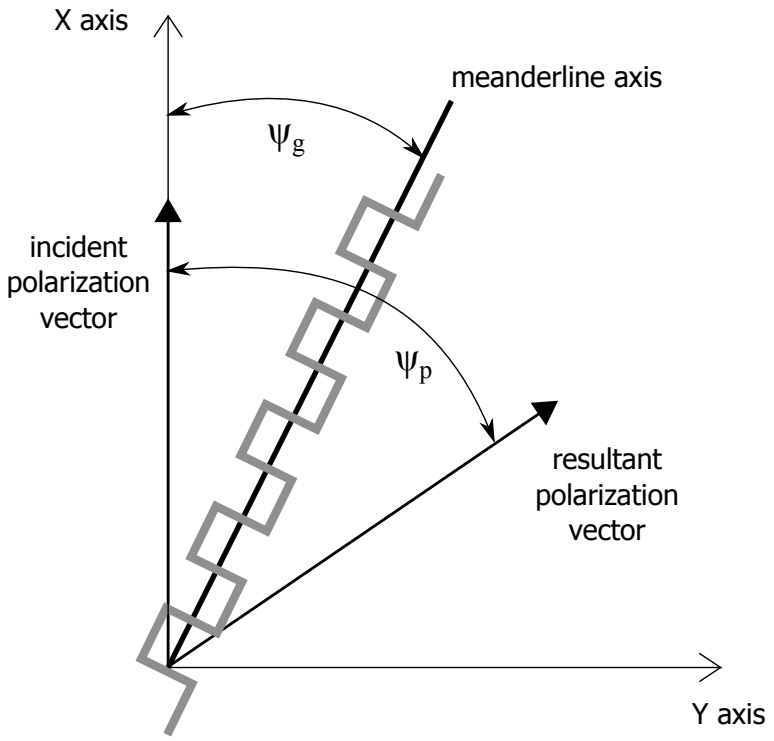

Figure 2.12: Polarizer axes and wave polarization for Configuration A

The relationship between the output polarization angle Ψ_p, polarizer #1 axis rotation angle Ψ_{g1} and polarizer #2 axis rotation angle Ψ_{g2}, are tabulated in Table 2.1. Since the two 90° polarizers are rotated in tandem, Ψ_{g1} is always equal to Ψ_{g2} in Configuration A. The linear grid polarizer axis, Ψ_w , is always positioned orthognal to output polarization vector. The subsequent sections will discuss three possible implementations of Configuration A.

Table 2.1: Polarizer rotation angles for Configuration A

Ψ_p	Ψ_{g1}	Ψ_{g2}	Ψ_w
-90°	-45°	-45°	-180°
-67.5°	-33.75°	-33.75°	-157.5°
-45°	-22.5°	-22.5°	-135°
-33.75°	-16.875°	-16.875°	-123.75°
-22.5°	-11.25°	-11.25°	-112.5°
-11.25°	-5.625°	-5.625°	-101.5°
0°	0°	0°	-90°
+11.25°	+5.625°	+5.625°	-78.75°
+22.5°	+11.25°	+11.25°	-67.5°
+33.75°	+16.875°	+16.875°	-56.25°
+45°	+22.5°	+22.5°	-45°
+67.5°	+33.75°	+33.75°	-22.5°
+90°	+45°	+45°	0°

2.4.1 Configuration A1

The first implementation of Configuration A is to stack the two 90° polarizers and rotate them in tandem above the antenna array to achieve the desired polarization angle, Figure 2.13. The spacer #1 is constructed from 6.35 mm thick Rohacell foam.

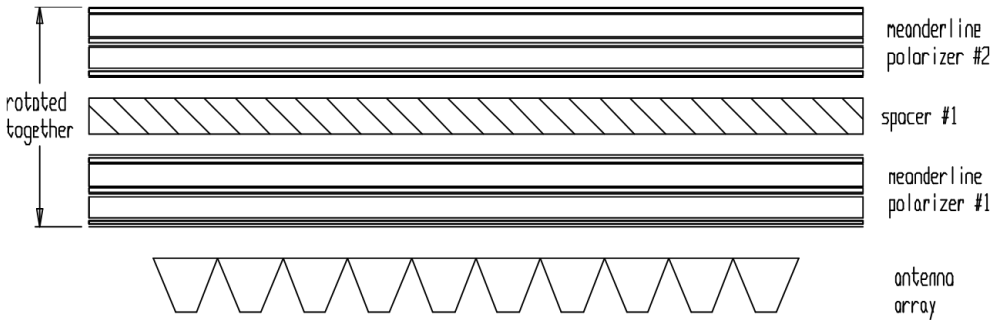

Figure 2.13: Layout of Configuration A1

The reflection coefficient, cross-polarization isolation and polarization vector orientation for normal TE and oblique 45° TE incidence are plotted in Figures 2.14 – 2.19. It can be seen that by rotating the polarizer between −45° to +45°, any desired resultant polarization angle can be achieved. The resultant polarization vector angle, Ψ_τ, is approximately 2 times the meanderline axis rotation angle, Ψ_g. The cross polarization isolation, which drops below 20 dB when the meanderline axis is more than 25°, is relatively poor given that the typical cross polarization isolation requirement for SATCOM and VSAT applications is at least 15 dB for receive and 20 dB for transmit.

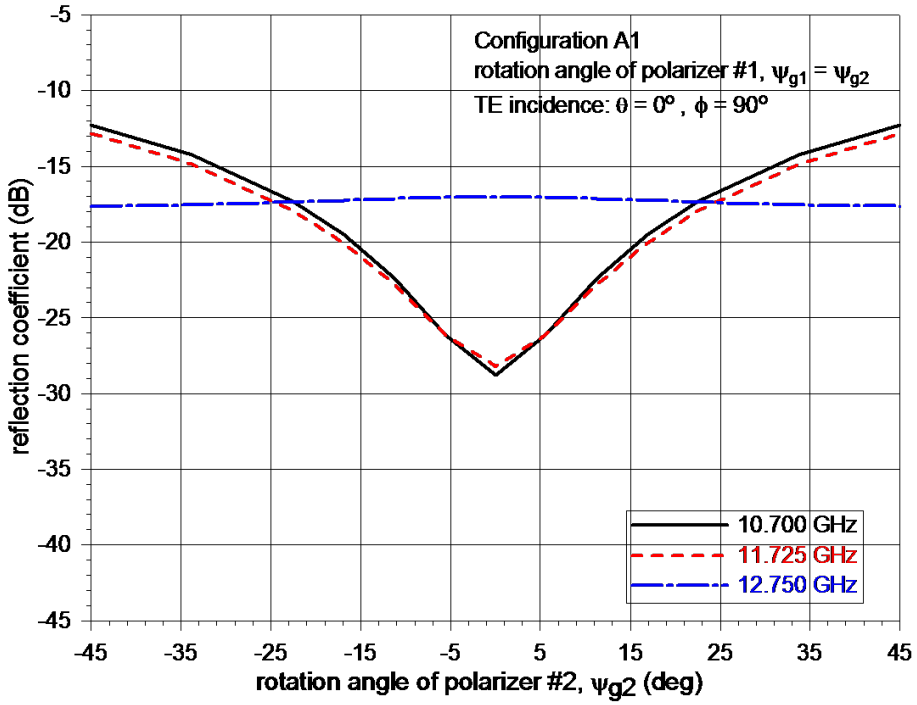

Figure 2.14: Reflection coefficient for normal TE incidence – Configuration A1

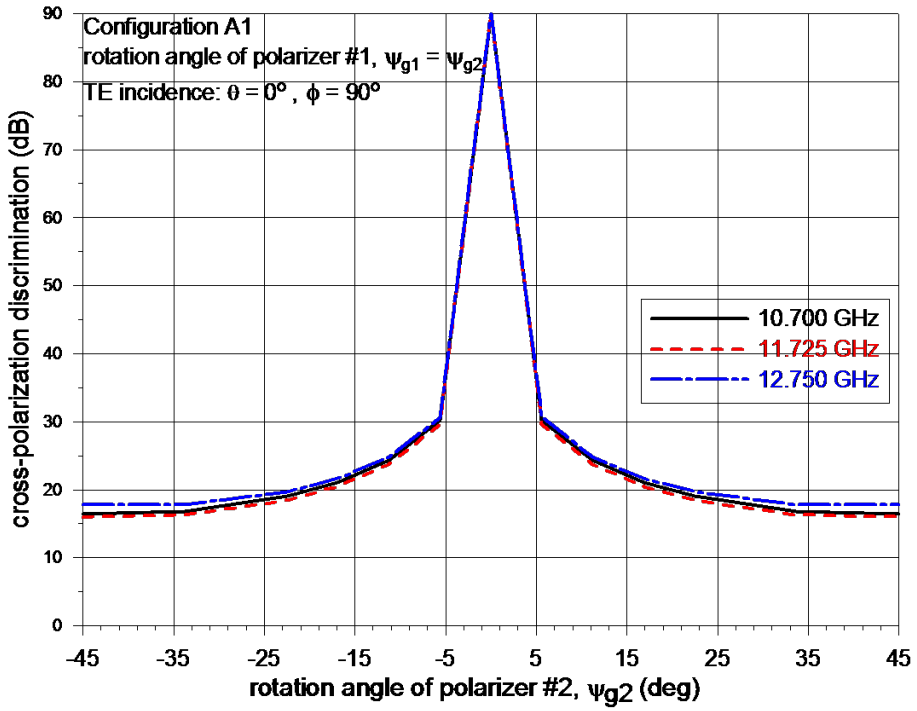

Figure 2.15: Cross polarization isolation for normal TE incidence – Configuration A1

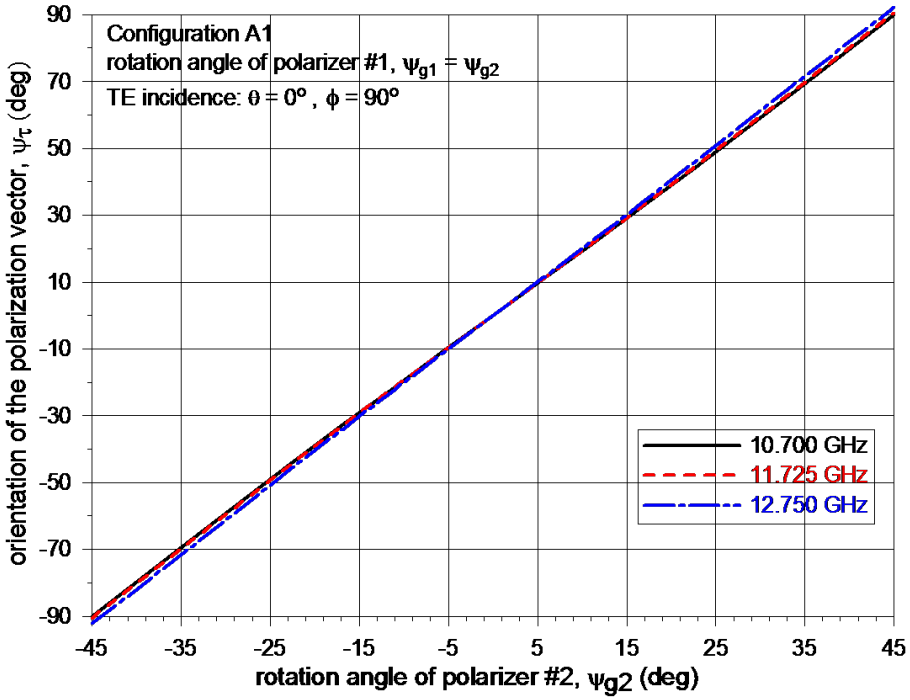

Figure 2.16: Polarizer rotation angles for normal TE incidence – Configuration A1

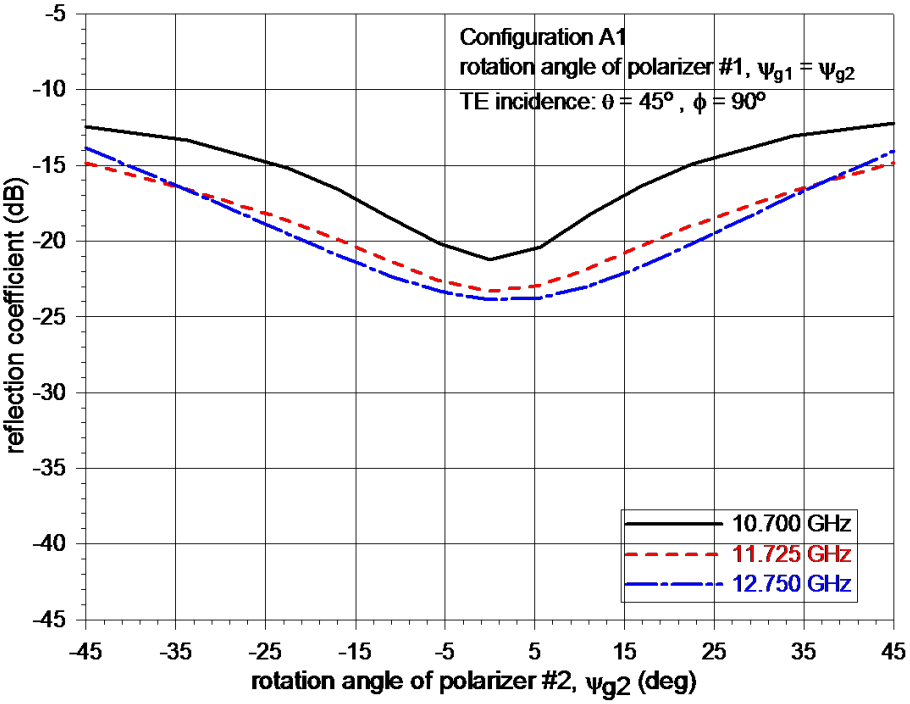

Figure 2.17: Reflection coefficient for oblique TE incidence – Configuration A1

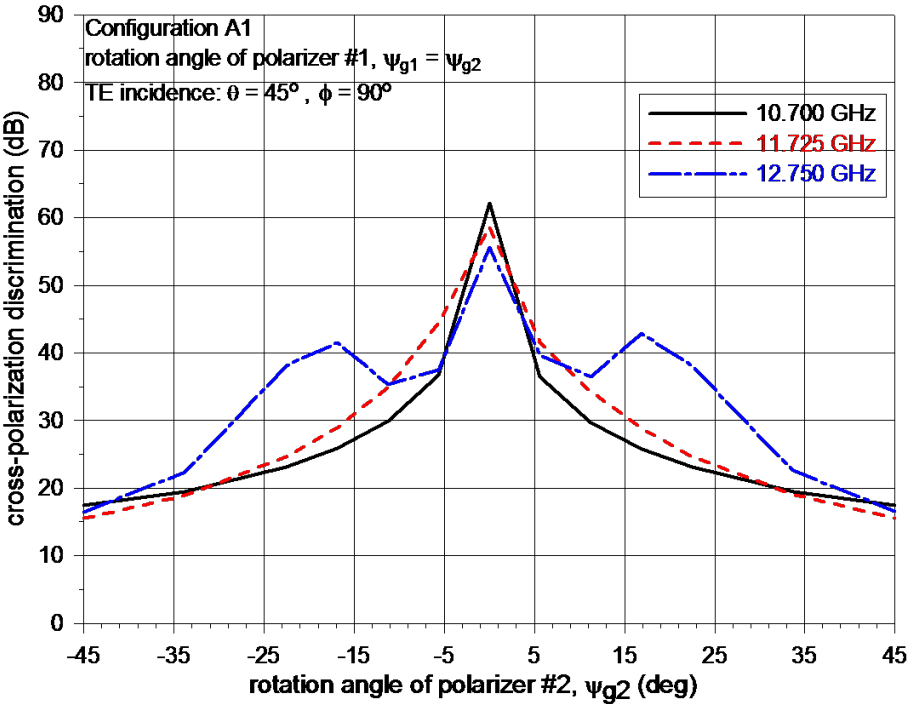

Figure 2.18: Cross polarization isolation for oblique TE incidence – Configuration A1

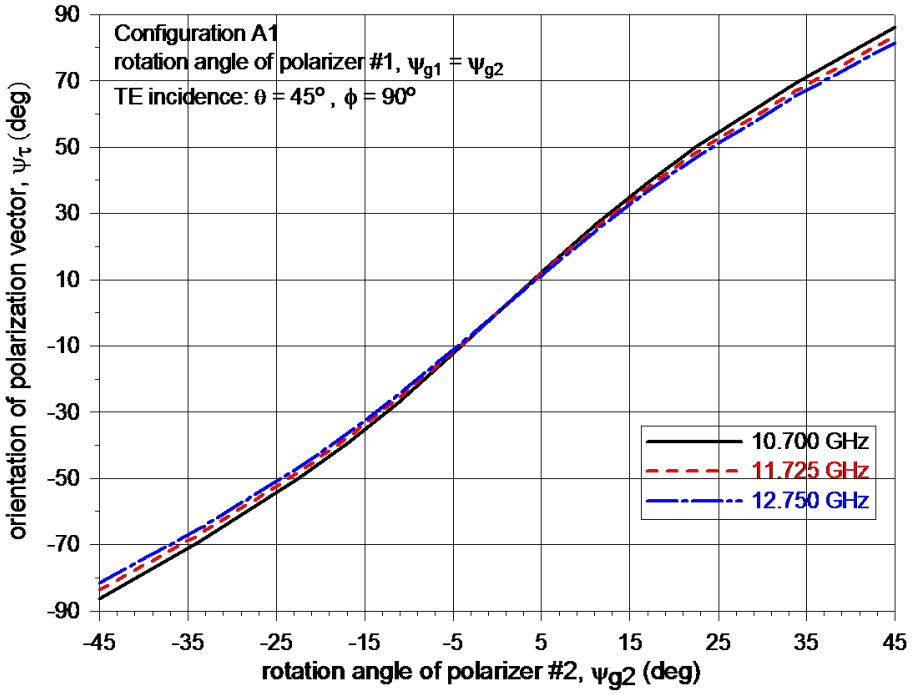

Figure 2.19: Polarizer rotation angles for oblique TE incidence – Configuration A1

2.4.2 Configuration A2

In this implementation, a linear grid polarizer is added on top of the 180° polarizer to improve the cross polarization isolation, Figure 2.20. This linear grid will be rotated independently from the underlying 180° polarizer and optimized for normal TE incidence. By positioning the axis of the linear grid to be orthogonal to the resultant polarization vector angle, the linear grid acts as a polarization filter to suppress the cross polarization component from passing through. Two rotation mechanisms, one for the 180° polarizer and the other for the linear grid, will be required to realize this implementation.

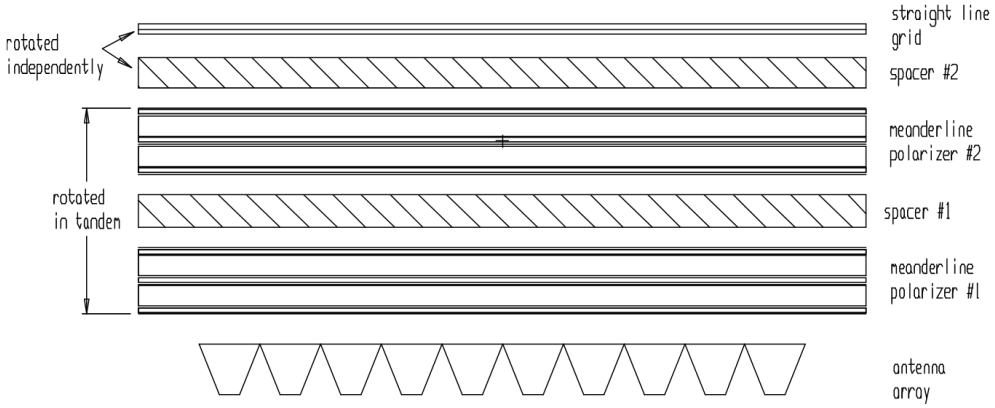

Figure 2.20: Layout of Configuration A2

The reflection coefficient, cross-polarization isolation and polarization vector orientation for normal TE and oblique 45° TE incidence are plotted in Figures 2.21 – 2.26.

It can be seen that while the reflection coefficient for normal incidence is better than -10 dB (Figure 2.21), the match is poor for oblique 45° incidence (Figure 2.24). Analysis of the polarization vector orientation plots, Figures 2.23 and 2.26, revealed that the resultant polarization rotation angle does not vary proportionately to the meanderline axis rotation angle for oblique incidence angle. This is the cause for poor reflection coefficient in Figure 2.24. The

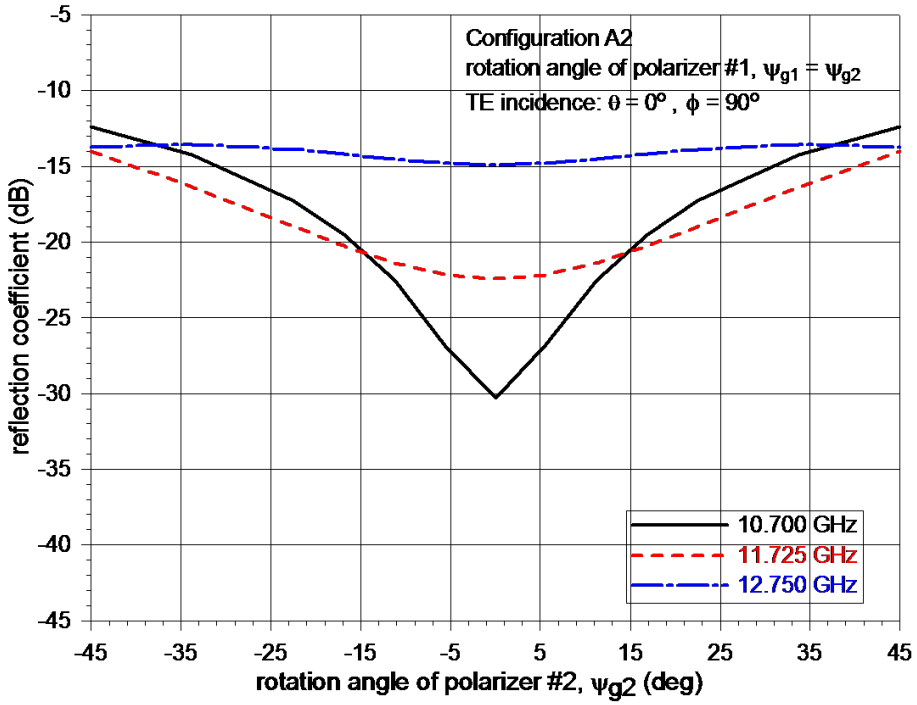

Figure 2.21: Reflection coefficient for normal TE incidence – Configuration A2

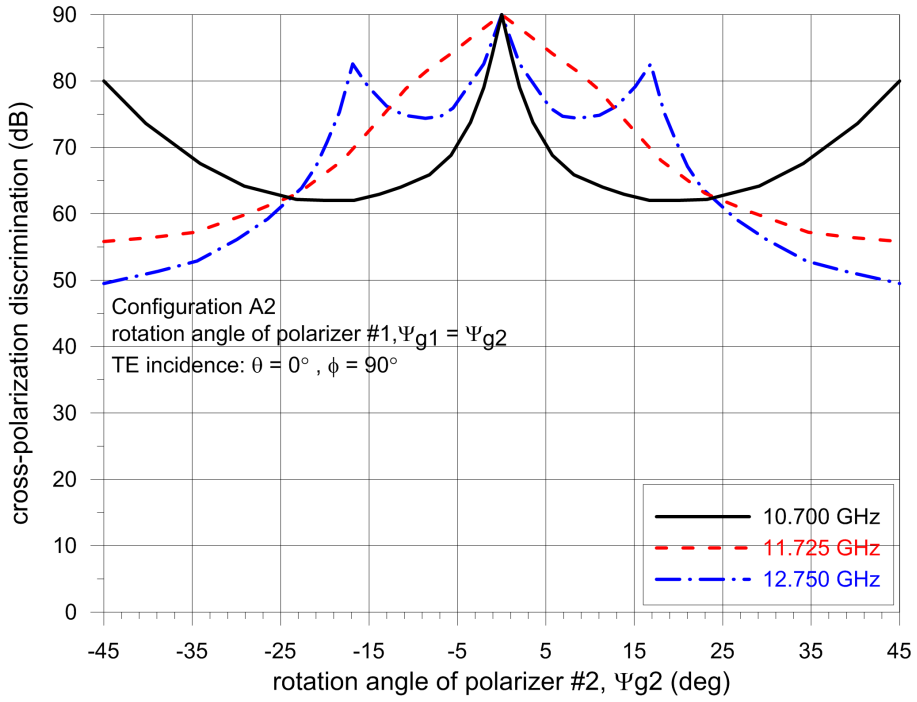

Figure 2.22: Cross polarization isolation for normal TE incidence – Configuration A2

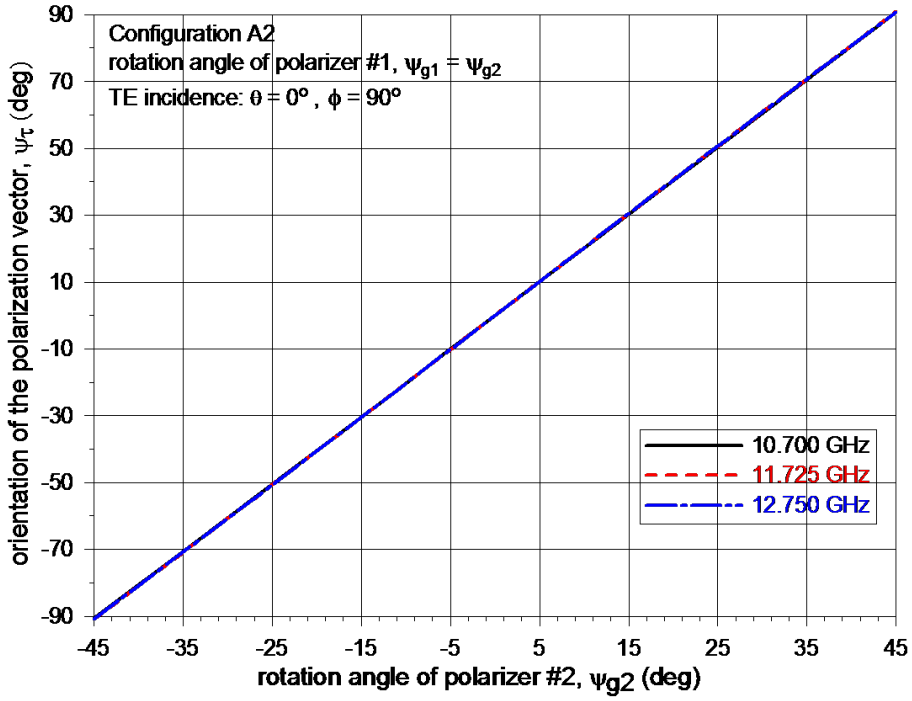

Figure 2.23: Polarizer rotation angles for normal TE incidence – Configuration A2

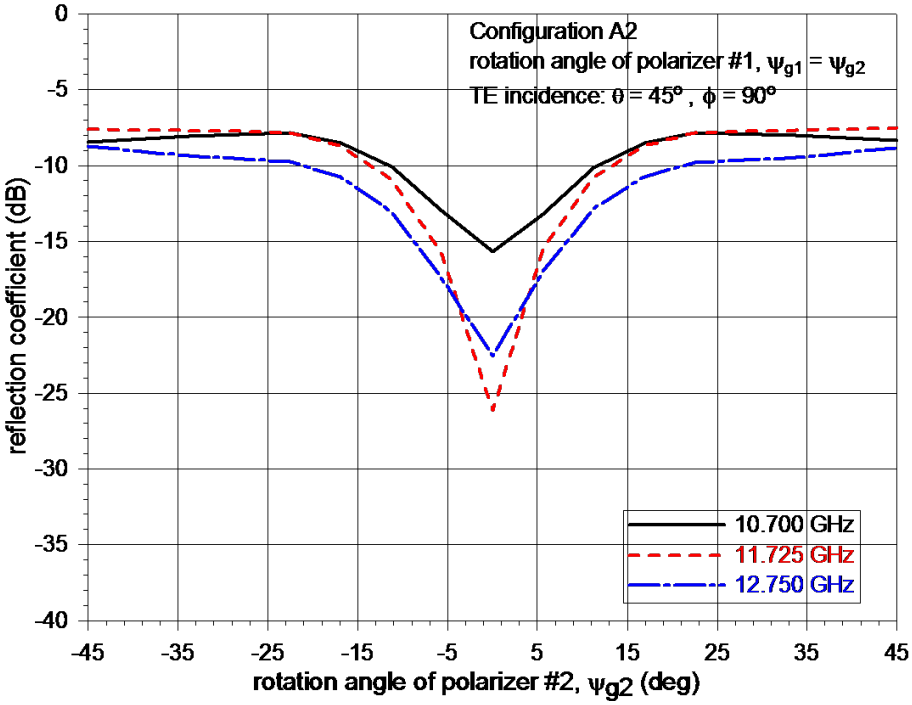

Figure 2.24: Reflection coefficient for oblique TE incidence – Configuration A2

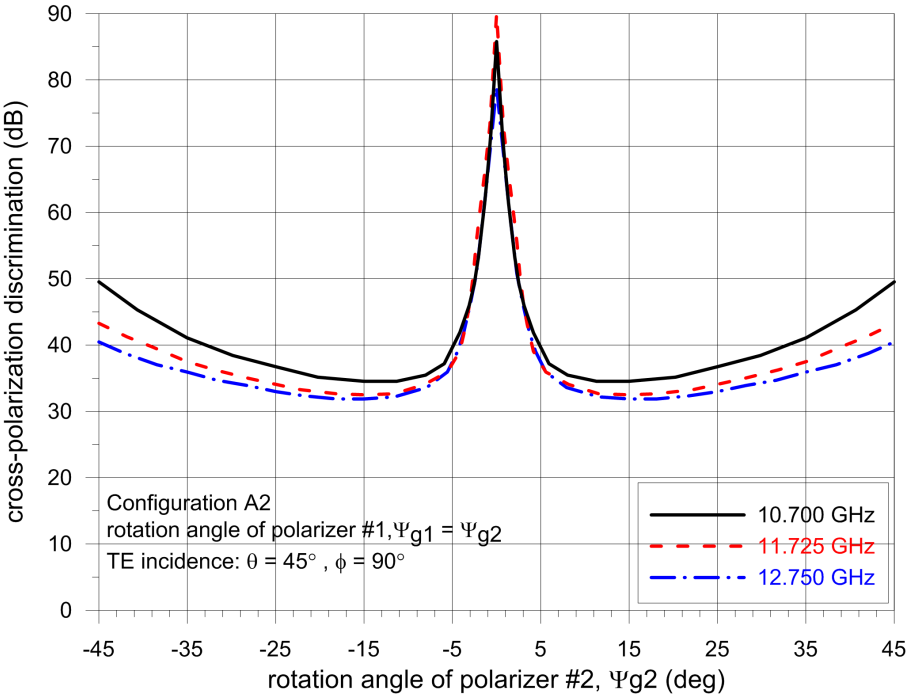

Figure 2.25: Cross polarization isolation for oblique TE incidence – Configuration A2

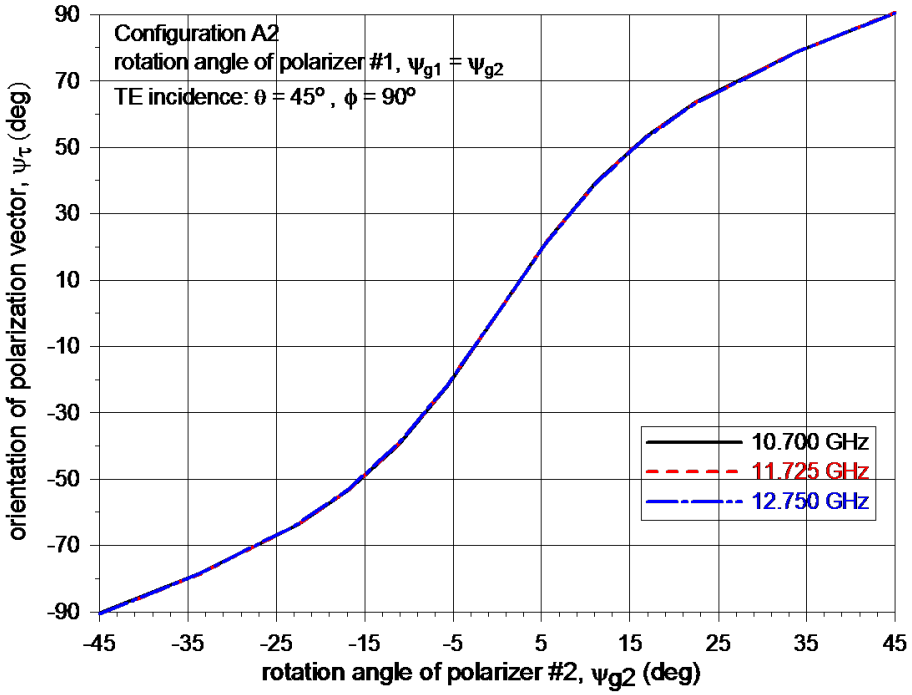

Figure 2.26: Polarizer rotation angles for oblique TE incidence – Configuration A2

additional linear grid polarizer indeed improves the cross polarization isolation of the 180° polarizer significantly as shown in Figures 2.22 and 2.25. Isolation better than 30 dB can be achieved throughout the scan angle across the entire bandwidth.

2.4.3 Configuration A3

This implementation is similar to Configuration A2 except that the position of the linear grid polarizer is optimized for every polarization rotation angle and wave incidence angle, Figure 2.27. The reflection coefficient, cross-polarization isolation and polarization vector orientation for normal TE and oblique 45° TE incidence are plotted in Figures 2.27 – 2.34.

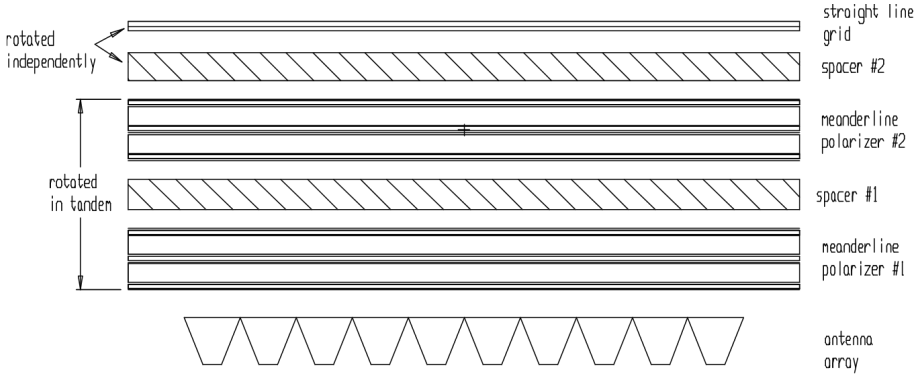

Figure 2.27: Layout of Configuration A3

The reflection coefficient for both normal and oblique 45° incidence are now better than -10 dB, Figure 2.29 and 2.32. The cross polarization isolation achieved is also better than 40 dB throughout the scan angle across the entire bandwidth. Similar to Configuration A2, two rotation mechanisms are required.

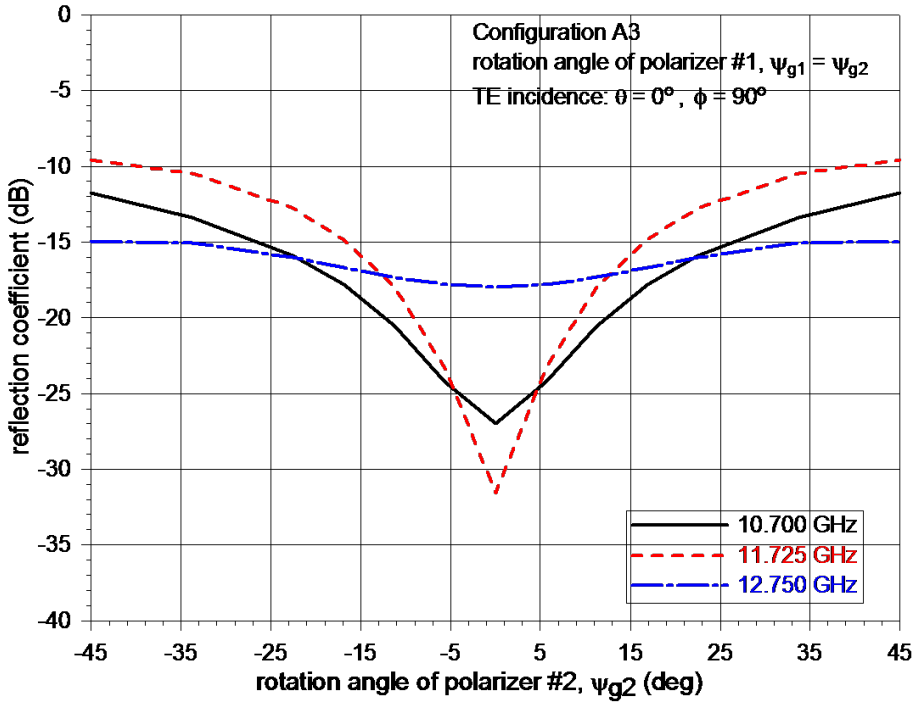

Figure 2.28: Reflection coefficient for normal TE incidence – Configuration A3

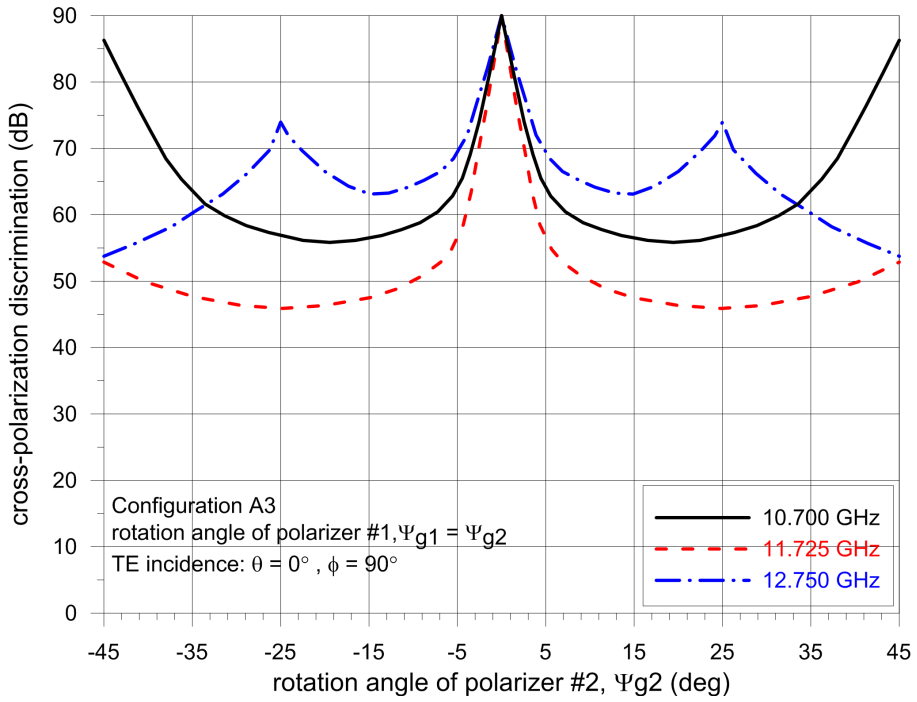

Figure 2.29: Cross polarization isolation for normal TE incidence – Configuration A3

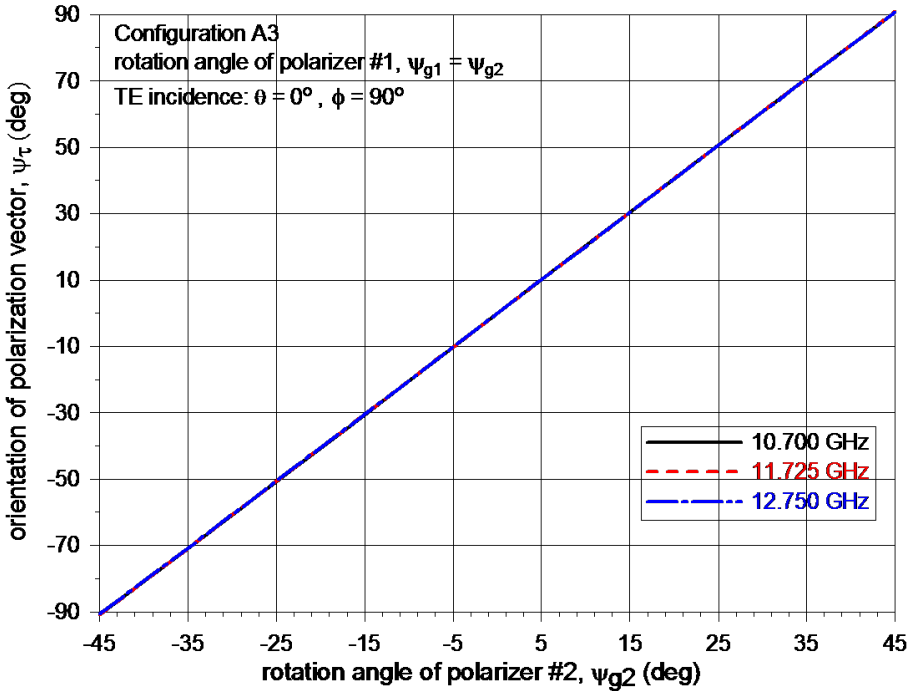

Figure 2.30: Polarizer rotation angles for normal TE incidence – Configuration A3

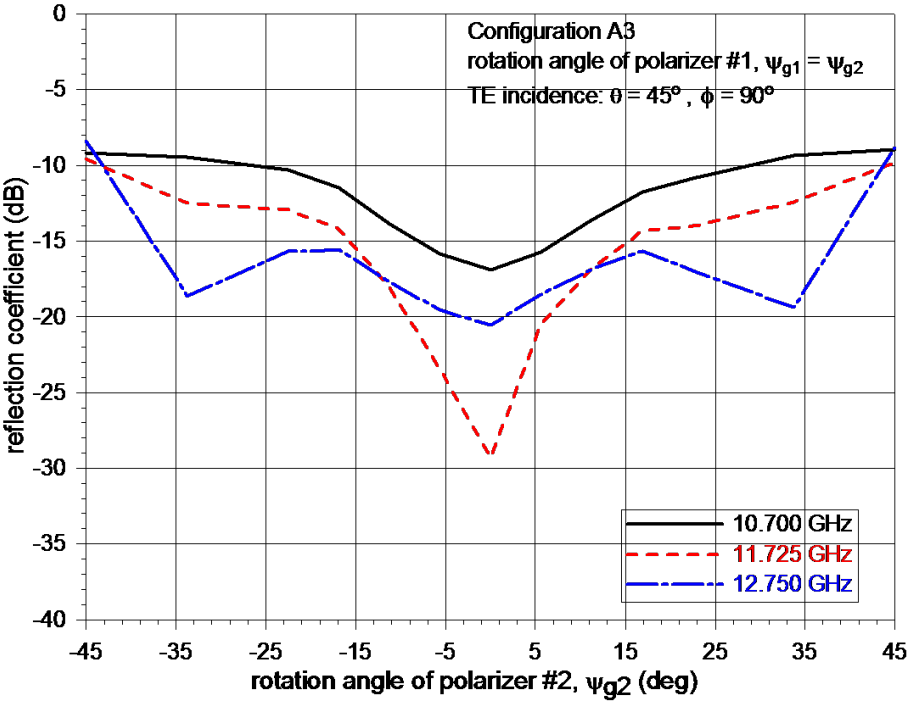

Figure 2.31: Reflection coefficient for oblqiue TE incidence – Configuration A3

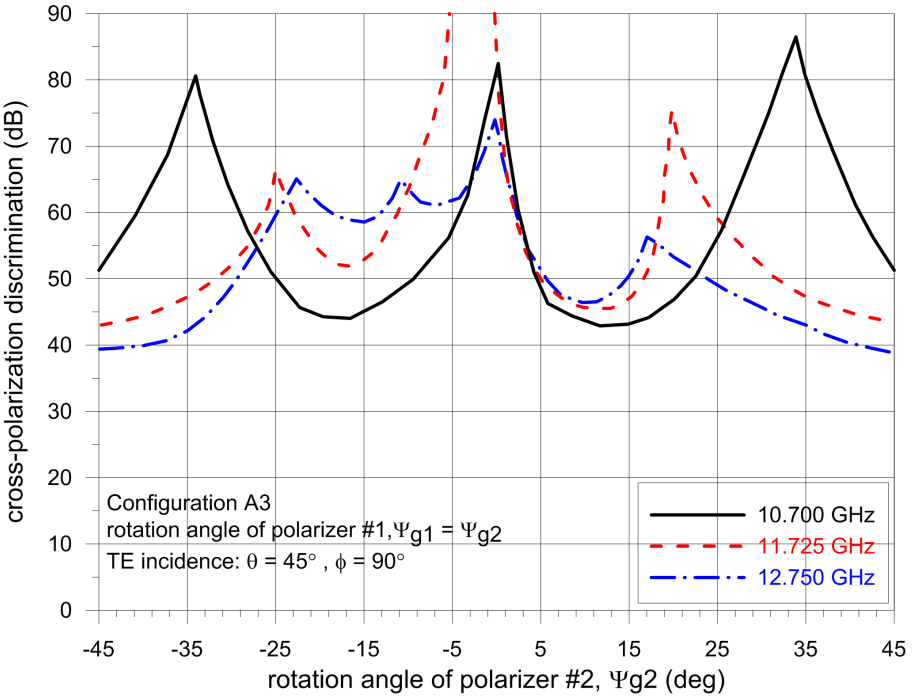

Figure 2.32: Cross polarization isolation for oblqiue TE incidence – Configuration A3

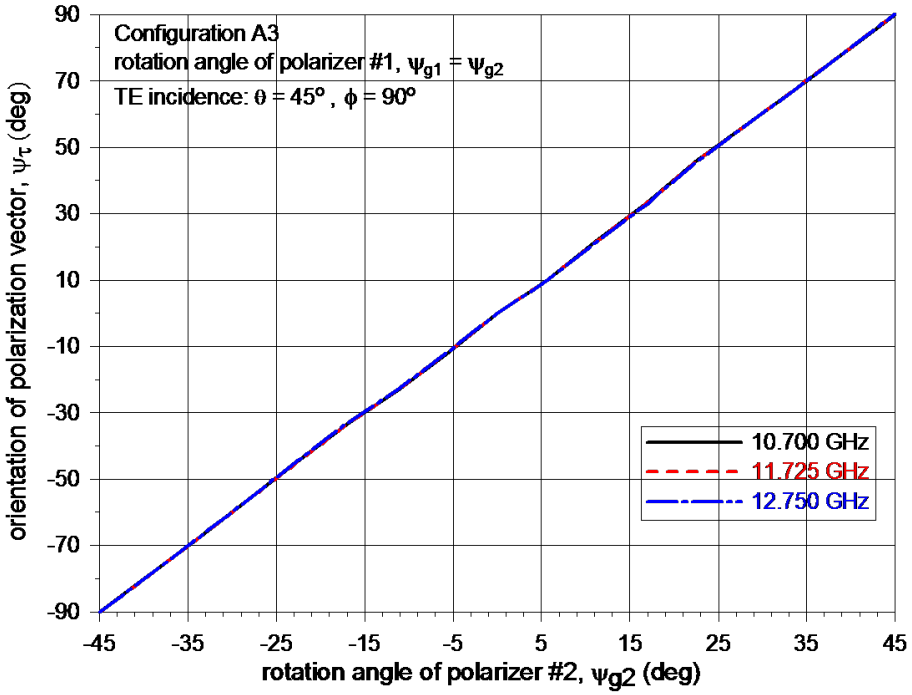

Figure 2.33: Polarizer rotation angles for oblique TE incidence – Configuration A3

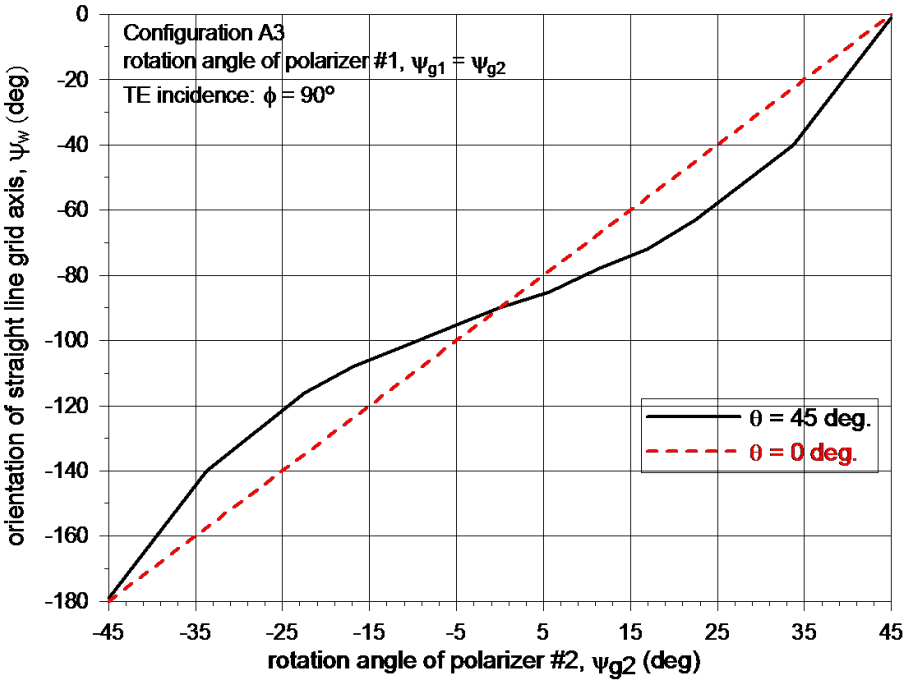

Figure 2.34: Linear grid rotation angles for oblique TE incidence – Configuration A3

2.5 Configuration B

In Configuration B, the 90° polarizer #1 is fixed with its meanderline axis rotated 45° with respect to the linear polarization of the antenna array to generate a circularly polarized wave. The 90° polarizer #2 is then positioned on top of polarizer #1 and rotated freely to convert the circularly polarized wave back into linearly polarized wave with the polarization vector at the desired orientation. Similar to Configuration A, a linear grid polarizer can be added to improve the cross polarization isolation. Three possible implementations of Configuration B will be discussed in the following sections.

2.5.1 Configuration B1

This is the basic implementation of Configuration B where only one rotation mechanism is required to achieve polarization rotation, Figure 2.35. The spacer #1 is constructed from 6.35 mm thick Rohacell foam. The relationship between

the meanderline polarizer's axes and wave polarization is illustrated in Figure 2.36. The relationship between the desired polarization direction – Ψ_p, 90° polarizer #1 rotation angle – Ψ_{g1}, and 90° polarizer #2 rotation angle – Ψ_{g2}, is tabulated in Table 2.2. The reflection coefficient, cross-polarization isolation and polarization vector orientation for normal TE and oblique 45° TE incidence are plotted in Figures 2.37 – 2.42.

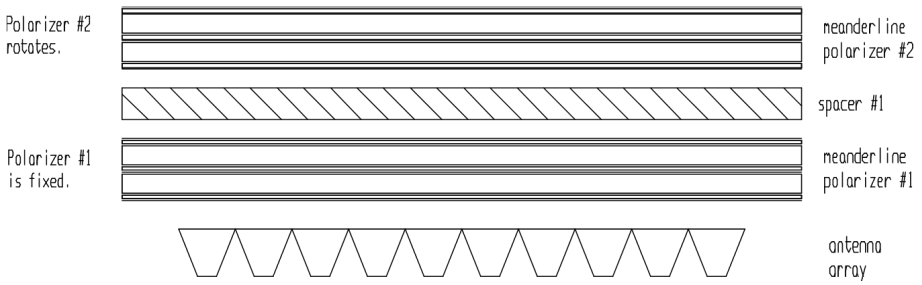

Figure 2.35: Layout of Configuration B1

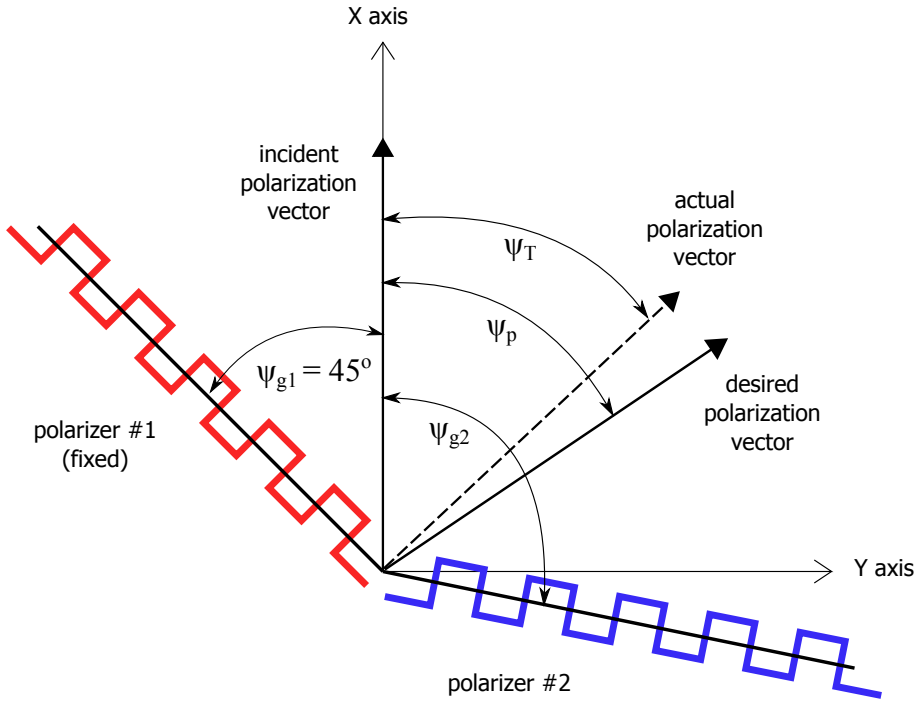

Figure 2.36: Polarizer axes and waves polarization for Configuration B

Table 2.2: Polarizer rotation angles for Configuration B1

Ψ_p	Ψ_{g1}	Ψ_{g2}	Ψ_w
-90°	-45°	-45°	-180°
-67.5°	-45°	-22.5°	-157.5°
-45°	-45°	0°	-135°
-33.75°	-45°	+11.25°	-123.75°
-22.5°	-45°	+22.5°	-112.5°
-11.25°	-45°	+33.75°	-101.5°
0°	-45°	+45°	-90°
+11.25°	-45°	+56.25°	-78.75°
+22.5°	-45°	+67.5°	-67.5°
+33.75°	-45°	+78.75°	-56.25°
+45°	-45°	+90°	-45°
+67.5°	-45°	+112.5°	-22.5°
+90°	-45°	+135°	0°

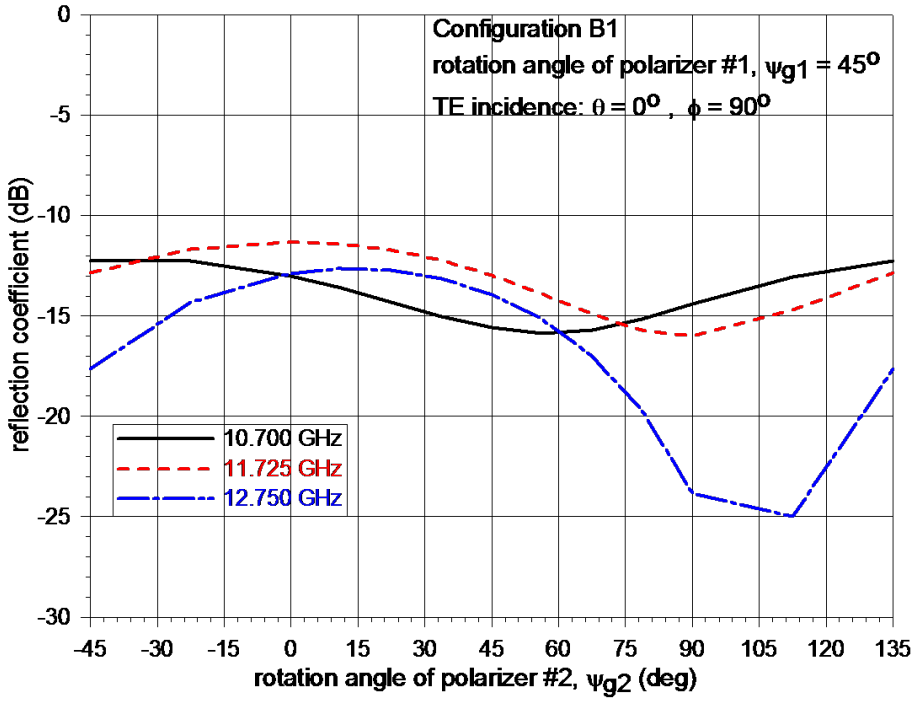

Figure 2.37: Reflection coefficient for normal TE incidence – Configuration B1

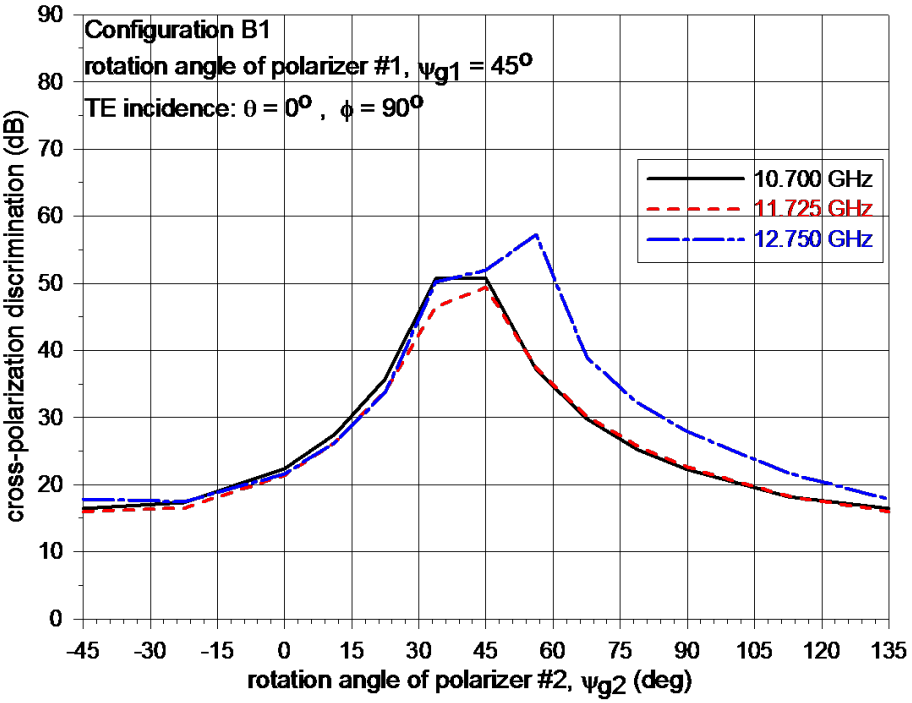

Figure 2.38: Cross polarization isolation for normal TE incidence – Configuration B1

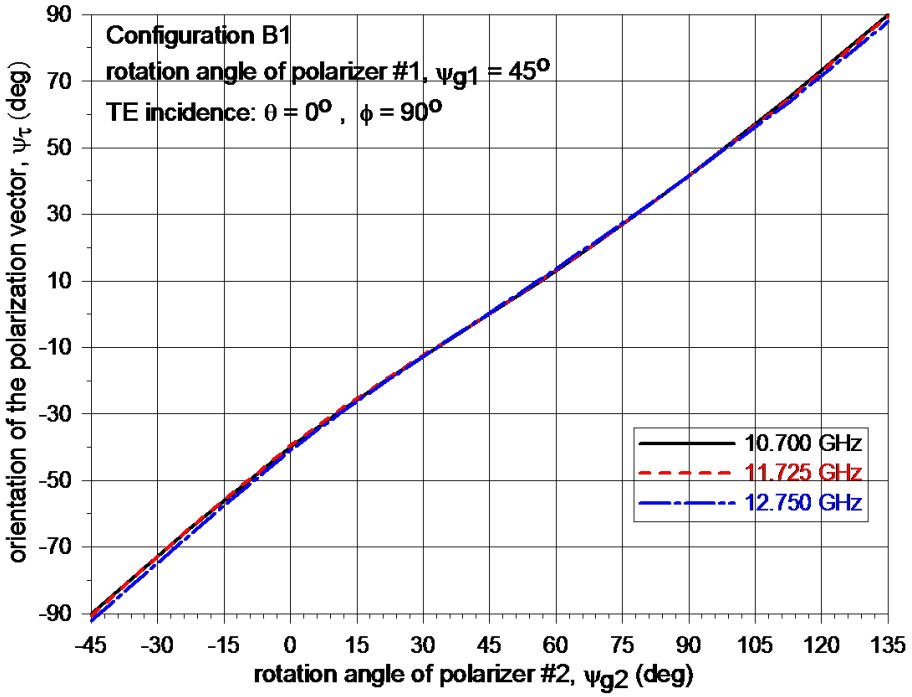

Figure 2.39: Polarizer rotation angles for normal TE incidence – Configuration B1

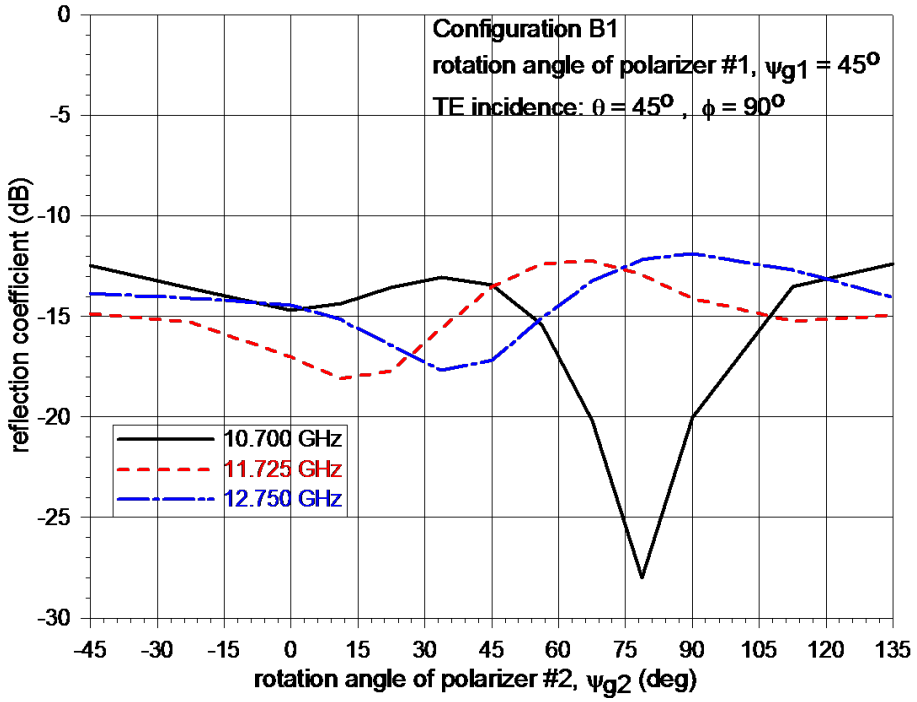

Figure 2.40: Reflection coefficient for oblique TE incidence – Configuration B1

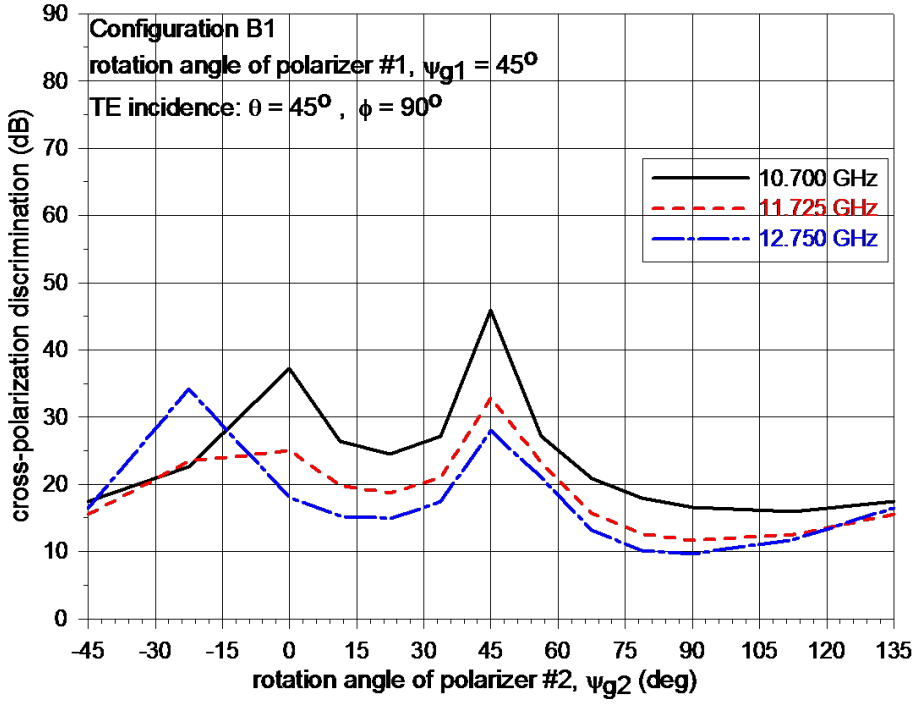

Figure 2.41: Cross polarization isolation for oblique TE incidence – Configuration B1

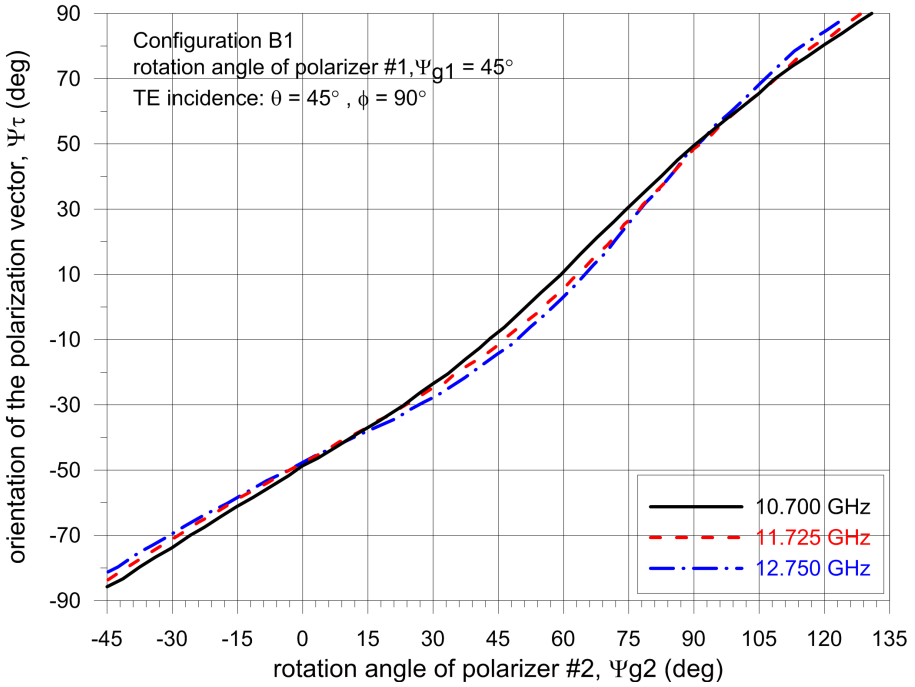

Figure 2.42: Polarizer rotation angles for oblique TE incidence – Configuration B1

The results showed that the minimum cross polarization of this configuration is only 10 dB. Although only one rotation mechanism is required, the cross polarization isolation is insufficient to meet the operational requirement for VSAT applications.

2.5.2 Configuration B2

In this implementation, a linear grid polarizer is aligned at 45° with respect to the meanderline polarizer #2. The linear grid and polarizer #2 are rotated in tandem to convert the circularly polarized wave back into linearly polarized wave, Figure 2.43. Similar to Configuration A2 and A3, the motivation for introducing the linear grid is to suppress the orthogonal polarization component. The relationship between the desired polarization direction – Ψ_p, 90° polarizer #1 rotation angle – Ψ_{g1}, 90° polarizer #2 rotation angle – Ψ_{g2}, and linear grid polarizer rotation angle – Ψ_w are tabulated in Table 2.3.

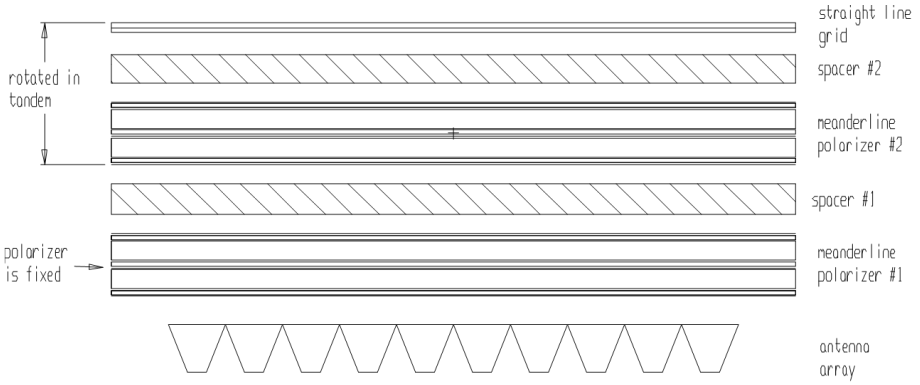

Figure 2.43: Layout of Configuration B2

Table 2.3: Polarization rotation angles for Configuration B2

Ψ_p	Ψ_{g1}	Ψ_{g2}	Ψ_w
-90°	-45°	-45°	-180°
-67.5°	-45°	-22.5°	-157.5°
-45°	-45°	0°	-135°
-33.75°	-45°	+11.25°	-123.75°
-22.5°	-45°	+22.5°	-112.5°
-11.25°	-45°	+33.75°	-101.5°
0°	-45°	+45°	-90°
+11.25°	-45°	+56.25°	-78.75°
+22.5°	-45°	+67.5°	-67.5°
+33.75°	-45°	+78.75°	-56.25°
+45°	-45°	+90°	-45°
+67.5°	-45°	+112.5°	-22.5°
+90°	-45°	+135°	0°

The reflection coefficient, cross-polarization isolation and polarization vector orientation for normal TE and oblique 45° TE incidence are plotted in Figures 2.44 – 2.49.

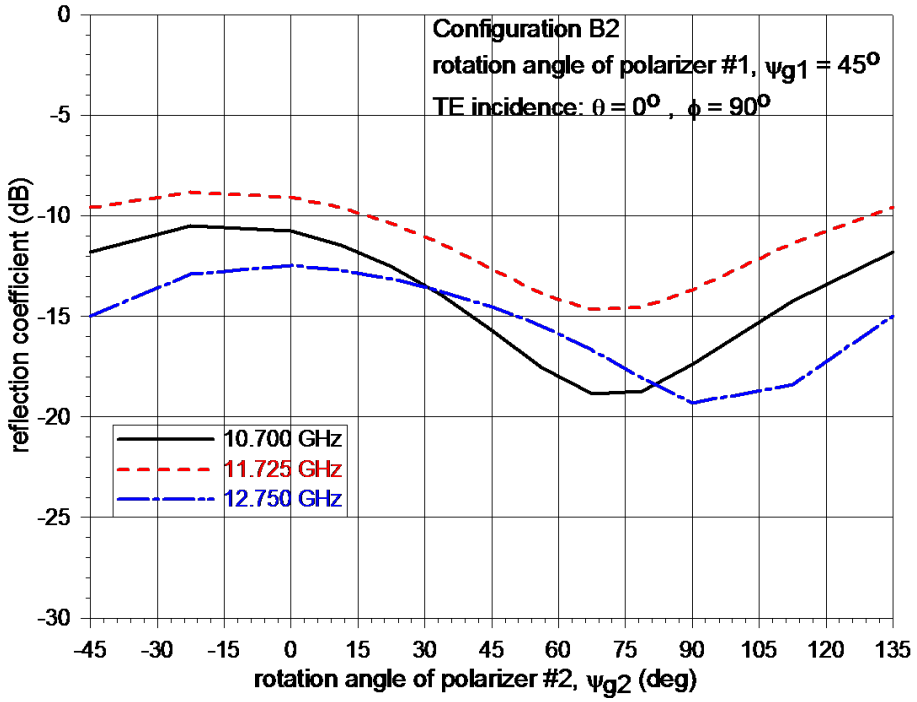

Figure 2.44: Reflection coefficient for normal TE incidence – Configuration B2

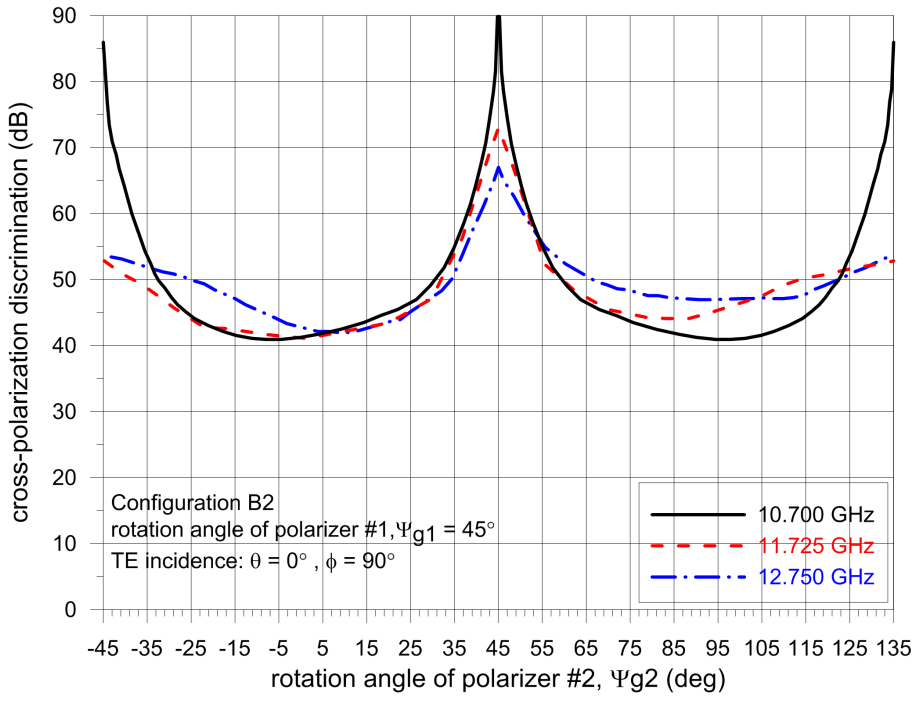

Figure 2.45: Cross polarization isolation for normal TE incidence – Configuration B2

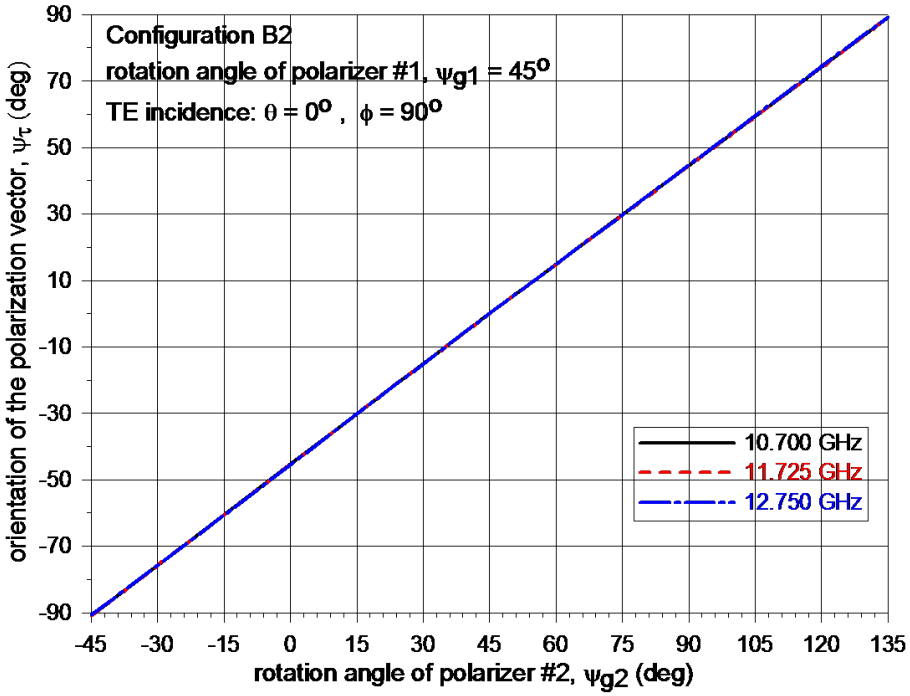

Figure 2.46: Polarizer rotation angles for normal TE incidence – Configuration B2

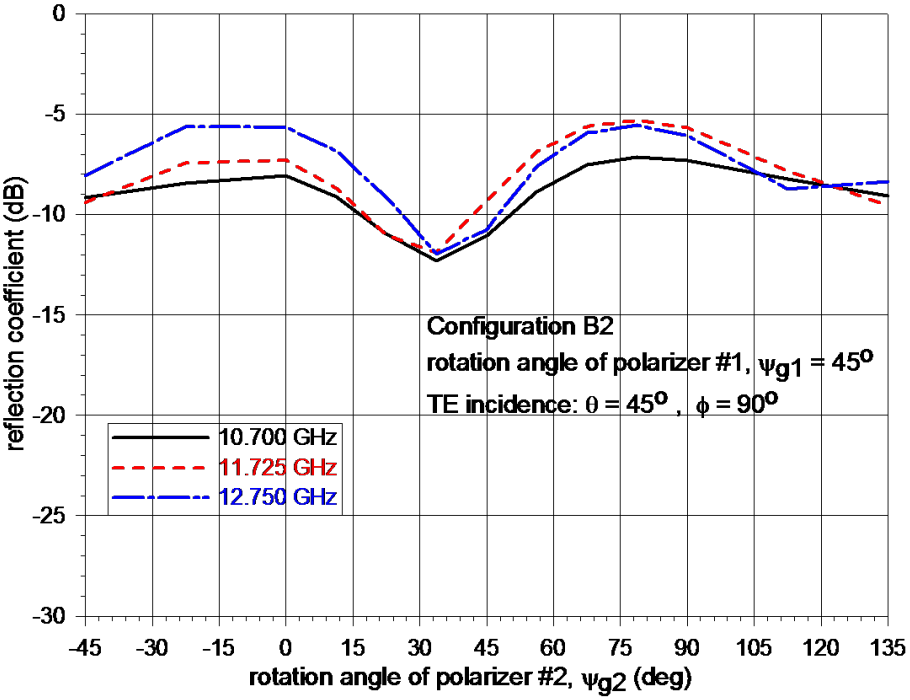

Figure 2.47: Reflection coefficient for oblique TE incidence – Configuration B2

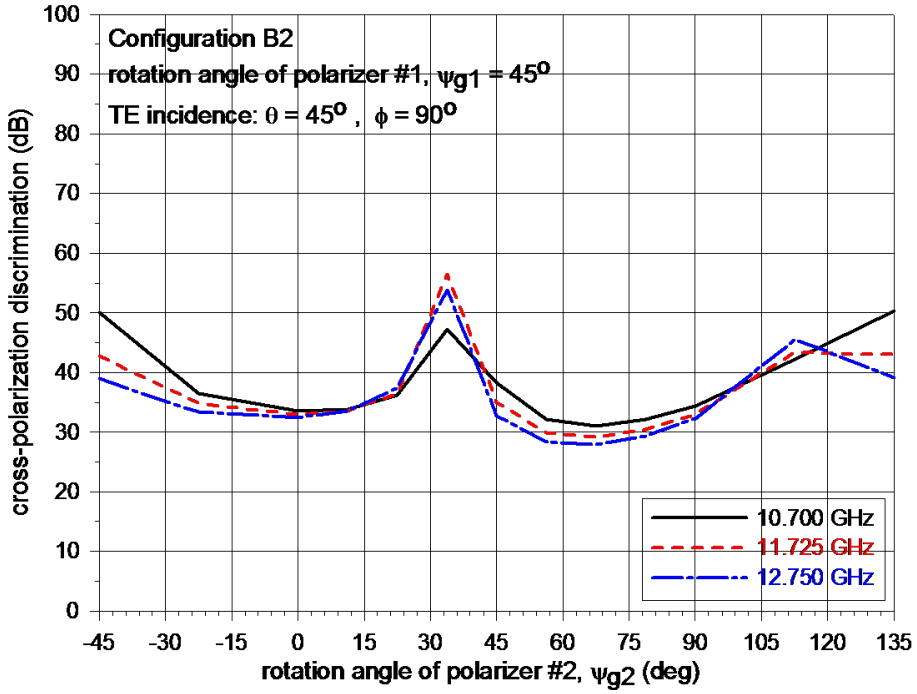

Figure 2.48: Cross polarization isolation for oblique TE incidence – Configuration B2

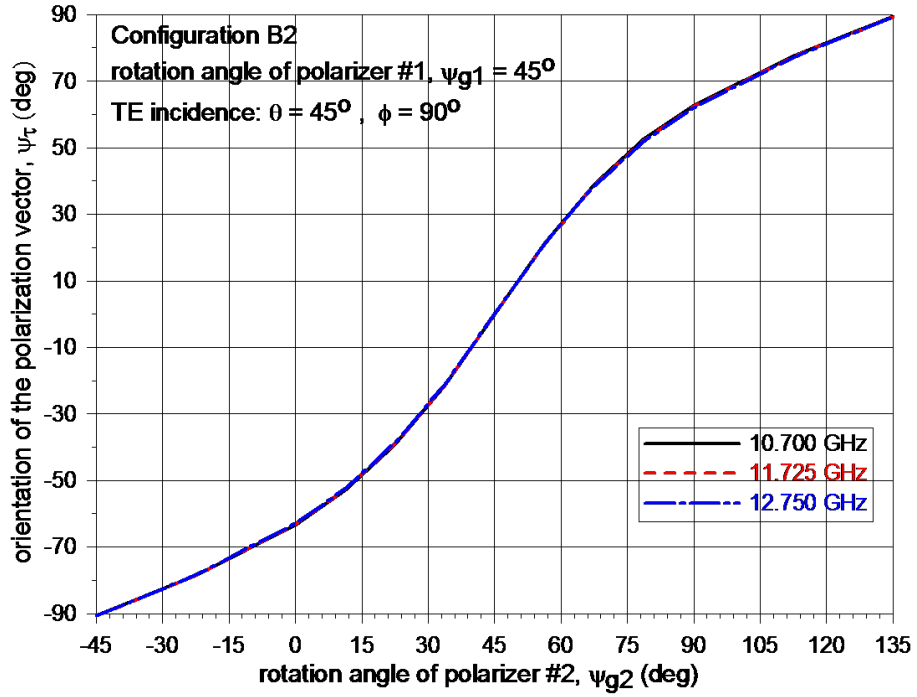

Figure 2.49: Polarizer rotation angles for normal TE incidence – Configuration B2

Figures 2.45 and 2.48 showed that the linear grid polarizer has improved the cross polarization isolation to better than 25 dB across the scan range. Due to the mis-alignment between the resultant polarization vector angle and linear grid polarizer, the mismatch loss of this configuration is only –5 dB for oblique incidence. This mis-alignment is not corrected in this configuration as the linear grid polarizer is rotating in tandem with polarizer #2.

2.5.3 Configuration B3

By introducing an additional degree of freedom to the linear grid polarizer as shown in Figure 2.50, the mismatch loss in Configuration B2 can be improved by allowing the linear grid to be optimally aligned with respect to the resultant polarization vector. The relationship between the desired polarization direction – Ψ_p, 90° polarizer #1 rotation angle – Ψ_{g1}, 90° polarizer #2 rotation angle – Ψ_{g2}, and linear grid polarizer rotation angle – Ψ_w are tabulated in Table 2.4. The optimized reflection coefficient, cross-polarization isolation and polarization vector orientation for oblique 45° TE incidence are plotted in Figures 2.51 – 2.54.

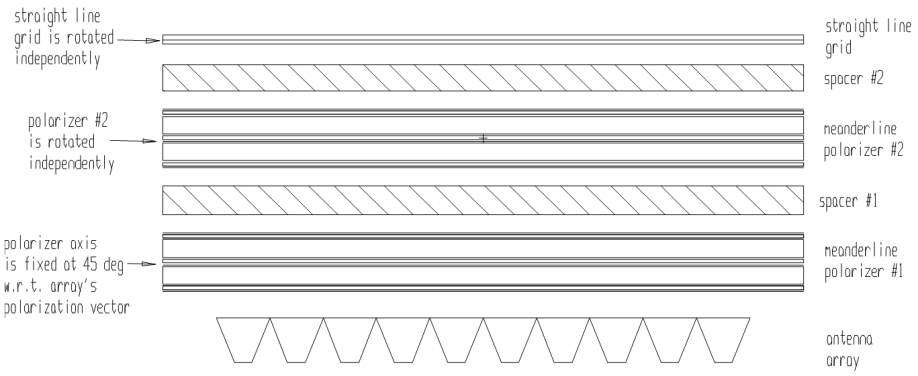

Figure 2.50: Layout of Configuration B3

Table 2.4: Polarization rotation angles for Configuration B3

Ψ_p	Ψ_{g1}	Ψ_{g2}	Ψ_w
-90°	-45°	-45°	-179°
-67.5°	-45°	-22.5°	-140°
-45°	-45°	0°	-117°
-33.75°	-45°	+11.25°	-109°
-22.5°	-45°	+22.5°	-112.5°
-11.25°	-45°	+33.75°	-96°
0°	-45°	+45°	-90°
+11.25°	-45°	+56.25°	-84°
+22.5°	-45°	+67.5°	-77.5°
+33.75°	-45°	+78.75°	-71°
+45°	-45°	+90°	-63°
+67.5°	-45°	+112.5°	-38°
+90°	-45°	+135°	+1°

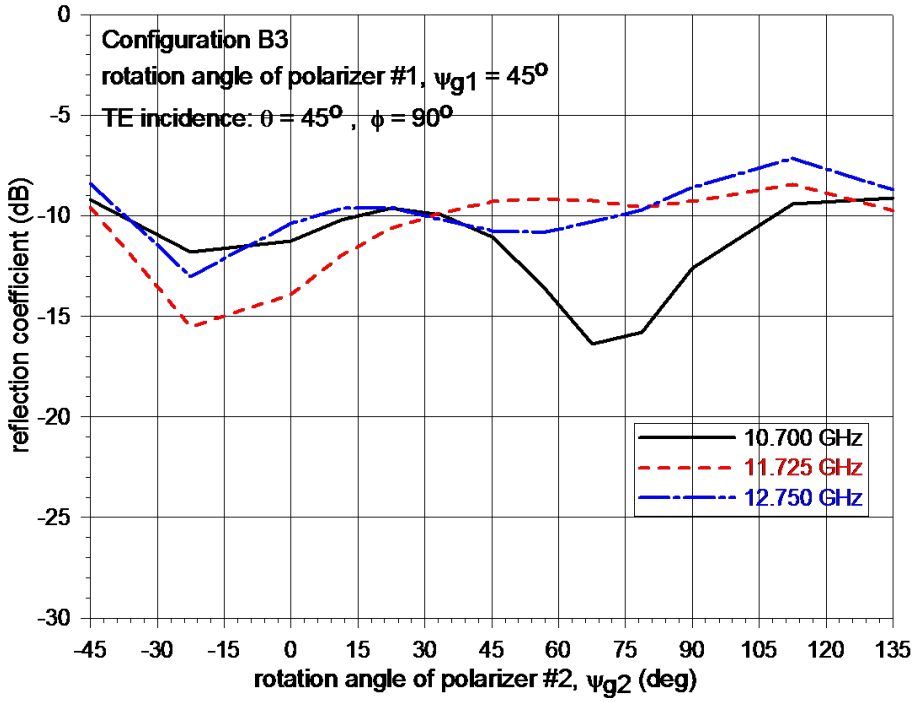

Figure 2.51: Reflection coefficient for oblique TE incidence – Configuration B3

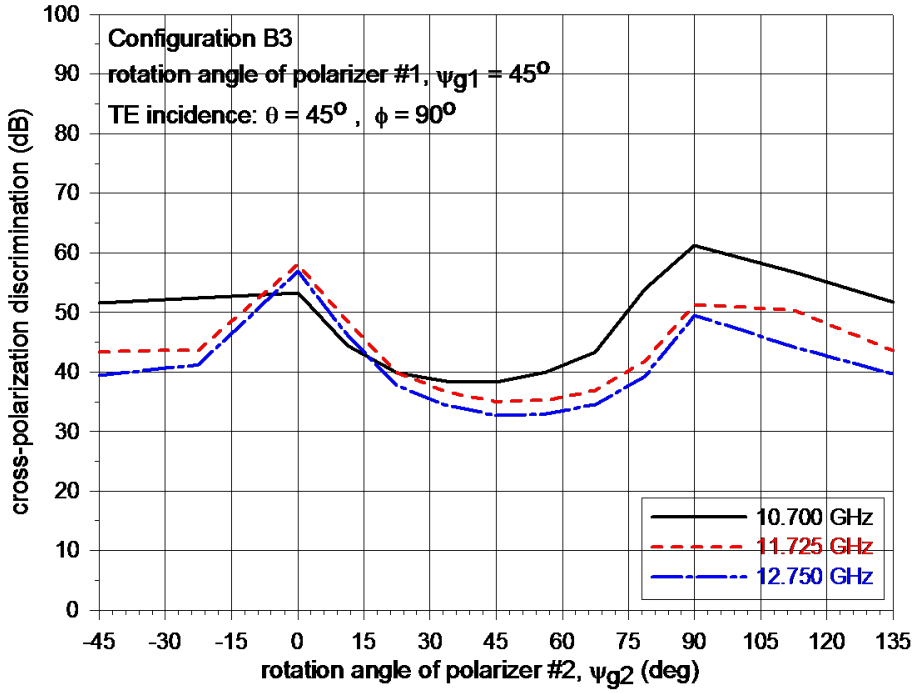

Figure 2.52: Cross polarization isolation for oblique TE incidence – Configuration B3

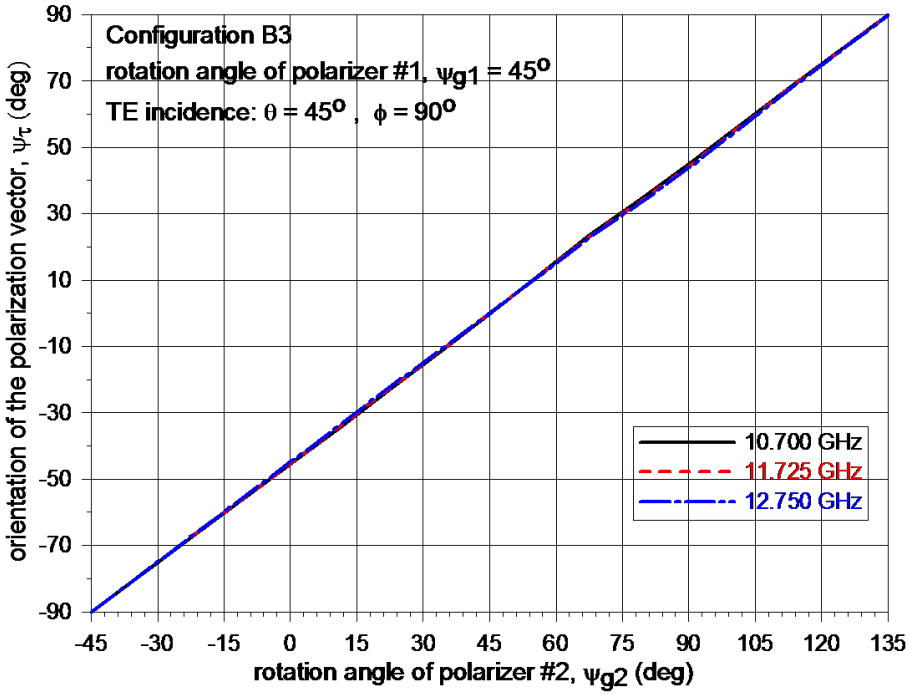

Figure 2.53: Polarizer rotation angles for normal TE incidence – Configuration B3

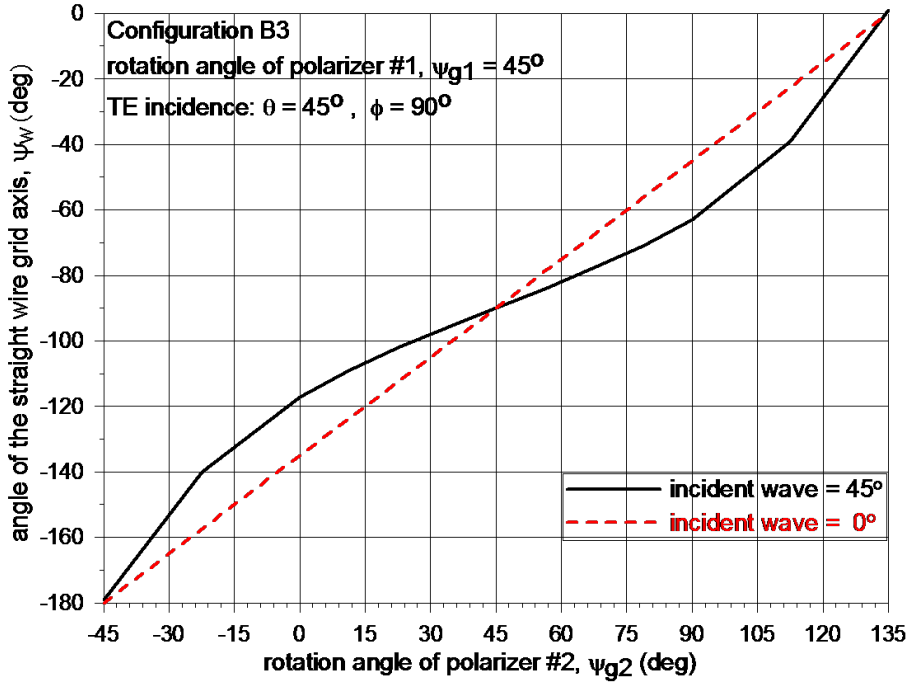

Figure 2.54: Linear grid polarizer rotation angles for normal TE incidence – Configuration B3

2.6 Design Summary

The performance summary for the six configurations is tabulated in Table 2.5 below. The worst case performance listed in the table is evaluated over the 10.7 – 12.75 GHz frequency band and 180° polarization rotation range. For standalone antenna or an array requiring only small scan angle, configuration B2 can provide a cross polarization isolation of at least 40 dB with the use of a single rotation mechanism. Compared to conventional design which requires multiple rotating layers [36–38], the 180° polarizer design presented here is much simpler to control and implement in operational systems. For wide scanning array, configuration A3 and B3 will be able to achieve at least 30 dB cross polarization isolation through the use of one additional rotation mechanism.

In this chapter, a novel design approach for polarization rotator with good cross polarization isolation is presented. By cascading two 90° meanderline polarizers and incorporating a linear grid polarizer, a polarization rotator with at most two rotating layers can be realized.

Table 2.5: Summary of design performance for various configurations

Type	No. of Rotating Mechanism	Worst Case Reflection Coefficient (dB)		Worst Case Cross-Polar Discrimination (dB)	
		$\Theta = 0°$	$\Theta = 45°$	$\Theta = 0°$	$\Theta = 45°$
A1	1	-11.6	-11.0	-16.6	-15.7
A2	2	-11.3	-6.0	-50.3	-32.0
A3	2	-9.1	-8.3	-45.6	-39.8
B1	1	-10.7	-10.3	-16.4	-9.6
B2	1	-8.4	-4.6	-41.1	-28.3
B3	2	-8.4	-8.2	-41.1	-33.2

Chapter 3

Fabrication and Measurement of Polarization Rotator

Fabrication and measurement were carried out to validate the concept of the novel polarization rotator described in Chapter 2. The objectives were to ascertain the feasibility of the concept as well as to explore the challenges related to the realization and characterization of such a polarization rotator.

3.1 Design and Fabrication

Based on the concept proposed in Chapter 2, a polarization rotator designed for operation in Ku-band was constructed using two identical 90° polarizers and a 250 mil thick Rohacell 31 HF foam arranged in a stacked configuration as illustrated in Figure 3.1.

Each of the 90° polarizers was constructed from 3 layers of meanderline grids whose dimensions are shown in Figure 3.2. All the grids were etched on 3 mil thick Dupont Pyralux substrate with 17.5 μm thick copper (0.5 oz). To minimize the effect of edge diffraction during off-axis measurement, an 18 inch wide substrate – which was the maximum substrate size that the fabrication

house can handle, was used for this design, Figure 3.3. There were 32 holes and slots created on the substrates and spacer to enable rotation of the grids in steps of 11.25°. A fabricated meanderline grid etched on Dupont Pyralux substrate is shown in Figure 3.4. The 90 layers° polarizer is then realized by stacking the 3 meanderline grids in the configuration illustrated in Figure 3.5.

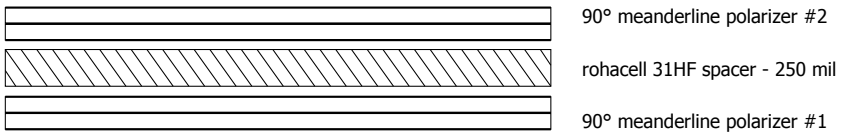

Figure 3.1: Construction of polarization rotator

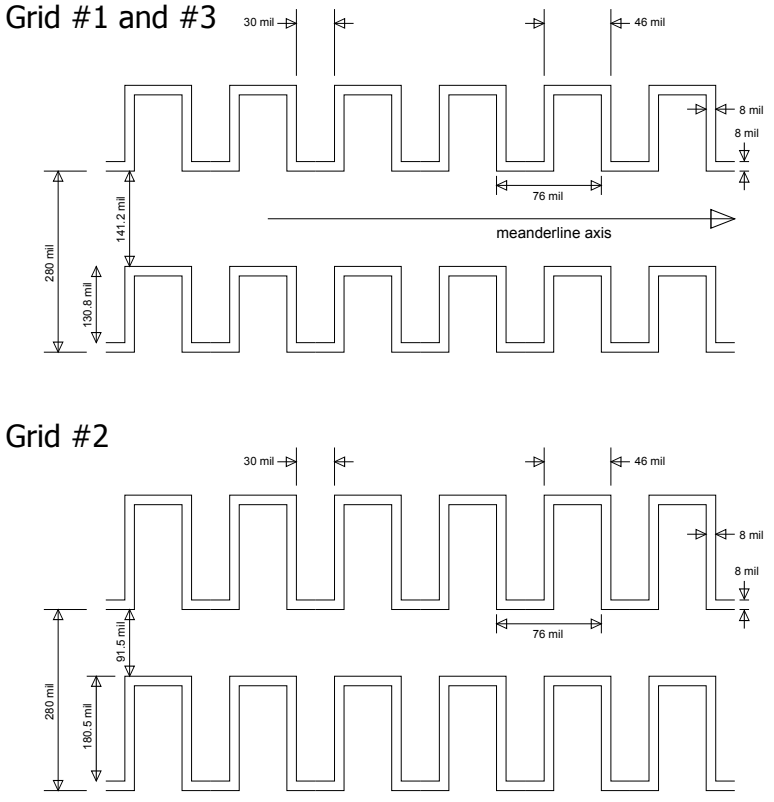

Figure 3.2: Dimensions of meanderline grids for 90° polarizer

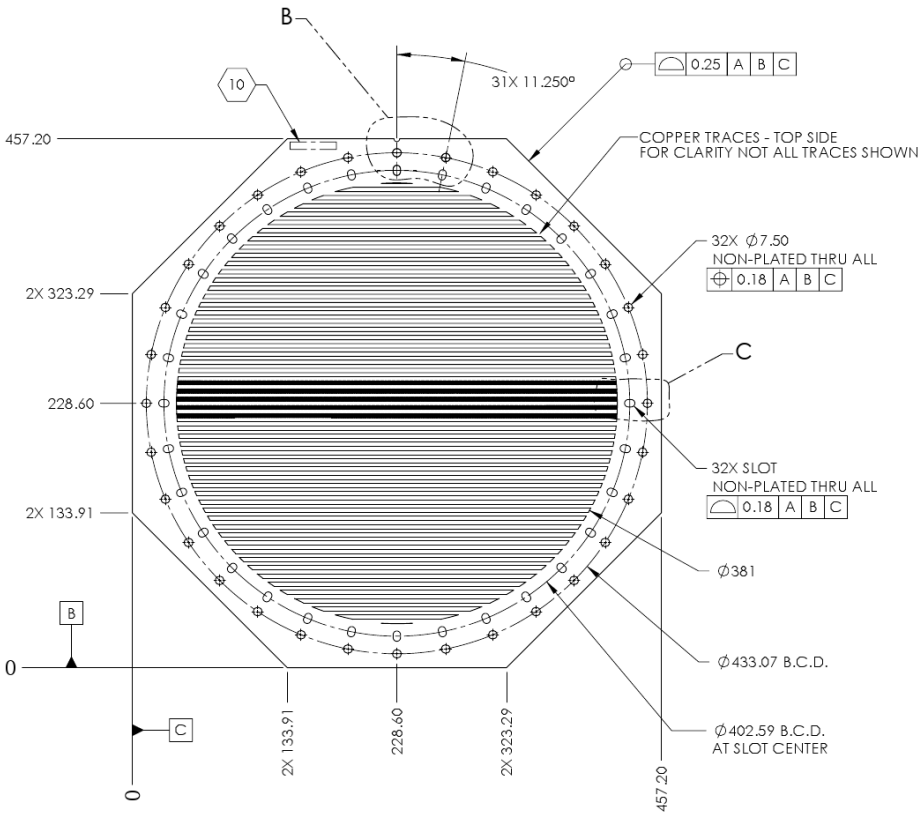

Figure 3.3: Substrate outline of meanderline grid layer

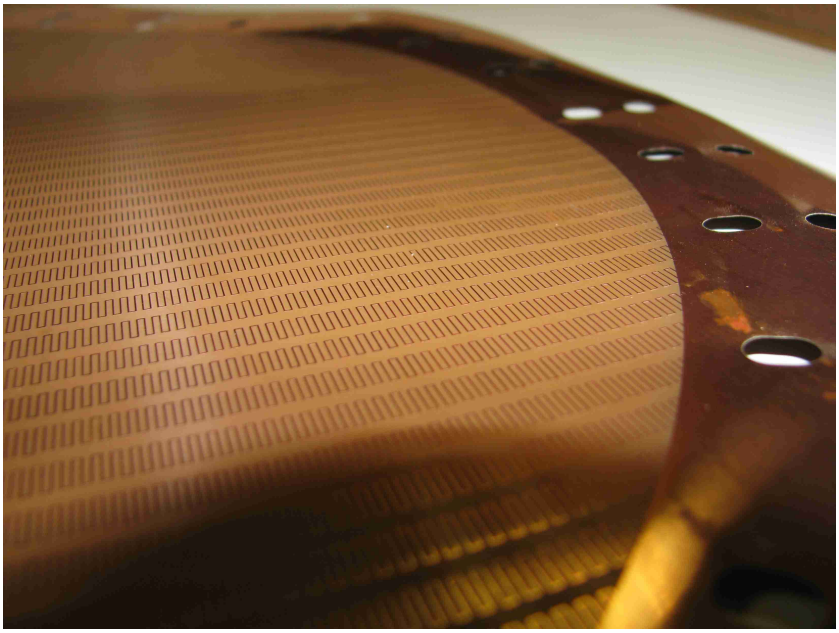

Figure 3.4: Etched meanderline grid on Dupont Pyralux substrate

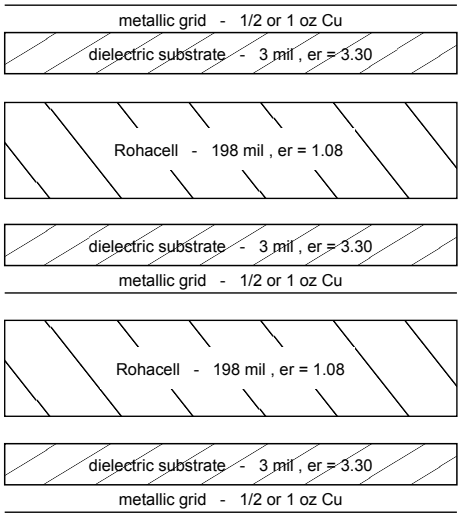

Figure 3.5: Construction of 90° meanderline polarizer

Due to the size of the fabricated substrate, which was 18 inches wide, it was difficult to achieve even adhesion of the epoxy between the substrate and spacer foam, Figure 3.6. To ensure the layers were tightly bound, an octagon support frame was constructed to bind the substrates and spacer foam, Figure 3.7. The assembled polarization rotator is shown in Figure 3.8

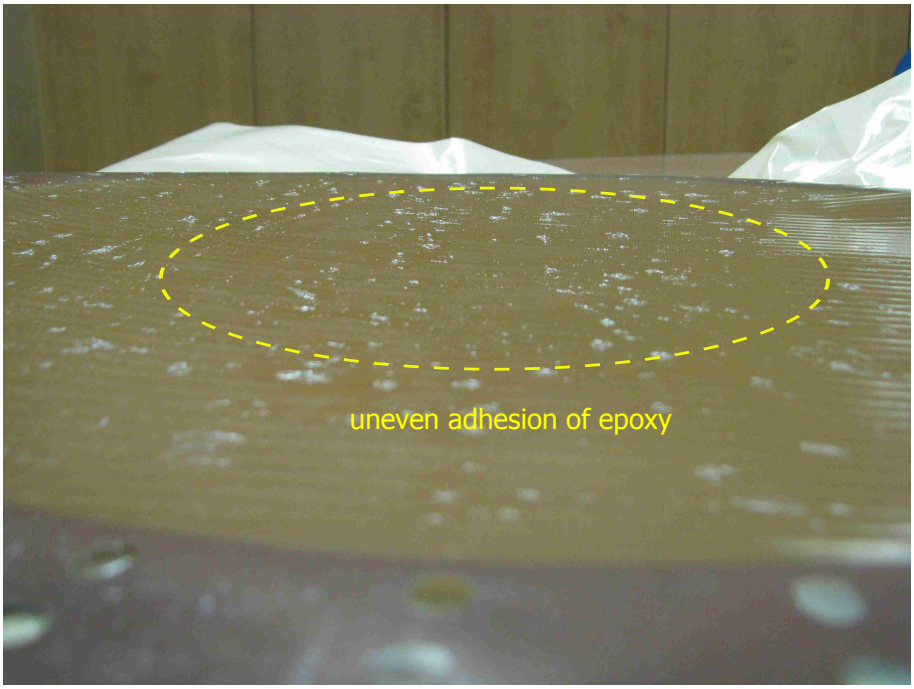

Figure 3.6: Uneven adhesion of epoxy on substrate

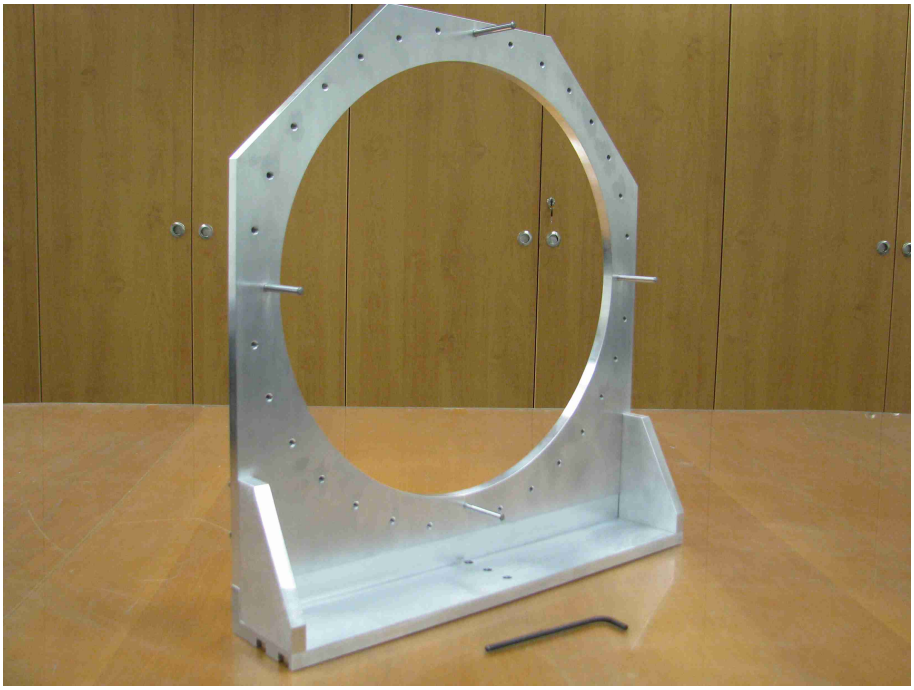

Figure 3.7: Mechanical frame for mounting polarization rotator

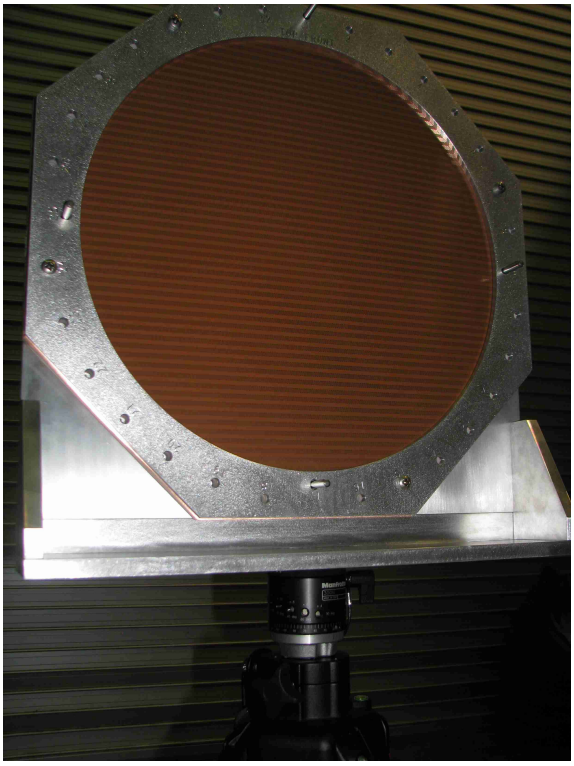

Figure 3.8: Assembled polarization rotator with octagon frame

3.2 Measurement Setup

The polarization rotator was mounted on a tripod for measurement in an anechoic chamber as shown in Figure 3.9. A 2–18 GHz circular quad ridge horn was used as the transmit antenna, Figure 3.10. The receiving antenna is a small vertically polarized Ku-band scanning array placed approximately 1 inch behind the polarization rotator, Figure 3.11. During measurement, the octagon mounting frame was covered with ECCOSORB LS-20 absorber to minimize scattering from the metallic surfaces and edges, Figure 3.12. Plan view of the measurement setup in anechoic chamber is shown in Figure 3.13.

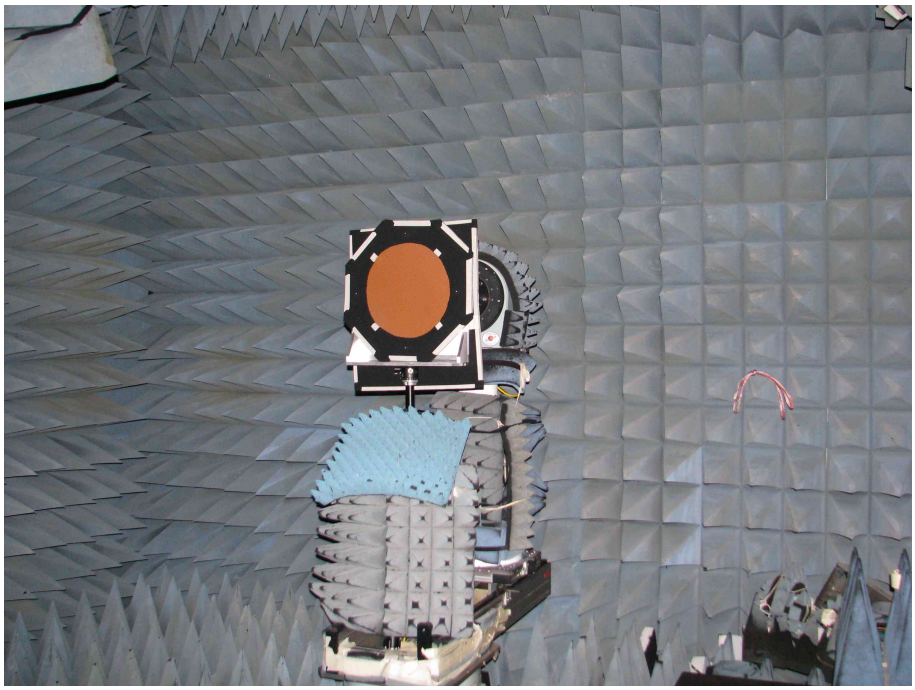

Figure 3.9: Polarization rotator mounted on tripod in anechoic chamber

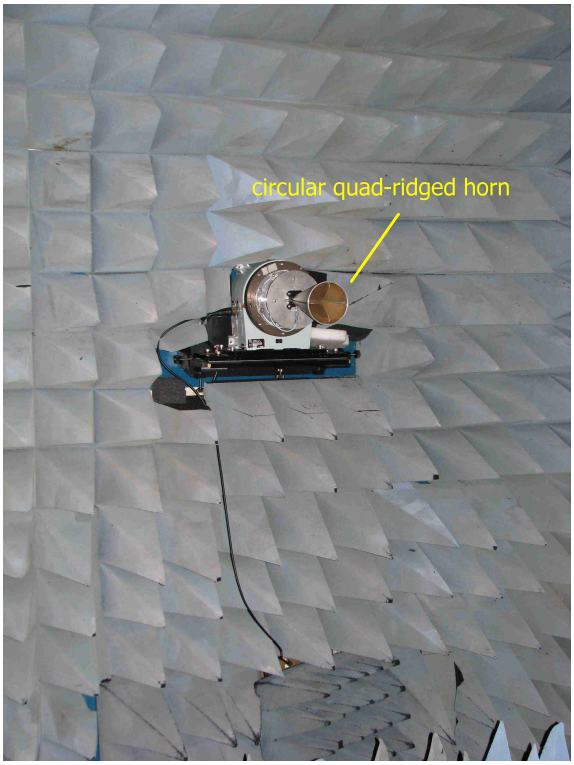

Figure 3.10: Transmit antenna – circular quad-ridged horn

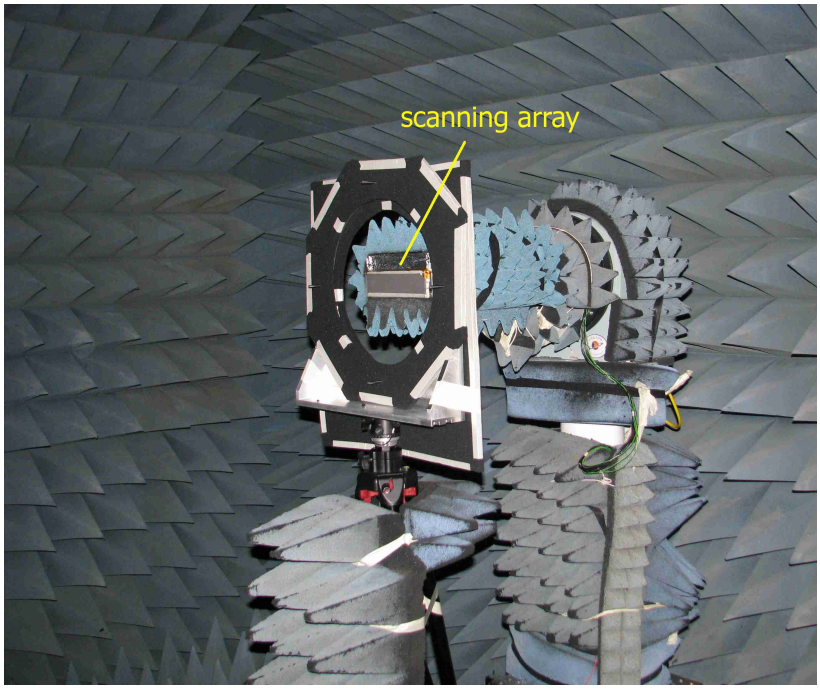

Figure 3.11: Receive antenna – scanning array

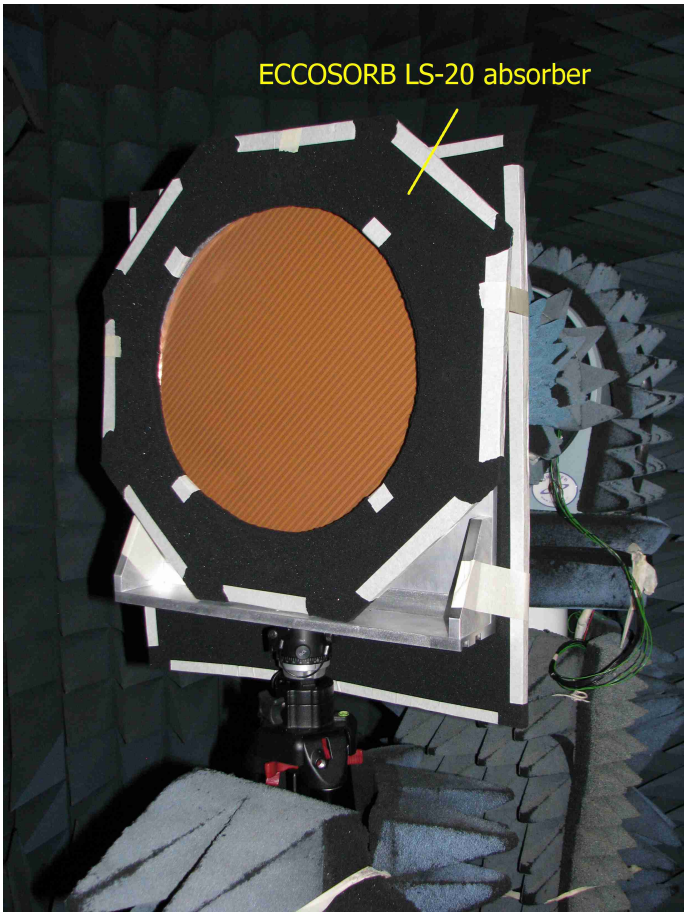

Figure 3.12: Setup of polarization rotator during measurement

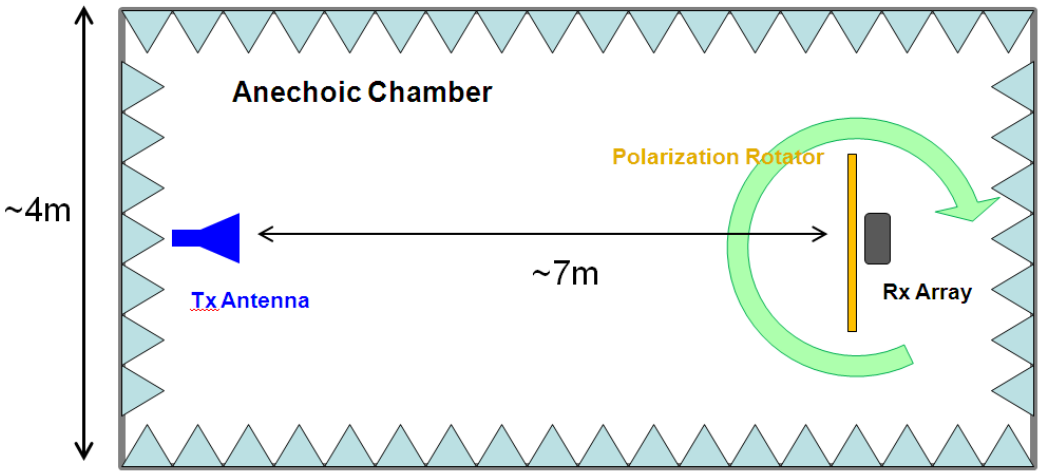

Figure 3.13: Plan view of measurement setup in anechoic chamber

3.3 Measurement Results

3.3.1 90° Polarizer

The axial ratio of the underlying 90° polarizer was measured using the rotating probe technique [43]. As plotted in Figures 3.14 and 3.15, the measured axial ratio of the polarizer for both 0° and 45° scan are better than 2.5 dB from 10.7 – 12.75 GHz and compares well with predicted results.

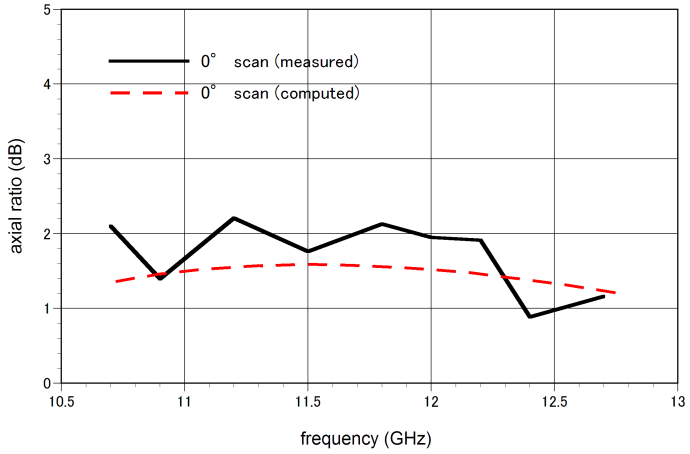

Figure 3.14: Measured versus computed axial ratio of 90° polarizer – 0° scan

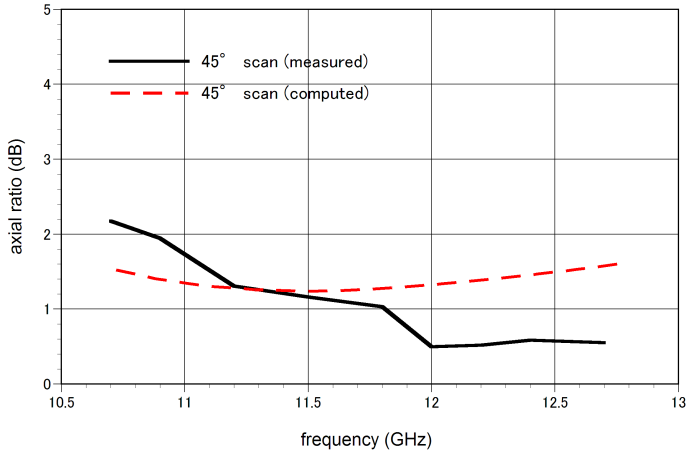

Figure 3.15: Measured versus computed axial ratio of 90° polarizer – 45° scan

3.3.2 Scanning Array with Mechanical Frame

A pattern measurement of the scanning array antenna in the presence of the mechanical frame was carried out at 11.7 GHz to obtain the baseline results without the polarization rotator. The measured co-polarized and cross-polarized patterns of the array for 11 scan angles in the azimuth plane (-45°, -40°, -30°, -20°, -10°, 0°, 10°, 20°, 30°, 40° and 45°) are plotted in Figure 3.16. The magnitudes are normalized to the peak gain for each beam. The results showed that the array antenna has a cross polarization isolation of approximately 25 dB in the H-plane. Subsequent pattern measurements involving the polarization rotator will be normalized to the peak gain measured at each scan angle.

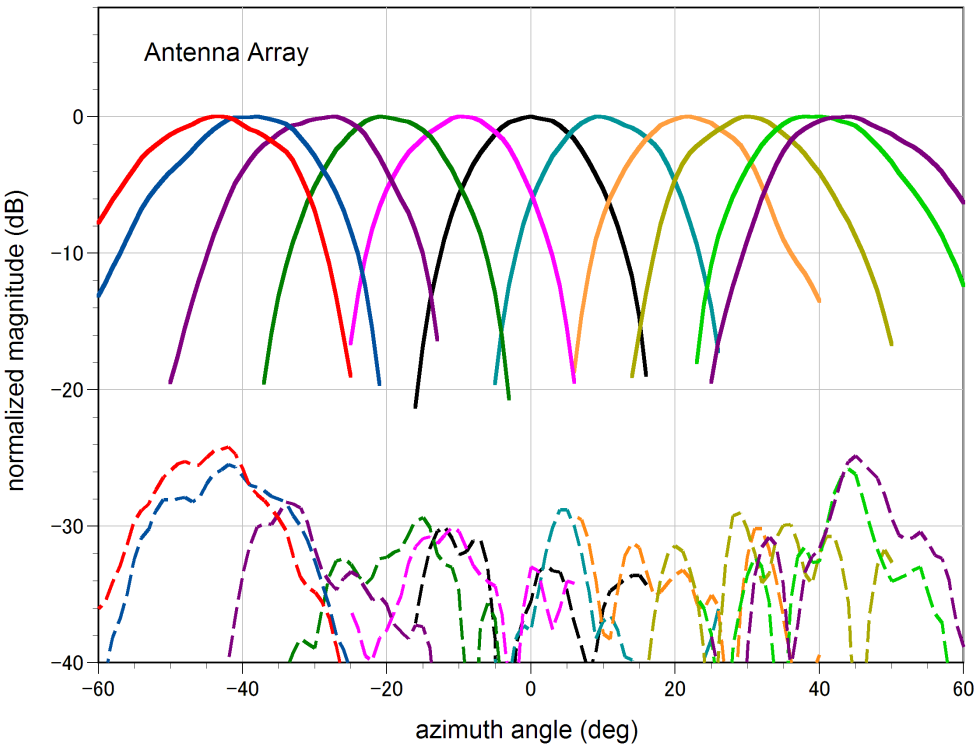

Figure 3.16: Measured H-plane beam patterns of scanning array in the presence of mechanical frame for various scan angles

3.3.3 Configuration A1

In Configuration A1, the two 90° meanderline polarizers are rotated in tandem to achieve polarization rotation, Figure 3.17. Using the coordinate reference from Figure 2.12, the resultant polarization rotation angle, Ψ_p, is twice the angle between the incident polarization vector and meanderline axis, Ψ_g. Figures 3.18 and 3.19 plots the resultant polarization angle against normalized magnitude for 0° and 45° incidence, respectively. Comparison with simulation results in Figures 3.20 and 3.21 show that the measured polarization rotation angles agree very well with the predicted $2\Psi_g$ relationship.

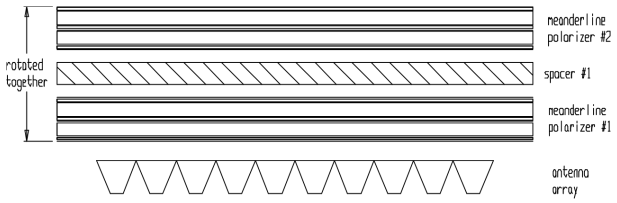

Figure 3.17: Polarization rotator concept for Configuration A1

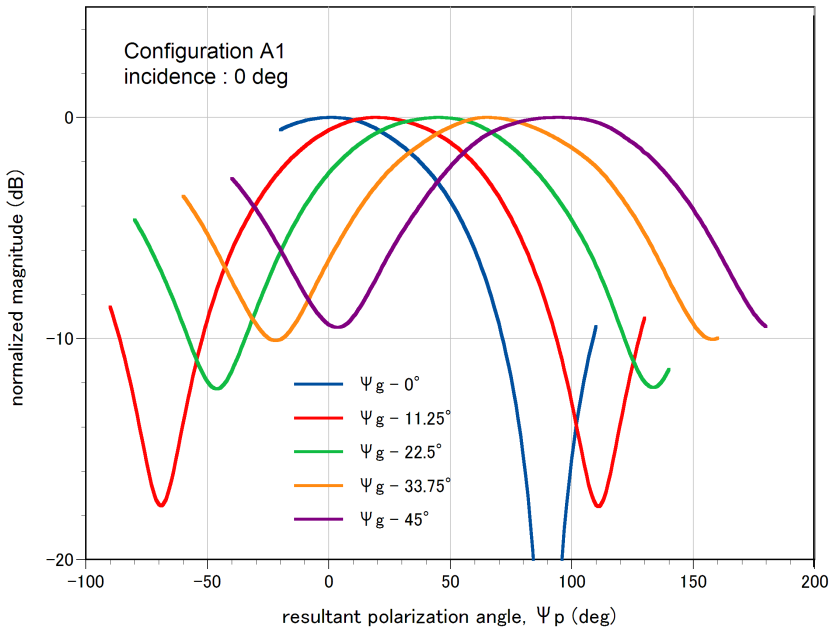

Figure 3.18: Measured polarization rotation angles for Configuration A1 – 0° incidence

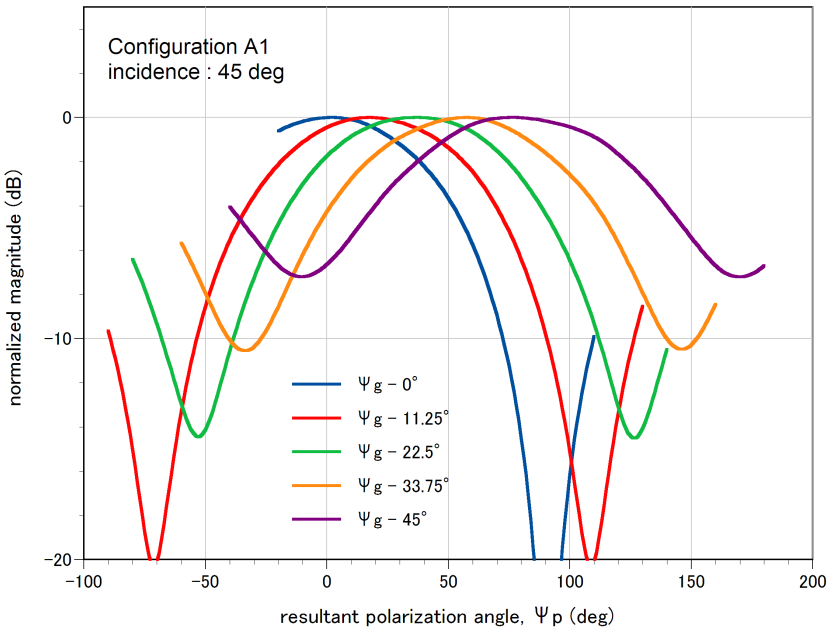

Figure 3.19: Measured polarization rotation angles for Configuration A1 – 45° incidence

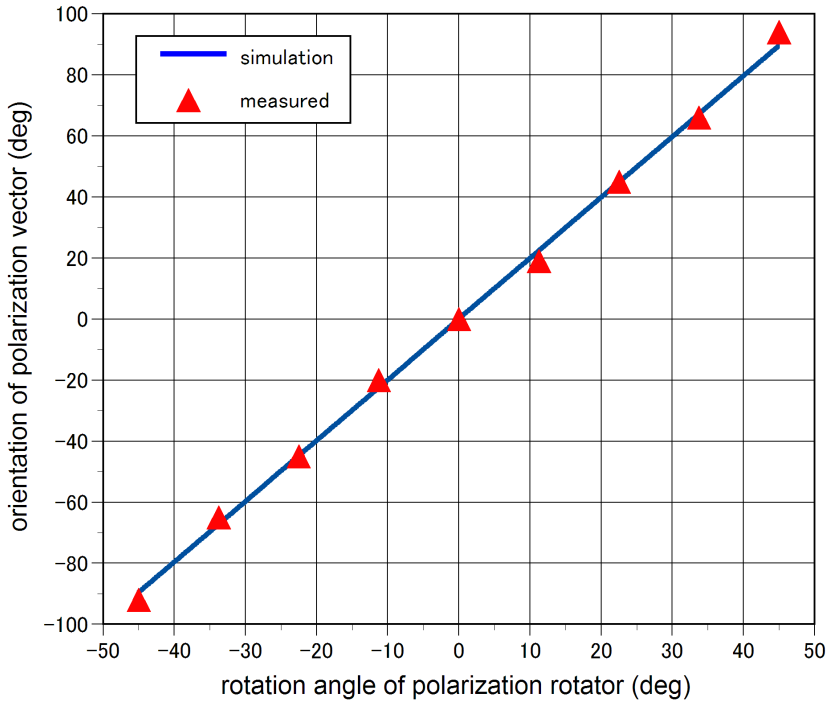

Figure 3.20: Comparison of simulated versus measured polarization rotation angles for Configuration A1 – 0° incidence

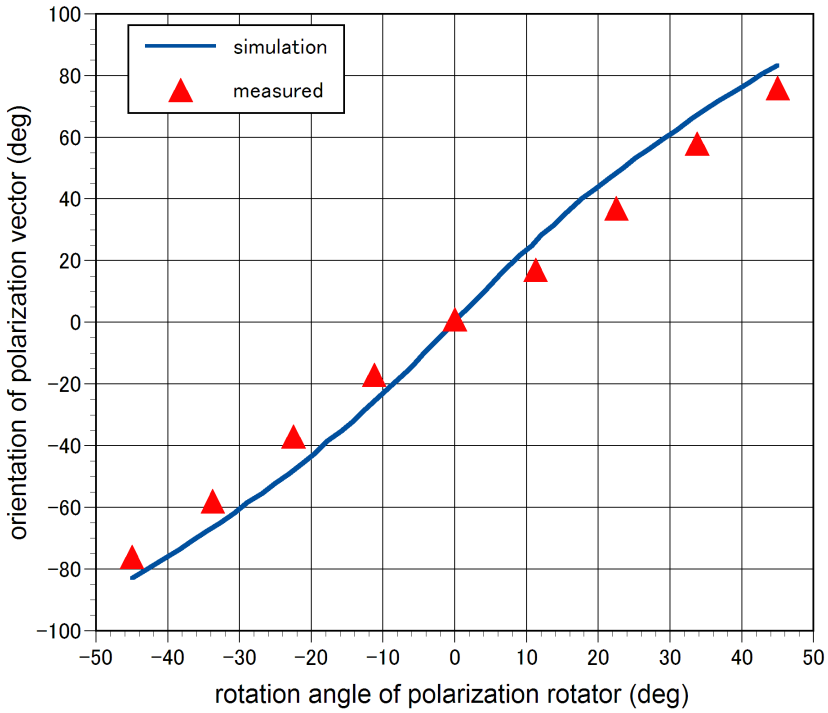

Figure 3.21: Comparison of simulated versus measured polarization rotation angles for Configuration A1 – 45° incidence

The performance of the polarization rotator with respect to various scan angles was characterized by measuring the co-polarized and cross-polarizer beam patterns of the scanning array from +45° to -45°. The results are then normalized to the measurement without the polarization rotator.

The beam patterns for polarization rotation of 0° and 90° are plotted in Figures 3.22 and 3.23, respectively. The results showed that the measured beam patterns were very close to the standalone array measurement. The average insertion losses for 0° and 90° polarization rotations are 0.1 dB and 0.8 dB, respectively. This indicates that the polarization rotator is relatively well matched for all polarization rotation angles within the scan angle of ±45° incidence.

It was also observed that the cross-polarization isolation of the polarization rotator deteriorates as the rotator rotates from 0° to 45°. This agrees with the prediction in Section 2.4.1 which showed that the cross-polarization isolation for this configuration degrades with increasing scan angle and polarizer rotation.

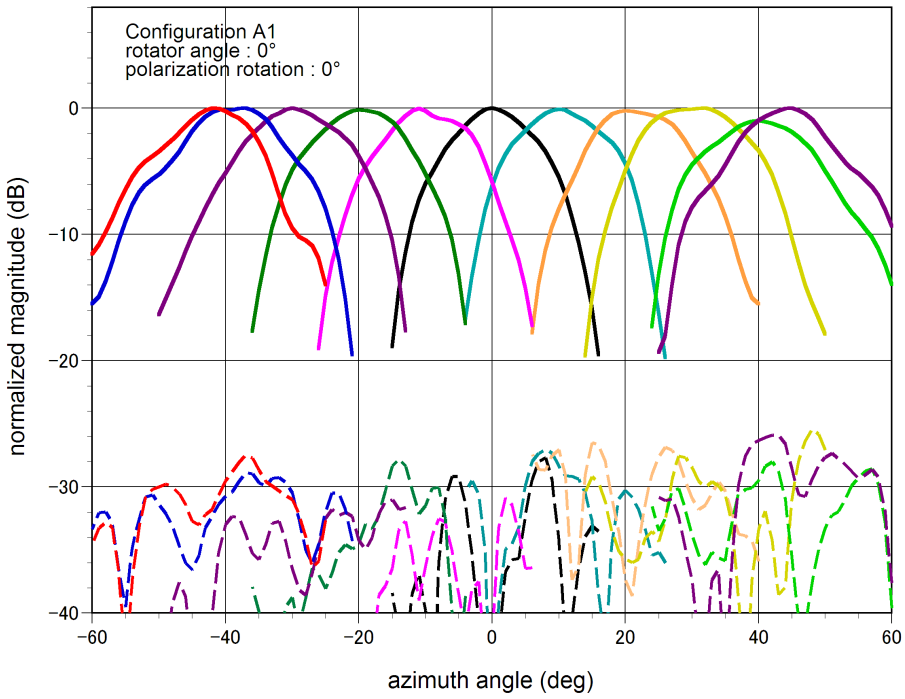

Figure 3.22: Measured beam patterns for Configuration A1 – 0° polarization rotation

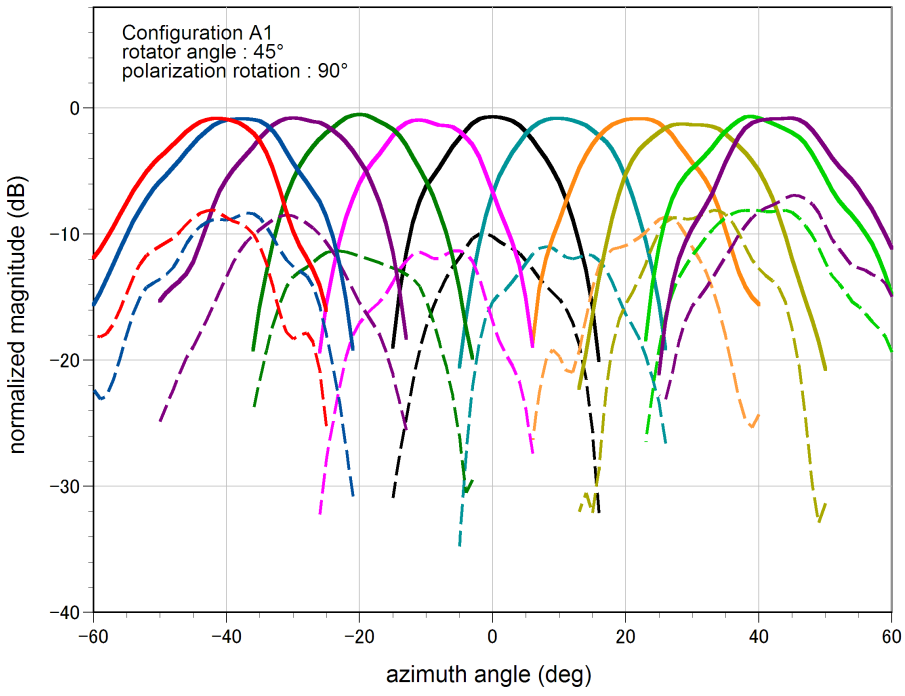

Figure 3.23: Measured beam patterns for Configuration A1 – 90° polarization rotation

3.3.4 Configuration A2

In Configuration A2, a linear grid is incorporated on top of the two 90° meanderline polarizers as shown in Figure 3.24. The objective of this design is to achieve improvement in cross-polarization isolation over that of Configuration A1. As in the case for Configuration A1, the resultant polarization rotation angle, Ψ_p, is twice the angle between the incident polarization vector and meanderline axis, Ψ_g.

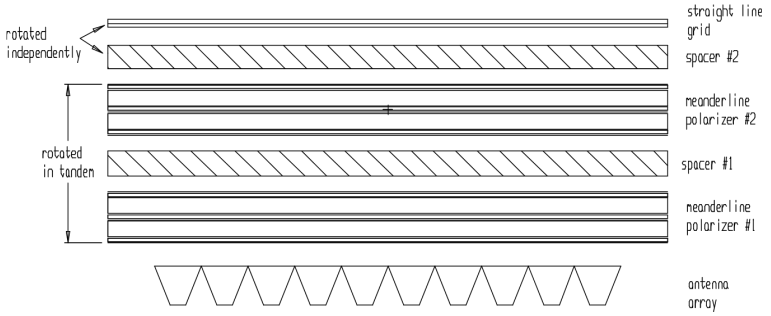

Figure 3.24: Polarization rotator concept for Configuration A2

Figures 3.25 and 3.26 plot the resultant polarization angle against normalized magnitude for 0° and 45° incidence, respectively. Similar to the case of Configuration A1, the measured resultant polarization rotation angles were very close to the predicted angles, Figures 3.27 and 3.28.

The performance of the polarization rotator with respect to various scan angles was characterized by measuring the co-polarized and cross-polarizer beam patterns of the scanning array from +45° to -45°. The results are then normalized to the measurement without the polarization rotator.

The beam patterns for polarization rotation of 0° and 90° are plotted in Figures 3.29 and 3.30, respectively. The results showed that the measured beam patterns were very close to the standalone array measurement with an insertion loss of 0.1 dB and 0.6 dB for polarization rotation of 0° and 90°, respectively. This indicates that the polarization rotator is relatively well matched for all po-

larization rotation angles within the scan angle of ±45° incidence. As predicted in Section 2.4.2, the average cross-polarization isolation of this configuration is better than 30 dB for ±45° incidence across polarization rotation angles.

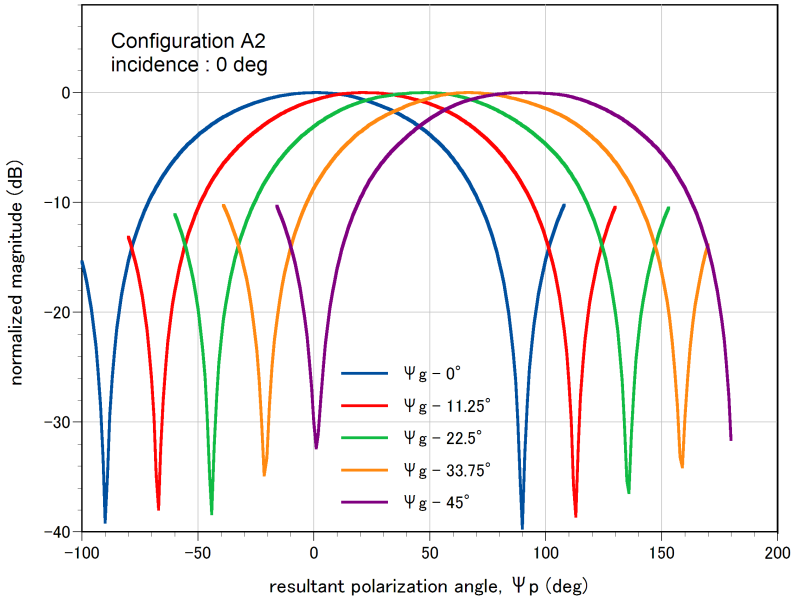

Figure 3.25: Measured polarization rotation angles for Configuration A2 – 0° incidence

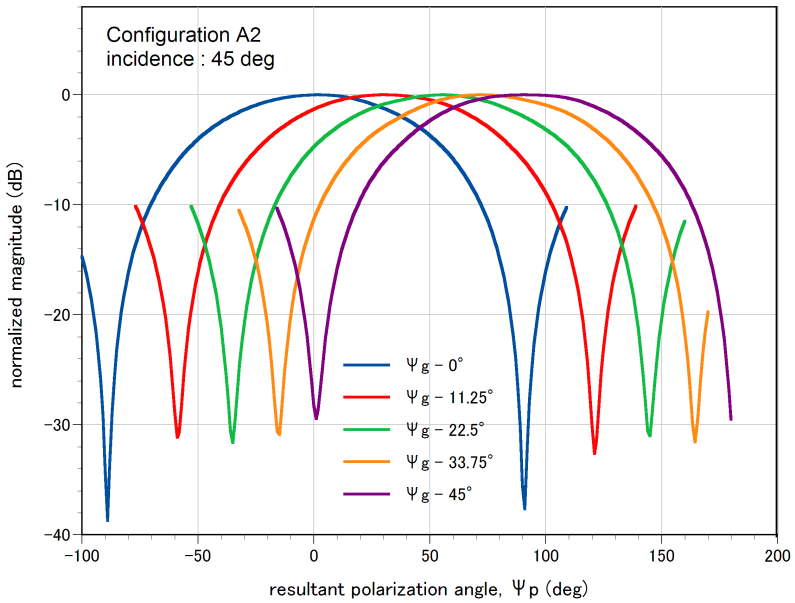

Figure 3.26: Measured polarization rotation angles for Configuration A2 – 45° incidence

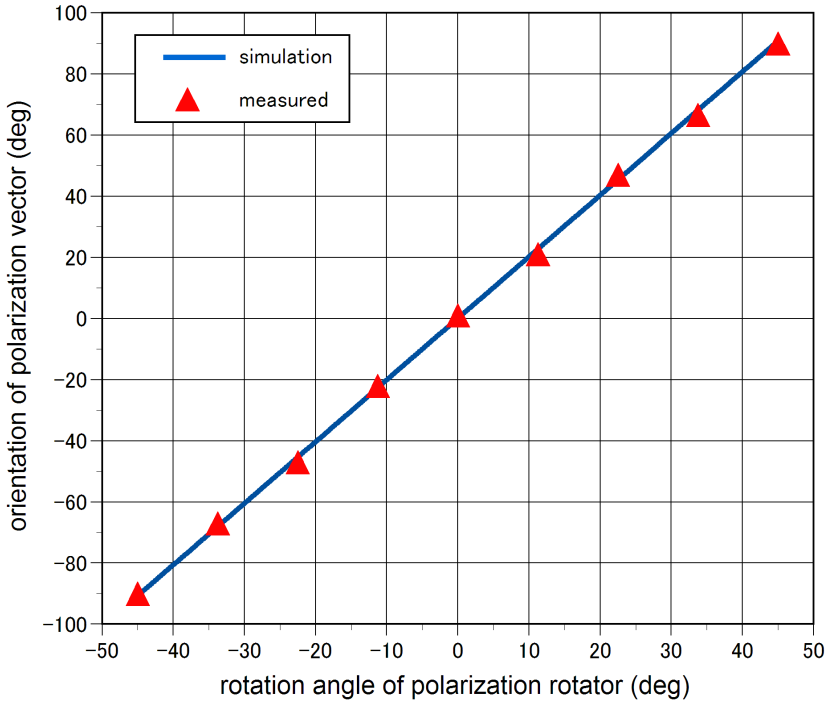

Figure 3.27: Comparison of simulated versus measured polarization rotation angles for Configuration A2 – 0° incidence

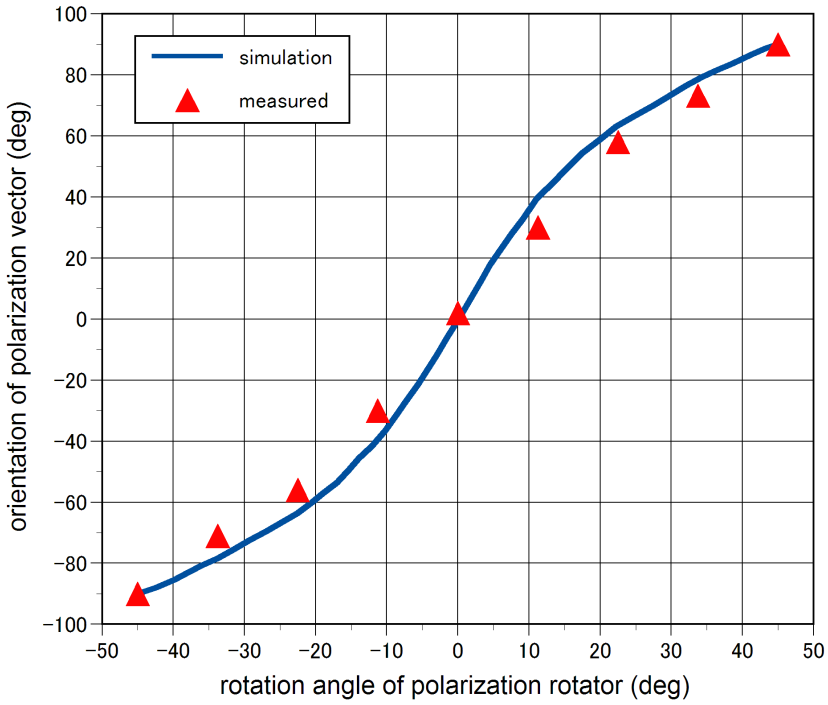

Figure 3.28: Comparison of simulated versus measured polarization rotation angles for Configuration A2 – 45° incidence

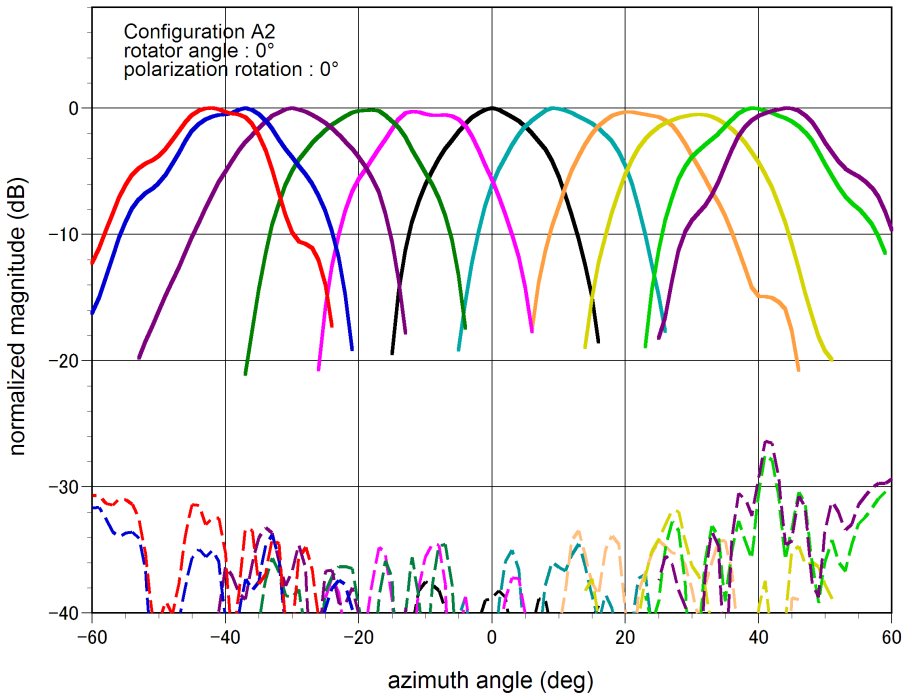

Figure 3.29: Measured beam patterns for Configuration A2 – 0° polarization rotation

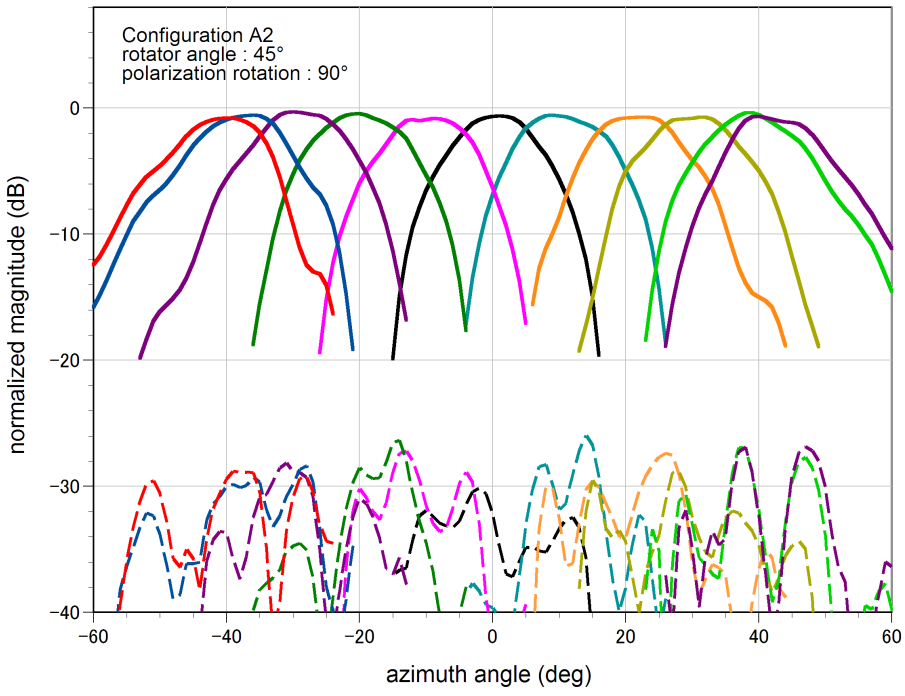

Figure 3.30: Measured beam patterns for Configuration A2 – 90° polarization rotation

3.3.5 Configuration B1

In Configuration B1, one of the 90° meanderline polarizers is fixed with its meanderline axis rotated 45° with respect to the linear polarization of the antenna array while the second 90° meanderline polarizer is rotated to achieve the desired polarization rotation angle, Figure 3.31. The predicted relationship between polarizer axes and polarization angle is listed in Table 2.2.

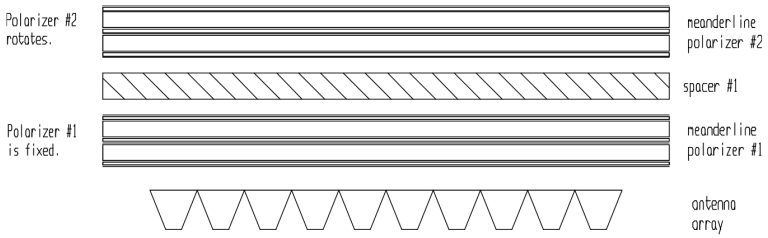

Figure 3.31: Polarization rotator concept for Configuration B1

Figures 3.32 and 3.33 plot the resultant polarization angle against normalized magnitude for 0° and 45° incidence, respectively. In agreement with the simulation results, the measured resultant polarization rotation angles at oblique 45° incidence exhibit a slight non-linear relationship against rotation angle of polarizer #2, Figures 3.34 and 3.35.

The performance of the polarization rotator with respect to various scan angles was characterized by measuring the co-polarized and cross-polarizer beam patterns of the scanning array from +45° to -45°. The results are then normalized to the measurement without the polarization rotator.

The beam patterns for polarization rotation of 0° and 90° are plotted in Figures 3.29 and 3.30, respectively. The insertion loss for 0° and 90° polarization rotation are 0.1 dB and 0.9 dB, respectively. In agreement with the prediction in Section 2.5.1, the worst case cross-polarization isolation of this configuration is about 9 dB for oblique 45° incidence.

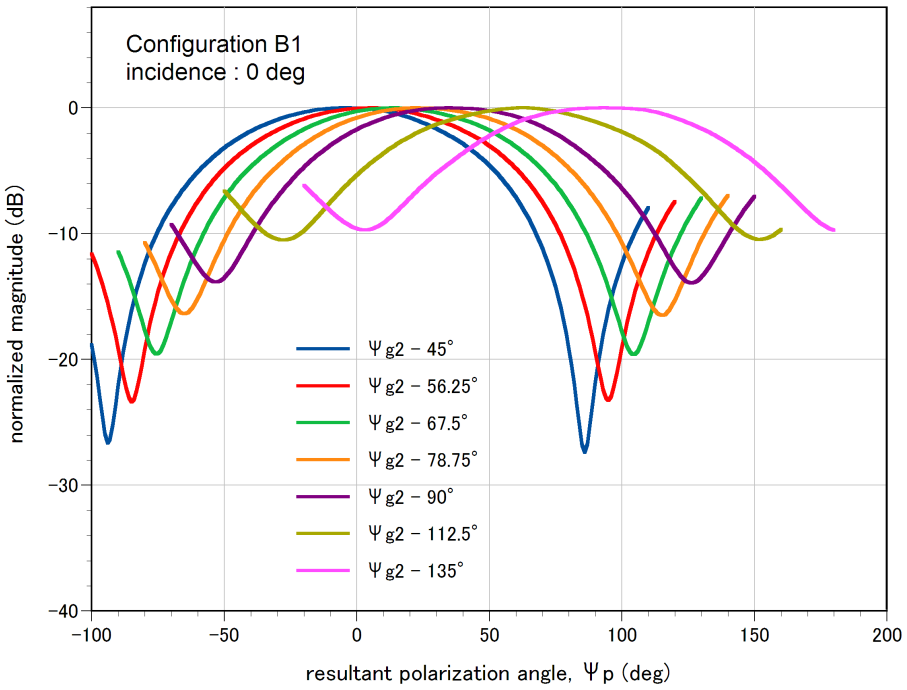

Figure 3.32: Measured polarization rotation angles for Configuration B1 – 0° incidence

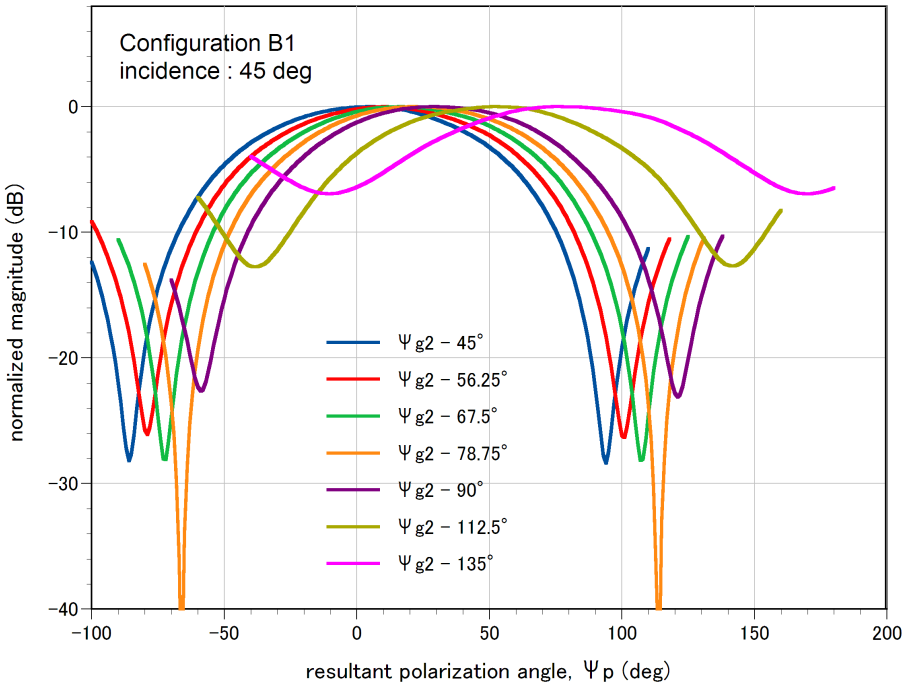

Figure 3.33: Measured polarization rotation angles for Configuration B1 – 45° incidence

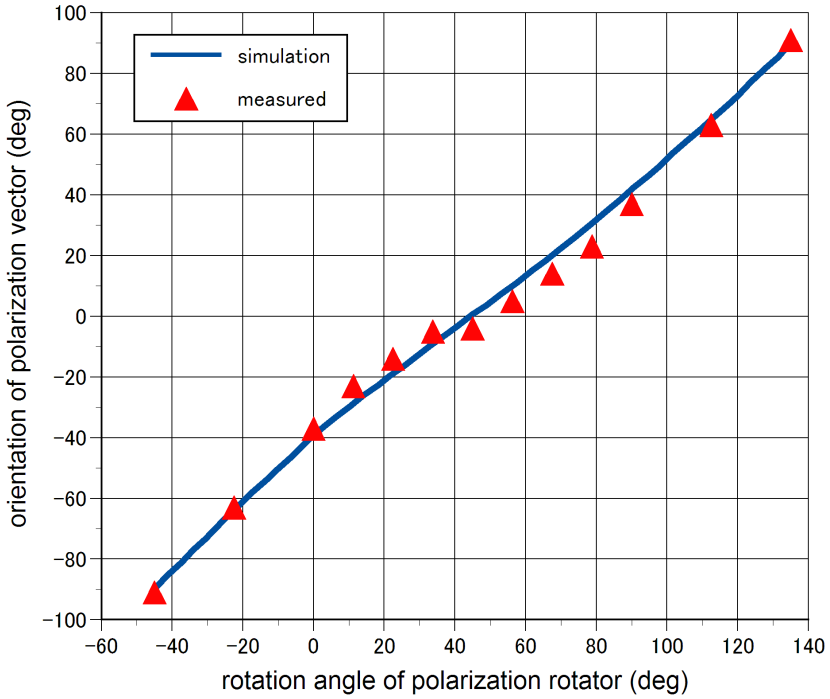

Figure 3.34: Comparison of simulated versus measured polarization rotation angles for Configuration B1 – 0° incidence

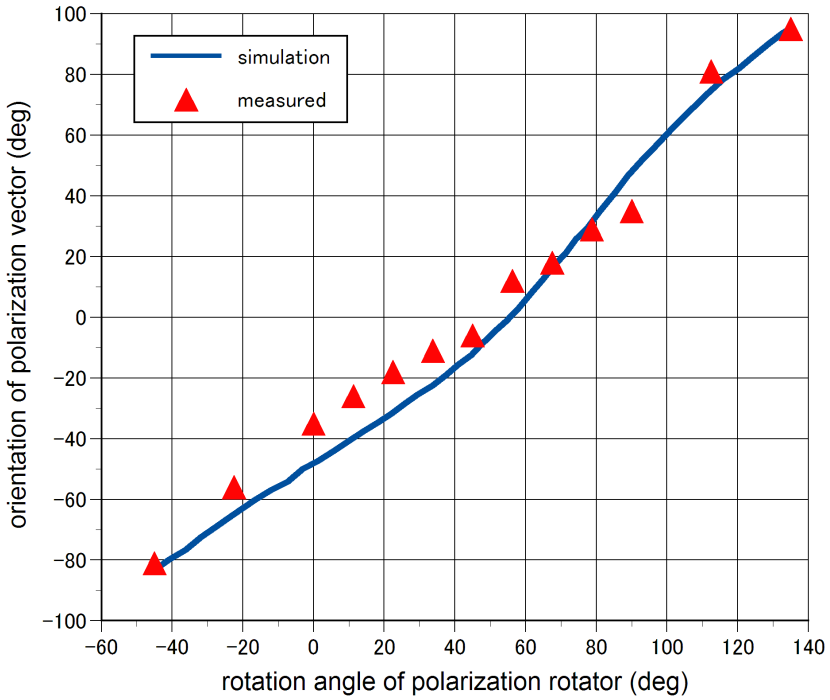

Figure 3.35: Comparison of simulated versus measured polarization rotation angles for Configuration B1 – 45° incidence

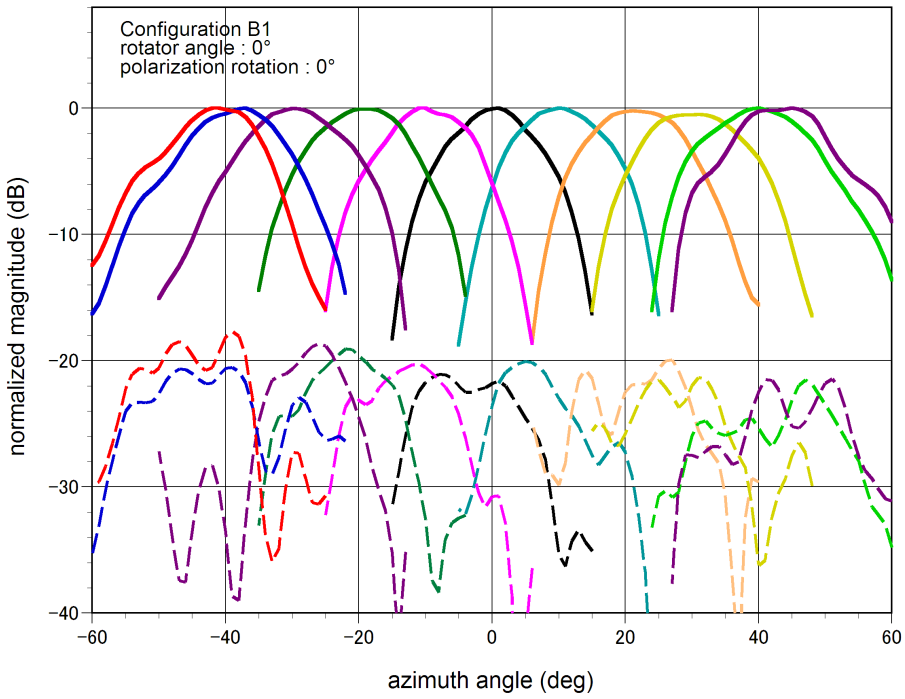

Figure 3.36: Measured beam patterns for Configuration B1 – 0° polarization rotation

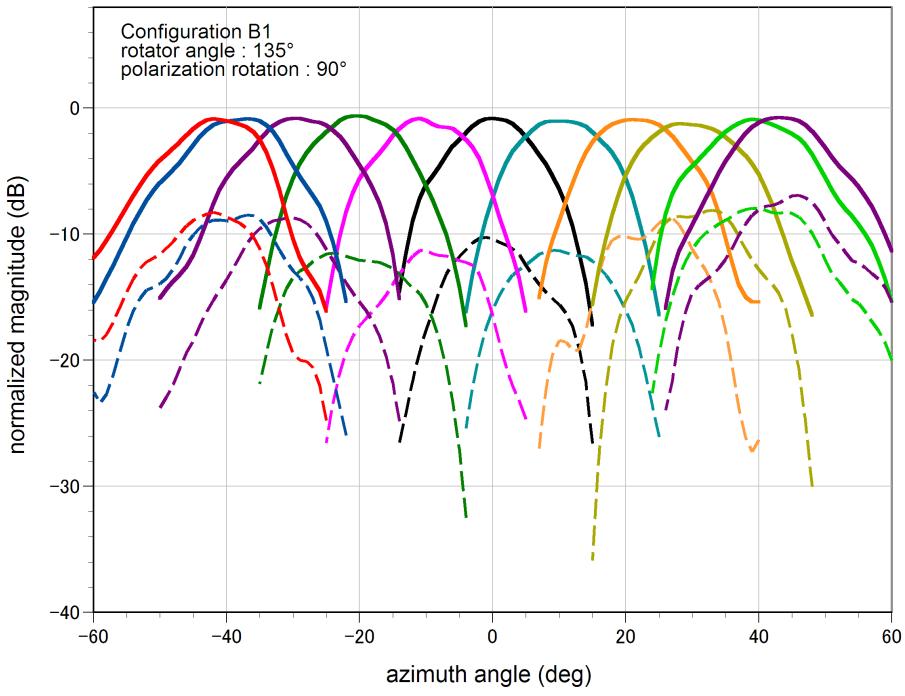

Figure 3.37: Measured beam patterns for Configuration B1 – 90° polarization rotation

3.3.6 Configuration B2

In Configuration B2, a linear grid is attached on top of the rotating 90° meanderline polarizer in Configuration B1, Figure 3.38. The objective is to improve the cross-polarization isolation as the polarizer rotates to convert the polarization angle. The predicted relationship between polarizer axes and polarization angle is listed in Table 2.3.

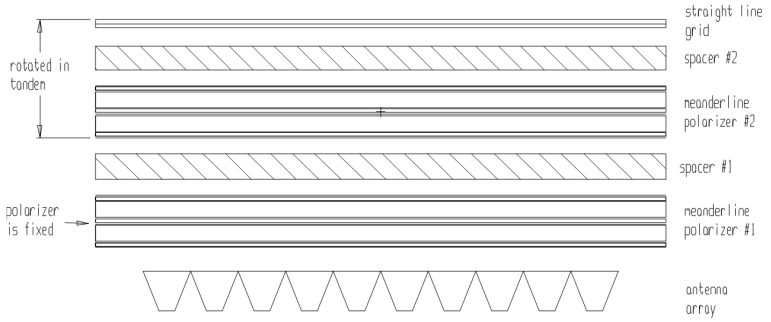

Figure 3.38: Polarization rotator concept for Configuration B2

Figures 3.39 and 3.40 plot the resultant polarization angle against normalized magnitude for 0° and 45° incidence, respectively. The measured resultant polarization rotation angles for normal and oblique incidence were very close to the predicted angles, Figures 3.41 and 3.42.

The performance of the polarization rotator with respect to various scan angles was characterized by measuring the co-polarized and cross-polarizer beam patterns of the scanning array from +45° to -45°. The results are then normalized to the measurement without the polarization rotator.

The beam patterns for polarization rotation of 0° and 90° are plotted in Figures 3.43 and 3.44, respectively. The results showed that the measured beam patterns were very close to the standalone array measurement. The insertion loss for 0° and 90° polarization rotation are 0.1 dB and 0.8 dB, respectively. In agreement with the predicted results in Section 2.5.2, the better than 25 dB

cross polarization isolation is a significant improvement over that of Configuration B1.

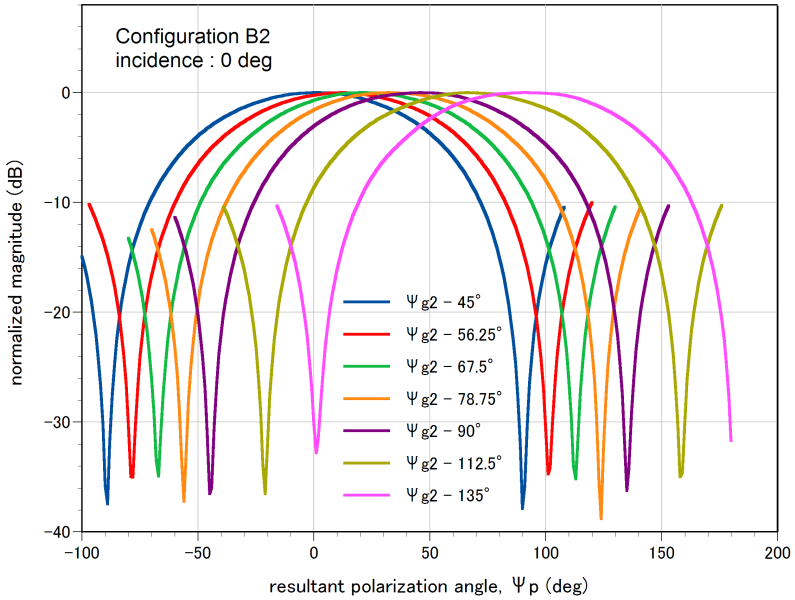

Figure 3.39: Measured polarization rotation angles for Configuration B2 – 0° incidence

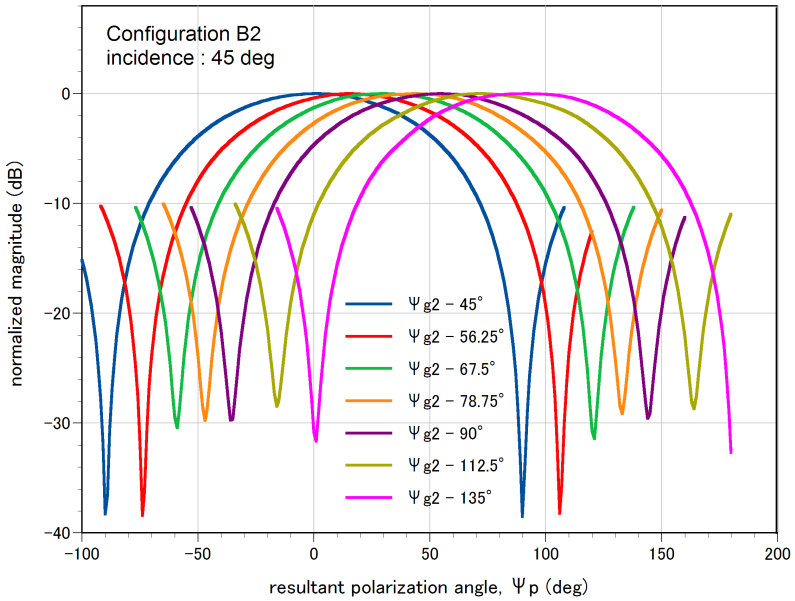

Figure 3.40: Measured polarization rotation angles for Configuration B2 – 45° incidence

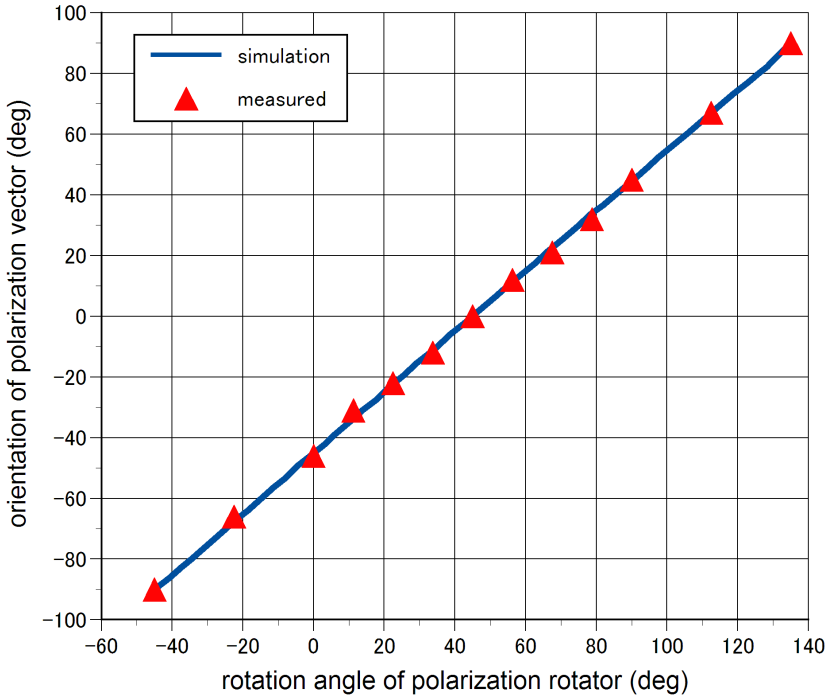

Figure 3.41: Comparison of simulated versus measured polarization rotation angles for Configuration B2 – 0° incidence

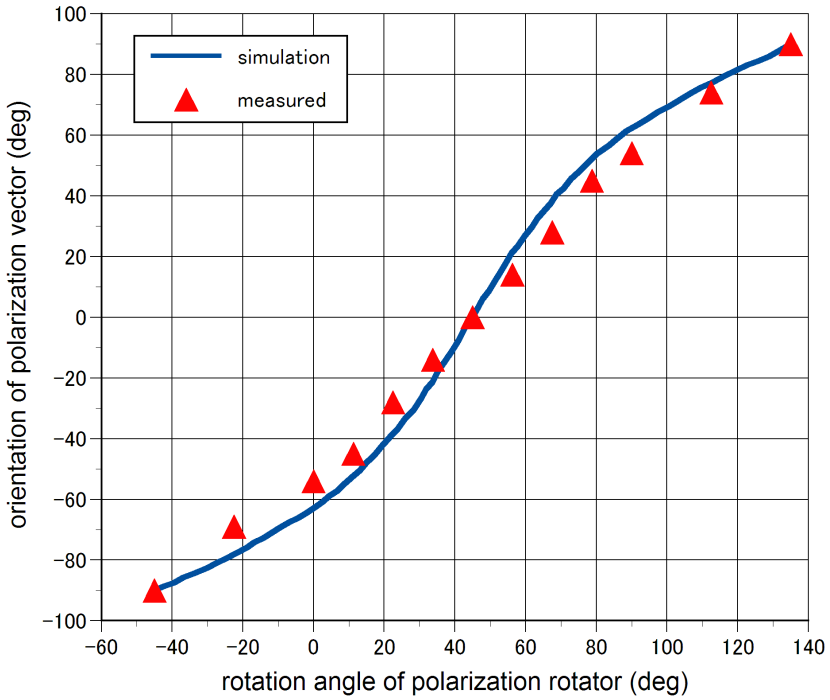

Figure 3.42: Comparison of simulated versus measured polarization rotation angles for Configuration B2 – 45° incidence

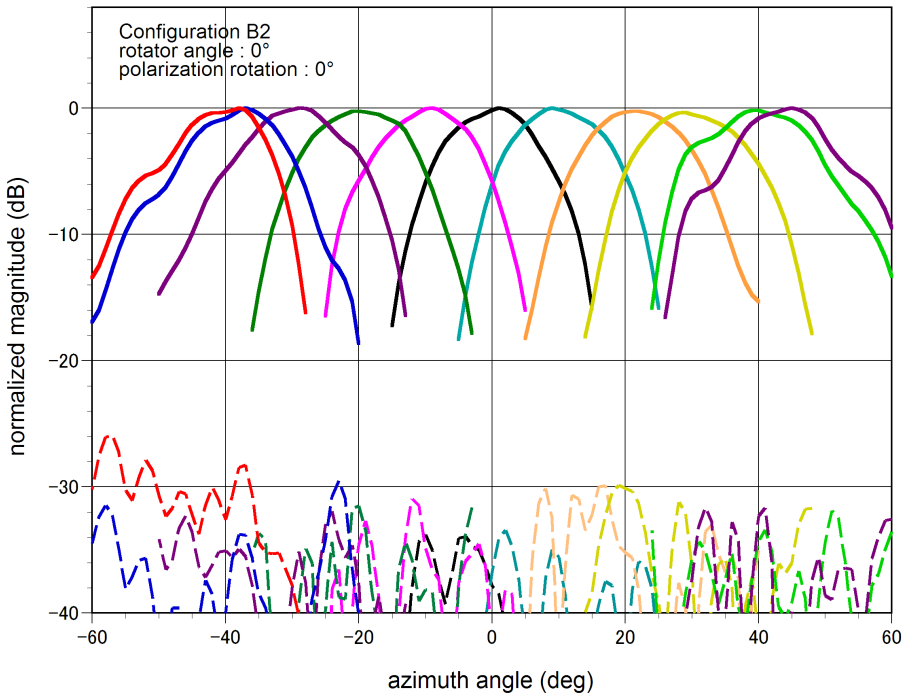

Figure 3.43: Measured beam patterns for Configuration B2 – 0° polarization rotation

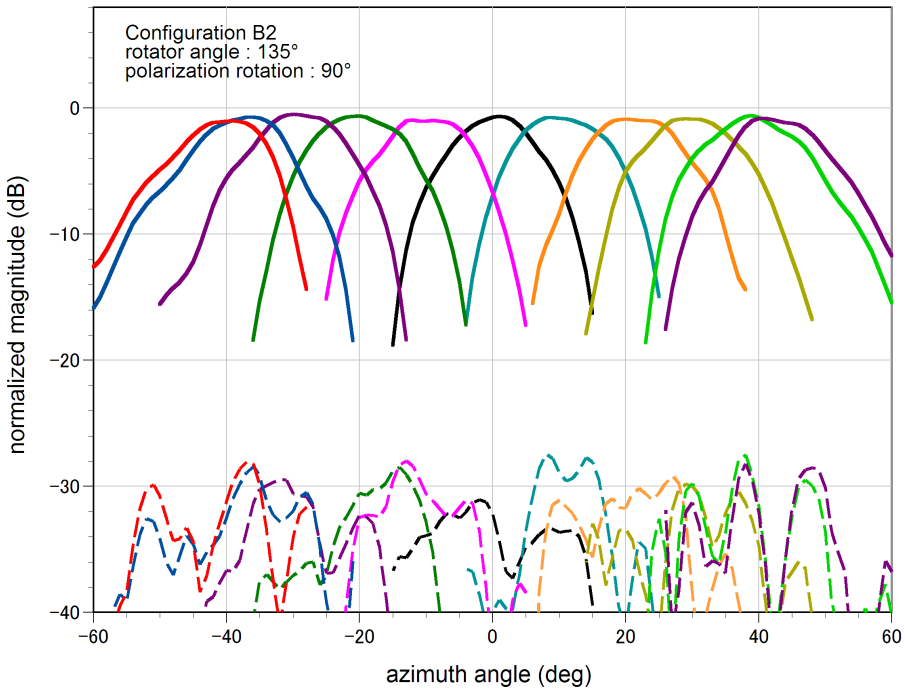

Figure 3.44: Measured beam patterns for Configuration B2 – 90° polarization rotation

3.4 Summary

In this chapter, a polarization rotator based on the concept presented in Chapter 2 was fabricated and measured. The versatility of the concept was demonstrated by measurements which showed that the various configurations were able to achieve polarization rotation for wave incidence within $\pm 45^\circ$ with an insertion loss of less than 1 dB. For the configurations tested, only one rotating layer was required to realize the polarization rotator instead of the multiple rotating grids in conventional design. The incorporation of a linear grid maintained the cross polarization isolation to levels required for VSAT applications.

In the fabrication and assembly process of the polarization rotator, a number of important lessons on the implementation of microwave polarizers were gained,

1. The alignment of the grid layers is critical for high frequency design. At Ku-band, a 1° phase error will result in a 0.15 dB change in axial ratio.
2. The substrate and copper thickness should be as thick as possible to minimize warping of the grid layer. Alignment and bonding gets easier with increasing rigidity of grid layer.
3. For multi-layer polarizer with diameter larger than 10 inches, the use of epoxy should be avoided as it will be difficult to maintain bonding consistency over a large area.
4. For measurement of polarizer with low axial ratio (< 1.5 dB), the metallic surfaces and edges of the mounting structure can have a significant impact on the accuracy of the measurement if they are not shielded probably with microwave absorbers.

Chapter 4

Accurate and Efficient Analysis of Microwave Polarizer with Finite Metallization Thickness

One of the key assumptions in the Grid Current approach, presented in Chapter 2, is that the meanderline grid is infinitely thin. For electrically thick metallization, such as in free-standing grid or high frequency operation, this assumption will result in discrepancies between measured and predicted performance as the thickness have a significant impact on the differential transmission phase. Please see Section 5.4 for more details.

To analyze a meanderline grid with finite thickness, a new formulation based on Transverse Resonance approach [44; 45] and Generalized Scattering Matrix (GSM) technique [46; 47] is proposed. Instead of modeling the periodic cell by a section of the meanderline conductor (Figure 4.1) in the grid current approach, the meanderline polarizer is represented as a periodic structure whose unit cell is shown in Figure 4.2 below.

The space bounded by two adjacent rows of meanderline grid can be viewed as a uniform cylinderical waveguide in the z-axis direction with meanderline

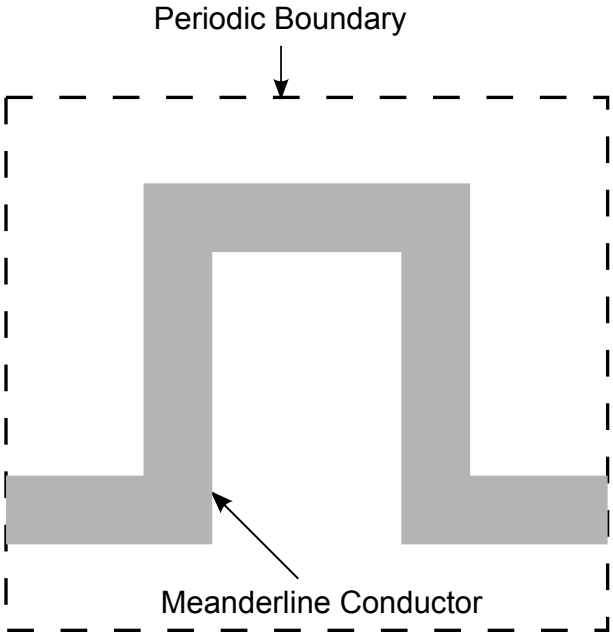

Figure 4.1: Periodic cell in grid current approach

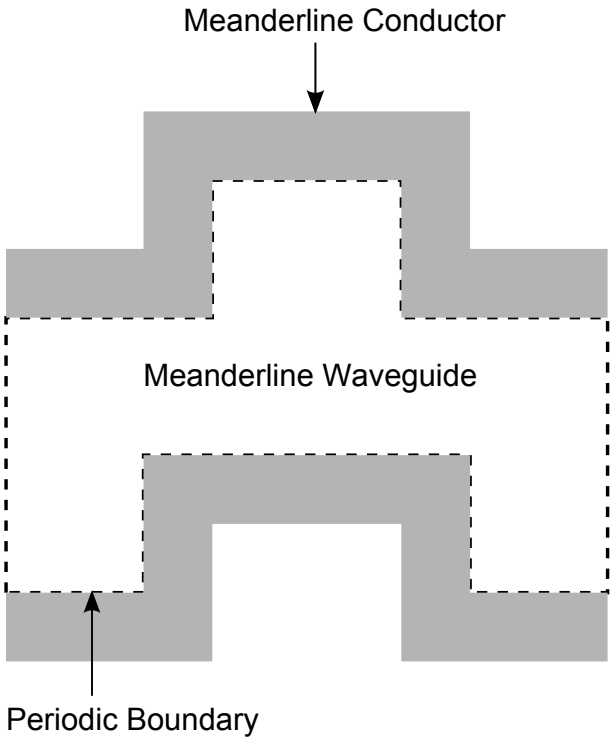

Figure 4.2: Periodic cell in new approach

cross-section in the transverse direction, Figure 4.3. This waveguide is henceforth termed the Meanderline Waveguide (MLG). By solving for the fields in

this MLG, instead of the induced current on the meanderline conductors, the transmission and reflection characteristics of the meanderline grid can be determined. The configuration for a typical meanderline periodic cell is represented in Figure 4.4.

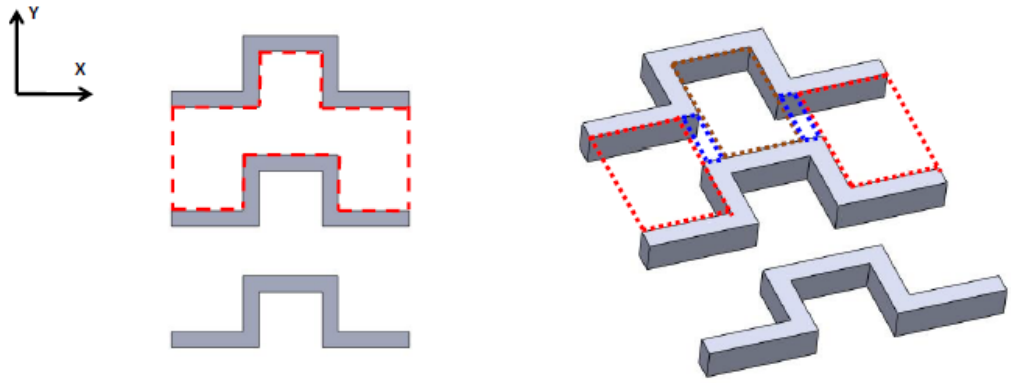

Figure 4.3: Meanderline Guide Bounded by Conductors

To solve for the fields in the MLG, modal analysis is chosen as it is computationally efficient and based directly on the solution of Maxwell's equations with the appropriate boundary conditions. Under normal incidence, EM wave impinging on the periodic cell can generate Transverse Electromagnetic (TEM), TE and TM modes in the MLG depending on the incident wave polarization. Since the MLG is symmetric about the Center Wall (CW), only the field representation in Region I, II and III need to be solved.

The Top Wall (TW) and Bottom Wall (BW) of the MLG are modelled as Pecfert Electric Conductor (PEC). For normal TE incidence, the Left Wall (LW), Right Wall (RW), and CW are Perfect Magnetic Conductor (PMC). Under normal TM incidence, LW, RW, and CW are PEC walls. For the MLG with magnetic side walls, TEM, TE and TM modes need to be determined. While TE and TM modes need to be determined for the MLG with electric side walls.

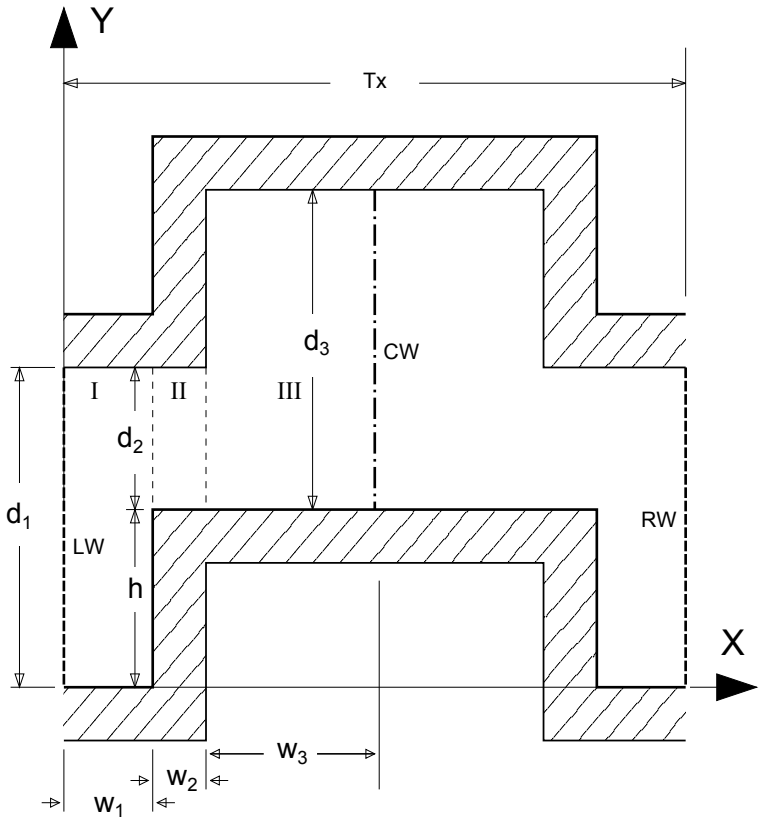

Figure 4.4: Configuration of meanderline polarizer unit cell

4.1 TEM Meanderline Waveguide Modes

TEM modes in the MLG only exist for TE wave incidence because the boundary conditions at LW and RW are PMC. For TM wave incidence, boundary conditions for the LW and RW are PEC and the MLG can be viewed as a rectangular waveguide – which does not support TEM mode propagation.

4.1.1 Derivation of TEM modes

The transverse electric field vector in the MLG can be derived from the scalar magnetic potential,

$$\bar{e}_m = -\nabla_t \Phi(x, y)$$

From the constitutive eqution,

$$\begin{aligned} \nabla \cdot \bar{D} &= \epsilon \nabla_t \cdot \bar{e}_m = 0 \\ \Rightarrow \quad \nabla_t^2 \Phi(x,y) &= 0 \end{aligned} \tag{4.1}$$

Equation (4.1) is the familiar Laplace equation encountered in electrostatic problems. The boundary conditions for Region I, II and III are then given by,
Region I :

$$\begin{aligned} E_x(x,0) = 0 \quad &, \quad E_x(x,d_1) = 0 \quad , \quad H_y(0,y) = 0 \\ \Phi(x,0) = 0 \quad &, \quad \Phi(x,d_1) = 1 \end{aligned}$$

Region II :

$$\begin{aligned} E_x(x,h) = 0 \quad &, \quad E_x(x,h+d_2) = 0 \\ \Phi(x,h) = 0 \quad &, \quad \Phi(x,h+d_2) = 1 \end{aligned}$$

Region III :

$$\begin{aligned} E_x(x,h) = 0 \quad &, \quad E_x(x,h+d_3) = 0 \quad , \quad H_y(T_x/2,y) = 0 \\ \Phi(x,h) = 0 \quad &, \quad \Phi(x,h+d_3) = 1 \end{aligned}$$

Solving the Laplace Equation (4.1) subject to the boundary conditions given above, the transverse field components in the MLG are given as,

Region I :

$$
\begin{aligned}
E_x^I &= -\nabla_x \Phi(x,y) \times \sqrt{\eta_0} \\
&= -\sqrt{\eta_0}\left[\sum_{l=1}^{\infty} A_l \left(\frac{l\pi}{d_1}\right) \sin\left(\frac{l\pi y}{d_1}\right) \sinh\left(\frac{l\pi x}{d_1}\right)\right] \\
E_y^I &= -\nabla_y \Phi(x,y) \times \sqrt{\eta_0} \\
&= -\sqrt{\eta_0}\left[\frac{1}{d_1} + \sum_{l=1}^{\infty} A_l \left(\frac{l\pi}{d_1}\right) \cos\left(\frac{l\pi y}{d_1}\right) \cosh\left(\frac{l\pi x}{d_1}\right)\right] \\
H_x^I &= \frac{1}{\eta_0}\left(-E_y^I\right) \\
&= \frac{1}{\sqrt{\eta_0}}\left[\frac{1}{d_1} + \sum_{l=1}^{\infty} A_l \left(\frac{l\pi}{d_1}\right) \cos\left(\frac{l\pi y}{d_1}\right) \cosh\left(\frac{l\pi x}{d_1}\right)\right] \\
H_y^I &= \frac{1}{\eta_0}\left(E_x^I\right) \\
&= \frac{1}{\sqrt{\eta_0}}\left[-\sum_{l=1}^{\infty} A_l \left(\frac{l\pi}{d_1}\right) \sin\left(\frac{l\pi y}{d_1}\right) \sinh\left(\frac{l\pi x}{d_1}\right)\right]
\end{aligned}
$$

Region II:

$$
\begin{aligned}
E_x^{II} =& -\sqrt{\eta_0}\left[\sum_{m=1}^{\infty}\left(\frac{m\pi}{d_2}\right)\sin\left(\frac{m\pi}{d_2}(y-h)\right)\left[B_m \cosh\left(\frac{m\pi}{d_2}(x-w_1)\right)\right.\right. \\
&\left.\left. + F_m \sinh\left(\frac{m\pi}{d_2}(x-w_1)\right)\right]\right] \\
E_y^{II} =& -\sqrt{\eta_0}\left[\frac{1}{d_2} + \sum_{m=1}^{\infty}\left(\frac{m\pi}{d_2}\right)\cos\left(\frac{m\pi}{d_2}(y-h)\right)\left[B_m \sinh\left(\frac{m\pi}{d_2}(x-w_1)\right)\right.\right. \\
&\left.\left. + F_m \cosh\left(\frac{m\pi}{d_2}(x-w_1)\right)\right]\right] \\
H_x^{II} =& \frac{1}{\sqrt{\eta_0}}\left[\frac{1}{d_2} + \sum_{m=1}^{\infty}\left(\frac{m\pi}{d_2}\right)\cos\left(\frac{m\pi}{d_2}(y-h)\right)\left[B_m \sinh\left(\frac{m\pi}{d_2}(x-w_1)\right)\right.\right. \\
&\left.\left. + F_m \cosh\left(\frac{m\pi}{d_2}(x-w_1)\right)\right]\right] \\
H_y^{II} =& -\frac{1}{\sqrt{\eta_0}}\left[\sum_{m=1}^{\infty}\left(\frac{m\pi}{d_2}\right)\sin\left(\frac{m\pi}{d_2}(y-h)\right)\left[B_m \cosh\left(\frac{m\pi}{d_2}(x-w_1)\right)\right.\right. \\
&\left.\left. + F_m \sinh\left(\frac{m\pi}{d_2}(x-w_1)\right)\right]\right]
\end{aligned}
$$

Region III:

$$E_x^{III} = -\sqrt{\eta_0}\left[\sum_{n=1}^{\infty} D_n \left(\frac{n\pi}{d_3}\right) \sin\left(\frac{n\pi}{d_3}(y-h)\right) \sinh\left(\frac{n\pi}{d_3}\left(x-\frac{T_x}{2}\right)\right)\right]$$

$$E_y^{III} = -\sqrt{\eta_0}\left[\frac{1}{d_3} + \sum_{n=1}^{\infty} D_n \left(\frac{n\pi}{d_3}\right) \cos\left(\frac{n\pi}{d_3}(y-h)\right) \cosh\left(\frac{n\pi}{d_3}\left(x-\frac{T_x}{2}\right)\right)\right]$$

$$H_x^{III} = \frac{1}{\sqrt{\eta_0}}\left[\frac{1}{d_3} + \sum_{n=1}^{\infty} D_n \left(\frac{n\pi}{d_3}\right) \cos\left(\frac{n\pi}{d_3}(y-h)\right) \cosh\left(\frac{n\pi}{d_3}\left(x-\frac{T_x}{2}\right)\right)\right]$$

$$H_y^{III} = -\frac{1}{\sqrt{\eta_0}}\left[\sum_{n=1}^{\infty} D_n \left(\frac{n\pi}{d_3}\right) \sin\left(\frac{n\pi}{d_3}(y-h)\right) \sinh\left(\frac{n\pi}{d_3}\left(x-\frac{T_x}{2}\right)\right)\right]$$

To solve for the unknown coefficients [A], [B], [D] and [F], the fields E_y and H_y are matched at $x = w_1$ and $x = w_1 + w_2$, boundaries between Region I, II and Region II, III.

4.1.2 Solution to TEM coefficients

Field matching at Junction I, II

Since the tangential electric field, E_y, must be continuous across the junction between Region I and II,

$$E_y^I(x = w_1, y) = E_y^{II}(x = w_1, y) \qquad \text{where } 0 \le y \le d_1$$

Limiting the number of basis functions in Region 1 and 2 to L and M terms respectivity,

$$E_y^I(x = w_1, y) = -\sqrt{\eta_0}\left[\frac{1}{d_1} + \sum_{l=1}^{L} A_l \left(\frac{l\pi}{d_1}\right) \cos\left(\frac{l\pi y}{d_1}\right) \cosh\left(\frac{l\pi x}{d_1}\right)\right]$$

$$E_y^{II}(x = w_1, y) = -\sqrt{\eta_0}\left[\frac{1}{d_2} + \sum_{m=1}^{M} F_m \left(\frac{m\pi}{d_2}\right) \cos\left(\frac{m\pi}{d_2}(y-h)\right)\right]$$

Therefore,

$$-\sqrt{\eta_0}\left[\frac{1}{d_1}+\sum_{l=1}^{L}A_l\left(\frac{l\pi}{d_1}\right)\cos\left(\frac{l\pi y}{d_1}\right)\cosh\left(\frac{l\pi x}{d_1}\right)\right]$$
$$=\begin{cases}-\sqrt{\eta_0}\left[\frac{1}{d_2}+\sum_{m=1}^{M}F_m\left(\frac{m\pi}{d_2}\right)\cos\left(\frac{m\pi}{d_2}(y-h)\right)\right] & \text{for } h\le y\le d_1\\ 0 & \text{for } 0\le y\le h\end{cases}$$

Multiplying by $\cos\left(\frac{k\pi y}{d_1}\right)$ and integrating from $y=0$ to d_1,

$$\frac{1}{d_1}\int_0^{d_1}\cos\left(\frac{k\pi y}{d_1}\right)\,\mathrm{d}y+\sum_{l=1}^{L}A_l\left(\frac{l\pi}{d_1}\right)\cosh\left(\frac{l\pi w_1}{d_1}\right)\times$$
$$\int_0^{d_1}\cos\left(\frac{l\pi y}{d_1}\right)\cos\left(\frac{k\pi y}{d_1}\right)\,\mathrm{d}y=\frac{1}{d_2}\int_0^{d_1}\cos\left(\frac{k\pi y}{d_1}\right)\,\mathrm{d}y+\sum_{m=1}^{M}F_m\left(\frac{m\pi}{d_2}\right)\times$$
$$\int_h^{h+d_2}\cos\left(\frac{m\pi}{d_2}(y-h)\right)\cos\left(\frac{k\pi y}{d_1}\right)\,\mathrm{d}y$$

It can be easily shown that,

$$\int_0^{d_1}\cos\left(\frac{k\pi y}{d_1}\right)\,\mathrm{d}y=0$$

and

$$\int_0^{d_1}\cos\left(\frac{l\pi y}{d_1}\right)\cos\left(\frac{k\pi y}{d_1}\right)\,\mathrm{d}y=\begin{cases}0 & \text{if } l\neq k\\ \frac{d_1}{2} & \text{if } l=k\end{cases}$$

Simplifying:

$$A_l\left(\frac{l\pi}{2}\right)\cosh\left(\frac{l\pi w_1}{d_1}\right)=\frac{1}{d_2}\int_h^{h+d_2}\cos\left(\frac{l\pi y}{d_1}\right)\,\mathrm{d}y+\sum_{m=1}^{M}F_m\left(\frac{m\pi}{d_2}\right)\times$$
$$\int_h^{h+d_2}\cos\left(\frac{m\pi}{d_2}(y-h)\right)\cos\left(\frac{l\pi y}{d_1}\right)\,\mathrm{d}y \qquad (4.2)$$

Equation (4.2) can be expressed into a linear system:

$$[C^I][A] = [G^{II}] + [Q^{II}][F]$$

where $[A]$ – $L \times 1$ column matrix for the unknown cofficients A_l

$[B]$ – $M \times 1$ column matrix for the unknown cofficients B_m

$[C^I]$ – $L \times L$ diagonal matrix with $C^I_{l,l} = \dfrac{l\pi}{2} \cosh\left(\dfrac{l\pi w_1}{d_1}\right)$

$[G^{II}]$ – $L \times 1$ column matrix with $G^{II}_l = \dfrac{1}{d_2}\displaystyle\int_h^{h+d_2} \cos\left(\frac{l\pi y}{d_1}\right) \mathrm{d}y$

$[Q^{II}]$ – $L \times M$ matrix with $Q^{II}_{l,m} = \dfrac{m\pi}{d_2}\displaystyle\int_h^{h+d_2} \cos\left(\frac{m\pi}{d_2}(y-h)\right) \times \cos\left(\frac{l\pi y}{d_1}\right) \mathrm{d}y$

Similarly, the tangential magnetic field is continuous across the junction between Region I and II,

$$H^I_y(x = w_1, y) = H^{II}_y(x = w_1, y) \qquad \text{where } h \le y \le h + d_2 \tag{4.3}$$

Limiting the number of basis functions in Region 1 and 2 to L and M terms respectivity,

$$H^I_y(x = w_1, y) = \frac{1}{-\sqrt{\eta_0}} \left[\sum_{l=1}^{L} A_l \left(\frac{l\pi}{d_1}\right) \sin\left(\frac{l\pi y}{d_1}\right) \sinh\left(\frac{l\pi x}{d_1}\right)\right]$$

$$H^{II}_y(x = w_1, y) = -\frac{1}{\sqrt{\eta_0}} \sum_{m=1}^{\infty} B_m \left(\frac{m\pi}{d_2}\right) \sin\left(\frac{m\pi}{d_2}(y-h)\right)$$

Multiplying Equation (4.3) by $\sin\left(\frac{k\pi}{d_2}(y-h)\right)$ and integrating from $y=h$ to $h+d_2$,

$$\sum_{l=1}^{L} A_l \left(\frac{l\pi}{d_1}\right) \sinh\left(\frac{l\pi x}{d_1}\right) \int_h^{h+d_2} \sin\left(\frac{l\pi y}{d_1}\right) \sin\left(\frac{k\pi}{d_2}(y-h)\right) \mathrm{d}y = \sum_{m=1}^{\infty} B_m \left(\frac{m\pi}{d_2}\right) \int_h^{h+d_2} \sin\left(\frac{m\pi}{d_2}(y-h)\right) \sin\left(\frac{k\pi}{d_2}(y-h)\right) \mathrm{d}y$$

Simplifying,

$$B_m = \sum_{l=1}^{L} A_l \left(\frac{l\pi}{d_1}\right) \cdot \sinh\left(\frac{l\pi x}{d_1}\right) \cdot \left(\frac{2}{d_1}\right) \left(\frac{2}{m\pi}\right) \times \int_h^{h+d_2} \sin\left(\frac{l\pi y}{d_1}\right) \sin\left(\frac{m\pi}{d_2}(y-h)\right) \mathrm{d}y \tag{4.4}$$

Equation (4.4) can be expressed into a linear system:

$$[B] = [R^{II}]^T + [S^I][A]$$

where $[R^{II}]$ – $L \times M$ matrix with $R^{II}_{l,m} = \frac{2}{d_1}\frac{2}{m\pi} \int_h^{h+d_2} \sin\left(\frac{l\pi y}{d_1}\right) \times \sin\left(\frac{m\pi}{d_2}(y-h)\right) \mathrm{d}y$

$[S^I]$ – $L \times L$ diagonal matrix with $S^I_{l,l} = \left(\frac{l\pi}{2}\right) \sinh\left(\frac{l\pi w_1}{d_1}\right)$

Field matching at Junction II, III

The same procedure discussed above is applied to the junction between region II and III. Matching of the electric field will yield,

$$D_n \left(\frac{n\pi}{2}\right) \cosh\left(\frac{n\pi w_3}{d_3}\right) = \frac{1}{d_2} \int_0^{d_2} \cos\left(\frac{n\pi y}{d_3}\right) \mathrm{d}y + \sum_{m=1}^{M} \left(\frac{m\pi}{d_2}\right) \times \left[B_m \sinh\left(\frac{m\pi w_2}{d_2}\right) + F_m \cosh\left(\frac{m\pi w_2}{d_2}\right)\right] \cdot \int_0^{d_2} cos\left(\frac{m\pi y}{d_2}\right) \cos\left(\frac{n\pi y}{d_3}\right) \mathrm{d}y$$

Expressing the equation into linear algebra form:

$$[C^{III}][D] = [G^{III}] + [Q^{III}]^T \left\{ [S^{II}][B] + [C^{II}][F] \right\}$$

where $[D]$ – $N \times 1$ column matrix for the unknown cofficients D_n

$[F]$ – $M \times 1$ column matrix for the unknown cofficients F_m

$[G^{III}]$ – $N \times 1$ matrix with $G_n^{III} = \dfrac{1}{d_2} \displaystyle\int_0^{d_2} \cos\left(\frac{n\pi y}{d_3}\right) \mathrm{d}y$

$[Q^{III}]$ – $M \times N$ matrix with $Q_{m,n}^{III} = \dfrac{2}{d_2} \displaystyle\int_0^{d_2} \cos\left(\frac{m\pi y}{d_2}\right) \cos\left(\frac{n\pi y}{d_3}\right) \mathrm{d}y$

$[S^{II}]$ – $M \times M$ diagonal matrix with $S_{m,m}^{II} = \left(\dfrac{m\pi}{2}\right) \sinh\left(\dfrac{m\pi w_2}{d_2}\right)$

$[C^{II}]$ – $M \times M$ diagonal matrix with $C_{m,m}^{II} = \left(\dfrac{m\pi}{2}\right) \cosh\left(\dfrac{m\pi w_2}{d_2}\right)$

$[C^{III}]$ – $N \times N$ diagonal matrix with $C_{n,n}^{III} = \left(\dfrac{n\pi}{2}\right) \cosh\left(\dfrac{n\pi w_3}{d_3}\right)$

Similary, matching the magnetic field at Juntion II, III gives,

$$\left(\frac{m\pi}{d_2}\right) \left[B_m \sinh\left(\frac{m\pi w_2}{d_2}\right) + F_m \cosh\left(\frac{m\pi w_2}{d_2}\right) \right] = - \sum_{n=1}^{N} D_n \left(\frac{n\pi}{d_3}\right) \sinh\left(\frac{n\pi w_3}{d_3}\right) \int_0^{d_2} \sin\left(\frac{n\pi y}{d_3}\right) \sin\left(\frac{m\pi y}{d_2}\right) \mathrm{d}y$$

Expressing the equation into linear algebra form:

$$[C^{II}][B] + [S^{II}][F] = -[R^{III}][S^{III}][D]$$

where $[R^{III}]$ – $M \times N$ matrix with $R^{III}_{m,n} = \frac{2}{d_3}\int_0^{d_2} \sin\left(\frac{m\pi y}{d_2}\right) \times \sin\left(\frac{n\pi y}{d_3}\right) \mathrm{d}y$

$[S^{III}]$ – $N \times N$ diagonal matrix with $S^{III}_{n,n} = \left(\frac{n\pi}{2}\right) \sinh\left(\frac{n\pi w_3}{d_3}\right)$

The unknown TEM coefficients, $[A], [B], [D]$ and $[F]$, can then be solved from the system of linear equations obtained through field matching at the two junctions in the MLG. The four linear equations obtained in the previous section are,

$$[C^I][A] = [G^{II}] + [Q^{II}][F] \tag{4.5}$$

$$[B] = [R^{II}]^T[S^I][A] \tag{4.6}$$

$$[C^{III}][D] = [G^{III}] + [Q^{III}]^T\left\{[S^{II}][B] + [C^{II}][F]\right\} \tag{4.7}$$

$$[C^{II}][B] + [S^{II}][F] = -[R^{III}][S^{III}][D] \tag{4.8}$$

Re-arranging Equation (4.7),

$$[D] = [C^{III}]^{-1}\left\{[G^{III}] + [Q^{III}]^T[S^{II}][B] + [Q^{III}]^T[C^{II}][F]\right\} \tag{4.9}$$

Substituting Equation (4.9) into (4.8)

$$[C^{II}][B] + [S^{II}][F] = -[R^{III}][S^{III}][C^{III}]^{-1}\left\{[G^{III}] + [Q^{III}]^T[S^{II}][B] + [Q^{III}]^T[C^{II}][F]\right\} \tag{4.10}$$

$$[F] = -[\gamma]^{-1}[R^{III}][S^{III}][C^{III}]^{-1}[G^{III}] - [\gamma]^{-1}[\delta][B] \tag{4.11}$$

where

$$[\gamma] = [S^{II}] + [R^{III}][S^{III}][C^{III}]^{-1}[Q^{III}]^T[C^{II}]$$
$$[\delta] = [C^{II}] + [R^{III}][S^{III}][C^{III}]^{-1}[Q^{III}]^T[S^{II}]$$

Substituting Equation (4.6) into (4.11),

$$[F] = -[\gamma]^{-1}\left\{[R^{III}][S^{III}][C^{III}]^{-1}[G^{III}] + [\delta][R^{II}]^T[S^I][A]\right\} \tag{4.12}$$

Subsituting Equation (4.12) into (4.5), the solution for all the TEM coefficients can be solved using the following equations,

$$\left\{[C^I] + [Q^{II}][\gamma]^{-1}[\delta][R^{II}]^T[S^I]\right\}[A] = [G^{II}] - [Q^{II}][\gamma]^{-1}[R^{III}][S^{III}][C^{III}]^{-1}[G^{III}] \tag{4.13}$$

$$[B] = [R^{II}]^T[S^I][A] \tag{4.14}$$

$$[F] = -[\gamma]^{-1}\left\{[R^{III}][S^{III}][C^{III}]^{-1}[G^{III}] + [\delta][R^{II}]^T[S^I][A]\right\} \tag{4.15}$$

$$[D] = [C^{III}]^{-1}\left\{[G^{III}] + [Q^{III}]^T\left\{[S^{II}][B] + [C^{II}][F]\right\}\right\} \tag{4.16}$$

4.1.3 Normalization TEM coefficients

To ensure the power propagating through the MLG is unity, the A, B, F and D coefficients need to be normalized by the total power flowing through the guide. The power flowing through a waveguide is given by the integral of the Poynting vector:

$$\text{Power, } \bar{P} = \oint_s \bar{E} \times \bar{H}^* \, \mathrm{d}\hat{s}$$

By integrating the electric and magnetic fields across each region, the normalization power for Region I, II and III are given by Equation (4.17), (4.18) and

(4.19), respectively.

$$N_e^I = \frac{2w_1}{d_1} + \sum_{l=1}^{L} A_l^2 \left(\frac{l\pi}{2}\right) \sinh\left(\frac{2l\pi w_1}{d_1}\right) \tag{4.17}$$

$$N_e^{II} = \frac{2w_2}{d_2} + \sum_{m=1}^{M} (m\pi) \sinh\left(\frac{m\pi w_2}{d_2}\right) \left[(B_m^2 + F_m^2) \cosh\left(\frac{m\pi w_2}{d_2}\right) + 2B_m F_m \sinh\left(\frac{m\pi w_2}{d_2}\right)\right] \tag{4.18}$$

$$N_e^{III} = \frac{2w_3}{d_3} + \sum_{n=1}^{N} D_n^2 \left(\frac{n\pi}{2}\right) \sinh\left(\frac{2n\pi w_3}{d_3}\right) \tag{4.19}$$

4.2 TE Meanderline Waveguide Modes

The TE meanderline waveguide modes are defined for the case where the electric field has no component in the z-axis propagation direction.

4.2.1 Derivation of TE Modes

The TE_z modes can be derived from a magnetic Hertzian potential $\bar{\Pi} = \hat{u}_z \Pi_h$ by means of Collin [48]:

$$\bar{E} = -j\omega\mu_0 \nabla \times \bar{\Pi}_h$$
$$\bar{H} = k_0^2 \bar{\Pi}_h + \nabla\nabla \cdot \bar{\Pi}_h = \nabla \times \nabla \times \bar{\Pi}_h$$

Assuming solution for $\bar{\Pi}_h$ is of the form:

$$\bar{\Pi}_h = \hat{u}_z \psi_h(x, y) e^{\pm \Gamma z}$$

The scalar potential ψ_h satisfies the 2D Helmholtz equation:

$$\nabla_t^2 \psi_h + k_c^2 \psi_h = 0 \qquad \text{where } k_c^2 = k_0^2 + \Gamma^2$$

The electric and magnetic field vectors can be expressed as,

$$\begin{aligned}\bar{H} &= \nabla \times \nabla \times \bar{\Pi}_h \\ &= \hat{u}_x \left(\pm\Gamma \frac{\partial \psi_h}{\partial x} e^{\pm\Gamma z} \right) + \hat{u}_y \left(\pm\Gamma \frac{\partial \psi_h}{\partial y} e^{\pm\Gamma z} \right) - \hat{u}_z \left(\frac{\partial^2 \psi_h}{\partial x^2} + \frac{\partial^2 \psi_h}{\partial y^2} \right) e^{\pm\Gamma z}\end{aligned}$$

$$\begin{aligned}\bar{E} &= -j\omega\mu_0 \nabla \times \bar{\Pi}_h \\ &= \hat{u}_x \left(-j\omega\mu_0 \frac{\partial \psi_h}{\partial y} e^{\pm\Gamma z} \right) + \hat{u}_y \left(j\omega\mu_0 \frac{\partial \psi_h}{\partial x} e^{\pm\Gamma z} \right)\end{aligned}$$

The scalar TE_z wave impedance is then given by:

$$Z_{TE} = \left|\frac{E_x}{H_y}\right| = -\left|\frac{E_y}{H_x}\right| = \frac{j\omega\mu_0}{\Gamma}$$

Solution for the magnetic Hertzian potential can be found by enforcing the appropriate boundary conditions in each of the MLG region. The fields in each of region can then be expressed in terms of the respective Hertzian potential.

TE mode for Region I

The scalar potential in Region I can be found by enforcing the following boundary conditions:

$$E_x^I(x, y = 0) = 0$$

$$E_x^I(x, y = d_1) = 0$$

Solution for the scalar potential is then given by:

$$\psi_h^I(x, y) = B\cos\left(\frac{l\pi y}{d_1}\right)e^{-\Gamma z}$$

By transverse resonanace, the scalar potential in Region I can be re-formulated in the transverse x-direction,

$$\Psi^I = \sum_{l=0}^{L-1}\left[-a_l^I e^{-jk_{xl}^I x} + b_l^I e^{jk_{xl}^I x}\right]\cos\left(\frac{l\pi y}{d_1}\right)e^{-jk_z z}$$

The TE_z field components in Region I are:

$$E_x = -\frac{\partial \psi^I}{\partial y} = \sum_{l=0}^{L-1} \left[-a_l^I e^{-jk_{xl}^I x} + b_l^I e^{jk_{xl}^I x} \right] \frac{l\pi}{d_1} \sin\left(\frac{l\pi y}{d_1}\right) e^{-jk_z z}$$

$$E_y = \frac{\partial \psi^I}{\partial x} = \sum_{l=0}^{L-1} \left[a_l^I e^{-jk_{xl}^I x} + b_l^I e^{jk_{xl}^I x} \right] jk_{xl}^I \cos\left(\frac{l\pi y}{d_1}\right) e^{-jk_z z}$$

$$H_x = \frac{1}{Z_{TE}}(-E_y) = -\frac{k_z}{\omega\mu} \sum_{l=0}^{L-1} \left[a_l^I e^{-jk_{xl}^I x} + b_l^I e^{jk_{xl}^I x} \right] jk_{xl}^I \cos\left(\frac{l\pi y}{d_1}\right) e^{-jk_z z}$$

$$H_y = \frac{1}{Z_{TE}}(E_x) = \frac{k_z}{\omega\mu} \sum_{l=0}^{L-1} \left[-a_l^I e^{-jk_{xl}^I x} + b_l^I e^{jk_{xl}^I x} \right] \frac{l\pi}{d_1} \sin\left(\frac{l\pi y}{d_1}\right) e^{-jk_z z}$$

$$H_z = \frac{k_c^2}{j\omega\mu} \sum_{l=0}^{L-1} \left[-a_l^I e^{-jk_{xl}^I x} + b_l^I e^{jk_{xl}^I x} \right] \cos\left(\frac{l\pi y}{d_1}\right) e^{-jk_z z}$$

where $k_c^2 = {k_{xl}^I}^2 + \left(\frac{l\pi}{d_1}\right)^2$

TE mode for Region II

Using the same approach in the previous section, the scalar potential in Region II is derived to be,

$$\Psi^{II} = \sum_{m=0}^{M-1} \left[a_m^{II} e^{jk_{xm}^{II} x'} - b_m^{II} e^{-jk_{xm}^{II} x'} \right] \cos\left(\frac{m\pi}{d_2}(y-h)\right) e^{-jk_z z}$$

where the relative origin (x', y') is located at $(x = w_1, y = 0)$.

The TE$_z$ field components in Region II are:

$$E_x = -\frac{\partial \psi^{II}}{\partial y} = \sum_{m=0}^{M-1} \left[a_m^{II} e^{jk_{xm}^{II} x} - b_m^{II} e^{-jk_{xm}^{II} x} \right] \frac{m\pi}{d_2} \sin\left(\frac{m\pi}{d_2}(y-h) \right) e^{-jk_z z}$$

$$E_y = \frac{\partial \psi^{II}}{\partial x} = \sum_{m=0}^{M-1} \left[a_m^{II} e^{jk_{xm}^{II} x} + b_m^{II} e^{-jk_{xm}^{II} x} \right] jk_{xm}^{II} \cos\left(\frac{m\pi}{d_2}(y-h) \right) e^{-jk_z z}$$

$$H_x = \frac{1}{Z_{TE}}(-E_y) = -\frac{k_z}{\omega\mu} \sum_{m=0}^{M-1} \left[a_m^{II} e^{jk_{xm}^{II} x} + b_m^{II} e^{-jk_{xm}^{II} x} \right] jk_{xm}^{II} \cos\left(\frac{m\pi}{d_2}(y-h) \right) e^{-jk_z z}$$

$$H_y = \frac{1}{Z_{TE}}(E_x) = \frac{k_z}{\omega\mu} \sum_{m=0}^{M-1} \left[a_m^{II} e^{jk_{xm}^{II} x} - b_m^{II} e^{-jk_{xm}^{II} x} \right] \frac{m\pi}{d_2} \sin\left(\frac{m\pi}{d_2}(y-h) \right) e^{-jk_z z}$$

$$H_z = \frac{k_c^2}{j\omega\mu} \sum_{m=0}^{M-1} \left[a_m^{II} e^{jk_{xm}^{II} x'} - b_m^{II} e^{-jk_{xm}^{II} x'} \right] \cos\left(\frac{m\pi}{d_2}(y-h) \right) e^{-jk_z z}$$

where $k_c^2 = {k_{xm}^{II}}^2 + \left(\frac{m\pi}{d_2} \right)^2$

TE mode for Region III

Similar to Region I and II, the scalar potential in Region III is derived to be,

$$\Psi^{III} = \sum_{n=0}^{N-1} \left[a_n^{III} e^{jk_{xn}^{III} x'} - b_n^{III} e^{-jk_{xn}^{III} x'} \right] \cos\left(\frac{n\pi y'}{d_3} \right) e^{-jk_z z}$$

where the relative origin (x', y') is located at $(x = w_1 + w_2, y = h)$.

The TE_z field components in Region III are:

$$E_x = -\frac{\partial \psi^{III}}{\partial y'} = \sum_{n=0}^{N-1} \left[a_n^{III} e^{jk_{xn}^{III} x'} - b_n^{III} e^{-jk_{xn}^{III} x'} \right] \frac{n\pi}{d_3} \sin\left(\frac{n\pi y'}{d_3}\right) e^{-jk_z z}$$

$$E_y = \frac{\partial \psi^{III}}{\partial x'} = \sum_{n=0}^{N-1} \left[a_n^{III} e^{jk_{xn}^{III} x'} + b_n^{III} e^{-jk_{xn}^{III} x'} \right] jk_{xn}^{III} \cos\left(\frac{n\pi y'}{d_3}\right) e^{-jk_z z}$$

$$H_x = \frac{1}{Z_{TE}}(-E_y) = -\frac{k_z}{\omega\mu} \sum_{n=0}^{N-1} \left[a_n^{III} e^{jk_{xn}^{III} x'} + b_n^{III} e^{-jk_{xn}^{III} x'} \right] jk_{xn}^{III} \cos\left(\frac{n\pi y'}{d_3}\right) e^{-jk_z z}$$

$$H_y = \frac{1}{Z_{TE}}(E_x) = \frac{k_z}{\omega\mu} \sum_{n=0}^{N-1} \left[a_n^{III} e^{jk_{xn}^{III} x'} - b_n^{III} e^{-jk_{xn}^{III} x'} \right] \frac{n\pi}{d_3} \sin\left(\frac{n\pi y'}{d_3}\right) e^{-jk_z z}$$

$$H_z = \frac{k_c^2}{j\omega\mu} \sum_{n=0}^{N-1} \left[a_n^{III} e^{jk_{xn}^{III} x'} - b_n^{III} e^{-jk_{xn}^{III} x'} \right] \cos\left(\frac{n\pi y'}{d_3}\right) e^{-jk_z z}$$

where $k_c^2 = k_{xn}^{III\,2} + \left(\frac{n\pi}{d_3}\right)^2$

4.2.2 Solution for TE Coefficients

To solve for the unknown TE coefficients, field matching is first carried out at the two step junctions to derive the individual scattering matrix of each junction. Next, the scattering matrix of the individual junctions and connecting waveguide sections are cascaded to obtain the overall scattering matrix of the MLG. Finally, the boundary conditions at both ends of the MLG – LW and CW, are imposed to obtain the characteristic equation for which the unknown coefficients can be solved.

Field matching – Junction I, II

The tangential electric field E_y in Region I and II is,

$$E_y^I = \sum_{l=0}^{L-1} \left[a_l^I + b_l^I\right] jk_{xl}^I \cos\left(\frac{l\pi y'}{d_1}\right) e^{-jk_z z} \qquad \text{for } 0 \le y' \le d_1$$

$$E_y^{II} = \begin{cases} \displaystyle\sum_{m=0}^{M-1} \left[a_m^{II} + b_m^{II}\right] jk_{xm}^{II} \cos\left(\frac{m\pi}{d_2}(y'-h)\right) e^{-jk_z z} & \text{for } h \le y' \le h+d_2 \\ 0 & \text{for } 0 \le y' \le h \end{cases}$$

Equating the fields in Region I and II,

$$\sum_{l=0}^{L-1} \left[a_l^I + b_l^I\right] k_{xl}^I \cos\left(\frac{l\pi y'}{d_1}\right) = \begin{cases} \displaystyle\sum_{m=0}^{M-1} \left[a_m^{II} + b_m^{II}\right] k_{xm}^{II} \cos\left(\frac{m\pi}{d_2}(y'-h)\right) & \\ & \text{for } h \le y' \le h+d_2 \\ 0 & \text{for } 0 \le y' \le h \end{cases}$$

Multiplying by $\cos\left(\frac{k\pi y'}{d_1}\right)$ and integrating from $y' = 0$ to d_1,

$$\sum_{l=0}^{L-1} \left[a_l^I + b_l^I\right] k_{xl}^I \int_0^{d_1} \cos\left(\frac{k\pi y'}{d_1}\right) \cos\left(\frac{l\pi y'}{d_1}\right) \mathrm{d}y' = \sum_{m=0}^{M-1} \left[a_m^{II} + b_m^{II}\right] k_{xm}^{II} \int_h^{h+d_2} \cos\left(\frac{k\pi y'}{d_1}\right) \cos\left(\frac{m\pi}{d_2}(y'-h)\right) \mathrm{d}y'$$

Using othorgonality of cosine function, the equation can be simplified to,

$$\left[a_l^I + b_l^I\right] \cdot k_{xl}^I d_1 = \sum_{m=0}^{M-1} \left[a_m^{II} + b_m^{II}\right] \cdot k_{xm}^{II} d_2 \cdot \frac{2}{\epsilon d_2} \int_h^{h+d_2} \cos\left(\frac{l\pi y'}{d_1}\right) \times \cos\left(\frac{m\pi}{d_2}(y'-h)\right) \mathrm{d}y'$$

$$\text{where } \epsilon = \begin{cases} 1 \text{ for } l \ne 0 \\ 2 \text{ for } l = 0 \end{cases}$$

In matrix form,

$$[K_x^I]\left\{[a^I]+[b^I]\right\} = [Q][K_x^{II}]\left\{[a^{II}]+[b^{II}]\right\}$$

where $[a^I]$ – $L \times 1$ column matrix for unknown coefficients a_l^I

$[b^I]$ – $L \times 1$ column matrix for unknown coefficients b_l^I

$[a^{II}]$ – $M \times 1$ column matrix for unknown coefficients a_m^{II}

$[b^{II}]$ – $M \times 1$ column matrix for unknown coefficients b_m^{II}

$[K_x^I]$ – $L \times L$ diagonal matrix with $K_{xl,l}^I = \sqrt{k_c^2 - \left(\frac{l\pi}{d_1}\right)^2} \cdot d_1$

$[K_x^{II}]$ – $M \times M$ diagonal matrix with $K_{xm,m}^{II} = \sqrt{k_c^2 - \left(\frac{m\pi}{d_2}\right)^2} \cdot d_2$

$[Q]$ – $L \times M$ matrix with $Q_{l,m} = \frac{2}{\epsilon d_2}\int_h^{h+d_2} \cos\left(\frac{l\pi y'}{d_1}\right) \times \cos\left(\frac{m\pi}{d_2}(y'-h)\right)\,\mathrm{d}y'$

Similary, the tangential magnetic field H_z in Region I and II are,

$$H_z^I = \frac{k_c^2}{j\omega\mu}\sum_{l=0}^{L-1}\left[-a_l^I + b_l^I\right]\cos\left(\frac{l\pi y'}{d_1}\right)e^{-jk_z z}$$

$$H_z^{II} = \frac{k_c^2}{j\omega\mu}\sum_{m=0}^{M-1}\left[a_m^{II} - b_m^{II}\right]\cos\left(\frac{m\pi}{d_2}(y'-h)\right)e^{-jk_z z}$$

Equating the fields in Region I and II,

$$\sum_{l=0}^{L-1}\left[-a_l^I + b_l^I\right]\cos\left(\frac{l\pi y'}{d_1}\right) = \sum_{m=0}^{M-1}\left[a_m^{II} - b_m^{II}\right]\cos\left(\frac{m\pi}{d_2}(y'-h)\right)$$

Multiplying by $\cos\left(\frac{k\pi}{d_2}(y'-h)\right)$ and integrating from $y'=h$ to $h+d_2$,

$$\sum_{l=0}^{L-1}\left[-a_l^I+b_l^I\right]\int_h^{h+d_2}\cos\left(\frac{k\pi}{d_2}(y'-h)\right)\cos\left(\frac{l\pi y'}{d_1}\right)\,\mathrm{d}y' = \sum_{m=0}^{M-1}\left[a_m^{II}-b_m^{II}\right]\int_h^{h+d_2}\cos\left(\frac{k\pi}{d_2}(y'-h)\right)\cos\left(\frac{m\pi}{d_2}(y'-h)\right)\,\mathrm{d}y'$$

Using othorgonality of cosine function, the equation can be simplified to,

$$\left[a_m^{II}-b_m^{II}\right]=\sum_{l=0}^{L-1}\left[-a_l^I+b_l^I\right]\frac{2}{\epsilon d_2}\int_h^{h+d_2}\cos\left(\frac{m\pi}{d_2}(y'-h)\right)\cos\left(\frac{l\pi y'}{d_1}\right)\,\mathrm{d}y'$$

$$\text{where } \epsilon=\begin{cases}1 \text{ for } l\neq 0\\ 2 \text{ for } l=0\end{cases}$$

In matrix notation,

$$[a^{II}]-[b^{II}]=[Q]^T\left\{[b^I]-[a^I]\right\}$$

Field matching – Junction II, III

The tangential electric field E_y in Region II and III are,

$$E_y^{II}=\begin{cases}\displaystyle\sum_{m=0}^{M-1}\left[a_m^{II}+b_m^{II}\right]jk_{xm}^{II}\cos\left(\frac{m\pi y'}{d_2}\right)e^{-jk_z z} & \text{for } 0\le y'\le d_2\\ 0 & \text{for } d_2\le y'\le d_3\end{cases}$$

$$E_y^{III}=\sum_{n=0}^{N-1}\left[a_n^{III}+b_n^{III}\right]jk_{xn}^{III}\cos\left(\frac{n\pi y'}{d_3}\right)e^{-jk_z z} \qquad \text{for } 0\le y'\le d_3$$

Equating the fields in Region II and III,

$$\sum_{n=0}^{N-1}\left[a_n^{III}+b_n^{III}\right]k_{xn}^{III}\cos\left(\frac{n\pi y'}{d_3}\right)=\begin{cases}\displaystyle\sum_{m=0}^{M-1}\left[a_m^{II}+b_m^{II}\right]k_{xm}^{II}\cos\left(\frac{m\pi y'}{d_2}\right) & \\ & \text{for } 0\le y'\le d_2\\ 0 & \text{for } 0\le y'\le d_3\end{cases}$$

Multiplying by $\cos\left(\frac{k\pi y'}{d_3}\right)$ and integrating from $y'=0$ to d_3,

$$\sum_{m=0}^{M-1}\left[a_m^{II}+b_m^{II}\right]k_{xm}^{II}\int_0^{d_2}\cos\left(\frac{k\pi y'}{d_3}\right)\cos\left(\frac{m\pi y'}{d_2}\right)\,\mathrm{d}y'=$$
$$\sum_{n=0}^{N-1}\left[a_n^{III}+b_n^{III}\right]k_{xn}^{III}\int_0^{d_2}\cos\left(\frac{k\pi y'}{d_3}\right)\cos\left(\frac{n\pi y'}{d_3}\right)\,\mathrm{d}y'$$

Using othorgonality of cosine function, the equation can be simplified to,

$$\left[a_n^{III}+b_n^{III}\right]\cdot k_{xn}^{III}d_3=\sum_{m=0}^{M-1}\left[a_m^{II}+b_m^{II}\right]\cdot k_{xm}^{II}d_2\cdot\frac{2}{\epsilon d_2}\int_0^{d_2}\cos\left(\frac{n\pi y'}{d_3}\right)\times\cos\left(\frac{m\pi y'}{d_2}\right)\,\mathrm{d}y'$$

$$\text{where }\epsilon=\begin{cases}1 \text{ for } n\neq 0\\ 2 \text{ for } n=0\end{cases}$$

In matrix notation,

$$[K_x^{III}]\left\{[a^{III}]+[b^{III}]\right\}=[R][K_x^{III}]\left\{[a^{II}]+[b^{II}]\right\}$$

where $[a^{III}]$ – $N \times 1$ column matrix for unknown coefficients a_n^{III}

$[b^{III}]$ – $N \times 1$ column matrix for unknown coefficients b_n^{III}

$[K_x^{III}]$ – $N \times N$ diagonal matrix with $K_{xn,n}^{III} = \sqrt{k_c^2 - \left(\frac{n\pi}{d_3}\right)^2} \cdot d_3$

$[R]$ – $N \times M$ matrix with $R_{n,m} = \frac{2}{\epsilon d_2} \int_0^{d_2} \cos\left(\frac{m\pi y'}{d_2}\right) \times \cos\left(\frac{n\pi y'}{d_3}\right) \, \mathrm{d}y'$

Similary, the tangential magnetic field H_z in Region II and III are,

$$H_z^{II} = \frac{k_c^2}{j\omega\mu} \sum_{m=0}^{M-1} \left[-a_m^{II} + b_m^{II}\right] \cos\left(\frac{m\pi y'}{d_2}\right)$$
$$H_z^{III} = \frac{k_c^2}{j\omega\mu} \sum_{n=0}^{N-1} \left[a_n^{III} - b_n^{III}\right] \cos\left(\frac{n\pi y'}{d_3}\right)$$

Equating the fields in Region II and III,

$$\sum_{m=0}^{M-1} \left[-a_m^{II} + b_m^{II}\right] \cos\left(\frac{m\pi y'}{d_2}\right) = \sum_{n=0}^{N-1} \left[a_n^{III} - b_n^{III}\right] \cos\left(\frac{n\pi y'}{d_3}\right)$$

Multiplying by $\cos\left(\frac{k\pi y'}{d_2}\right)$ and integrating from $y' = 0$ to d_2,

$$\sum_{m=0}^{M-1} \left[-a_m^{II} + b_m^{II}\right] \int_0^{d_2} \cos\left(\frac{k\pi y'}{d_2}\right) \cos\left(\frac{m\pi y'}{d_2}\right) \, \mathrm{d}y' = \sum_{n=0}^{N-1} \left[a_n^{III} - b_n^{III}\right] \int_0^{d_2} \cos\left(\frac{k\pi y'}{d_2}\right) \cos\left(\frac{n\pi y'}{d_3}\right) \, \mathrm{d}y'$$

Using othorgonality of cosine function, the equation can be simplified to,

$$\left[-a_m^{II} + b_m^{II}\right] = \sum_{n=0}^{N-1} \left[a_n^{III} - b_n^{III}\right] \cdot \frac{2}{\epsilon d_2} \int_0^{d_2} \cos\left(\frac{n\pi y'}{d_3}\right) \cos\left(\frac{m\pi y'}{d_2}\right) \, \mathrm{d}y'$$

$$\text{where } \epsilon = \begin{cases} 1 \text{ for } n \neq 0 \\ 2 \text{ for } n = 0 \end{cases}$$

In matrix notation,

$$[b^{II}] - [a^{II}] = [R]^T \left\{[a^{III}] - [b^{III}]\right\}$$

S-Parameter for Junction I,II

From field matching of the TE_z electric and magnetic fields at the junction between Region I and II,

$$[K_x^I] \left\{[a^I] + [b^I]\right\} = [Q][K_x^{II}] \left\{[a^{II}] + [b^{II}]\right\} \tag{4.20}$$

$$[a^{II}] - [b^{II}] = [Q]^T \left\{[b^I] - [a^I]\right\} \tag{4.21}$$

Omitting the paranthesis for clarity, Equation (4.21) can be re-expressed as,

$$b^{II} = a^{II} - Q^T(b^I - a^I) \tag{4.22}$$

Substituting Equation (4.22) into (4.20),

$$K_x^I(a^I + b^I) = QK_x^{II}(a^{II} - Q^T(b^I - a^I) + a^{II})$$

$$I(a^I + b^I) = [K_x^I]{-}1QK_x^{II}(2a^{II} + Q^T a^I - Q^T b^I)$$

Letting,

$$[P] = [K_x I]^{-1}[Q][K_x II]$$

$$[I] - \quad L \times L \quad \text{unit matrix}$$

$$[U] - \quad M \times M \quad \text{unit matrix}$$

$$\Rightarrow \quad [I + PQ^T]b^I = (PQ^T - I)a^I + 2Pa^{II}$$

$$\therefore \quad b^I = (I + PQ^T)^{-1}(PQ^T - I)a^I + 2(I + PQ^T)^{-1}Pa^{II}$$

Subsitituting Equation (4.20) into (4.21),

$$a^{II} - b^{II} = Q^T(Pa^{II} + Pb^{II} - a^I - a^I)$$

$$(U + Q^T P)b^{II} = 2Q^T a^I + (U - Q^T P)a^{II}$$

$$\therefore \quad b^{II} = 2(U + Q^T P)^{-1}Q^T a^I + (U + Q^T P)^{-1}(U - Q^T P)a^{II}$$

Thus, the overall S-matrix of Step Junction B for TE mode is,

$$[S_{11}^A] = \{[I] + [P][Q]^T\}^{-1}\{[P][Q]^T - [I]\}$$

$$[S_{12}^A] = 2 \cdot \{[I] + [P][Q]^T\}^{-1}[P]$$

$$[S_{21}^A] = 2 \cdot \{[U] + [Q]^T[P]\}^{-1} \cdot [Q]^T$$

$$[S_{22}^A] = \{[U] + [Q]^T[P]\}^{-1}\{[U] - [Q]^T[P]\}$$

S-Parameter for Junction II,III

From field matching of the TE_z electric and magnetic fields at the junction between Region II and III,

$$[K_x^{III}]\left\{[a^{III}]+[b^{III}]\right\} = [R][K_x^{III}]\left\{[a^{II}]+[b^{II}]\right\} \tag{4.23}$$

$$[b^{II}]-[a^{II}] = [R]^T\left\{[a^{III}]-[b^{III}]\right\} \tag{4.24}$$

Omitting the paranthesis for clarity, Equation (4.24) can be re-expressed as,

$$b^{II} = a^{II} + R^T(a^{III} - b^{III}) \tag{4.25}$$

Substituting Equation (4.25) into (4.23),

$$K_x^{III}(a^{III}+b^{III}) = RK_x^{III}(a^{II}+a^{II}+R^Ta^{III}-R^Tb^{III})$$

$$a^{III}+b^{III} = [K_x^{III}]^{-1}RK_x^{III}(2a^{II}+R^Ta^{III}-R^Tb^{III})$$

Letting,

$$[H] = [K_xIII]^{-1}[R][K_xII]$$

$$[U] - \quad M \times M \quad \text{unit matrix}$$

$$[V] - \quad N \times N \quad \text{unit matrix}$$

$$\Rightarrow \quad [V+HR^T]b^{III} = 2Ha^{II} + (HR^T - V)a^{III}$$

$$\therefore \quad b^{III} = 2(V+HR^T)^{-1}Ha^{II} + (V+HR^T)^{-1}(HR^T-V)a^{III}$$

Subsitituting Equation (4.23) into (4.24),

$$
\begin{aligned}
b^{II} - a^{II} &= R^T(a^{III} - Ha^{II} - Hb^{II} + a^{III}) \\
(U + R^T H)b^{II} &= (U - R^T H)a^{II} + 2R^T a^{III} \\
\therefore \quad b^{II} &= (U + R^T H)^{-1}(U - R^T H)a^{II} + 2(U + R^T H)^{-1}R^T a^{III}
\end{aligned}
$$

Thus, the overall S-matrix of Step Junction B for TE mode is,

$$
\begin{aligned}
[S_{11}^B] &= \{[U] + [R]^{-1}[H]\}^{-1} \cdot \{[U] - [R]^T[H]\} \\
[S_{12}^B] &= 2 \cdot \{[U] + [R]^T[H]\}^{-1} \cdot [R]^T \\
[S_{21}^B] &= 2 \cdot \{[V] + [H][R]^T\}^{-1} \cdot [H] \\
[S_{22}^B] &= \{[V] + [H][R]^T\}^{-1} \cdot \{[H][R]^T - [V]\}
\end{aligned}
$$

4.3 TM Meanderline Waveguide Modes

4.3.1 Derivation of TM Modes

The TM_z modes can be derived from a electric Hertzian potential $\bar{\Phi} = \hat{u}_z \Phi_m$ by means of Collin [48]:

$$
\begin{aligned}
\bar{e}_m &= -\nabla_t \Phi_m \\
\bar{h}_m &= \hat{z}_0 \times \bar{e}_m
\end{aligned}
$$

The scalar TM_z wave impedance is then given by:

$$
\begin{aligned}
Z_{TM} = \left|\frac{E_x}{H_y}\right| &= -\left|\frac{E_y}{H_x}\right| \\
&= \frac{\Gamma}{j\omega\epsilon}
\end{aligned}
$$

Solution for the magnetic Hertzian potential can be found by enforcing the appropriate boundary conditions in each of the MLG region. The fields in each of region can then be expressed in terms of the respective Hertzian potential.

TM mode for Region I

The scalar potential in Region I can be found by enforcing the following boundary conditions:

$$E_z^I(x, y = 0) = 0$$

$$E_z^I(x, y = d_1) = 0$$

Solution for the scalar potential is then given by:

$$\Phi_m^I(x, y) = A \sin\left(\frac{l\pi y}{d_1}\right) e^{-\Gamma z}$$

By transverse resonanace, the scalar potential in Region I can be re-formulated in the transverse x-direction,

$$\Phi^I = \sum_{l=1}^{L} \left[a_l^I e^{-jk_{xl}^I x} + b_l^I e^{jk_{xl}^I x}\right] \sin\left(\frac{l\pi y}{d_1}\right) e^{-jk_z z}$$

The TM_z field components in Region I are:

$$E_x = -\frac{\partial \phi^I}{\partial x} = \sum_{l=1}^{L} \left[a_l^I e^{-jk_{xl}^I x} - b_l^I e^{jk_{xl}^I x} \right] jk_{xl}^I \sin\left(\frac{l\pi y}{d_1}\right) e^{-jk_z z}$$

$$E_y = -\frac{\partial \phi^I}{\partial y} = \sum_{l=1}^{L} \left[-a_l^I e^{-jk_{xl}^I x} - b_l^I e^{jk_{xl}^I x} \right] \frac{l\pi}{d_1} \cos\left(\frac{l\pi y}{d_1}\right) e^{-jk_z z}$$

$$E_z = \frac{k_c^2}{j\omega\mu} \sum_{l=1}^{L} \left[a_l^I e^{-jk_{xl}^I x} + b_l^I e^{jk_{xl}^I x} \right] \sin\left(\frac{l\pi y}{d_1}\right) e^{-jk_z z}$$

$$H_x = \frac{1}{Z_{TM}}(-E_y) = \frac{\omega\epsilon}{k_z} \sum_{l=1}^{L} \left[-a_l^I e^{-jk_{xl}^I x} - b_l^I e^{jk_{xl}^I x} \right] \frac{l\pi}{d_1} \cos\left(\frac{l\pi y}{d_1}\right) e^{-jk_z z}$$

$$H_y = \frac{1}{Z_{TE}}(E_x) = \frac{\omega\epsilon}{k_z} \sum_{l=1}^{L} \left[a_l^I e^{-jk_{xl}^I x} - b_l^I e^{jk_{xl}^I x} \right] jk_{xl}^I \sin\left(\frac{l\pi y}{d_1}\right) e^{-jk_z z}$$

where $k_c^2 = {k_{xl}^I}^2 + \left(\frac{l\pi}{d_1}\right)^2$

TM mode for Region II

Using the same approach in the previous section, the scalar potential in Region II is derived to be,

$$\Phi^{II} = \sum_{m=1}^{M} \left[a_m^{II} e^{jk_{xm}^{II} x} + b_m^{II} e^{-jk_{xm}^{II} x} \right] \sin\left(\frac{m\pi}{d_2}(y-h)\right) e^{-jk_z z}$$

The TM_z electric field components in Region II are:

$$E_x = -\frac{\partial \phi^{II}}{\partial x'} = \sum_{m=1}^{M} \left[a_m^{II} e^{jk_{xm}^{II} x'} - b_m^{II} e^{-jk_{xm}^{II} x'} \right] jk_{xm}^{II} \sin\left(\frac{m\pi}{d_2}(y'-h)\right) e^{-jk_z z}$$

$$E_y = -\frac{\partial \phi^{II}}{\partial y'} = \sum_{m=1}^{M} \left[-a_m^{II} e^{jk_{xm}^{II} x'} - b_m^{II} e^{-jk_{xm}^{II} x'} \right] \frac{m\pi}{d_2} \cos\left(\frac{m\pi}{d_2}(y'-h)\right) e^{-jk_z z}$$

$$E_z = \frac{k_c^2}{j\omega\epsilon} \sum_{m=1}^{M} \left[a_m^{II} e^{jk_{xm}^{II} x'} + b_m^{II} e^{-jk_{xm}^{II} x'} \right] \sin\left(\frac{m\pi}{d_2}(y'-h)\right) e^{-jk_z z}$$

where $k_c^2 = {k_{xm}^{II}}^2 + \left(\frac{m\pi}{d_2}\right)^2$

The TM_z magnetic field components in Region II are:

$$H_x = \frac{1}{Z_{TM}}(-E_y) = \frac{\omega\epsilon}{k_z}\sum_{m=1}^{M}\left[a_m^{II}e^{jk_{xm}^{II}x'} + b_m^{II}e^{-jk_{xm}^{II}x'}\right]\frac{m\pi}{d_2}\times \cos\left(\frac{m\pi}{d_2}(y'-h)\right)e^{-jk_z z}$$

$$H_y = \frac{1}{Z_{TE}}(E_x) = \frac{\omega\epsilon}{k_z}\sum_{m=1}^{M}\left[-a_m^{II}e^{jk_{xm}^{II}x'} + b_m^{II}e^{-jk_{xm}^{II}x'}\right]jk_{xm}^{II}\times \sin\left(\frac{m\pi}{d_2}(y'-h)\right)e^{-jk_z z}$$

TM mode for Region III

Similar to Region I and II, the scalar potential in Region III is derived to be,

$$\Phi^{III} = \sum_{n=1}^{N}\left[a_n^{III}e^{jk_{xn}^{III}x'} + b_n^{III}e^{-jk_{xn}^{III}x'}\right]\sin\left(\frac{n\pi y'}{d_3}\right)e^{-jk_z z}$$

where the relative origin (x', y') is located at $(x = w_1 + w_2, y = h)$.

The TM_z electric field components in Region III are:

$$E_x = -\frac{\partial\phi^{III}}{\partial x'} = \sum_{n=1}^{N}\left[-a_n^{III}e^{jk_{xn}^{III}x'} + b_n^{III}e^{-jk_{xn}^{III}x'}\right]jk_{xn}^{III}\sin\left(\frac{n\pi y'}{d_3}\right)e^{-jk_z z}$$

$$E_y = -\frac{\partial\phi^{III}}{\partial y'} = -\sum_{n=1}^{N}\left[a_n^{III}e^{jk_{xn}^{III}x'} + b_n^{III}e^{-jk_{xn}^{III}x'}\right]\frac{n\pi}{d_3}\cos\left(\frac{n\pi y'}{d_3}\right)e^{-jk_z z}$$

$$E_z = \frac{k_c^2}{j\omega\mu}\sum_{n=1}^{N}\left[a_n^{III}e^{jk_{xn}^{III}x'} + b_n^{III}e^{jk_{xn}^{III}x'}\right]\sin\left(\frac{n\pi y'}{d_3}\right)e^{-jk_z z}$$

where $k_c^2 = k_{xn}^{III\,2} + \left(\frac{n\pi}{d_3}\right)^2$

The TM_z magnetic field components in Region III are:

$$H_x = \frac{1}{Z_{TM}}(-E_y) = \frac{\omega\epsilon}{k_z}\sum_{n=1}^{N}\left[a_n^{III}e^{jk_{xn}^{III}x'} + b_n^{III}e^{-jk_{xn}^{III}x'}\right]\frac{n\pi}{d_3}\cos\left(\frac{n\pi y'}{d_3}\right)e^{-jk_z z}$$

$$H_y = \frac{1}{Z_{TE}}(E_x) = \frac{\omega\epsilon}{k_z}\sum_{n=1}^{N}\left[-a_n^{III}e^{jk_{xn}^{III}x'} + b_n^{III}e^{-jk_{xn}^{III}x'}\right]jk_{xn}^{III}\sin\left(\frac{n\pi y'}{d_3}\right)e^{-jk_z z}$$

4.3.2 Solution to TM Coefficients

Similar to the case for TE modes, the unknown TM coefficients can be solved by field matching at the two step junctions to derive the overall scattering matrix of the MLG. Boundary conditions at both ends of the MLG – LW and CW, are then imposed to obtain the characteristic equation for which the unknown coefficients can be solved.

TM modes – Junction I, II

The tangential electric field E_z in Region I and II at the junction between Region I and II are,

$$E_z^I = \sum_{l=1}^{L}\left[a_l^I + b_l^I\right]\sin\left(\frac{l\pi y'}{d_1}\right)e^{-jk_z z} \qquad \text{for } 0 \le y' \le d_1$$

$$E_z^{II} = \begin{cases} \displaystyle\sum_{m=1}^{M}\frac{k_{cm}^2}{j\omega\epsilon}\left[a_m^{II} + b_m^{II}\right]\sin\left(\frac{m\pi}{d_2}(y'-h)\right)e^{-jk_z z} & \text{for } h \le y' \le h + d_2 \\ 0 & \text{for } 0 \le y' \le h \end{cases}$$

Equating the fields in Region I and II,

$$\sum_{l=1}^{L}\left[a_l^I + b_l^I\right]\sin\left(\frac{l\pi y'}{d_1}\right) = \begin{cases} \displaystyle\sum_{m=1}^{M}\left[a_m^{II} + b_m^{II}\right]\sin\left(\frac{m\pi}{d_2}(y'-h)\right) & \\ & \text{for } h \le y' \le h + d_2 \\ 0 & \text{for } 0 \le y' \le h \end{cases}$$

Multiplying by $\sin\left(\frac{k\pi y'}{d_1}\right)$ and integrating from $y' = 0$ to d_1,

$$\sum_{l=1}^{L}\left[a_l^I + b_l^I\right]\int_0^{d_1}\sin\left(\frac{k\pi y'}{d_1}\right)\sin\left(\frac{l\pi y'}{d_1}\right)\,\mathrm{d}y' = \sum_{m=1}^{M}\left[a_m^{II} + b_m^{II}\right]\int_h^{h+d_2}\sin\left(\frac{k\pi y'}{d_1}\right)\sin\left(\frac{m\pi}{d_2}(y'-h)\right)\,\mathrm{d}y'$$

Using othorgonality of sine function, the equation can be simplified to,

$$\left[a_l^I + b_l^I\right] = \sum_{m=1}^{M}\left[a_m^{II} + b_m^{II}\right]\cdot\frac{2}{d_1}\int_h^{h+d_2}\sin\left(\frac{l\pi y'}{d_1}\right)\sin\left(\frac{m\pi}{d_2}(y'-h)\right)\,\mathrm{d}y'$$

In matrix form,

$$[a^I] + [b^I] = [Q]^T\left\{[a^{II}] + [b^{II}]\right\}$$

where $[a^I]$ – $L \times 1$ column matrix for unknown coefficients a_l^I

$[b^I]$ – $L \times 1$ column matrix for unknown coefficients b_l^I

$[a^{II}]$ – $M \times 1$ column matrix for unknown coefficients a_m^{II}

$[b^{II}]$ – $M \times 1$ column matrix for unknown coefficients b_m^{II}

$[Q]$ – $M \times L$ matrix with $Q_{m,l} = \frac{2}{d_1}\int_h^{h+d_2}\sin\left(\frac{l\pi y'}{d_1}\right)\times\sin\left(\frac{m\pi}{d_2}(y'-h)\right)\,\mathrm{d}y'$

The tangential magnetic field H_y in Region I and II at the junction between Region I and II are,

$$H_y^I = \frac{\omega\epsilon}{k_z}\sum_{l=1}^{L}\left[a_l^I - b_l^I\right]\cdot jk_{xl}^I\cdot\sin\left(\frac{l\pi y'}{d_1}\right)e^{-jk_z z}$$
$$H_y^{II} = \frac{\omega\epsilon}{k_z}\sum_{m=1}^{M}\left[-a_m^{II} + b_m^{II}\right]\cdot jk_{xm}^{II}\cdot\sin\left(\frac{m\pi}{d_2}(y'-h)\right)e^{-jk_z z}$$

Equating the fields in Region I and II,

$$\sum_{l=1}^{L}\left[a_l^I - b_l^I\right]\cdot k_{xl}^I\cdot\sin\left(\frac{l\pi y'}{d_1}\right) = \sum_{m=1}^{M}\left[-a_m^{II} + b_m^{II}\right]\cdot k_{xm}^{II}\cdot\sin\left(\frac{m\pi}{d_2}(y'-h)\right)$$

Multiplying by $\sin\left(\frac{k\pi}{d_2}(y'-h)\right)$ and integrating from $y'=h$ to $h+d_2$,

$$\sum_{l=1}^{L}\left[a_l^I - b_l^I\right]\cdot k_{xl}^I\cdot\int_h^{h+d_2}\sin\left(\frac{k\pi}{d_2}(y'-h)\right)\sin\left(\frac{l\pi y'}{d_1}\right)\,\mathrm{d}y' =$$
$$\sum_{m=1}^{M}\left[-a_m^{II} + b_m^{II}\right]\cdot k_{xm}^{II}\cdot\int_h^{h+d_2}\sin\left(\frac{k\pi}{d_2}(y'-h)\right)\sin\left(\frac{m\pi}{d_2}(y'-h)\right)\,\mathrm{d}y'$$

Using othorgonality of sine function, the equation can be simplified to,

$$\left[-a_m^{II} + b_m^{II}\right]\cdot k_{xm}^{II}\cdot d_2 = \sum_{l=1}^{L}\left[a_l^I - b_l^I\right]\cdot k_{xl}^I\cdot\frac{2}{d_1}\cdot\int_h^{h+d_2}\sin\left(\frac{l\pi y'}{d_1}\right)\times$$
$$\sin\left(\frac{m\pi}{d_2}(y'-h)\right)\,\mathrm{d}y'$$

In matrix notation,

$$[K_x^{II}]\left\{[b^{II}] - [a^{II}]\right\} = [Q][K_x^I]\left\{[a^I] - [b^I]\right\}$$

where $[K_x^I]$ – $L\times L$ diagonal matrix with element $K_{xl,l}^I = k_{xl}^I\cdot d_1$

$[K_x^{II}]$ – $M\times M$ diagonal matrix with element $K_{xm,m}^{II} = k_{xm}^{II}\cdot d_2$

TM modes – Junction II, III

The tangential electric fields E_z in Region II and III are,

$$E_z^{II} = \begin{cases} \sum_{m=1}^{M} \frac{k_{cm}^2}{j\omega\epsilon} \left[a_m^{II} + b_m^{II}\right] \sin\left(\frac{m\pi y'}{d_2}\right) e^{-jk_z z} & \text{for } 0 \le y' \le d_2 \\ 0 & \text{for } d_2 \le y' \le d_3 \end{cases}$$

$$E_z^{III} = \sum_{n=1}^{N} \frac{k_{cn}^2}{j\omega\epsilon} \left[a_n^{III} + b_n^{III}\right] \sin\left(\frac{n\pi y'}{d_3}\right) e^{-jk_z z} \qquad \text{for } 0 \le y' \le d_3$$

Equating the electric fields in Region II and III,

$$\sum_{n=1}^{N} \left[a_n^{III} + b_n^{III}\right] \sin\left(\frac{n\pi y'}{d_3}\right) = \begin{cases} \sum_{m=1}^{M} \left[a_m^{II} + b_m^{II}\right] \sin\left(\frac{m\pi y'}{d_2}\right) & \\ & \text{for } 0 \le y' \le d_2 \\ 0 & \text{for } 0 \le y' \le d_3 \end{cases}$$

Multiplying by $\sin\left(\frac{k\pi y'}{d_3}\right)$ and integrating from $y' = 0$ to d_3,

$$\sum_{n=1}^{N} \left[a_n^{III} + b_n^{III}\right] \int_0^{d_3} \sin\left(\frac{k\pi y'}{d_3}\right) \sin\left(\frac{n\pi y'}{d_3}\right) \mathrm{d}y' = \sum_{m=1}^{M} \left[a_m^{II} + b_m^{II}\right] \int_0^{d_2} \sin\left(\frac{k\pi y'}{d_3}\right) \sin\left(\frac{m\pi y'}{d_2}\right) \mathrm{d}y'$$

Using othorgonality of sine function, the equation can be simplified to,

$$\left[a_n^{III} + b_n^{III}\right] = \sum_{m=1}^{M} \left[a_m^{II} + b_m^{II}\right] \cdot \frac{2}{d_3} \cdot \int_0^{d_2} \sin\left(\frac{m\pi y'}{d_2}\right) \sin\left(\frac{n\pi y'}{d_3}\right) \mathrm{d}y'$$

In matrix notation,

$$[a^{III}] + [b^{III}] = [E]^T \left\{ [a^{II}] + [b^{II}] \right\}$$

where $[E]$ – $M \times N$ matrix with element $E_{m,n} = \dfrac{2}{d_3} \cdot \displaystyle\int_0^{d_2} \sin\left(\frac{m\pi y'}{d_2}\right) \times \sin\left(\frac{n\pi y'}{d_3}\right) \mathrm{d}y'$

The tangential magnetic field H_z in Region II and III are given by,

$$H_y^{II} = \frac{\omega\epsilon}{k_z} \sum_{m=1}^{M} \left[a_m^{II} - b_m^{II}\right] \cdot jk_{xm}^{II} \cdot \sin\left(\frac{m\pi y'}{d_2}\right)$$
$$H_y^{III} = \frac{\omega\epsilon}{k_z} \sum_{n=1}^{N} \left[-a_n^{III} + b_n^{III}\right] \cdot jk_{xn}^{III} \cdot \sin\left(\frac{n\pi y'}{d_3}\right)$$

Equating the fields in Region II and III,

$$\sum_{m=1}^{M} \left[a_m^{II} - b_m^{II}\right] \cdot k_{xm}^{II} \cdot \sin\left(\frac{m\pi y'}{d_2}\right) = \sum_{n=1}^{N} \left[b_n^{III} - a_n^{III}\right] \cdot k_{xn}^{III} \cdot \sin\left(\frac{n\pi y'}{d_3}\right)$$

Multiplying by $\sin\left(\frac{k\pi y'}{d_2}\right)$ and integrating from $y' = 0$ to d_2,

$$\sum_{m=1}^{M} \left[a_m^{II} - b_m^{II}\right] \cdot k_{xm}^{II} \cdot \int_0^{d_2} \sin\left(\frac{k\pi y'}{d_2}\right) \sin\left(\frac{m\pi y'}{d_2}\right) \mathrm{d}y' =$$
$$\sum_{n=1}^{N} \left[b_n^{III} - a_n^{III}\right] \cdot k_{xn}^{III} \cdot \int_0^{d_2} \sin\left(\frac{k\pi y'}{d_2}\right) \sin\left(\frac{n\pi y'}{d_3}\right) \mathrm{d}y'$$

Using othorgonality of sine function, the equation can be simplified to,

$$\left(-a_m^{II} + b_m^{II}\right) \cdot k_{xm}^{II} \cdot d_2 = \sum_{n=1}^{N} \left(b_n^{III} - a_n^{III}\right) \cdot k_{xn}^{III} \cdot d_3 \cdot \int_0^{d_2} \sin\left(\frac{m\pi y'}{d_2}\right) \times \sin\left(\frac{n\pi y'}{d_3}\right) \mathrm{d}y'$$

In matrix notation,

$$[K_x^{II}]\left\{[a^{II}] - [b^{II}]\right\} = [E][K_x^{III}]\left\{[b^{III}] - [a^{III}]\right\}$$

S-Parameter for Junction I,II

From field matching of the TM_z electric and magnetic fields at the junction between Region I and II,

$$[a^I] + [b^I] = [Q]^T\left\{[a^{II}] + [b^{II}]\right\} \tag{4.26}$$

$$[K_x^{II}]\left\{[b^{II}] - [a^{II}]\right\} = [Q][K_x^I]\left\{[a^I] - [b^I]\right\} \tag{4.27}$$

Omitting the paranthesis for clarity, Equation (4.26) can be re-expressed as,

$$b^I = Q^T(a^{II} + b^{II}) - a^I \tag{4.28}$$

Substituting Equation (4.28) into (4.27),

$$b^{II} - a^{II} = (K_x^{II})^{-1} Q K_x^I (a^I - Q^T a^{II} - Q^T b^{II} + a^I)$$

Letting

$$[P] = [K_x II]^{-1}[Q][K_x I]$$

$$[I] - \quad L \times L \quad \text{unit matrix}$$

$$[U] - \quad M \times M \quad \text{unit matrix}$$

$$\Rightarrow \quad [U + PQ^T]b^{II} = 2Pa^I + (U - PQ^T)a^{II}$$

$$\therefore \quad b^{II} = 2(U + PQ^T)^{-1}Pa^I + (U + PQ^T)^{-1}(U - PQ^T)a^{II}$$

Subsitituting Equation (4.27) into (4.26),

$$a^I + b^I = Q^T(a^{II} + Pa^I - Pb^I + a^{II})$$

$$(I + Q^T P)b^I = (Q^T P - I)a^I + 2Q^T a^{II}$$

$$\therefore \quad b^I = (Q^T P + I)^{-1}(Q^T P - I)a^I + 2(Q^T P + I)^{-1}Q^T a^{II}$$

Thus, the overall S-matrix of Step Junction A for TM mode is,

$$[S_{11}^A] = \{[Q]^T[P] + [I]\}^{-1}\{[Q]^T[P] - [I]\}$$

$$[S_{12}^A] = 2 \cdot \{[Q]^T[P] + [I]\}^{-1}[Q]^T$$

$$[S_{21}^A] = 2 \cdot \{[U] + [P][Q]^T\}^{-1}[P]$$

$$[S_{22}^A] = \{[U] + [P][Q]^T\}^{-1}\{[U] - [P][Q]^T\}$$

S-Parameter for Junction II,III

From field matching of the TM_z electric and magnetic fields at the junction between Region II and III,

$$[a^{III}] + [b^{III}] = [E]^T \left\{[a^{II}] + [b^{II}]\right\} \tag{4.29}$$

$$[K_x^{II}] \left\{[a^{II}] - [b^{II}]\right\} = [E][K_x^{III}] \left\{[b^{IIII}] - [a^{IIII}]\right\} \tag{4.30}$$

Omitting the paranthesis for clarity, Equation (4.29) can be re-expressed as,

$$b^{III} = E^T(a^{II} + b^{II}) - a^{III} \tag{4.31}$$

Substituting Equation (4.31) into (4.30),

$$a^{II} - b^{II} = (K_x^{II})^{-1} E (K_x^{III})(E^T a^{II} + E^T b^{II} - 2a^{III})$$

Letting

$$[F] = [K_x^{II}]^{-1}[E][K_x^{III}]$$

$$[U] - \quad M \times M \quad \text{unit matrix}$$

$$[V] - \quad N \times N \quad \text{unit matrix}$$

$$\Rightarrow \quad [U + FE^T]b^{II} = [U - FE^T]a^{II} + 2Fa^{III}$$

$$\therefore \quad b^{II} = [U + FE^T]^{-1}[U - FE^T]a^{II} + 2[U + FE^T]^{-1}Fa^{III}$$

Subsitituting Equation (4.30) into (4.29),

$$
\begin{aligned}
a^{III} + b^{III} &= E^T(a^{II} + a^{II} - Fb^{II} + Fa^{III}) \\
(V + E^T F)b^{III} &= 2E^T a^{II} + (E^T F - V)a^{III} \\
\therefore \quad b^{III} &= 2(V + E^T F)^{-1} E^T a^{II} + (V + E^T F)^{-1}(E^T F - V)a^{III}
\end{aligned}
$$

Thus, the overall S-matrix of Step Junction B for TM mode is,

$$
\begin{aligned}
[S_{11}^B] &= \{[U] + [F][E]^T\}^{-1}\{[U] - [F][E]^T\} \\
[S_{12}^B] &= 2 \cdot \{[U] + [F][E]^T\}^{-1}[F] \\
[S_{21}^B] &= 2 \cdot \{[V] + [E]^T[F]\}^{-1}[E]^T \\
[S_{22}^B] &= \{[V] + [E]^T[F]\}^{-1}\{[E]^T[F] - [V]\}
\end{aligned}
$$

4.4 Determination of Cutoff Wavenumbers

To solve for the MLG cutoff wavenumbers – k_c, the Transverse Resonanace Approach is applied to the step junction S-matrices that are derived in Sections 4.2.2 and 4.3.2. The transverse resonance solution is applied by considering the equivalent microwave network of the MLG in the direction transverse to the wave propagation vector, k_z, as shown in Figure 4.5.

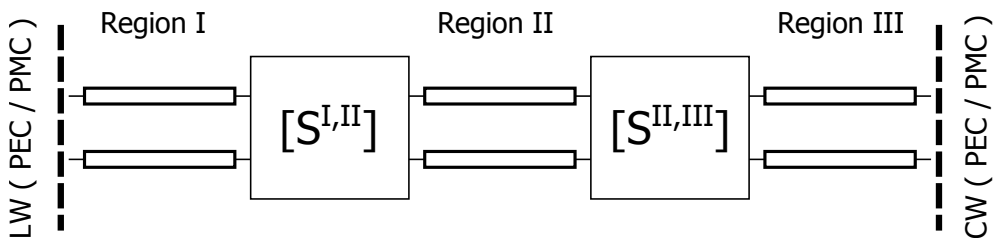

Figure 4.5: Equivalent microwave network of meanderline polarizer unit cell

For normal incidence, the modes generated in the MLG are symmetric about the center wall. Hence, the boundary conditions on the left and center walls of the MLG will be represented by PEC and PMC. The S-matrices of the individual waveguide sections and step junctions can be cascaded into an overall GSM, Figure 4.6.

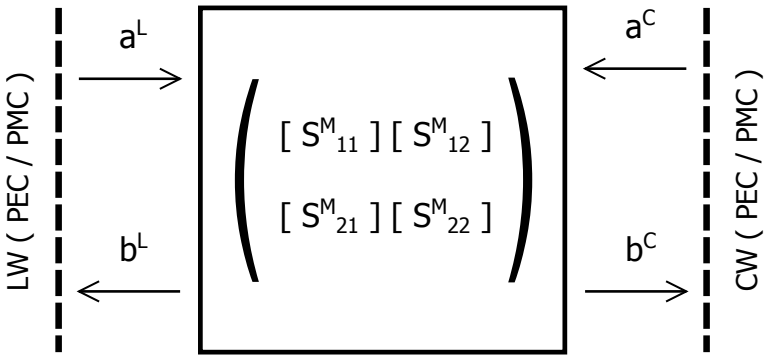

Figure 4.6: GSM representation of meanderline polarizer unit cell

The MLG network can then be represented by the following GSM,

$$\begin{pmatrix} [b^L] \\ [b^C] \end{pmatrix} = \begin{pmatrix} [S_{11}^M] & [S_{12}^M] \\ [S_{21}^M] & [S_{22}^M] \end{pmatrix} \begin{pmatrix} [a^L] \\ [a^C] \end{pmatrix}$$

where a^L and b^L denote transverse propagating waves on the left of the MLG while a^C and b^C represent transverse propagating waves on the right. Depending on the boundary conditions on LW and RW, the transverse propagating waves are governed by the following equality,

$$\text{PEC}: \qquad [b^L] = -[a^L] \quad \text{and} \quad [b^C] = -[a^C]$$

$$\text{PMC}: \qquad [b^L] = [a^L] \quad \text{and} \quad [b^C] = [a^C]$$

Therefore, the GSM of the MLG can be expressed in the form,

$$\begin{pmatrix} [D^L] & [0] \\ [0] & [D^C] \end{pmatrix} \begin{pmatrix} [a^L] \\ [a^C] \end{pmatrix} = \begin{pmatrix} [S_{11}^M] & [S_{12}^M] \\ [S_{21}^M] & [S_{22}^M] \end{pmatrix} \begin{pmatrix} [a^L] \\ [a^C] \end{pmatrix}$$

$$\Rightarrow \begin{pmatrix} [S_{11}^M] - [D^L] & [S_{12}^M] \\ [S_{21}^M] & [S_{22}^M] - [D^C] \end{pmatrix} \begin{pmatrix} [a^L] \\ [a^C] \end{pmatrix} = \begin{pmatrix} [0] \\ [0] \end{pmatrix} \tag{4.32}$$

where $[D^L]$, $[D^C]$ are diagonal matrices with diagonal elements being -1 and $+1$ when the end boundary condition is PEC and PMC, respectively.

For non trivial solution, the LHS matrix in Equation (4.32) is singular at the mode cutoff wave numbers, k_c. Traditional method such as bi-section technique [49] can be applied to determine the roots for the MLG [50]. An accurate and efficient approach to finding the roots will be discussed in subsequent section.

4.5 Least Square Approximation

For each of the valid cutoff wave number identified using the bracketing and bisection method, the least square approximation [49] to Equation (4.32) is employed to solve for the unknown coefficients $[a^L]$ and $[a^C]$ associated with each k_c.

To perform the least square approximation, the first unknown coefficient of the column matrix $[a^L]$ is set to 1. The first column of the characteristic

equation can then be transferred over to the right hand side,

$$\begin{pmatrix} C_{1,1} & C_{1,2} & \cdots & C_{1,K} \\ C_{2,1} & C_{2,2} & \cdots & C_{2,K} \\ \vdots & \vdots & \ddots & \vdots \\ C_{K,1} & C_{K,2} & \cdots & C_{K,K} \end{pmatrix} \begin{pmatrix} a_1^L \\ \vdots \\ a_M^L \\ a_1^C \\ \vdots \\ a_N^C \end{pmatrix} = \begin{pmatrix} 0 \\ \vdots \\ 0 \end{pmatrix}$$

where $K = M + N$. Let $a_1^L = 1$

$$\begin{pmatrix} C_{2,1} & C_{2,2} & \cdots & C_{2,K} \\ \vdots & \vdots & \ddots & \vdots \\ C_{K,1} & C_{K,2} & \cdots & C_{K,K} \end{pmatrix} \begin{pmatrix} a_2^L \\ \vdots \\ a_M^L \\ a_1^C \\ \vdots \\ a_N^C \end{pmatrix} = \begin{pmatrix} C_{1,1} \\ \vdots \\ C_{1,K} \end{pmatrix}$$

$$[C][A'] = [B]$$

Multiplying both sides of the equation by $[C]^T$,

$$([C]^T[C])[A'] = [C]^T[B] \tag{4.33}$$

The normal equation (4.33) can then be solved to obtain the coefficients $[a^L]$ and $[a^C]$.

4.5.1 Normalization of Coefficients

To ensure the power propagating through the MLG is unity, the coefficients $[a^L]$ and $[a^C]$need to be normalized by the total power flowing through the guide.

The normalization factor is computed from the integration of the Poynting vector over each of the region in the MLG.

MLG Region I - TE mode

The integration of the Poynting vector over Region I of the MLG can be evaluated in closed form for both the cases of propagating ($k_{xl}^I > 0$) and evanescent ($k_{xl}^I < 0$) transverse modes.

$$\oint_{S_1} \bar{E} \times \bar{H}^* \cdot \mathrm{d}\hat{s} = \int_0^{d_1} \int_{-w_1}^{0} \left[E_x^I \cdot H_y^{I^*} - E_y^I \cdot H_x^{I^*} \right] \mathrm{d}x \, \mathrm{d}y$$

For the case of propagating transverse mode ($k_{xl}^I > 0$):

$$\therefore \quad E_x^I \cdot H_y^{I^*} = \sum_{l=0}^{L-1} \left[\left(-a_l^I e^{-jk_{xl}^I x} + b_l^I e^{jk_{xl}^I x} \frac{l\pi}{d_1} \sin\left(\frac{l\pi y}{d_1}\right) \right) \right] \times \left[\frac{k_z^*}{\omega\mu} \left(-a_l^{I^*} e^{jk_{xl}^I x} + b_l^{I^*} e^{-jk_{xl}^I x} \right) \frac{l\pi}{d_1} \sin\left(\frac{l\pi y}{d_1}\right) \right]$$

$$\therefore \quad E_y^I \cdot H_x^{I^*} = \sum_{l=0}^{L-1} \left[\left(a_l^I e^{-jk_{xl}^I x} + b_l^I e^{jk_{xl}^I x} jk_{xl}^I \cos\left(\frac{l\pi y}{d_1}\right) \right) \right] \times \left[-\frac{k_z^*}{\omega\mu} \left(a_l^{I^*} e^{jk_{xl}^I x} + b_l^{I^*} e^{-jk_{xl}^I x} \right) (-jk_{xl}^I) \cos\left(\frac{l\pi y}{d_1}\right) \right]$$

$$\therefore \quad \int_0^{d_1} \int_{-w_1}^{0} E_x^I \cdot H_y^{I^*} = \sum_{l=0}^{L-1} \left(\frac{k_z^*}{\omega\mu} \right) \cdot \left(\frac{l\pi}{d_1} \right)^2 \cdot \int_0^{d_1} \int_{-w_1}^{0} \sin^2\left(\frac{l\pi y}{d_1}\right) \cdot \left[|a_l^I|^2 + |b_l^I|^2 - a_l^I b_l^{I^*} e^{-2jk_{xl}^I x} - a_l^{I^*} b_l^I e^{2jk_{xl}^I x} \right] \mathrm{d}x \, \mathrm{d}y$$

$$\therefore \quad \int_0^{d_1} \int_{-w_1}^{0} E_y^I \cdot H_x^{I^*} = \sum_{l=0}^{L-1} \left(-\frac{k_z^*}{\omega\mu} \right) \cdot \left| k_{xl}^I \right|^2 \cdot \int_0^{d_1} \int_{-w_1}^{0} \cos^2\left(\frac{l\pi y}{d_1}\right) \cdot \left[|a_l^I|^2 + |b_l^I|^2 + a_l^I b_l^{I^*} e^{-2jk_{xl}^I x} + a_l^{I^*} b_l^I e^{2jk_{xl}^I x} \right] \mathrm{d}x \, \mathrm{d}y$$

The integrals $\int_0^{d_1} \sin^2\left(\frac{l\pi y}{d_1}\right) \mathrm{d}y$, $\int_0^{d_1} \cos^2\left(\frac{l\pi y}{d_1}\right) \mathrm{d}y$ and $\int_{-w_1}^{0} e^{\pm 2jk_{xl}^I x} \mathrm{d}x$ can be evaluated in closed form to give,

$$\int_0^{d_1} \sin^2\left(\frac{l\pi y}{d_1}\right) \mathrm{d}y = \begin{cases} \frac{d_1}{2} & \text{when } l \neq 0 \\ 0 & \text{when } l = 0 \end{cases}$$

$$\int_0^{d_1} \cos^2\left(\frac{l\pi y}{d_1}\right) \mathrm{d}y = \begin{cases} \frac{d_1}{2} & \text{when } l \neq 0 \\ 0 & \text{when } l = 0 \end{cases}$$

$$\int_{-w_1}^{0} e^{\pm 2jk_{xl}^I x} \mathrm{d}x = e^{\mp jk_{xl}^I w_1} \cdot \frac{\sin(k_{xl}^I w_1)}{k_{xl}^I}$$

For the case of evanescent transverse mode ($k_{xl}^I < 0$):

$$\therefore \quad E_x^I \cdot H_y^{I^*} = \sum_{l=0}^{L-1} \left[\left(-a_l^I e^{-|k_{xl}^I|x} + b_l^I e^{|k_{xl}^I|x} \frac{l\pi}{d_1} \sin\left(\frac{l\pi y}{d_1}\right) \right) \right] \times \left[\frac{k_z^*}{\omega\mu} \left(-a_l^{I^*} e^{-|k_{xl}^I|x} + b_l^{I^*} e^{|k_{xl}^I|x} \right) \frac{l\pi}{d_1} \sin\left(\frac{l\pi y}{d_1}\right) \right]$$

$$\therefore \quad E_y^I \cdot H_x^{I^*} = \sum_{l=0}^{L-1} \left[\left(a_l^I e^{-|k_{xl}^I|x} + b_l^I e^{|k_{xl}^I|x} \left|k_{xl}^I\right| \cos\left(\frac{l\pi y}{d_1}\right) \right) \right] \times \left[-\frac{k_z^*}{\omega\mu} \left(a_l^{I^*} e^{-|k_{xl}^I|x} + b_l^{I^*} e^{|k_{xl}^I|x} \right) \left|k_{xl}^I\right| \cos\left(\frac{l\pi y}{d_1}\right) \right]$$

$$\therefore \quad \int_0^{d_1} \int_{-w_1}^{0} E_x^I \cdot H_y^{I^*} = \sum_{l=0}^{L-1} \left(\frac{k_z^*}{\omega\mu}\right) \cdot \left(\frac{l\pi}{d_1}\right)^2 \cdot \int_0^{d_1} \int_{-w_1}^{0} \sin^2\left(\frac{l\pi y}{d_1}\right) \cdot \left[|a_l^I|^2 e^{-2|k_{xl}^I|x} + |b_l^I|^2 e^{2|k_{xl}^I|x} - a_l^I b_l^{I^*} - a_l^{I^*} b_l^I \right] \mathrm{d}x\, \mathrm{d}y$$

$$\therefore \quad \int_0^{d_1} \int_{-w_1}^{0} E_y^I \cdot H_x^{I^*} = \sum_{l=0}^{L-1} \left(-\frac{k_z^*}{\omega\mu}\right) \cdot \left|k_{xl}^I\right|^2 \cdot \int_0^{d_1} \int_{-w_1}^{0} \cos^2\left(\frac{l\pi y}{d_1}\right) \cdot \left[|a_l^I|^2 e^{-2|k_{xl}^I|x} + |b_l^I|^2 e^{2|k_{xl}^I|x} - a_l^I b_l^{I^*} - a_l^{I^*} b_l^I \right] \mathrm{d}x\, \mathrm{d}y$$

The integral $\int_{-w_1}^{0} e^{\pm 2|k_{xl}^I|x}\,\mathrm{d}x$ can be evaluated in closed form to give,

$$\int_{-w_1}^{0} e^{\pm 2|k_{xl}^I|x}\,\mathrm{d}x = \frac{\pm 1}{2\,|k_{xl}^I|}\left[1 - e^{\mp 2|k_{xl}^I|w_1}\right]$$

MLG Region II - TE mode

Similar to Region I, the integration of the Poynting vector over Region II of the MLG can be evaluated in closed form for both the cases of propagating ($k_{xl}^I > 0$) and evanescent ($k_{xl}^I < 0$) transverse modes.

$$\oint_{S_2} \bar{E} \times \bar{H}^* \cdot\,\mathrm{d}\hat{s} = \int_h^{h+d_2}\int_0^{w_2} \left[E_x^{II} \cdot H_y^{II*} - E_y^{II} \cdot H_x^{II*}\right]\,\mathrm{d}x\,\mathrm{d}y$$

For the case of propagating transverse mode ($k_{xm}^{II} > 0$):

$$\int_h^{h+d_2}\int_0^{w_2} E_x^{II} \cdot H_y^{II*} = \sum_{m=0}^{M-1}\left(\frac{k_z^*}{\omega\mu}\right)\cdot\left(\frac{m\pi}{d_2}\right)^2 \cdot \int_h^{h+d_2}\int_0^{w_2} \sin^2\left(\frac{m\pi}{d_2}(y-h)\right)\cdot \left[|a_m^{II}|^2 + |b_m^{II}|^2 - a_m^{II} b_m^{II} I^* e^{2jk_{xm}^{II}x} - a_l^{I*} b_l^I e^{-2jk_{xm}^{II}x}\right]\,\mathrm{d}x\,\mathrm{d}y$$

$$\int_h^{h+d_2}\int_0^{w_2} E_y^{II} \cdot H_x^{II*} = \sum_{m=0}^{M-1}\left(-\frac{k_z^*}{\omega\mu}\right)\cdot\left|k_{xm}^{II}\right|^2 \cdot \int_h^{h+d_2}\int_0^{w_2} \cos^2\left(\frac{m\pi}{d_2}(y-h)\right)\cdot \left[|a_m^{II}|^2 + |b_m^{II}|^2 + a_m^{II} b_m^{II*} e^{2jk_{xm}^{II}x} + a_m^{II*} b_m^{II} e^{-2jk_{xm}^{II}x}\right]\,\mathrm{d}x\,\mathrm{d}y$$

For the case of evanescent transverse mode ($k_{xm}^{II} < 0$):

$$\int_h^{h+d_2}\int_0^{w_2} E_x^{II}\cdot H_y^{II*} = \sum_{m=0}^{M-1}\left(\frac{k_z^*}{\omega\mu}\right)\cdot\left(\frac{m\pi}{d_2}\right)^2\cdot\int_h^{h+d_2}\int_0^{w_2}\sin^2\left(\frac{m\pi}{d_2}(y-h)\right)\cdot \Big[|a_m^{II}|^2 e^{2|k_{xm}^{II}|x} + |b_m^{II}|^2 e^{-2|k_{xm}^{II}|x} - a_m^{II} b_m^{II*} - a_m^{II*} b_m^{II}\Big]\,\mathrm{d}x\,\mathrm{d}y$$

$$\int_h^{h+d_2}\int_0^{w_2} E_y^{II}\cdot H_x^{II*} = \sum_{m=0}^{M-1}\left(-\frac{k_z^*}{\omega\mu}\right)\cdot\left|k_{xm}^{II}\right|^2\cdot\int_h^{h+d_2}\int_0^{w_2}\cos^2\left(\frac{m\pi}{d_2}(y-h)\right)\cdot \Big[|a_m^{II}|^2 e^{2|k_{xm}^{II}|x} + |b_m^{II}|^2 e^{-2|k_{xm}^{II}|x} + a_m^{II} b_m^{II*} + a_m^{II*} b_m^{II}\Big]\,\mathrm{d}x\,\mathrm{d}y$$

MLG Region III - TE mode

Similar to Region I and II, the integration of the Poynting vector over Region III of the MLG can be evaluated in closed form for both the cases of propagating ($k_{xn}^{III} > 0$) and evanescent ($k_{xn}^{III} < 0$) transverse modes.

$$\oint_{S_3}\bar{E}\times\bar{H}^*\cdot\,\mathrm{d}\hat{s} = \int_h^{h+d_3}\int_0^{w_3}\left[E_x^{III}\cdot H_y^{III*} - E_y^{III}\cdot H_x^{III*}\right]\mathrm{d}x\,\mathrm{d}y$$

For the case of propagating transverse mode ($k_{xn}^{III} > 0$):

$$\int_h^{h+d_2}\int_0^{w_2} E_x^{III}\cdot H_y^{III*} = \sum_{n=0}^{N-1}\left(\frac{k_z^*}{\omega\mu}\right)\cdot\left(\frac{n\pi}{d_3}\right)^2\cdot\int_h^{h+d_3}\int_0^{w_3}\sin^2\left(\frac{n\pi y}{d_3}\right)\cdot \Big[|a_n^{III}|^2 + |b_n^{III}|^2 - a_n^{III} b_n^{III*} e^{2jk_{xn}^{III}x} - a_n^{III*} b_n^{III} e^{-2jk_{xn}^{III}x}\Big]\,\mathrm{d}x\,\mathrm{d}y$$

$$\int_h^{h+d_3}\int_0^{w_3} E_y^{III}\cdot H_x^{III*} = \sum_{n=0}^{N-1}\left(-\frac{k_z^*}{\omega\mu}\right)\cdot\left|k_{xn}^{III}\right|^2\cdot\int_h^{h+d_3}\int_0^{w_3}\cos^2\left(\frac{n\pi y}{d_3}\right)\cdot \Big[|a_n^{III}|^2+|b_n^{III}|^2+a_n^{III}b_n^{III*}e^{2jk_{xn}^{III}x}+ a_n^{III*}b_n^{III}e^{-2jk_{xn}^{III}x}\Big]\,\mathrm{d}x\,\mathrm{d}y$$

For the case of evanescent transverse mode ($k_{xm}^{II}<0$):

$$\int_h^{h+d_3}\int_0^{w_3} E_x^{III}\cdot H_y^{III*} = \sum_{n=0}^{N-1}\left(\frac{k_z^*}{\omega\mu}\right)\cdot\left(\frac{n\pi}{d_3}\right)^2\cdot\int_h^{h+d_3}\int_0^{w_3}\sin^2\left(\frac{n\pi y}{d_2}\right)\cdot \Big[|a_n^{III}|^2e^{2|k_{xn}^{III}|x}+|b_n^{III}|^2e^{-2|k_{xn}^{III}|x}- a_n^{III}b_n^{III*}-a_n^{II*}b_n^{III}\Big]\,\mathrm{d}x\,\mathrm{d}y$$

$$\int_h^{h+d_3}\int_0^{w_3} E_y^{III}\cdot H_x^{III*} = \sum_{n=0}^{N-1}\left(-\frac{k_z^*}{\omega\mu}\right)\cdot\left|k_{xn}^{III}\right|^2\cdot\int_h^{h+d_3}\int_0^{w_3}\cos^2\left(\frac{n\pi y}{d_2}\right)\cdot \Big[|a_n^{III}|^2e^{2|k_{xn}^{III}|x}+|b_n^{III}|^2e^{-2|k_{xn}^{III}|x}+ a_n^{III}b_n^{III*}+a_n^{III*}b_n^{III}\Big]\,\mathrm{d}x\,\mathrm{d}y$$

MLG Region I - TM mode

Similar to TE mode for Region I, the integration of the Poynting vector over Region I for TM mode can be evaluated in closed form for both the cases of propagating ($k_{xl}^I>0$) and evanescent ($k_{xl}^I<0$) transverse modes.

$$\oint_{S_1}\bar{E}\times\bar{H}^*\cdot\,\mathrm{d}\hat{s} = \int_0^{d_1}\int_0^{-w_1}\left[E_x^I\cdot H_y^{I*}-E_y^I\cdot H_x^{I*}\right]\,\mathrm{d}x\,\mathrm{d}y$$

For the case of propagating transverse mode ($k_{xl}^I > 0$):

$$\int_h^{h+d_2}\int_0^{w_2} E_x^I \cdot H_y^{I^*} = \sum_{l=1}^{L}\left(\frac{\omega\epsilon}{k_z^*}\right)\cdot {k_{xl}^I}^2 \cdot \int_0^{d_1}\int_0^{-w_1} \sin^2\left(\frac{l\pi y}{d_1}\right)\cdot \left[|a_l^I|^2 + |b_l^I|^2 - a_l^I b_l^I I^* e^{-2jk_{xl}^I x} - a_l^{I^*} b_l^I e^{2jk_{xl}^I x}\right] \mathrm{d}x\,\mathrm{d}y$$

$$\int_0^{d_1}\int_0^{-w_1} E_y^I \cdot H_x^{I^*} = \sum_{l=0}^{L-1}\left(-\frac{\omega\epsilon}{k_z^*}\right)\cdot \left(\frac{l\pi}{d_1}\right)^2 \cdot \int_0^{d_1}\int_0^{-w_1} \cos^2\left(\frac{l\pi y}{d_1}\right)\cdot \left[|a_l^I|^2 + |b_l^I|^2 + a_l^I b_l^I I^* e^{-2jk_{xl}^I x} + a_l^{I^*} b_l^I e^{2jk_{xl}^I x}\right] \mathrm{d}x\,\mathrm{d}y$$

For the case of evanescent transverse mode ($k_{xl}^I < 0$):

$$\int_0^{d_1}\int_0^{-w_1} E_x^I \cdot H_y^{I^*} = \sum_{l=0}^{L-1}\left(\frac{\omega\epsilon}{k_z^*}\right)\cdot \left|k_{xl}^I\right|^2 \cdot \int_0^{d_1}\int_0^{-w_1} \sin^2\left(\frac{l\pi y}{d_1}\right)\cdot \left[|a_l^I|^2 e^{-2|k_{xl}^I|x} + |b_l^I|^2 e^{2|k_{xl}^I|x} - a_l^I b_l^{I^*} - a_l^{I^*} b_l^I\right] \mathrm{d}x\,\mathrm{d}y$$

$$\int_0^{d_1}\int_0^{-w_1} E_y^I \cdot H_x^{I^*} = \sum_{l=0}^{L-1}\left(-\frac{\omega\epsilon}{k_z^*}\right)\cdot \left(\frac{l\pi}{d_1}\right)^2 \cdot \int_0^{d_1}\int_0^{-w_1} \cos^2\left(\frac{l\pi}{d_1}\right)\cdot \left[|a_l^I|^2 e^{-2|k_{xl}^I|x} + |b_l^I|^2 e^{2|k_{xl}^I|x} + a_l^I b_l^{I^*} + a_l^{I^*} b_l^I\right] \mathrm{d}x\,\mathrm{d}y$$

MLG Region II - TM mode

Similar to Region I, the integration of the Poynting vector over Region II of the MLG can be evaluated in closed form for both the cases of propagating ($k_{xm}^{II} > 0$) and evanescent ($k_{xm}^{II} < 0$) transverse modes.

$$\oint_{S_2} \bar{E}\times\bar{H}^*\cdot \mathrm{d}\hat{s} = \int_h^{h+d_2}\int_0^{w_2} \left[E_x^{II}\cdot H_y^{II^*} - E_y^{II}\cdot H_x^{II^*}\right] \mathrm{d}x\,\mathrm{d}y$$

For the case of propagating transverse mode ($k_{xm}^{II} > 0$):

$$\int_h^{h+d_2}\int_0^{w_2} E_x^{II}\cdot H_y^{II^*} = \sum_{m=1}^{M}\left(\frac{\omega\epsilon}{k_z^*}\right)\cdot {k_{xm}^{II}}^2\cdot\int_h^{h+d_2}\int_0^{w_2}\sin^2\left(\frac{m\pi}{d_2}(y-h)\right)\cdot \Big[|a_m^{II}|^2+|b_m^{II}|^2-a_m^{II}b_m^{II}I^*e^{2jk_{xm}^{II}x}- a_m^{II^*}b_m^{II}e^{-2jk_{xm}^{II}x}\Big]\,\mathrm{d}x\,\mathrm{d}y$$

$$\int_h^{h+d_2}\int_0^{w_2} E_y^{II}\cdot H_x^{II^*} = \sum_{m=1}^{L}\left(-\frac{\omega\epsilon}{k_z^*}\right)\cdot\left(\frac{m\pi}{d_2}\right)^2\cdot\int_h^{h+d_2}\int_0^{w_2}\cos^2\left(\frac{m\pi}{d_2}(y-h)\right)\cdot \Big[|a_m^{II}|^2+|b_m^{II}|^2+a_m^{II}b_m^{II^*}e^{2jk_{xm}^{II}x}+ a_m^{II^*}b_m^{II}e^{-2jk_{xm}^{II}x}\Big]\,\mathrm{d}x\,\mathrm{d}y$$

For the case of evanescent transverse mode ($k_{xm}^{II} < 0$):

$$\int_h^{h+d_2}\int_0^{w_2} E_x^{II}\cdot H_y^{II^*} = \sum_{m=1}^{M}\left(\frac{\omega\epsilon}{k_z^*}\right)\cdot\left|k_{xm}^{II}\right|^2\cdot\int_0^{d_1}\int_0^{-w_1}\sin^2\left(\frac{m\pi}{d_2}(y-h)\right)\cdot \Big[|a_m^{II}|^2e^{2|k_{xm}^{II}|x}+|b_m^{II}|^2e^{-2|k_{xm}^{II}|x}- a_m^{II}b_m^{II^*}-a_m^{II^*}b_m^{II}\Big]\,\mathrm{d}x\,\mathrm{d}y$$

$$\int_h^{h+d_2}\int_0^{w_2} E_y^{II}\cdot H_x^{II^*} = \sum_{m=1}^{M}\left(-\frac{\omega\epsilon}{k_z^*}\right)\cdot\left(\frac{m\pi}{d_2}\right)^2\cdot\int_h^{h+d_2}\int_0^{w_2}\cos^2\left(\frac{m\pi}{d_2}(y-h)\right)\cdot \Big[|a_m^{II}|^2e^{2|k_{xm}^{II}|x}+|b_m^{II}|^2e^{-2|k_{xm}^{II}|x}+ a_m^{II}b_m^{II^*}+a_m^{II^*}b_m^{II}\Big]\,\mathrm{d}x\,\mathrm{d}y$$

MLG Region III - TM mode

Similar to Region I and II, the integration of the Poynting vector over Region III of the MLG can be evaluated in closed form for both the cases of propagating

($k_{xn}^{III} > 0$) and evanescent ($k_{xn}^{III} < 0$) transverse modes.

$$\oint_{S_3} \bar{E} \times \bar{H}^* \cdot \mathrm{d}\hat{s} = \int_0^{d_3} \int_0^{w_3} \left[E_x^{III} \cdot H_y^{III*} - E_y^{III} \cdot H_x^{III*} \right] \mathrm{d}x \, \mathrm{d}y$$

For the case of propagating transverse mode ($k_{xn}^{III} > 0$):

$$\int_0^{d_3} \int_0^{w_3} E_x^{III} \cdot H_y^{III*} = \sum_{n=1}^{N} \left(\frac{\omega\epsilon}{k_z^*} \right) \cdot k_{xn}^{III2} \cdot \int_0^{d_3} \int_0^{w_3} \sin^2 \left(\frac{n\pi y}{d_3} \right) \cdot \left[|a_n^{III}|^2 + |b_n^{III}|^2 - a_n^{III} b_n^{III*} e^{2jk_{xn}^{III}x} - a_n^{III*} b_n^{III} e^{-2jk_{xn}^{III}x} \right] \mathrm{d}x \, \mathrm{d}y$$

$$\int_0^{d_3} \int_0^{w_3} E_y^{III} \cdot H_x^{III*} = \sum_{n=1}^{N} \left(-\frac{\omega\epsilon}{k_z^*} \right) \cdot \left(\frac{n\pi}{d_3} \right)^2 \cdot \int_0^{d_3} \int_0^{w_3} \cos^2 \left(\frac{m\pi}{d_2}(y-h) \right) \cdot \left[|a_n^{III}|^2 + |b_n^{III}|^2 + a_n^{III} b_n^{III*} e^{2jk_{xn}^{III}x} + a_n^{III*} b_n^{III} e^{-2jk_{xn}^{III}x} \right] \mathrm{d}x \, \mathrm{d}y$$

For the case of evanescent transverse mode ($k_{xn}^{III} < 0$):

$$\int_0^{d_3} \int_0^{w_3} E_x^{III} \cdot H_y^{III*} = \sum_{n=1}^{N} \left(\frac{\omega\epsilon}{k_z^*} \right) \cdot \left| k_{xn}^{III} \right|^2 \cdot \int_0^{d_3} \int_0^{w_3} \sin^2 \left(\frac{n\pi y}{d_3} \right) \cdot \left[|a_n^{III}|^2 e^{2|k_{xn}^{III}|x} + |b_n^{III}|^2 e^{-2|k_{xn}^{III}|x} - a_n^{III} b_n^{III*} - a_n^{III*} b_n^{III} \right] \mathrm{d}x \, \mathrm{d}y$$

$$\int_0^{d_3} \int_0^{w_3} E_y^{III} \cdot H_x^{III*} = \sum_{n=1}^{N} \left(-\frac{\omega\epsilon}{k_z^*} \right) \cdot \left(\frac{n\pi}{d_3} \right)^2 \cdot \int_0^{d_3} \int_0^{w_3} \cos^2 \left(\frac{n\pi y}{d_3} \right) \cdot \left[|a_n^{III}|^2 e^{2|k_{xn}^{III}|x} + |b_n^{III}|^2 e^{-2|k_{xn}^{III}|x} + a_n^{III} b_n^{III*} + a_n^{III*} b_n^{III} \right] \mathrm{d}x \, \mathrm{d}y$$

4.6 Coupling of Floquet Modes to Waveguide Modes

To compute the scattering characteristics of the meanderline polarizer, solution for the coupling of MLG modes to free space Floquet modes will be developed in this section. Figure 4.7 illustrates the coupling between MLG and free space, the coupling can be solved by matching the tangential electric and magnetic fields at the junction between MLG and free space.

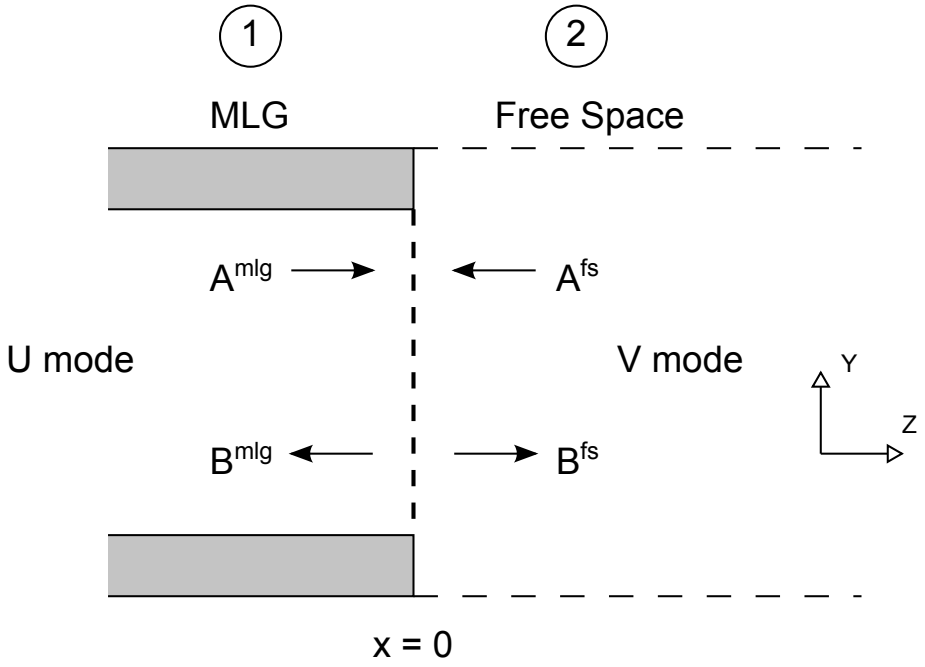

Figure 4.7: Meanderline Waveguide to Free Space Junction

The electric and magnetic fields in the MLG can be represented by summation of waveguide modes,

$$\bar{E}^{mlg} = \sum_{u=1}^{U} \left(A_u^{mlg} e^{-jk_z z} + B_u^{mlg} e^{jk_z z} \right) \bar{e}_u^{mlg} \cdot \sqrt{\eta_u^{mlg}}$$

$$\bar{H}^{mlg} = \sum_{u=1}^{U} \left(A_u^{mlg} e^{-jk_z z} - B_u^{mlg} e^{jk_z z} \right) \bar{h}_u^{mlg} \cdot \frac{1}{\sqrt{\eta_u^{mlg}}}$$

where A_u^{mlg}, B_u^{mlg} – modal coefficients

$\bar{e}_u^{mlg}$ – normalized vector tangential electric field mode

$\bar{h}_u^{mlg}$ – normalized vector tangential magnetic field mode

η_u^{mlg} – characteristic impedance of uth waveguide mode

In free space, the electric and magnetic field is represented by summation of Floquet modes,

$$\bar{E}^{fs} = \sum_{v=1}^{V} \left(A_v^{fs} e^{jk_z z} + B_v^{fs} e^{-jk_z z} \right) \bar{e}_v^{fs} \cdot \sqrt{\eta_v^{fs}}$$

$$\bar{H}^{fs} = \sum_{v=1}^{V} \left(A_v^{fs} e^{jk_z z} - B_v^{fs} e^{-jk_z z} \right) \bar{h}_v^{fs} \cdot \frac{1}{\sqrt{\eta_v^{fs}}}$$

where A_v^{fs}, B_v^{fs} – modal coefficients

$\bar{e}_v^{fs}$ – normalized vector tangential electric field mode

$\bar{h}_v^{fs}$ – normalized vector tangential magnetic field mode

η_v^{fs} – characteristic impedance of vth Floquet mode

Matching the tangential electric field at the meanderline waveguide – free space junction in Figure 4.7:

$$\sum_{u=1}^{U} \left(A_u^{mlg} + B_u^{mlg} \right) \bar{e}_u^{mlg} \cdot \sqrt{\eta_u^{mlg}} = \sum_{v=1}^{V} \left(A_v^{fs} + B_v^{fs} \right) \bar{e}_v^{fs} \cdot \sqrt{\eta_v^{fs}}$$

Taking the inner product of $\bar{h}_w^{fs*}$ with both sides and integrating over free space grid interface S_{fs}:

$$\sum_{u=1}^{U} \sqrt{\eta_u^{mlg}} \left(A_u^{mlg} + B_u^{mlg}\right) \cdot \iint_{S_{fs}} (\bar{e}_u^{mlg} \times \bar{h}_w^{fs*}) \cdot \hat{z} \, \mathrm{d}s = \sum_{v=1}^{V} \sqrt{\eta_v^{fs}} \left(A_v^{fs} + B_v^{fs}\right) \iint_{S_{fs}} (\bar{e}_v^{fs} \times \bar{h}_w^{fs*}) \cdot \hat{z} \, \mathrm{d}s$$

Applying orthogonality of Floquet modes,

$$A_v^{fs} + B_v^{fs} = \sum_{u=1}^{U} \left(A_u^{mlg} + B_u^{mlg}\right) \cdot \sqrt{\frac{\eta_u^{mlg}}{\eta_v^{fs}}} \iint_{S_{mlg}} (\bar{e}_u^{mlg} \times \bar{h}_v^{fs*}) \cdot \hat{z} \, \mathrm{d}s$$

In matrix notation,

$$\left[A^{fs}\right] + \left[B^{fs}\right] = [H] \left(\left[A^{mlg}\right] + \left[B^{mlg}\right]\right)$$

Matching the tangential magnetic field at the meanderline waveguide – free space junction in Figure 4.7:

$$\sum_{u=1}^{U} \left(A_u^{mlg} - B_u^{mlg}\right) \bar{h}_u^{mlg} \cdot \sqrt{\frac{1}{\eta_u^{mlg}}} = \sum_{v=1}^{V} \left(-A_v^{fs} + B_v^{fs}\right) \bar{h}_v^{fs} \cdot \sqrt{\frac{1}{\eta_v^{fs}}}$$

Taking the inner product of $\bar{e}_w^{fs*}$ with both sides and integrating over free space grid interface S_{mlg}:

$$\sum_{u=1}^{U} \sqrt{\frac{1}{\eta_u^{mlg}}} \left(A_u^{mlg} - B_u^{mlg}\right) \cdot \iint_{S_{mlg}} (\bar{e}_w^{mlg*} \times \bar{h}_u^{mlg}) \cdot \hat{z} \, \mathrm{d}s = \sum_{v=1}^{V} \sqrt{\frac{1}{\eta_v^{fs}}} \left(-A_v^{fs} + B_v^{fs}\right) \cdot \iint_{S_{mlg}} (\bar{e}_w^{mlg*} \times \bar{h}_v^{fs}) \cdot \hat{z} \, \mathrm{d}s$$

Applying orthogonality of waveguide modes,

$$A_u^{mlg} - B_u^{mlg} = \sum_{v=1}^{V} \left(B_v^{fs} - A_v^{fs}\right) \cdot \sqrt{\frac{\eta_u^{mlg}}{\eta_v^{fs}}} \cdot \iint_{S_{mlg}} (\bar{e}_u^{mlg*} \times \bar{h}_v^{fs}) \cdot \hat{z}\, \mathrm{d}s$$

In matrix notation,

$$\left[A^{mlg}\right] - \left[B^{mlg}\right] = [R]\left(\left[B^{fs}\right] - \left[A^{fs}\right]\right)$$

4.7 Root Finding Optimization

For any numerical technique to be a practical design tool, computation efficiency is one of the key requirement. In this section, the computation time required for various stages of meanderline analysis will be profiled. It will be shown that the root searching process dominates majority of the CPU time in a design cycle. An approach based on Singular Value Decomposition (SVD) and Golden Ratio Search (GRS) technique will be presented. Benchmarking showed that this proposed approach can reduce the root search time by half.

4.7.1 Profiling of Meanderline Polarizer Analysis

The flowchart for a meanderline polarizer analysis is illustrated in Figure 4.8 below. The key routines are root search, computation of coefficients, coupling coefficients, GSM computation. To determine the computational resources required, profiling simulation was carried out for a 3-layer polarizer whose dimensions are given in Table 4.1 and layout depicted in Figure 5.5.

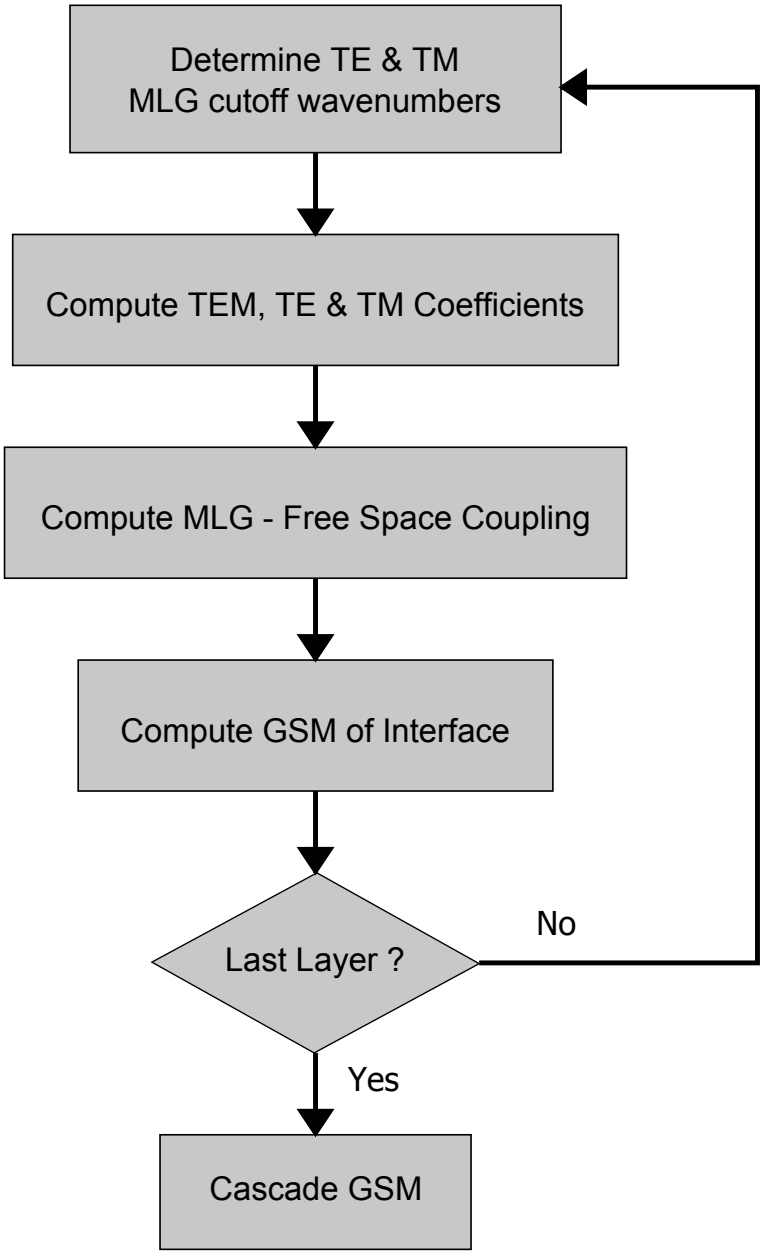

Figure 4.8: Flowchart of meanderline polarizer analysis

Table 4.1: Meanderline parameters for profiling analysis

(unit=inch)	Tx	Ty	w1	w2	w3	d1	d2	d3
Grid #1, #3	0.15	0.277	0.0325	0.01	0.0325	0.267	0.124	0.267
Grid #2	0.15	0.277	0.0325	0.01	0.0325	0.267	0.08	0.267

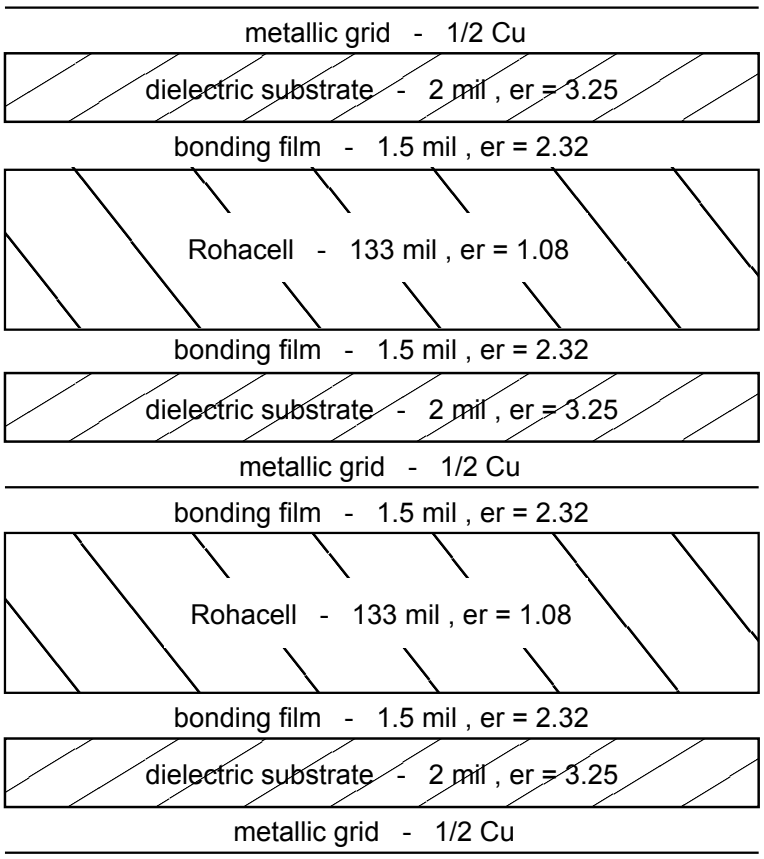

Figure 4.9: Layout of 3-layer meanderline polarizer for profiling simulation

A computer running on Intel Core 2 Duo T8100 2.1GHz CPU with 3GB of DRAM was used for this analysis. Although the processor is dual core, only a single CPU is utilized during the profiling. No code parallelization is carried out to minimize distortion of results due to parallelization issues such as load balancing, latency and bandwidth.

The total CPU time required to perform the analysis is 75.6 secs and the percentage breakdown for various subroutines in the analysis are plotted in Figure 4.10. The profiling revealed that the root search algorithm accounts for more than 80% of the total CPU time in an analysis cycle. The total memory required to perform the analysis is less than 30 MByte and can be easily handled by modern personal computers. For the algorithm to be a practical design tool, low CPU time is critical as this will lend itself well to optimization routines.

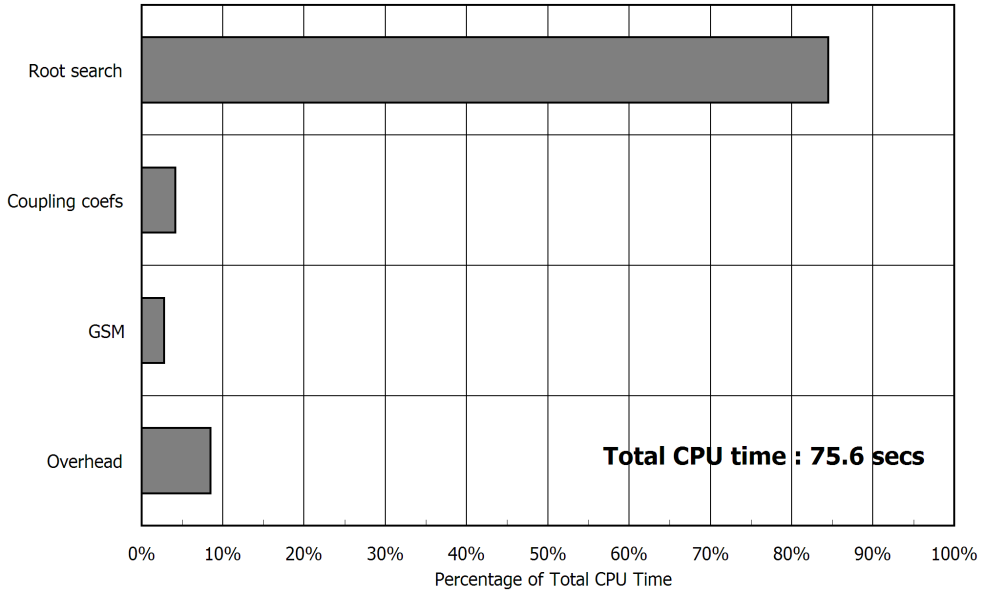

Figure 4.10: Profile of typical meanderline polarizer analysis

The conventional approach to finding the roots of a meanderline guide is to track the complex determinant of the characteristic equation while incrementing the cutoff frequency, k_c, in small steps. When the real and imaginary part of the complex determinant is zero, the k_c is flagged as a valid root (cutoff frequency) for the meanderline waveguide. Although the concept appears intuitively simple, this method suffers from a number of deficiencies.

A plot of the complex determinant against k_c for the TE meanderline waveguide modes is shown in Figure 4.11. It can be seen that the real and imaginary part of the determinant fluctuate incoherently across frequencies. Both the real and imaginary components of the determinant need to be tracked as it is not necessary that both values will exhibit zero crossing characteristics, Figure 4.12. Many iterations are thus required to discern the valid roots from the multitude of false positives. In addition, a small Δk_c is also necessary in order not to miss any valid roots which can be spaced very closely apart – such as the adjacent roots 145.278 and 145.381. However, a small Δk_c will increase the number of computations required. An adaptive Δk_c could reduce the number of com-

putations but the unpredictable fluctuation would make such implementation difficult. The complexity of tracking both the real and imaginary components, coupled with the small Δk_c, resulted in the root search algorithm accounting for more than 80% of the total CPU time in an analysis cycle.

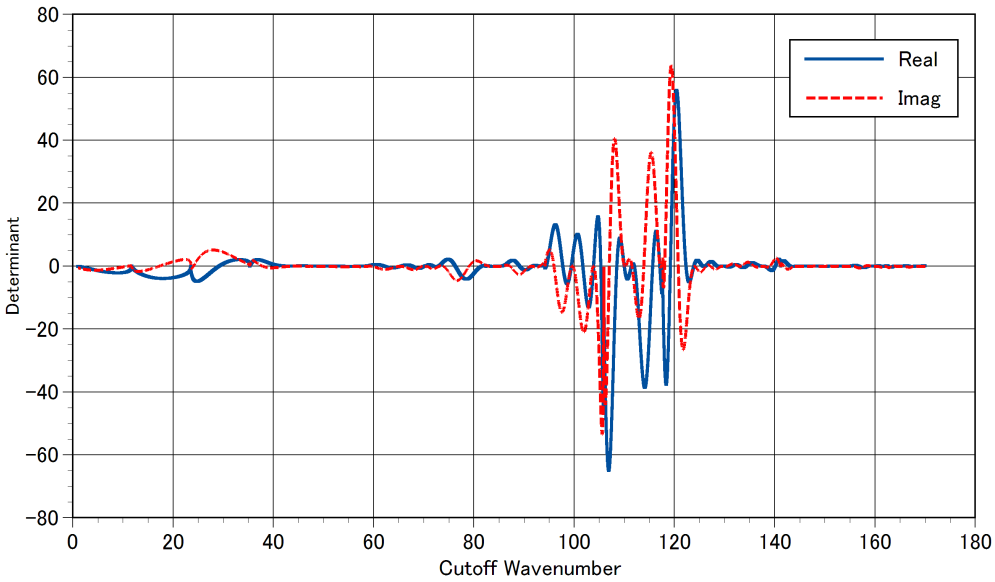

Figure 4.11: Complex determinant versus cutoff wavenumber for TE meanderline waveguide modes

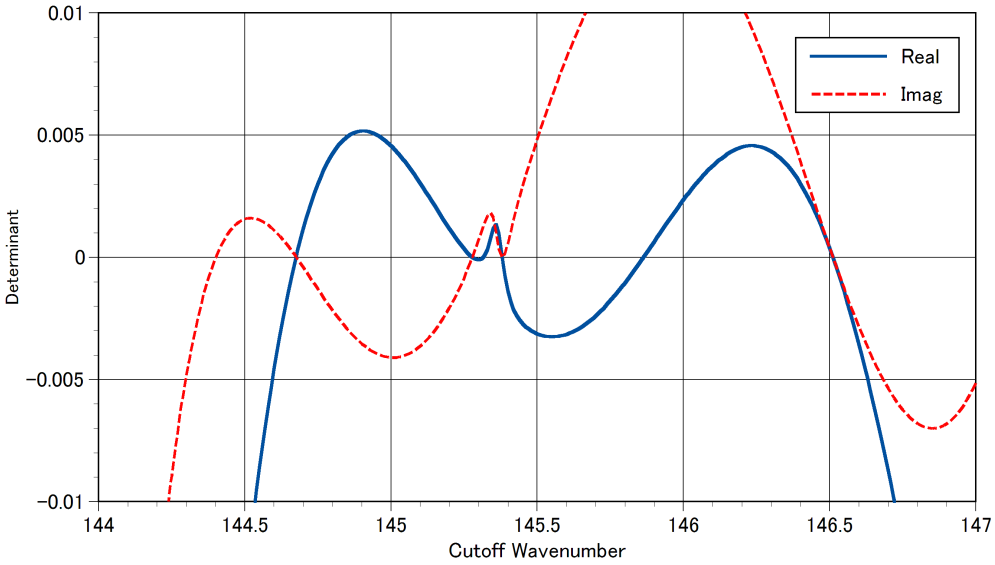

Figure 4.12: Incoherent behaviour and closely spaced roots for TE meanderline waveguide modes

4.7.2 Singular Value Decomposition

The Singular Value Decomposition (SVD) is a powerful factorization technique for dealing with matrices that are either singular or numerically very close to singular [51; 52]. Since the characteristic equation is singular at all valid k_c, the SVD will be a very efficient alternative for determining the cutoff frequencies of the meanderline waveguide.

By definition, the SVD of the $m \times m$ complex characteristic matrix M is a factorization of the form,

$$M = U\Sigma V^*$$

where U is an $m \times m$ complex unitary matrix, Σ is an $m \times m$ diagonal matrix with non-negative real numbers on the diagonal, and V^* is an $m \times m$ complex unitary matrix. The diagonal entries $\Sigma_{j,j}$ of Σ are known as the singular values of M.

Using the previous meanderline polarizer, the singular value $\Sigma_{m,m}$ of the characteristic equation for the meanderline waveguide is plotted against the k_c, Figure 4.13. The results revealed that the behavior of $\Sigma_{m,m}$ is very well behaved compared to the complex determinant in Figure 4.11. In addition, the minima of $\Sigma_{m,m}$ indicates location of possible roots for the characteristic equation. Finally, there are two distinct orders of magnitude in the minima of the singular values, those larger than 10^{-5} and those smaller than 10^{-7}.

To compare the use of SVD against Bisection method, the singular values and complex determinant are plotted together in Figure 4.14. Using SVD, the false root around 141.2 can easily be classified. Four valid roots between 144 – 147 are distinguished by their singular values which are less than 10^{-7}.

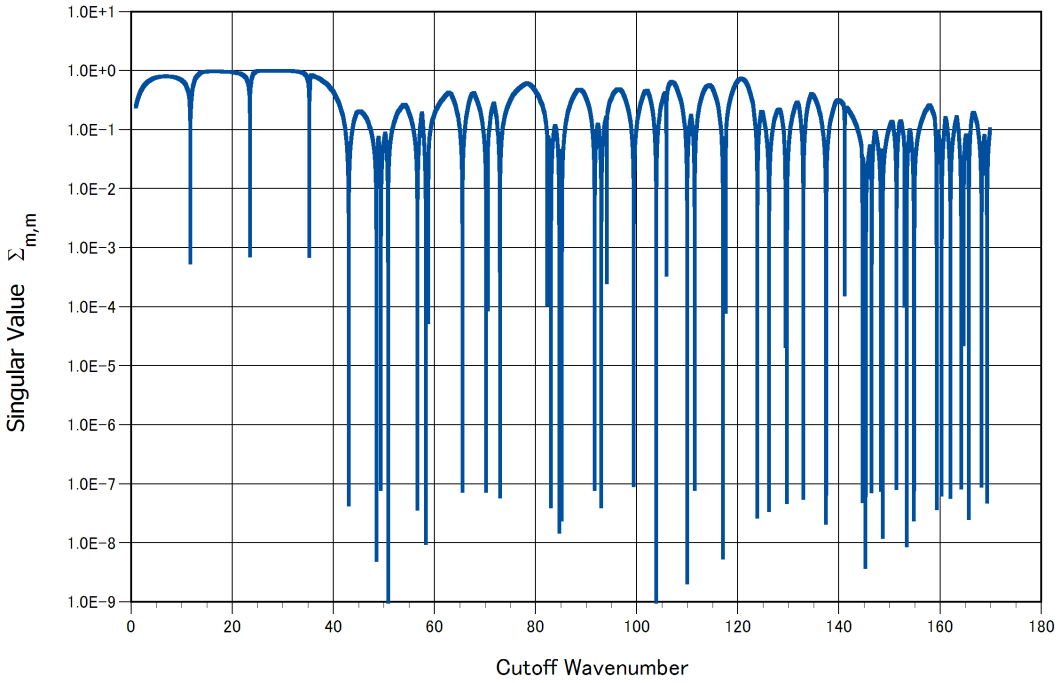

Figure 4.13: Singular value versus cutoff wavenumber for TE meanderline waveguide modes

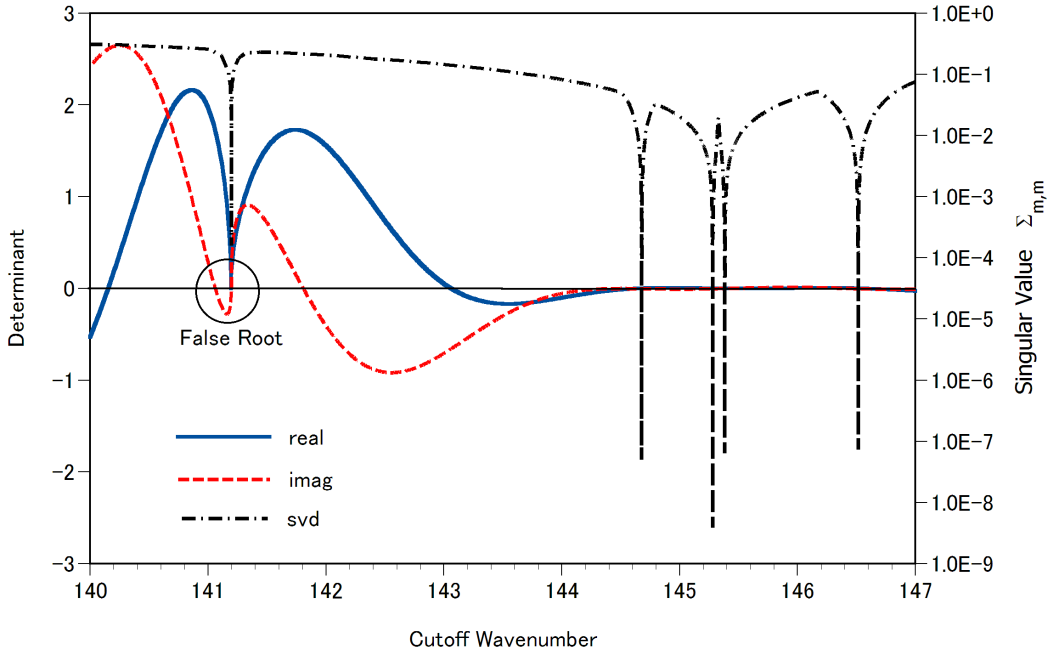

Figure 4.14: Singular value and complex determinant versus cutoff wavenumber for TE meanderline waveguide modes

4.7.3 Golden Ratio Search

The golden ratio search (GRS) is a technique for finding the extremum of a function by successively narrowing the range of values inside which the extremum is known to exist [49]. The concept for a single iteration is illustrated in Figure 4.15. For a minima is bounded between x_1 and x_3, the function values, f(x_2) and f(x_4), at two other points, x_2 and x_4, are first evaluated. If f(x_4) is less than f(x_2), it implies that the minima is bounded within the region between x_3 and x_3. Whereas, the minina is bounded between x_1 and x_4 if f(x_4) is greater than f(x_2). In either case, the new search range is now narrowed and the process repeated until a required accuracy for the mimina is achieved.

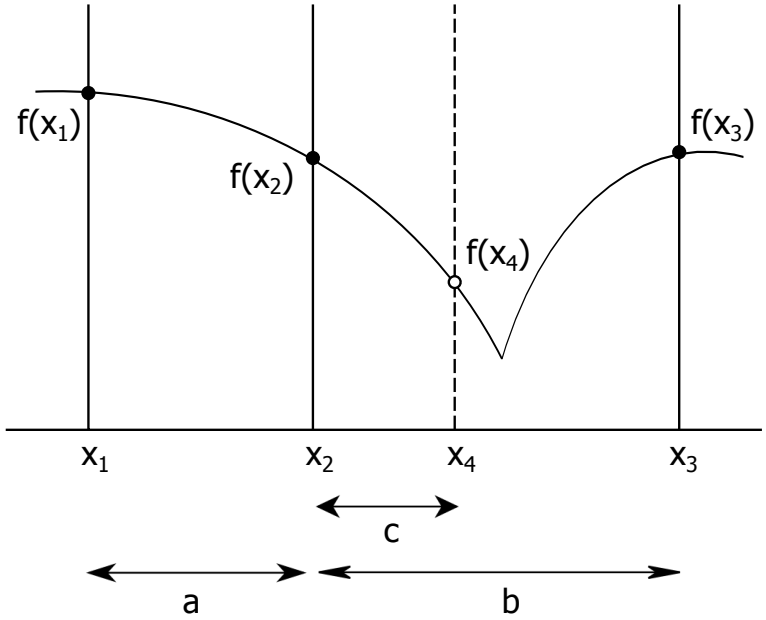

Figure 4.15: Golden section search

The choices of x_2 and x_4 can be arbitrary but if they are chosen such that the same proportion of spacing is maintained throughout the iteration, it will ensure that the point x_2 will not be too close to either x_1 or x_3. In addition, the interval will be reduced by the same constant proportion in each step. To maintain the same proportion of spacing,

$$\frac{c}{a} = \frac{a}{b} \tag{4.34}$$

$$\frac{c}{b-c} = \frac{a}{b} \tag{4.35}$$

The two simultaneous equations will yield the following constraint,

$$\frac{b}{a} = \frac{a}{c} = \varphi$$

where φ is the well known golden ratio:

$$\varphi = \frac{1+\sqrt{5}}{2} = 1.618033988...$$

The GRS method is a robust and efficient method in which only one function evaluation is required after the first iteration. The reduction in search range is 38.2% after each iteration and independent of the function behavior.

4.7.4 SVD–GRS Implementation

To compute the value of the minima, it is necessary to first bound the minima within a range of k_c. This is easily accomplished by detecting a negative to postive change in the gradient of $\Sigma_{m,m}$. Once this range is identified, the GRS method described previously is employed to converge to the local minimum singular value. The order of magnitude of the minima value will then indicate if the singular value is a valid root.

The relatively smooth varying nature of $\Sigma_{m,m}$ lends itself well to adaptive search technique in which the step size Δk_c is proportional to the value of $\Sigma_{m,m}$. Once a minimum is identified, the singular value at the location can be efficiently tested to determine if it is a valid or false root.

Using the 3-layer meanderline polarizer in Figure 5.5 and Table 4.1, the total

time taken to compute the valid roots are plotted for both the Bisection and SVD–GRS method in Figure 4.17. While this SVD–GRS method requires an additional step of computing for the singular values, the reduction in number of iterations and use of adaptive Δk_c almost halved the time required to analyze the meanderline polarizer.

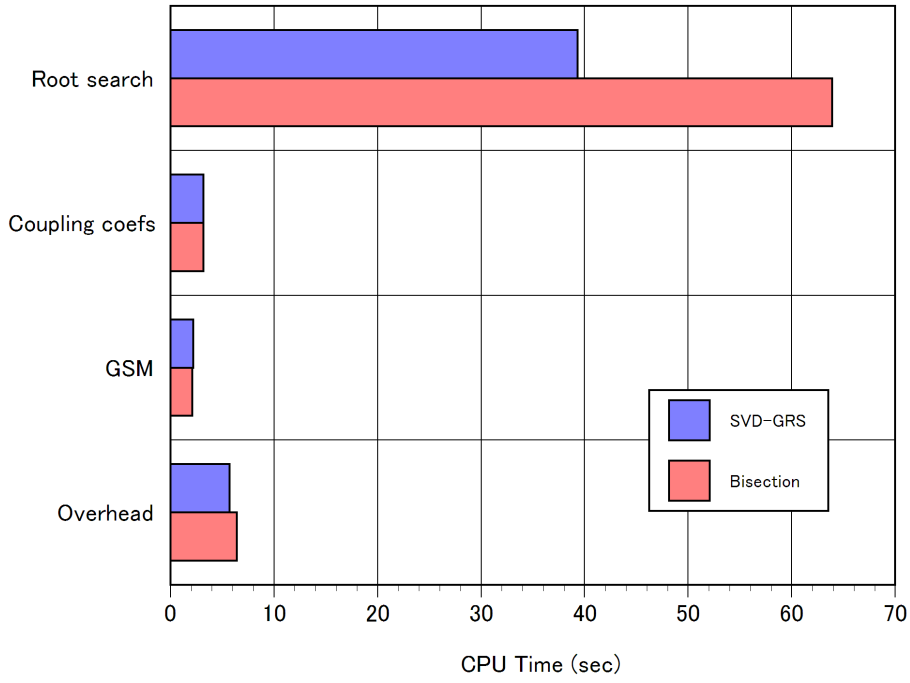

Figure 4.16: Profile of Bisection and SVD–GRS methods

To verify that this root finding approach is scalable with the complexity of the problem, the total CPU time taken to analyze the meanderline polarizer is plotted against an increasing number of MLG modes used to model the problem. The results plotted in Figure 4.17 showed that this SVD–GRS approach achieved speed improvement consistently even as the complexity of the problem increases.

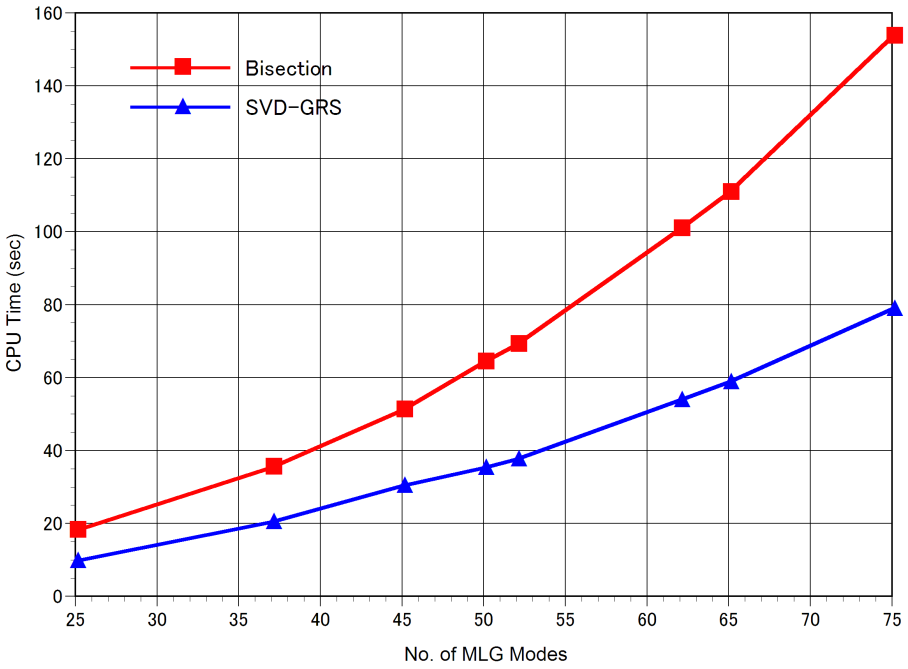

Figure 4.17: CPU time versus number of MLG modes

In summary, the SVD–GRS method improves the efficiency of the root search algorithm by making use of characteristic equation's singular values instead of direct tracking of the complex determinant. The advantages of this approach are (1) better differentiation between false and real roots, (2) faster convergence due to well behaved response around the roots of the characteristic equation, and (3) ease of incorporating adaptive search technique to further improves computational efficiency.

Chapter 5

Validation of Proposed Numerical Technique

The theoretical formulation of the proposed techique presented in Chapter 4 was verified through comparison with other numerical techniques and measurement data reported in open literatures.

5.1 Meanderline Waveguide Cutoff Frequencies

Each of the meanderline cutoff wavenumber constitutes a MLG mode used to represent the field distribution in the unit cell. To verify the accuracy of the proposed formulation in determining the cutoff wavenumbers, results of the cutoff frequencies for the meanderline waveguide cross section illustrated in Figure 5.1 were compared against results obtained using the Finite Element Method (FEM). The dimensions of the meanderline waveguide cross section were based on the meanderline grids published by Terret et al. [9].

Table 5.1 lists the first 10 cutoff frequencies computed using the two methods. Both the proposed technique and FEM showed very good agreement with each other. On a computer equipped with Intel 2.1 GHz T8100 CPU, the time

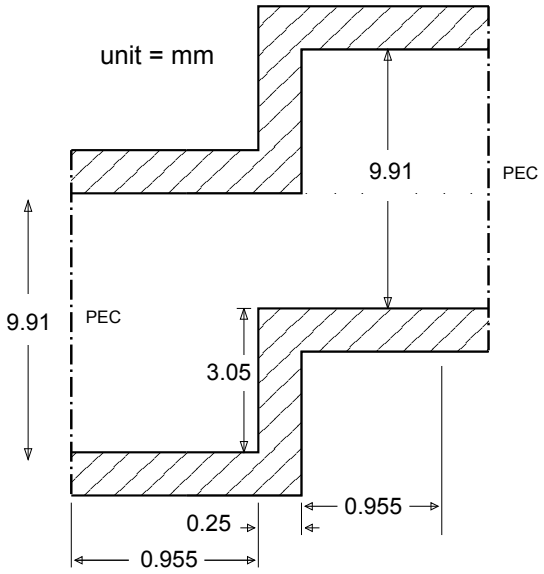

Figure 5.1: Dimensions of meanderline waveguide

taken to compute the cutoff frequencies using the proposed technique is 8 secs while FEM requires 44 mins.

Table 5.1: Cutoff frequencies for waveguide illustrated in Figure 5.1

	Cutoff Frequency (GHz)	
Mode No.	Proposed Technique	FEM
1	14.1	14.0
2	22.1	22.0
3	30.5	30.5
4	45.2	45.2
5	58.6	58.4
6	63.4	63.2
7	68.6	68.3
8	72.7	72.7
9	74.7	74.5
10	77.7	77.6

5.2 Single Layer Polarizer

The theoretical formulation presented in chapter 4 was verified by predicting the transmission phases of meanderline grids printed on a dielectric substrate as shown in Figure 5.2. Measurement results for two such grids were published by Terret et al. [9]. The dimensions of both grids are listed in Table 5.2. A metallization thickness of 0.036 mm (1.4 mil), which is equivalent to 1 oz copper, is assumed as the grid thickness was not published by the author. The transmission phases and the differential phase shift of the TE_{00} and TM_{00} modes for Grid A are plotted in Figure 5.3.

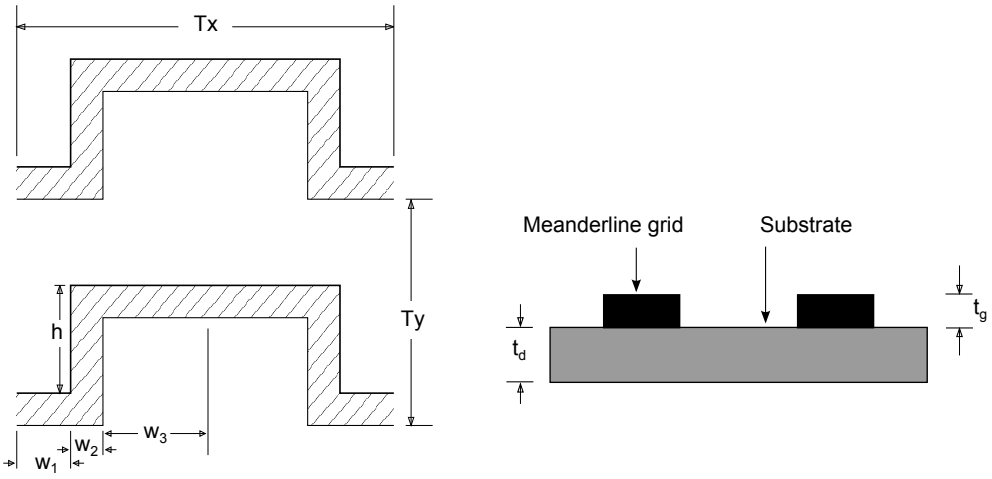

Figure 5.2: Geometry of meanderline polarizer by Terret et al.

Table 5.2: Dimensions of meanderline grids

(unit=mm)	Tx	Ty	w1	w2	w3	h	t_d	t_g
Grid A	4.32	10.16	0.955	0.25	0.955	3.05	0.254	0.036
Grid B	4.32	10.16	0.915	0.33	0.915	3.73	0.254	0.036

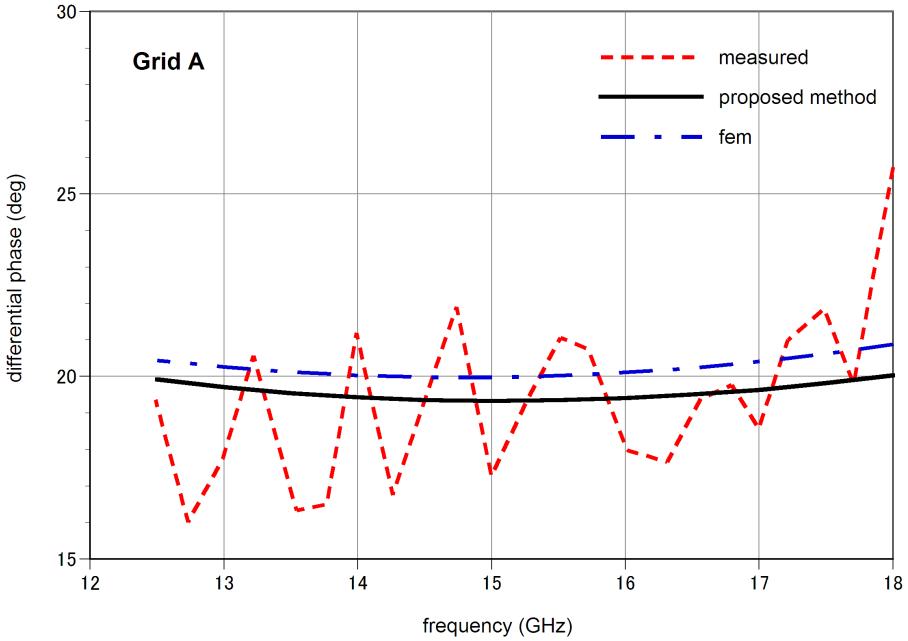

Figure 5.3: Differential phase shift of TE_{00} and TM_{00} modes for Grid A

For the simulation, the highest MLG cutoff wavenumber required for convergence is approximately 3.3 rad/mm. This yields 40 MLG modes for the PMC sidewalls and 32 MLG modes for the PEC sidewalls. To generate these MLG mode, the number of functions used in region I, II and III is L = 13, M = 9 and N = 13, respectively. The number of free space Floquet modes used to compute the scattering characteristics was 138, corresponding to a highest cutoff wavenumber of approximately 4.4 rad/mm. To ensure proper convergent behavior, the number of field expansion functions in both grids were chosen such that the mode ratio between the regions is as close as possible to the height ratio of the MLG step junctions [53–57]. The result using the proposed method compares well with published measurement data by Terret et al. [9] and FEM simulation using ANSYS HFSS, Figure 5.3. A total of 12 frequency points were simulated on a computer equipped with Intel 2.1 GHz T8100 CPU. The proposed method and FEM took 24 secs and 310 secs, respectively. The amount of computer memory utilized was 6 MB for the proposed method and 95 MB using FEM.

For Grid B, 32 and 33 MLG modes were used for the case of PMC and PEC sidewalls, respectively. The number of expansion functions in the 3 regions are 13, 8 and 13. Similar to Grid A, 138 free space Floquet modes were used to compute the scattering characteristics. The differential phase shift measured by Terret et al. [9] is compared against results computed using the technique proposed in chapter 4 and FEM solution obtained using ANSYS HFSS. The results in Figure 5.4 showed that the proposed technique exhibits very good agreement with measurement data and FEM solution. Between the proposed method and FEM, the difference is less than 1 degrees.

On a computer equipped with Intel 2.1 GHz T8100 CPU, the time and memory required to compute the results using the proposed technique were 22 secs and 6 MB. In contrast, FEM took 370 secs and 105 MB.

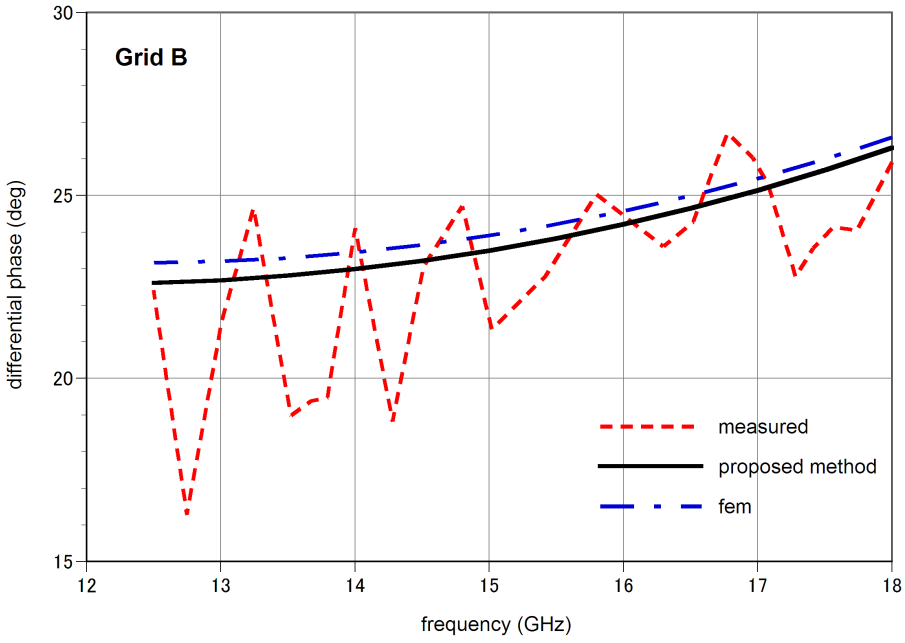

Figure 5.4: Differential phase shift of TE_{00} and TM_{00} modes for Grid B

5.3 Multi-Layer Polarizer

To evaluate the accuracy of the proposed method for multi-layered polarizers. The axial ratio of a microwave polarizer for LEO satellite communications was computed and compared with measurement results published by [3]. The polarizer was constructed from three layers of meanderline grid separated by Rohacell spacers, Figure 5.5. The dimensions of the individual grid geometries are tabulated in Table 5.3 with Grid #1 and #3 being identical.

Table 5.3: Dimensions of multi-layer polarizer grids

(unit=mil)	Tx	Ty	w1	w2	w3	h
Grid #1, #3	150	277	32.5	10	32.5	143
Grid #2	150	277	32.5	10	32.5	187

The three meanderline grids were etched on polyimide substrates and bonded to two layers of support foam using epoxy. The material thickness and properties of the polarizer constituents are tabulated in Table 5.4.

Table 5.4: Composition of multi-layer polarizer

Layer	Material	Thickness	Permittivity
grid	copper	0.7 mil	–
substrate	polyimide	2 mil	3.25
epoxy	prepreg	1.5 mil	3.4
support	rohacell	133 mil	1.08

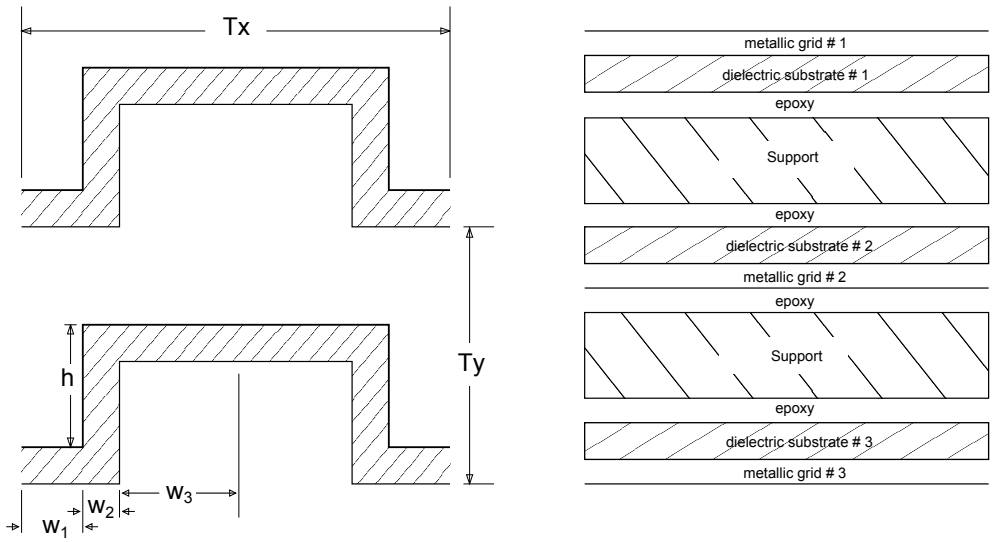

Figure 5.5: Geometry and structure of multi-layer polarizer

Simulation was conducted using three numerical techniques: the technique proposed in Chapter 4, the finite element method, and the moment method. Using the proposed technique, the highest MLG cutoof wavenumber required for convergence was approximately 6.69 rad/mm. For TM incidence, this yielded 83, 81 and 83 MLG modes for Grid #1, #2 and #3, respectively. For TE incidence, Grid #1, #2 and #3 were represented by 90, 88 and 90 MLG modes, respectively. The number of waveguide functions used in Region I, II and II of Grid #1 and #3 was L = 15, M = 7 and N = 15, respectively. For Grid #2, the number of waveguide functions used in Region I, II and II of Grid #1 and #3 was L = 15, M = 4 and N = 15, respectively. A total of 242 and 274 free space Floquet modes were used to compute the scattering characteristics for TM and TE incidence, respectively.

The finite element and moment method computations were carried out using ANSYS HFSS and ANSYS Designer, respectively. For the finite element method, adaptive meshing and Floquet ports were employed to model the multi-layer polarizer. With the convergence criteria set to be less than 0.02, solutions for adaptive meshing at three different frequencies (30, 40, and 50 GHz).

The on-axis axial ratio computed using the proposed technique, finite element method, and moment method are compared with measurement data [3] in Figure 5.6. The results showed that solution computed using the proposed technique has good agreement with the measured data and moment method solution. It is also interesting to note that the finite element method solution, which showed discrepancies at higher frequencies, appeared to converge towards the measured data when the adaptive meshing frequency was increased from 30 to 50 GHz. The probable reason is the difficulty in modeling thin metallization thickness accurately in the presence of relatively thick dielectric layers and conductor width.

On a computer equipped with Intel 2.1 GHz T8100 CPU, the proposed method took an average of 38 secs per frequency point and 50 MB of memory. In comparison, the finite element method using 30 GHz mesh required 420 secs per frequency point and approximately 750 MB of memory. Using 50 GHz mesh, the finite element method required 6700 secs per frequency point and 2.7 GB of memory.

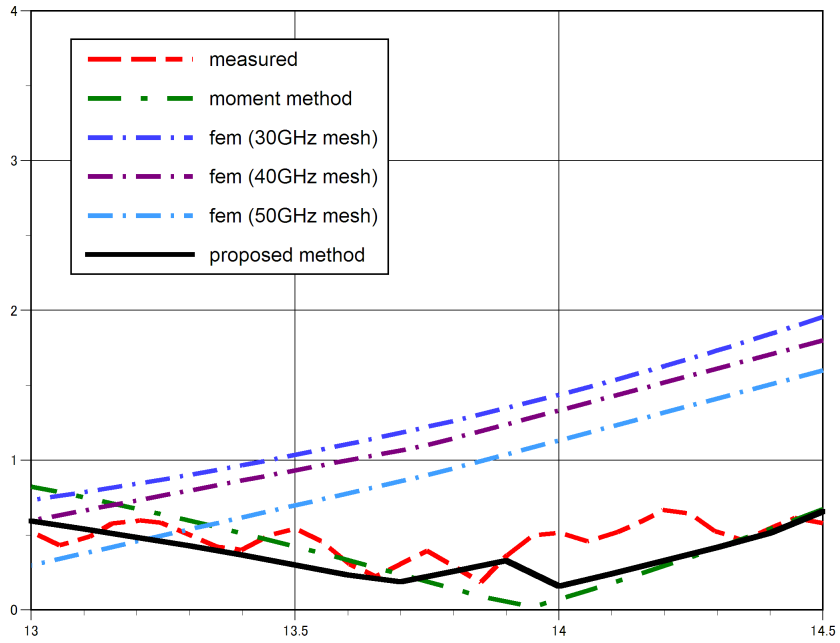

Figure 5.6: Measured and computed axial ratio of multi-layer polarizer

5.4 Effect of Grid Metallization Thickness

In this section, the effect of grid metallization thickness on single layer and multi-layer polarizer are investigated. Standard copper weights of 0.5-, 1.0-, 2.0- and 4.0-oz will be analyzed. The corresponding relationship between copper weight and metallization thickness is tabulated in Table 5.5.

Table 5.5: Copper weight versus metallization thickness

Copper weight (oz)	Metallization thickness (mil)
0.5	0.7
1.0	1.4
2.0	2.8
4.0	5.6

5.4.1 Single Layer Polarizer

The two single layer polarizers discussed in Section 5.2 are analyzed for grid thickness tabulated in Table 5.5. The differential phases of the two grids are shown in Figures 5.7 and 5.8. For every 0.5-oz increase in copper weight, the differential phase shift increases by approximately 0.25 degree. Similar responses were obtained when the polarizers are solved using FEM, Figures 5.9 and 5.10. The increase in differential phase shift due to metallization thickness becomes problematic, if not corrected, in a multi-layer low axial ratio polarizer design.

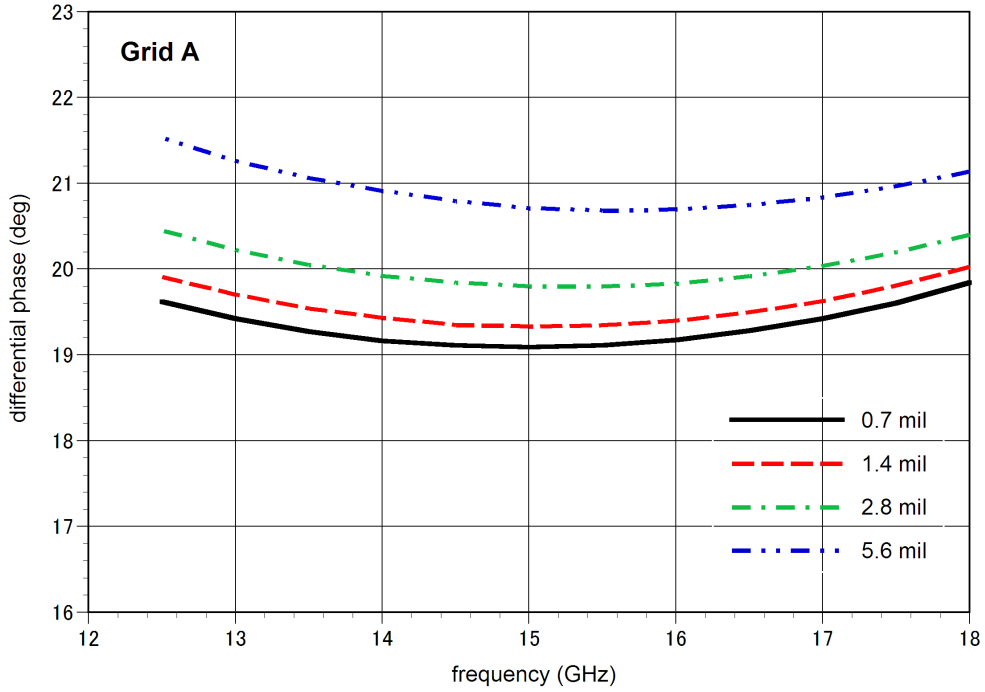

Figure 5.7: Effect of grid thickness on differential phase of Grid A – proposed method

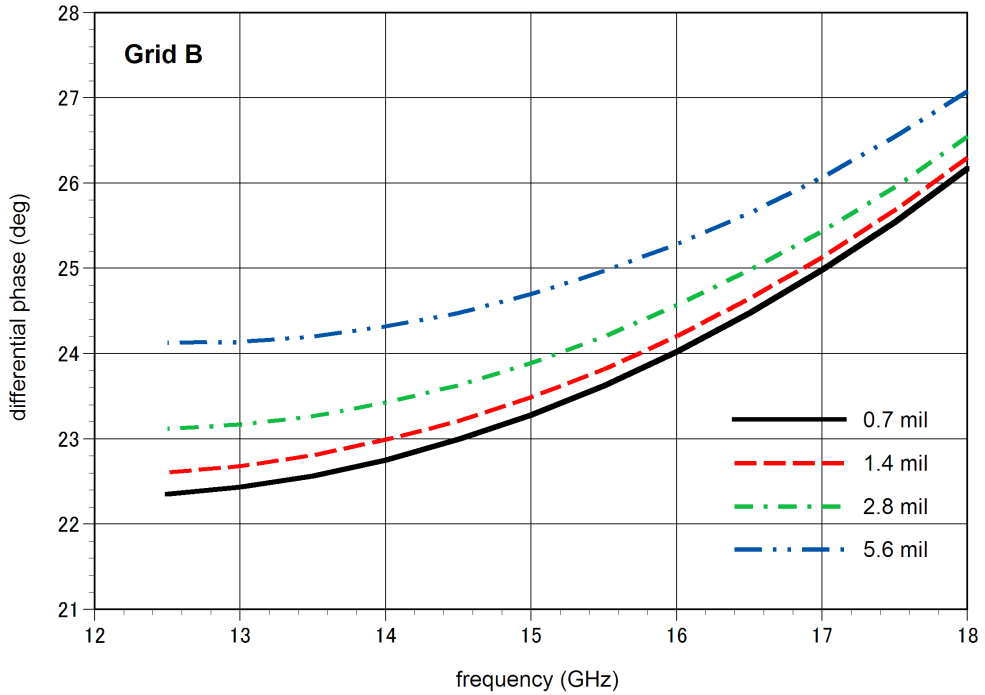

Figure 5.8: Effect of grid thickness on differential phase of Grid B – proposed method

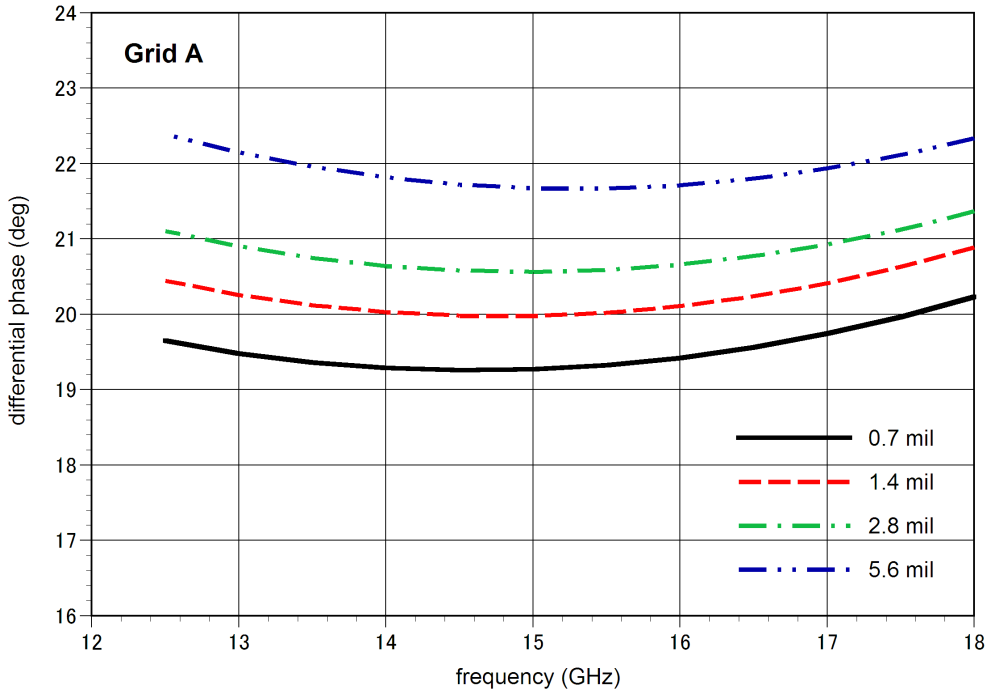

Figure 5.9: Effect of grid thickness on differential phase of Grid A – FEM

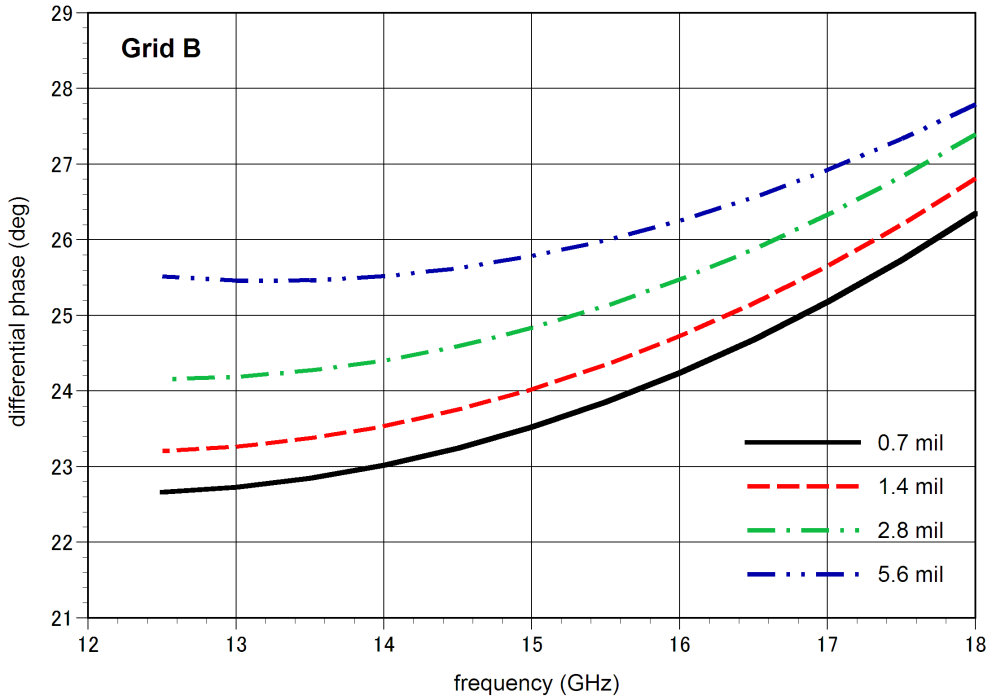

Figure 5.10: Effect of grid thickness on differential phase of Grid B – FEM

5.4.2 Multi-layer Polarizer

The axial ratio of the multi-layer polarizer for different grid metallization thickness are plotted in Figure 5.11. For frequencies below 13.5 GHz, the axial ratio of this polarizer can be improved by using copper weight of 1-oz. However, at higher frequencies, changing the copper weight from 0.5-oz to thicker metallization can degrade the axial ratio by up to 1.5 dB. Unlike the case for single layer polarizer, the relationship between metallization thickness and axial ratio / differential phase shift for a multi-layer polarizer is not straightforward. Therefore, an analysis method that can account for the finite grid thickness is especially important in order to achieve an optimized polarizer design. From the perspective of both numerical accuracy and computational efficiency, the proposed method is well suited to be a synthesis and analysis tool for microwave polarizer design.

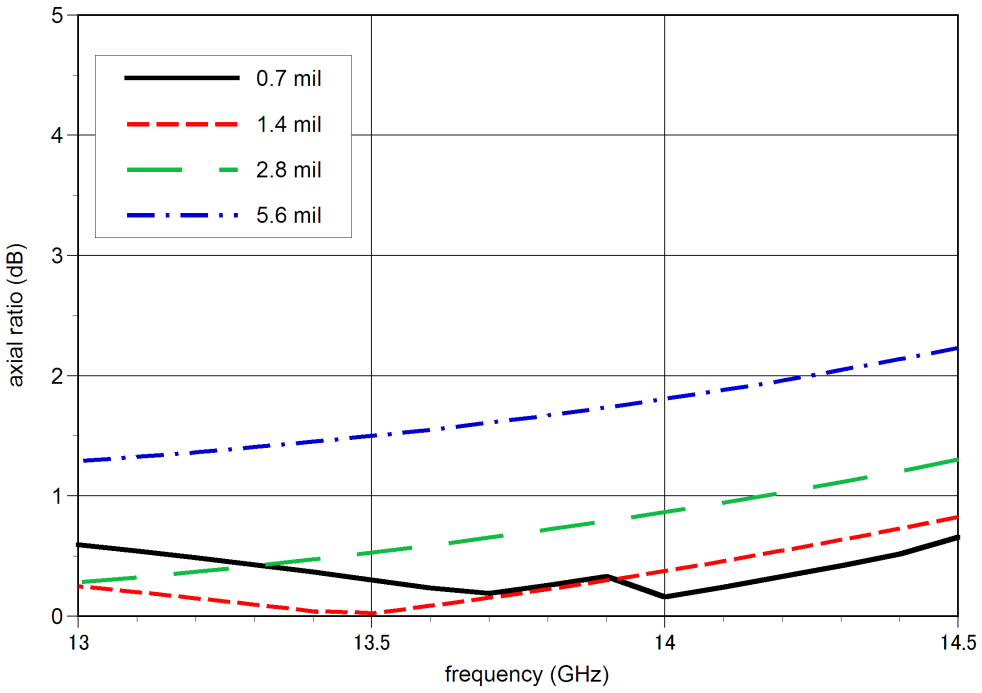

Figure 5.11: Effect of grid thickness on axial ratio of multi-layer polarizer

Chapter 6

Conclusions and Future Work

Effective design and implementation of microwave polarizers are important given the wide-ranging applications of polarizer in both commercial and military systems. This thesis presents research work on two important aspects: novel design of polarization rotator which is practical to implement and development of a numerical approach for accurate and efficient analysis of polarizer.

Polarization rotators, which are very useful in systems that requires polarization tracking capability, are complex and cumbersome to realize in practice because conventional design requires multiple rotating layers to achieve arbitrary rotation of polarization angle. A design that minimizes the number of rotating layers has far ranging impact as it will significantly reduce the overall system complexity. In this thesis, a polarization rotator design that utilizes two 90° polarizers and a linear grid constructed in a stacked configuration is proposed. This novel design can achieve arbitrary polarization rotation angle using one and at most two rotating layers while providing up to 25 dB cross polarization isolation required for VSAT applications. The viability of this design has been validated through simulation and measurement.

Effective design of microwave polarizer requires both accurate and efficient numerical modelling. Accuracy minimizes the number of fabrication iterations

required and efficiency determines the number of optimization cycle that can be carried out within a given schedule. For high performance microwave polarizer that demands good axial ratio performance, approaches based on grid current or moment method are unable to account for the finite thickness of the grid metallization; and it was shown that metallization thickness does have an impact on the performance of the polarizer.

To model the finite metallization thickness, methods such as the popular finite element method could theoretically be used. However, it was shown that as the number of grid layers increases, the computational time required using the finite element method increases tremendously. The reason is because the ratio of spacer to grid thickness is approximately two orders of magnitude and this requires very dense meshing around the grid metallization.

In this thesis, a new technique that utilizes transverse resonance technique coupled with singular value decomposition and generalized scattering matrix is proposed. The meanderline grids are first modelled as periodic finite length waveguides. Transverse resonance and SVD are then applied to determine the mode cutoff frequencies of the waveguides. GSM is then used to compute the interactions of both propagating and evanescent waveguide modes with the free-space Floquet modes. Comparison with measurements and FEM simulations showed that the proposed method is an accurate and efficient technique for the analysis and design of microwave polarizer.

6.1 Recommendations for Future Work

There is a constant need for better microwave polarizers as these are very cost effective solutions compared to alternatives such electronic polarization tuning. While this thesis has addressed challenges in polarizer design and analysis, there are a number of areas that can be investigated to further the work developed in this thesis,

1. Optimization of polarizer design. Today, design optimization algorithms are still mainly confined to variants of parametric search routines. Investigation and development of design rules will be very useful for achieving either faster convergence or better performing polarizers.
2. Analysis for off normal incidence. The proposed new technique for analysis of polarizer with finite metallization thickness is currently limited to on axis incidence. Extension to off axis incidence by including phase shift boundary conditions will enable design of microwave polarizer for scanning array.
3. Exploitation of additional degree of freedom. To date, all polarizer designs are based on the optimization of planar structures such as meanderline and linear grids. The additional degree of freedom that is now available from the proposed technique in this thesis can potentially enable development of higher performance microwave polarizer.

Bibliography

[1] P. W. Hannan. Microwave Antennas Derived from the Cassegrain Telescope. *IRE Trans. Antennas and Propagat.*, AP-9(2):140–153, March 1961.

[2] T. K. Wu and D. Helms. Wide-Angle-Scanning Polarization Twister. In *IEEE AP-S Int. Symp. Dig.*, pages 429–431, May 1983.

[3] K. K. Chan, F. Marcoux, M. Forest, and L. Martins-Camelo. A Circularly Polarized Waveguide Array for LEO Satellite Communications. In *IEEE AP-S Int. Symp. Dig.*, pages 154–157, July 1999.

[4] R. W. Martin and L. Schwartzman. A Rapid Wide-Angle Scanning Antenna with Minimum Beam Distortion. In *Proceedings of East Coast A.N.E. Conference*, 1958.

[5] O. B. Kesler, W. F. Montgomery, and C. C. Liu. A Millimeter-Wave Scanning Antenna for Radar Application. In *Proceedings Antenna Applications Symposium*, September 1979.

[6] R. Kastner and R. Mittra. A Spectral-Iteration Technique for Analyzing a Corrugated-Surface Twist Polarizer for Scanning Reflector Antennas. *IEEE Trans. Antennas and Propagat.*, AP-30(4):673–676, July 1982.

[7] D. Collier, M. Greenspan, D. MacFadyen, and L. Orwig. RF Propagation from a Flatplate Array Antenna with Polarizing Lenses. In *Proceedings Int. Radar Conference*, pages 219–223, May 1995.

[8] E. Ongareau, A. Roussaud, E. Marouby, and J. Levrel. Radar Cross-Section Reduction by Polarization Rotation. *Microwave and Optical Technology Letters*, 8(6):316–318, April 1995.

[9] C. Terret, J. R. Levrel, and K. Mahdjoubi. Susceptance Computation of a Meander Line Polarizer Layer. *IEEE Trans. Antennas and Propagat.*, AP-32:1007–1011, September 1984.

[10] R. S. Chu and K. M. Lee. Analytical Model of a Multilayered Meander Line Polarizer Plate with Normal and Oblique Plane-Wave Incidence. *IEEE Trans. Antennas and Propagat.*, AP-35:652–661, June 1987.

[11] K. K. Chan and S. R. Gauthier. Design of Meanderline Polarizer Based on Modal Technique. In *IEEE AP-S Int. Symp. Dig.*, pages 699–702, July 1992.

[12] K. K. Chan, S. R. Gauthier, and G. Dinham. A Broadband and Wide Angle Meanderline Polarizer. In *Proceedings of the 3rd Int. Conference on Electromagnetics in Aerospace Applications*, pages 171–174, September 1993.

[13] A. K. Bhattacharyya. Analysis of Multilayer Infinite Periodic Array Structures with Different Periodicities and Axes Orientations. *IEEE Trans. Antennas and Propagat.*, AP-48(3):357–369, March 2000.

[14] D. S. Lerner. A Wave Polarization Converter for Circular Polarization. *IEEE Trans. Antennas and Propagat.*, AP-13:3–7, January 1965.

[15] C. A. Hacking, D. J. Hall, and D. E. Wolf. Man/Machine Design of a Broadband Microwave Circular Polarizer. In *2nd Hawaii Int. Conf. System Sciences*, 1969.

[16] L. Young, L. A. Robinson, and C. A. Hacking. Meander-Line Polarizer. *IEEE Trans. Antennas and Propagat.*, AP-21:376–379, May 1973.

[17] A. K. Bhattacharyya. Investigation of Meanderline Polarizers. In *IEEE AP-S Int. Symp. Dig.*, pages 892–895, 1992.

[18] R. Mittra, C. H. Chan, and T. A. Cwik. Techniques for Analyzing Frequency Selective Surfaces – A Review. *Proc. IEEE*, 76:1593–1615, December 1988.

[19] R. A. Kipp and C. H. Chan. A Numerically Efficient Technique for the Method of Moments Solution for Planar Periodic Structures in Layered Media. *IEEE Trans. Microwave Theory Techniques*, MTT-42(4):635–643, April 1994.

[20] C. H. Chan. A Numerically Efficient Technique for the Method of Moments Solution of Electromagnetic Problem Associated with Planar Periodic Structures. *Microwave Optical Technology Letter*, 1:372–374, December 1988.

[21] C. H. Chan and R. Mittra. On the Analysis of Frequency Selective Surfaces Using Subdomain Basis Functions. *IEEE Trans. Antennas and Propagat.*, 38:40–50, January 1990.

[22] R. M. Shubair and Y. L. Chow. A Rapidly Convergent Summation of the Periodic Green's Function in Layered Media. *IEEE AP-S Int. Symp. Dig.*, 1:200–203, July 1992.

[23] T. L. Blackney, J. R. Burnett, and S. B. Cohn. A Design Method for Meander-line Circular Polarizers. In *22nd Antenna Application Symp.*, pages 1–5, October 1972.

[24] S. Uckin and T. Ege. Computation of Susceptance for Thick Meander-Line Polarizer. *IEE Electronics Letters*, pages 2076–2077, October 1991.

[25] K.M.K.H. Leong and W. A. Shiroma. Waffle-Grid Polarizer. *IEE Electronics Letters*, 38(22):1360–1361, October 2002.

[26] C. C. Chen. Scattering by a Two-Dimensional Periodic Array of Conducting Plates. *IEEE Trans. Antennas and Propagat.*, AP-18:660–665, September 1970.

[27] J. P. Montgomery. Scattering by an Infinite Periodic Array of Thin Conductors on a Dielectric Sheet. *IEEE Trans. Antennas and Propagat.*, AP-23:70–75, January 1975.

[28] R. A. Marino. Accurate and Efficient Modeling of Meander-line Polarizers. *Microwave Journal*, pages 22–30, November 1998.

[29] B. S. Abbe, R. E. Frye, and T. C. Jedrey. ACTS Mobile Satcom Experiments. In *Proc. 3rd Int. Mobile Satellite Conf.*, pages 225–230, June 1993.

[30] A. Densmore, V. Jamnejad, T. K. Wu, and K. Woo. K/Ka-band Antenna System for Mobile Satellite Service. In *IEEE AP-S Int. Symp. Dig.*, pages 124–127, June 1993.

[31] R. Baggen, S. Voccaro, and D. L. del Rio. Design Considerations for Compact Mobile Ku-Band Satellite Terminals. In *EuCAP2007*, pages 1–5, November 2007.

[32] S. Hasegawa, T. Yasuzumi, O. Hashimoto, and Y. Kazama. Polarization Tracking Phased Array Antenna with Cross Dipole Antenna. In *IEEE AP-S Int. Symp. Dig.*, pages 1–5, June 2009.

[33] D. L. Adamy. *EW 101: A First Course in Electronic Warfare*. Artech House, Massachusetts, 2001.

[34] H. Zhang and Z. Du. A Novel Countermeasure to Polarization Interference for Circular Polarization Phased Array Radar. In *CIE International Conference on Radar Proceedings*, pages 453–455, August 2001.

[35] E. Orleansky, C. Samson, and M. Havkin. A Broadband Meander-line Twist Rflector for the Inverse Cassegrain Antenna. *Microwave Journal*, pages 185–192, October 1987.

[36] B. Gimeno, J. L. Cruz, E. A. Navarro, and V. Such. A Polarizer Rotator System for Three-Dimensional Oblique Incidence. *IEEE Trans. Antennas and Propagat.*, AP-42(7):912–919, July 1994.

[37] R. P. Torres and M. F. Catedra. Analysis and Design of a Two-Octave Polarization Rotator for Microwave Frequency. *IEEE Trans. Antennas and Propagat.*, AP-41(2):208–213, February 1993.

[38] R. Lech, M. Mazur, and J. Mazur. Analysis and Design of a Polarizer Rotator System. *IEEE Trans. Antennas and Propagat.*, AP-56(3):844–847, March 2008.

[39] T. K. Wu. Meander-Line Polarizer for Arbitrary Rotation of Linear Polarization. *IEEE Microwave and Guided Wave Letters*, 4(6):316–318, June 1994.

[40] N. Amitay, V. Galindo, and C. P. Wu. *Theory and Analysis of Phased Array Antennas*. Wiley-InterScience, New York, 1972.

[41] G. Floquet. Sur les équations différentielles linéaires á coefficients périodiques. *Annales de l'École Normale Supérieure*, 12:47–88, 1883.

[42] R. F. Harrington. *Time-Harmonic Electromagnetic Fields*. McGraw-Hill, New York, 1961.

[43] W. H. Kummer and E. S. Gillespie. Antenna Measurements – 1978. *Proceedings of the IEEE*, 66(4):483–507, 1978.

[44] H. Y. Yee. Transverse Modal Analysis for Printed Circuit Transmission Lines. *IEEE Trans. Microwave Theory Techniques*, MTT-33:808–816, September 1985.

[45] C. A. Olley and T. E. Rozzi. Systematic Characterization of the Spectrum of Unilateral Finline. *IEEE Trans. Microwave Theory Techniques*, MTT-34 (11):1147–1156, November 1986.

[46] G. Figlia and F. Mercurio. A New Method for Microwave Cascade Networks. In *Proceedings Antenna Applications Symposium*, June 1989.

[47] J. L. Lynch and J. S. Colburn. Modeling Polarization Mode Coupling in Frequency-Selective Surfaces. *IEEE Trans. Microwave Theory Techniques*, MTT-52(4):1328–1338, April 2004.

[48] R. E. Collin. *Field Theory of Guided Waves*. Wiley-IEEE Press, New York, 1990.

[49] W. H. Press, S. A. Teukolsky, W. T. Vetterling, and B. P. Flannery. *Numerical Recipes: The Art of Scientific Computing*. Cambridge University Press, New York, 1992.

[50] K. K. Chan, T. W. Ang, T. H. Chio, and T. S. Yeo. Accurate Analysis of Meanderline Polarizers with Finite Thickness using Mode Matching. *IEEE Trans. Antennas and Propagat.*, AP-56(11):3580–3585, November 2008.

[51] G. H. Golub and C. F. Van Loan. *Matrix Computations*. The Johns Hopkins University Press, Maryland, 1996.

[52] G. Strang. *Introduction to Linear Algebra.* Wellesley-Cambridge Press, Massachusetts, 2005.

[53] R. Mittra and S. W. Lee. *Analytical Technique in the Theory of Guided Waves.* Macmillan, New York, 1971.

[54] S. W. Lee, W. R. Jones, and J. J. Campbell. Convergence of Numerical Solutions of Iris-Type Discontinuity Problems. *IEEE Trans. Microwave Theory Techniques*, MTT-19:528–536, June 1971.

[55] R. Mittra, T. Itoh, and T. S. Li. Analytical and Numerical Studies of the Relative Convergence Phenomenon Arising in the Solution of an Integral Equation by the Moment Method. *IEEE Trans. Microwave Theory Techniques*, MTT-20:96–104, February 1972.

[56] Y. C. Shih and K. G. Gray. Convergence of numerical solutions of step-type waveguide discontinuity problems by modal analysis. *IEEE Microwave Theory Tech. Int. Symp. Dig.*, pages 233–235, 1983.

[57] G. Schiavon, R. Sorrentino, and P. Tognolatti. Characterization of Coupled Finlines by Generalized Transverse Resonance Method. *Int. J. Numerical Model*, 1:45–59, March 1988.